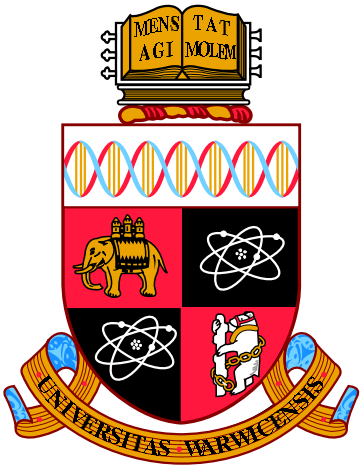

Optical imaging of space debris in low and high altitude orbits

by

James Anthony Blake

Thesis

Submitted to the University of Warwick

for the degree of

Doctor of Philosophy

Department of Physics

April 2021

Contents

List of Tables

List of Figures

Acknowledgments

First of all, I would like to thank my supervisor, Don Pollacco, for giving me the opportunity to work in such an exciting and thriving field. Six years ago, I first approached him as a wide-eyed, second-year undergraduate in search of something to do with my summer break. Three research projects and a PhD later, his unwavering support continues to shape me into the scientist I have always aspired to be. He has helped me through some of the toughest times I've faced, both personally and professionally, always giving me the freedom I needed, while never failing to remind me that everything has a deadline! Special thanks are also owed to Paul Chote, for the countless discussions that have taken place at times that make "out-of-office" seem like an understatement. Thank you for the knowledge you've shared, for showing me the sights of La Palma, and for making this thesis possible.

I am grateful to our collaborators at Dstl, in particular to Will Feline and Grant Privett for their assistance and company during the DebrisWatch-INT observing run. Thanks also to: the folks at ESA Academy for giving me the opportunity to learn from experts in the field during my trip to Belgium, and the many young, like-minded scientists I met there; the AMOS Conference organisers in Maui for inviting me back to co-chair multiple sessions, giving me the opportunity to be a part of the EMERGEN cohort, and providing me the platform I needed to network and establish myself within the field; Katherine and the Steering Board of GNOSIS for welcoming me as secretary, alongside Stuart and Dinz for a number of insightful conversations throughout.

I would also like to thank the members of both the Astronomy and Astrophysics Group, and the wider Department of Physics as a whole, who have made

my time here fun and enjoyable, come rain or pandemic. I am grateful to Dave Armstrong, David Brown, James McCormac, Elizabeth and Dimitri for all the wisdom they've imparted over the years. Thank you to James Jackman, Elena, Tim, George, et al., for making the back office a really fun place to work, and to the "Telescopes 'R' Us" team for providing a far less distracting environment in the latter stages of my PhD!

I am truly grateful to my parents and grandparents for all their love and support, through the good, the bad and the ugly! Thank you to Hoskin, Beaum, all the other members of the Linux Minted quiz team, and friends from past and present that have somehow managed to keep me sane in recent years. Finally, thank you to my partner, Helen, for the love and kindness she's shown me in these past few months of writing.

The work presented herein was funded by the Science and Technology Facilities Council (Grant number: ST/R505195/1). I am also grateful to the Royal Astronomical Society, Warwick Ventures and the Maui Economic Development Board for awarding me additional travel grants during my PhD.

Declarations

I submit this thesis to the University of Warwick Doctoral College for the degree of Doctor of Philosophy. I declare that the work contained herein is my own original research, except where stated otherwise, carried out in the period October 2017 to March 2021, under the supervision of Prof. Don Pollacco. The contents of this thesis have not previously been submitted to the University of Warwick, nor any other institution, for another degree.

The work in Chapter 3 is based on findings that I presented at the 2019 Advanced Maui Optical and Space Surveillance Technologies Conference in the technical proceeding, Blake et al. [2019], which won the award for Best Student Paper, and associated poster. The material was later adapted and published as the paper, Blake et al. [2021]. Time on the Isaac Newton Telescope was awarded upon the successful review of a proposal drafted by Don Pollacco (University of Warwick), with named collaborators: myself, Paul Chote, Tom Marsh, Dimitri Veras (University of Warwick); Stuart Eves (SJE Space Ltd); and Chris Watson (Queen's University Belfast). Much of the analysis presented in Section 3.4.3 takes inspiration from the findings of Chote [2020]; elements of reproduced or extended work are included with the author's permission, and clearly indicated in the chapter, where appropriate.

The works in Chapters 3 and 6 form separate instalments of DebrisWatch, an ongoing collaboration between the University of Warwick and the Defence Science and Technology Laboratory (Dstl, UK). Paul Chote and myself were accompanied by collaborators at Dstl, Will Feline and Grant Privett, for the observing run, both of whom assisted with initial eye-balling of the survey frames. The control script that was used to carry out observational sequences and synchronise instruments for

the DebrisWatch survey was developed by Paul Chote. Collaborators at Dstl, Will Feline and Nick Harwood, performed the correlation between orbital arcs detected by the survey and known objects in the publicly available USSPACECOM catalogue. The DebrisWatch instalment presented in Chapter 6 is based on the 2020 AMOS Conference technical proceeding, Blake et al. [2020a], and associated poster. Elements of the discussion in this chapter are also explored in the technical reports, Chote et al. [2020] and Chote [2020].

In Chapter 4, I provide an overview of early contributions to the light curve surveys described in the 2019 AMOS Conference technical proceeding, Chote et al. [2019], and associated poster. The presented observations were carried out by myself, including the target selection, scheduling and data reduction procedures referenced in the chapter, following training from Paul Chote. The image processing pipelines that are briefly outlined in the chapter were written and developed by Paul Chote, who led the aforementioned study.

The work in Chapter 5 is based on the technical report, Blake et al. [2020b], which served as a deliverable for GEOMON, a Phase 1 Defence and Security Accelerator (DASA) project, carried out by members of the Warwick Satellites Group, in contract with Harwell Associates Ltd. The observational datasets used as test cases for the `tlemcee` orbit refinement algorithm were sourced from the light curve surveys introduced in Chapter 4, acquired during the full survey operations that were overseen by Paul Chote. The analysis pipelines described in Chote et al. [2019] were used to extract the orbital arcs and their associated light curves from the available observations.

Elements of the work presented in this thesis have also formed the basis for a number of additional research talks, seminars and poster presentations:

- "*The Sticky Issue of Space Debris*":
  - Loughton Astronomical Society, UK (talk, 2021);
  - Newbury Astronomical Society, UK (talk, 2021);
  - GoSpaceWatch, UK (talk, 2021).

- "*Monitoring the Mess of Near-Earth Space*":
  - SERENE Group, University of Birmingham, UK (seminar, 2020);
  - Birmingham Astronomical Society, UK (talk, 2020);
  - Warwick Astronomy Society, University of Warwick, UK (talk, 2019).
- "*DebrisWatch: Eyes on the Sky*":
  - Royal Astronomical Society Poster Exhibition, UK (poster, 2020).
- "*A Watchful Eye on the Sky*":
  - NASA Jet Propulsion Laboratory, California, US (talk, 2019);
  - University of California, Irvine, California, US (seminar, 2019);
  - Warwick Aerospace Society, University of Warwick, UK (talk, 2019).
- "*Applying Astronomical Tools and Techniques to SSA*":
  - National Astronomy Meeting, Lancaster University, UK (talk, 2019).
- "*The Warwick DebrisWatch Campaign*":
  - Royal Astronomical Society Specialist Meeting, UK (poster, 2018).

Abstract

The past six decades of space exploration have taken their toll on the safety of satellite operations in near-Earth space. A large population of mission-threatening debris has accumulated in key orbital regions, comprising a mixture of abandoned spacecraft, fragments from collisions or explosions, and mission-related objects that no longer serve a purpose. Of particular concern is the situation in low Earth orbit (LEO), where certain bands are expected to be on the cusp of a "Kessler" cascade, whereby collisional fragments seed further collisions, and so on. Large LEO constellations look set to place an even greater strain on space surveillance systems, with several thousand spacecraft licenced to launch over the coming decade. That said, the problem is by no means limited to the LEO region. Indeed, the population of small debris at geosynchronous (GSO) altitudes remains largely uncharacterised, owing to the limited time available on sufficiently sensitive sensors.

A wide variety of solutions have been posed across different sectors, from the drafting of universal debris mitigation guidelines, to the development of *in situ* technologies for servicing or removing spacecraft. Meanwhile, it is essential that the debris environment continues to be probed by surveillance sensors, in order to better inform future avenues for research into the safe and sustainable use of outer space. This thesis explores a number of ways in which optical imaging can contribute to enhanced levels of space situational awareness, using datasets acquired by a selection of instruments at the Roque de los Muchachos Observatory on La Palma.

The 2.54 m Isaac Newton Telescope was used to conduct a blind survey of the GSO region, uncovering debris fragments too faint to be reliably tracked and catalogued by the US Space Surveillance Network. Photometric light curves were extracted from the survey frames, and many of the detected objects were found to exhibit signs of rapid tumbling. Simultaneous observations of the survey fields were acquired using a 36 cm robotic astrograph. A comparative analysis of the resulting datasets was performed to investigate the benefits of pairing a large aperture telescope with a wide-field commercial-off-the-shelf instrument when tasked with surveying the GSO region. In two further surveys, the repurposed SuperWASP-North array and the astrograph were used to carry out targeted observations of catalogued LEO and GSO spacecraft, respectively. Light curves were extracted from early prototype observations, and orbital arcs from the surveys were used as case studies to test a custom orbit refinement algorithm.

Abbreviations

ADR Active Debris Removal

ADU/C Analog-to-Digital Unit/Converter

AFSPC Air Force Space Command

AIUB Astronomical Institute of the University of Bern

AMOS Advanced Maui Optical and Space Surveillance Technologies [Conference]

APASS All-Sky Photometric Survey

ASAT Anti-Satellite

CCD Charge-Coupled Device

CDT CCD Debris Telescope

COTS Commercial-off-the-Shelf

CSpOC Combined Space Operations Center

DASA Defence and Security Accelerator

DISCOS Database and Information System Characterising Objects in Space

DoD Department of Defence

Dstl Defence Science and Technology Laboratory

DW DebrisWatch

EGO Extended Geosynchronous Orbit

EO Electro-Optical

EOARD European Office of Aerospace Research and Development

EOL End-Of-Mission/Life

ESA European Space Agency

FOV Field of View

GEO Geostationary [Orbit]

GEODSS Ground-Based Electro-Optical Deep Space Surveillance

GLONASS [Russian] Global Satellite Navigation System

GNSS Global Navigation Satellite System

GOES Geostationary Operational Environmental Satellite

GPS Global Positioning System

GSO Geosynchronous [Orbit]

GSOPR Geosynchronous Protected Region

GTO Geosynchronous Transfer Orbit

HAMR High Area-to-Mass Ratio

HEO Highly Eccentric Orbit

IADC Inter-Agency Space Debris Coordination Committee

IGO Inclined Geosynchronous Orbit

INT Isaac Newton Telescope

IOD Initial Orbit Determination

IRAS Infrared Astronomical Satellite

ISON International Scientific Optical Network

ISS International Space Station

KIAM Keldysh Institute of Applied Mathematics

LEO Low Earth Orbit

MASTER Meteoroid and Space Debris Terrestrial Environment Reference

MCAT Meter-Class Autonomous Telescope

MCMC Markov Chain Monte Carlo [Method]

MEO Medium Earth Orbit

MEV Mission Extension Vehicle

MODEST Michigan Orbital Debris Survey Telescope

MRO Mission-Related Object

NASA National Aeronautics and Space Administration

NEO Near-Earth Object

NORAD North American Aerospace Defence Command

ODMSP Orbital Debris Mitigation Standard Practices

OMM Orbit Mean-Elements Message

ORDEM Orbital Debris Engineering Model

Pan-STARRS Panoramic Survey Telescope and Rapid Response System

PMD Post-Mission Disposal

PSF Point Spread Function

QE Quantum Efficiency

RAAN Right Ascension of the Ascending Node

RASA Rowe Ackermann Schmidt Astrograph

RCS Radar Cross Section

RMS Root Mean Square

RORSAT Radar Ocean Reconnaissance Satellite

sCMOS Scientific Complementary Metal-Oxide Semiconductor [device]

SDA Space Domain Awareness

SDP Simplified Deep Space Perturbations [Model]

SGP Simplified General Perturbations [Model]

SNR Signal-to-Noise Ratio

SP Simplified Perturbations

[18] SPCS [18^{th}] Space Control Squadron

SRP Solar Radiation Pressure

SSA Space Situational Awareness

SSN Space Surveillance System

TCS Telescope Control System

TLE Two-Line Element [Set]

UNCOPUOS United Nations Committee on the Peaceful Uses of Outer Space

USAF United States Air Force

USSF United States Space Force

USSPACECOM United States Space Command

USSTRATCOM United States Strategic Command

WASP Wide Angle Search for Planets

WCS World Coordinate System

WFC Wide Field Camera

Chapter 1

Introduction

There's so many different worlds, so many different suns.
And we have just one world, but we live in different ones.

–Mark Knopfler, Dire Straits - *Brothers in Arms*
from the album *Brothers in Arms*, 1984

On 4$^{\text{th}}$ October 1957, the Soviet Union launched the first artificial satellite into space: Sputnik 1. While the pioneering spacecraft orbited the Earth for a mere three months, its mission paved the way for an era of exploration that has endured to the present day. The Space Age has brought about a host of remarkable developments in science and technology, oftentimes influencing society from both a political and cultural perspective. As a society, we have become heavily reliant on the satellites that have been launched into Earth orbit for a wide variety of applications, including communication, navigation and weather monitoring. Alongside these essential day-to-day services, satellites afford us the opportunity to carry out astronomical observations that are unobstructed by the Earth's atmosphere, monitor the Earth itself for civil and military purposes, and conduct a variety of space-based experiments and crewed missions aboard space stations.

However, as has historically been the case for much of human exploration, a great deal of mess has accrued in our wake. The issue of orbital debris is one that requires prompt attention on a global scale. In a similar vein to climate change, the problem can only truly be alleviated by the universal cooperation of actors in space. More comprehensive and effective space situational awareness (SSA) is necessary, in order to avoid collisions between active satellites and mission-threatening debris, and to maintain a sustainable use of space. This thesis explores the ways in which optical telescopes can contribute to improved SSA.

1.1 Near-Earth orbital regimes

An object in orbit around the Earth follows a curved trajectory, primarily governed by the gravitational interaction between the two bodies. As the orbiting body's mass is small compared to that of the Earth, its motion can be described by Newton's equation for the unperturbed two body problem [Klinkrad, 2006],

$$\ddot{\mathbf{r}} = -\frac{\mu}{r^3}\mathbf{r}, \tag{1.1}$$

where $\ddot{\mathbf{r}}$ is the acceleration vector, $\mu \approx 3.986 \times 10^{14}\,\mathrm{m^3 s^{-2}}$ is the standard gravitational parameter, $\mathbf{r}$ is the geocentric position vector and r is the scalar distance between the two bodies. The dynamics of the unperturbed two body problem give rise to Kepler's laws and result in a planar motion mapping out a conic section, such as a circle or an ellipse.

In reality, the orbits of satellites and debris are influenced by a variety of perturbative forces, acting in addition to the Earth's gravitational pull. The force of gravity itself warrants a more detailed treatment, owing to asymmetries in the gravitational field that arise from the Earth's non-spherical shape and non-uniform density (see Section 1.3.1), alongside solar/lunar third body effects. Aerodynamic perturbations can have a significant impact on low altitude orbits, which evolve on rapid timescales due to the dissipative effects of atmospheric drag (see Section 1.1.1), while higher altitude orbits are more severely affected by solar radiation pressure (SRP). The complex orbital environment that results from this perturbative blend poses a variety of challenges from both a modelling and observational perspective, many of which are discussed further in Section 1.2.2.

The orbital state vector $(\mathbf{r}, \mathbf{v})$, where $\mathbf{v} = \dot{\mathbf{r}}$, at any given time, uniquely specifies the motion of an orbiting body, though the orbits of satellites and debris are commonly quoted in terms of the Keplerian orbital elements (e, a, i, Ω, ω, θ), illustrated in Fig. 1.1. The eccentricity e and semi-major axis a govern the shape and extent of the orbital ellipse, respectively. For geocentric orbits, the semi-major axis stems from the Earth's centre, while the orbital altitude Z is instead measured from the Earth's surface. If the orbit is non-circular, yet closed, it is common to reference the perigee Z_p and apogee Z_a altitudes, corresponding to the closest and farthest point from the Earth, respectively. The ascending node is where the orbit ascends through the plane of reference (the equatorial plane), and the right ascension of the ascending node Ω orients the orbital ellipse within that plane, relative to the reference direction (the vernal equinox). The inclination i defines the tilt angle between the orbital plane and the reference plane, while the argument of perigee ω

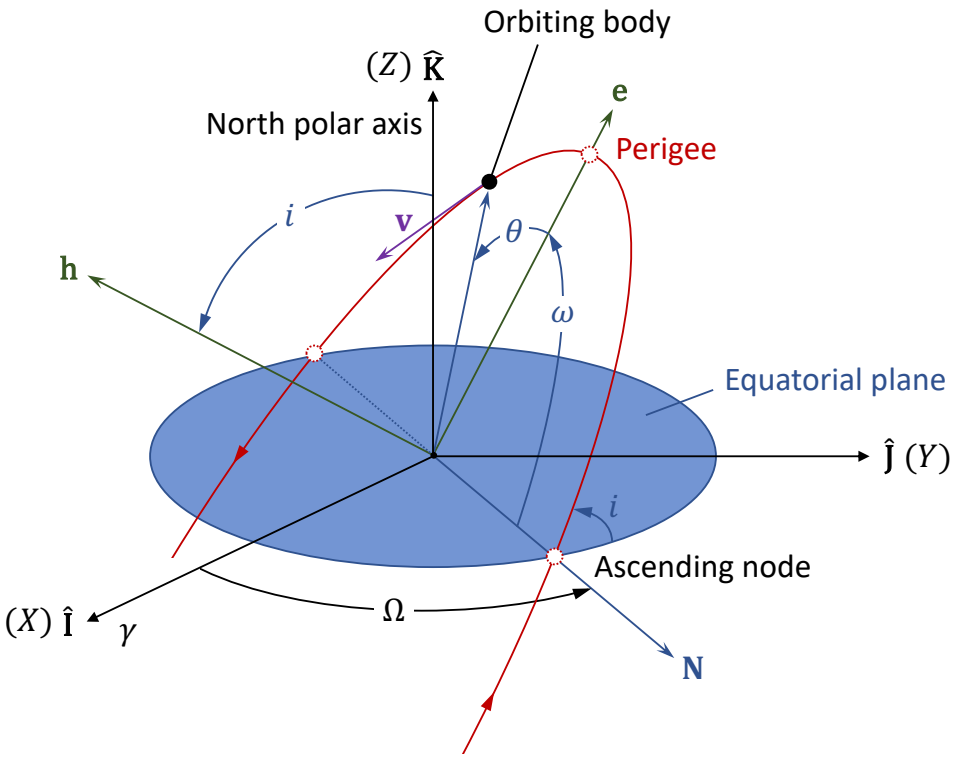

Figure 1.1: The Keplerian orbital elements in the context of the geocentric equatorial frame. The equatorial plane (blue) acts as the plane of reference XY. The vernal equinox γ serves as the frame's reference direction X. An orbiting body (black dot) is shown traversing its orbit (red) with a velocity vector $\mathbf{v}$. The eccentricity $\mathbf{e}$ and specific angular momentum $\mathbf{h}$ vectors, which govern the semi-major axis a, are illustrated alongside the four angular parameters: inclination i, right ascension of the ascending node Ω, argument of perigee ω and true anomaly θ.

gives the angle between the ascending node and the orbital perigee. Finally, the true anomaly θ specifies the position of the orbiting body along the orbit at a particular epoch.

Over time, a plethora of near-Earth orbital regimes have become populated with artificial objects, as operators have learned to exploit their unique and desirable characteristics for a variety of purposes. A scale map of the most populous regions is provided in Fig. 1.2, while Table 1.1 lists standard definitions for orbital regimes that are referenced frequently throughout the work presented herein.

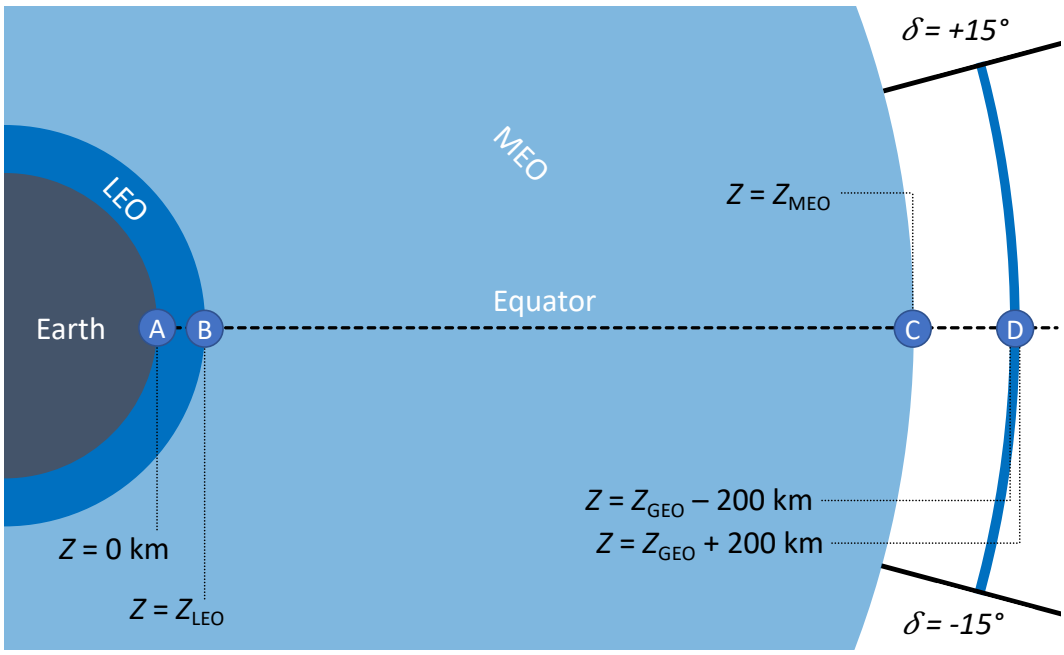

Figure 1.2: A scale map of the most populous near-Earth orbital regions. Low Earth orbits (LEO) reside within a spherical shell spanning the altitude range $0 < Z < Z_{\mathrm{LEO}}$, where $Z_{\mathrm{LEO}} = 2000\,\mathrm{km}$. Medium Earth orbits (MEO) reside within a spherical shell spanning the altitude range $Z_{\mathrm{LEO}} < Z < Z_{\mathrm{MEO}}$, where $Z_{\mathrm{MEO}} = 31570\,\mathrm{km}$. The geosynchronous region can be defined in several ways, depending on the sub-categories of orbits that are included (see Table 1.1). The geosynchronous Protected Region (discussed further in Section 1.2.4) is a segment of a spherical shell spanning the altitude range $Z_{\mathrm{GEO}} - 200\,\mathrm{km} < Z < Z_{\mathrm{GEO}} + 200\,\mathrm{km}$, where $Z_{\mathrm{GEO}} = 35786\,\mathrm{km}$ is the geostationary (GEO) altitude, and the declination range $-15° < \delta < +15°$ relative to the equatorial plane of the Earth.

1.1.1 Low Earth orbit

The low Earth orbit (LEO) region is where the majority of artificial satellites are based. To date, all crewed space station missions have taken place in LEO, most famously the International Space Station (ISS), possessing a modular structure that has been continuously occupied for over 20 years.

A comparatively low amount of energy is required for a satellite to be placed in LEO, as a result of its proximity to the Earth's surface. Satellites in LEO can achieve low signal latencies; light travelling from the ISS altitude would take just over 1 ms to reach the Earth's surface, an order of magnitude improvement on the delays associated with submarine cables. That said, low altitudes result in limited fields of view at any given time, thus constellations of LEO satellites are necessary

Table 1.1: A selection of near-Earth orbital regimes populated by artificial objects. Ranges defining the orbital regimes are given in terms of semi-major axis, eccentricity, inclination, declination δ, perigee altitude and apogee altitude, as sourced from ESA [2020].

Abbr.	Orbit Type	Definition
GEO	Geostationary Orbit	$i = 0$;
		$Z_\mathrm{p} = Z_\mathrm{a} = 35786$.
GSO	Geosynchronous Orbit	$i \in [0, 25]$;
		$Z_\mathrm{p} \in [35586, 35986]$;
		$Z_\mathrm{a} \in [35586, 35986]$.
GSOPR	Geosynchronous Protected Region	$\delta \in [-15, +15]$;
		$Z_\mathrm{p} \in [35586, 35986]$;
		$Z_\mathrm{a} \in [35586, 35986]$.
IGO	Inclined Geosynchronous Orbit	$a \in [37948, 46380]$;
		$e \in [0.00, 0.25]$;
		$i \in [25, 180]$.
EGO	Extended Geosynchronous Orbit	$a \in [37948, 46380]$;
		$e \in [0.00, 0.25]$;
		$i \in [0, 25]$.
GTO	Geosynchronous Transfer Orbit	$i \in [0, 90]$;
		$Z_\mathrm{p} \in [0, 2000]$;
		$Z_\mathrm{a} \in [31570, 40002]$.
MEO	Medium Earth Orbit	$Z_\mathrm{p} \in [2000, 31570]$;
		$Z_\mathrm{a} \in [2000, 31570]$.
LEO	Low Earth Orbit	$Z_\mathrm{p} \in [0, 2000]$;
		$Z_\mathrm{a} \in [0, 2000]$.
HEO	Highly Eccentric Orbit	$Z_\mathrm{p} \in [0, 31570]$;
		$Z_\mathrm{a} > 40002$.

to achieve continuous coverage for on-ground service provision, such as the network of more than 70 active satellites operated by Iridium Communications Inc[1].

Objects orbiting within the LEO region are subjected to an atmospheric drag force caused by collisions with gas molecules in the upper atmosphere (thermosphere and exosphere). The lower the altitude of a given satellite, the denser the surrounding atmosphere and thus more significant the drag force acting upon it. For this reason, satellites in the lower bands of LEO require regular station-keeping boosts to counteract the orbital decay induced by atmospheric drag. In LEO, an uncontrolled object's orbit will continue to decay until it re-enters the atmosphere, either burning up or returning to the Earth's surface. In this sense, the LEO region has a natural sink for debris. Objects with a high area-to-mass ratio (HAMR) will decay more quickly. For example, the two experimental payloads released as part of the RemoveDebris mission (see Section 1.2.4) re-entered the atmosphere after several months of decay, following their deployment at the $\sim$ 400 km altitude of the ISS [Aglietti et al., 2020]. Orbital decay was accelerated for the first payload as a result of an increased area brought about by towing a bundle of entangled netting that had played a part in its demonstration. The rate of decay is also dependent on external factors, such as the solar cycle; at solar maximum, the increase in irradiation from ultraviolet rays heats and expands the atmosphere's envelope, increasing the drag force for a given altitude band and thus accelerating orbital decay [Lewis et al., 2011]. At the solar maximum, station-keeping manoeuvres may be required every few weeks, while timescales of months are typical during the solar minimum [Doornbos and Klinkrad, 2006].

Polar and sun-synchronous orbits

A popular choice of orbit for LEO operators is the polar orbit, enabling the satellite to pass over both the North and South poles of the Earth, intersecting a different longitude at the Equator on each revolution. Satellites in polar orbits are thus well suited to Earth-mapping activities, including observations, reconnaissance and telecommunications; the aforementioned Iridium constellation makes use of polar orbits for the latter, residing at an altitude of around 780 km.

For many remote sensing satellites, the near-polar sun-synchronous orbit is preferred. Sun-synchronous orbits utilise precession with a year-long period to ensure that the illumination angle remains approximately the same every time the satellite passes a given ground site. Typically, sun-synchronous satellites are placed

[1]The factsheet downloadable via https://www.iridium.com/network/ specifies 66 Iridium constellation satellites and 9 spares in orbit (accessed March 2021)

within the 700–800 km altitude band, with inclinations of roughly 98°, resulting in an orbital period of around 100 minutes. The unique properties offered by sun-synchronous orbits have led to this altitude–inclination band becoming one of the most densely populated in LEO, and consequently one of particular concern from an orbital debris perspective.

1.1.2 Geosynchronous orbit

The geosynchronous (GSO) region comprises prograde, low-inclination orbits that match the rotational period of the Earth, such that one revolution takes one sidereal day ($23^{\mathrm{h}}56^{\mathrm{m}}04^{\mathrm{s}}$). As a result, GSO satellites appear to remain near-fixed at a given longitude on Earth, tracing out a simple closed analemma (e.g., an ellipse or figure-of-eight) and returning to the same point in the sky at the same time each day. A brief overview of the key types of GSO orbits is given below. A more detailed introduction to the GSO region is provided in Section 1.3, covering the relevant background for much of the work contained herein.

Geostationary orbit

A geostationary (GEO) orbit is a special case of a GSO orbit, with both an eccentricity and inclination of zero. The concept of a GEO orbit was first popularised by Arthur C. Clarke who, in his 1945 article "Extra-Terrestrial Relays: Can Rocket Stations Give World-wide Radio Coverage?", highlighted the potential uses of such a vantage point in space [see Clarke, 1966]. For this reason, the circular belt of GSO orbits that lies within the equatorial plane of the Earth is often referred to as the "Clarke belt" in popular culture, though "GEO belt" will be used here.

Satellites within the GEO belt are at rest relative to the Earth's rotation, and thus appear as fixed points in the sky, enabling tracking with ground-based fixed direction antennas [Kelso, 1998]. This, alongside the impressive coverage afforded by their high altitude, makes GEO satellites an attractive option for telecommunications operators. However, the high altitude of the GEO belt also gives rise to a high signal latency, two orders of magnitude higher than that of the LEO region, meaning that GEO communications satellites are predominantly limited to unidirectional activities in their service provision.

A number of navigation payloads reside in the GEO belt, designed to augment global navigation satellite systems (GNSS) by supplying an additional reference signal and relaying error corrections. GNSS provide users with positional estimates based on the triangulation of signal travel times between multiple satel-

lites and a network of ground-based receivers [see e.g., Hofmann-Wellenhof et al., 2007; Dautermann, 2014]. Notable examples of GEO augmentation systems include the US Wide Area Augmentation System, the European Geostationary Navigation Overlay Service and the Russian System for Differential Correction and Monitoring [Enge et al., 1996; Lawrence et al., 2007; Siergiejczyk et al., 2013]. Several meteorological satellite networks also occupy the GEO belt, including the US Geostationary Operational Environmental Satellite (GOES) series, the European Meteosats, the Chinese Fengyun satellites and the Russian Elektro-L spacecraft [Menzel and Purdom, 1994; Schmetz et al., 2002; Tan, 2013].

Transfer orbit

Payloads are injected into the GSO region using a GSO transfer orbit (GTO). With perigees in LEO and apogees in the GSO region, GTOs qualify both as highly eccentric orbits (HEOs), and Hohmann transfer orbits, namely elliptical orbits that can be used to transition from one circular orbit to a second of different radius, each residing in the same plane about a central body [Curtis, 2013].

Inclination reduction is a very expensive manoeuvre, requiring a lot of fuel, so GEO operators will typically opt for near-equatorial launch sites in order to access near-equatorial GTOs. After the launch vehicle has successfully placed its payload into a GTO, orbit-raising and circularisation is subsequently carried out using onboard satellite propulsion, ultimately achieving the desired GSO orbit. Traditional methods that use chemical propulsion to conduct orbit-raising are expensive owing to the high masses involved, so cheaper low thrust alternatives like electric propulsion are very attractive to operators [see e.g., Corey et al., 2010; Kluever, 2012]. However, low thrust methods can take several months to raise an orbit to the GSO region, increasing the amount of time spent by the satellite traversing the high radiation environments of the Van Allen belts [Messenger et al., 2014].

1.1.3 Other orbits of interest

Tundra and Molniya orbits

In high latitude locations upon the Earth, the GEO belt will only be visible at low elevation angles in the sky, if indeed it is visible at all above obstructions that line the horizon. Tundra orbits offer a potential solution to this problem. A Tundra orbit is a highly eccentric GSO with an inclination of around 63.4° [Capderou, 2002]. A satellite placed in such an orbit will spend extended periods of time over a chosen region on Earth, 'dwelling' in its apogee. Two Tundra orbits acting in tandem can

therefore provide similar coverage to a GEO communications satellite for northerly areas. Still a relatively new concept, Tundra orbits have seen limited exploitation thus far [see e.g., Bruno and Pernicka, 2005], though their potential use as disposal orbits for retired, highly inclined spacecraft in the GSO region has been the subject of recent study [Jenkin et al., 2017].

Molniya orbits offer a solution very similar to that of Tundra orbits, and have been used to provide GEO-like coverage over Russian (formerly Soviet) territory since the 1960s. Unlike their Tundra counterparts, Molniya orbits have an orbital period of around half a sidereal day. It is possible for a mere three Molniya satellites to provide continuous coverage of half the globe, owing to their unique ground tracks [McGraw et al., 2017]. On successive revolutions, the apogee of a Molniya orbit will alternate between one half of the covered hemisphere and the other, for example dwelling over both Russia and the USA. In this sense, the apogee of a Molniya orbit occurs at two separate longitudes, while that of a Tundra orbit resides over a single longitude.

Medium Earth orbit

In cases where a balance must be struck between signal latency and field of view (FOV), operators will opt to place their satellites in a medium Earth orbit (MEO), the vast spherical shell of space situated above LEO and below the GSO region. Most notably, MEO is populated by constellations of navigation satellites that supply the geolocation and time information that is relied upon for transportation by land, air and sea, alongside a host of other applications.

The Global Positioning System (GPS), operated by the US Space Force (USSF), was the first of these constellations to provide global coverage, and has been the world's most widely utilised navigation system ever since. The space segment of the GPS comprises over 30 operational satellites, with 24–27 making up the baseline for service provision. The 24+ satellites are arranged into six equally-spaced orbital planes, ensuring that at least four can be reached from any point on Earth at any given time [Renfro et al., 2018].

As of December 2020, and in addition to the GPS, the fully operational global satellite navigation systems are: the Russian Global Navigation Satellite System (GLONASS), the Chinese BeiDou Navigation Satellite System and Europe's Galileo network. These systems, alongside other regional counterparts, feed into the International GNSS Service [Dow et al., 2009]. A combination of signals from multiple GNSS sources has been found to provide significant improvements in both availability and accuracy of positional and timing information, owing to the higher

number of satellites visible from a location on Earth at a given time [Hadas et al., 2019; Tian et al., 2019].

Cislunar orbit

Owing primarily to the National Aeronautics and Space Administration (NASA) Artemis Programme[2], interest in cislunar space has grown rapidly in recent years. Although cislunar nominally refers to space "between Earth and the Moon", a variety of orbital definitions exist: orbits within the Moon's gravitational sphere of influence; those with an altitude beyond that of the GSO region, extending out to the lunar orbital radius; or indeed any orbit within the framework of the Earth-Moon three-body problem. Regardless of the definition chosen, the challenges posed to SSA by an expansion of space activities to the cislunar regime remain largely similar: the spacecraft (and accompanying debris) will be further away, thus calling for more sensitive equipment to account for a diminished signal-to-noise as reflected light from the source drops off with an inverse square law; the volume of space in need of monitoring is much larger, calling for a more extensive array of ground- and space-based SSA capabilities; and the view of spacecraft in certain non-geocentric orbits will frequently be obstructed by the Moon, or eclipsed in shadow, calling for more effective algorithms that are able to reliably predict future states when fed with sparse information [Bolden et al., 2020].

While cislunar space has historically been a peaceful and explorative domain, it will likely become a strategic outpost as the world's military superpowers carry out planned returns to the Moon in the next decade and beyond [see e.g., Haws et al., 2019]. In particular, this would reflect a recent change of attitude by the US military towards space surveillance activities; henceforth, outer space is to be considered a domain of warfare, and this has led to the introduction of "Space Domain Awareness" (SDA) as a new overarching descriptor. Though the terms SSA and SDA mean largely the same thing, SDA is designed to encompass additional concerns brought about by increasing access to space across the globe [Kennewell and Vo, 2013; Jaunzemis et al., 2016]. As more nations, commercial entities and even academic institutions and small businesses become spacefaring, and the population of artificial objects in orbit continues to rise, the need to fuse and exploit datasets from a wide variety of sources is becoming increasingly vital to ensure safe and sustainable use of the space domain [Jah, 2016]. Moreover, SDA brings into question the ground-based elements of space surveillance, including operators and decision makers, in support of gathering the actionable evidence necessary to at-

[2] https://www.nasa.gov/specials/artemis/ (accessed March 2021)

tribute cause if norms of behaviour are not adhered to, or capabilities and services suffer a degradation due to malpractice.

The proliferation of activities in the cislunar regime will expand the space domain far beyond the "high altitude" GSO region, and open up a wealth of uncharted territories, both literally and politically. The establishment of a so-called "cislunar economy" by a mix of government agencies and the private sector would warrant military protection as a matter of national security, an endeavour that would require extensive and reliable SDA. For this reason, a number of studies have started to investigate possible observational features that may be exploited by the next generation of remote sensing architectures to monitor the behaviour of objects in cislunar orbits [see e.g., Chow et al., 2020; Dao et al., 2020; Greaves and Scheeres, 2020].

The work presented herein focuses on the detection, tracking and characterisation of artificial objects in geocentric orbits; additional factors that discern SDA from SSA fall outside the scope of this thesis, thus the term "SSA" is used throughout when referring to these activities.

1.2 Orbital debris

Not all artificial objects in space continue to serve a purpose. In fact, only around 1 in 7 objects that are regularly tracked by the US Space Surveillance Network (SSN) are active satellites carrying out their primary mission, according to recent figures provided by the European Space Agency (ESA) Space Debris Office[3]. The remainder comprises various forms of orbital debris: non-functional, artificial objects of any size orbiting in near-Earth space.

In Fig. 1.3, the locations of objects tracked by the SSN are shown for a particular epoch. Unsurprisingly, certain regions are more densely populated than others, as operators have targeted specific orbital regimes that benefit their primary mission goals. Most notably, the LEO region is particularly vivid with its clustered bands in altitude–inclination space, many of which contain satellites and rocket bodies that are defunct and uncontrolled. The GSO region is also clearly visible, with most of its active satellites residing in the GEO belt that aligns with the Equator, and other objects fanning out in a surrounding band of inclined and potentially eccentric orbits.

Orbital debris can originate for a number of reasons, some of which unavoid-

[3] https://www.esa.int/Safety_Security/Space_Debris/Space_debris_by_the_numbers (accessed: March 2021)

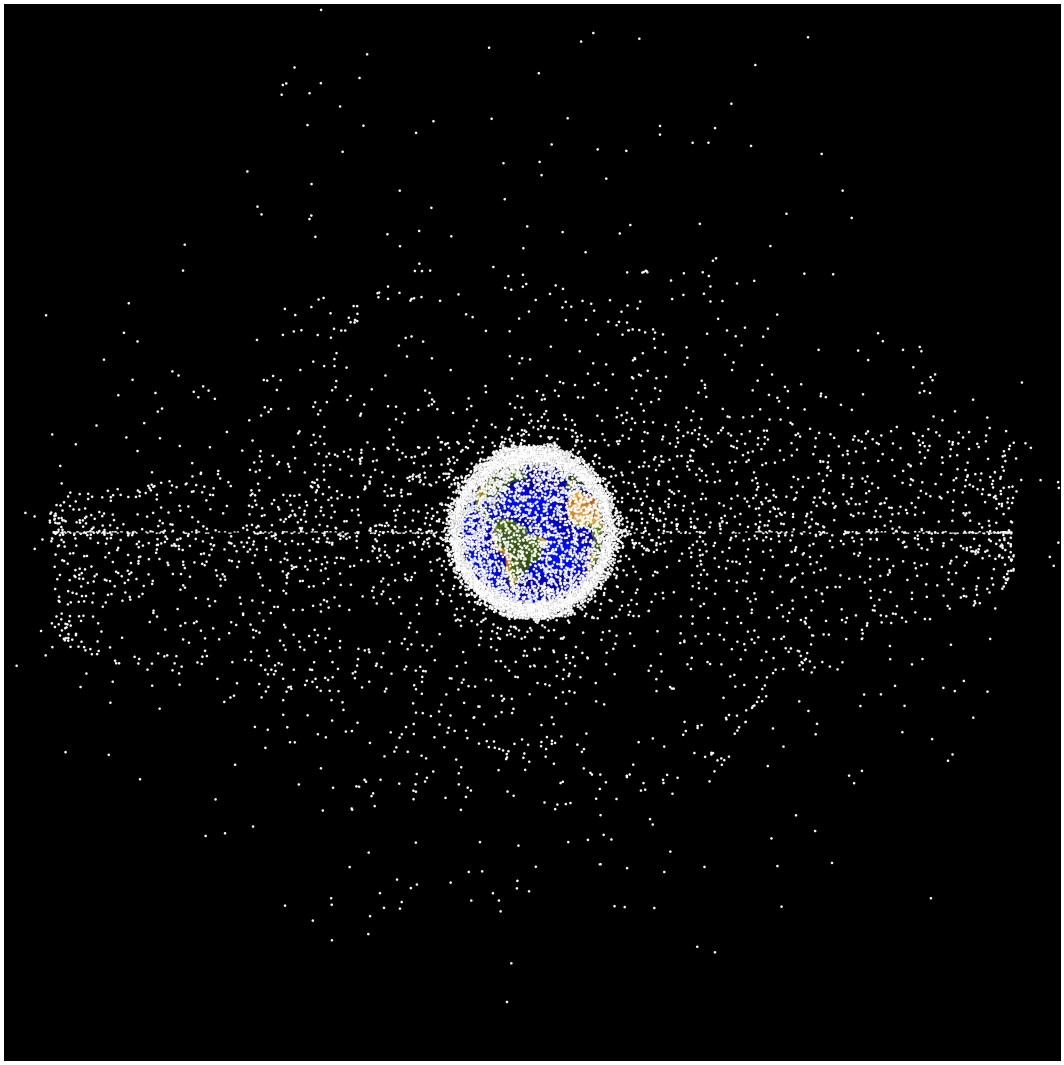

Figure 1.3: A snapshot of the near-Earth environment, showing the instantaneous location of all objects tracked by the SSN, as of January 1 2019. The line of sight is parallel to the equatorial plane, such that the geostationary ring appears as a horizontal line despite its circular nature. Points representing tracked objects (white) are scaled for optimal visibility, not relative to the Earth. [Credit: NASA]

able given past and present technological constraints, others arising from a lack of foresight or a disregard for the safe and sustainable use of space:

- *Defunct satellites* — Satellites themselves become debris when they reach the end of their mission lifetime (EOL). The extent of this lifetime will vary on a case-by-case basis, and will depend on a variety of factors, including: the size of the fuel reservoir available for station-keeping, collision avoidance manoeuvres and other mission-related activities; the level of onboard battery power required for operation and service provision, a particularly important consideration for LEO operators whose spacecraft will spend extended periods of time eclipsed in the Earth's shadow, rendering solar-powered recharging temporarily obsolete and contributing to degradation over time [Hussein et al., 2014]; the extent to which capabilities advance and more effective alternatives become available over the course of the satellite's mission. In this sense, the definitive source of orbital debris is indeed the launch of material into orbit.

  While some LEO payloads orbit at a sufficiently low altitude for orbital decay and atmospheric re-entry to serve as viable EOL options, higher altitude satellites will remain in orbit for centuries, if not indefinitely. Vanguard 1, for example, is the oldest human-made object in space, alongside its corresponding upper stage. Having been launched into an elliptical MEO by NASA in 1958, it is expected to remain in orbit for at least another two centuries [Green and Lomask, 2012]. A more detailed discussion of EOL standard practices is provided in Section 1.2.4.

- *Rocket bodies and mission-related objects* — Historically, launch procedures have been a major contributor to the population of orbital debris. Large clusters of spent upper stages (used to boost payloads into their final orbital configuration) exist across a range of regimes, most concerningly within the LEO region [Pardini and Anselmo, 2016]. Smaller mission-related objects (MROs) can also be released during the launch phase, such as adapter rings, payload shrouds, clamps and instrument covers. As of the end of 2019, rocket bodies and MROs constituted around 40 % of the total mass tracked by space surveillance networks [ESA, 2020].

- *Fragmentations* — By far the biggest contributor to the tracked population of orbital debris in terms of number has been fragmentation events. A total of 561 fragmentations had taken place in orbit by the end of 2019 [ESA, 2020], though this figure varies significantly depending on the categorisation used. The 15$^{\text{th}}$ Edition of the *History of on-orbit satellite fragmentation*, for instance, quotes a

total of 242 break-ups and 78 anomalous events [Anz-Meador et al., 2018]. The latter figures only include events that have been observed or corroborated by the SSN, and neglect to include so-called aerodynamic break-ups that typically occur as atmospheric drag builds up prior to re-entry, such that the resulting debris has no lasting effect on the near-Earth environment.

In the past, spent upper stages and boosters have often been abandoned with residual fuel or other sources of stored energy on board. Explosions resulting from self-ignition of these remnant components can destroy the stage, typically creating a debris cloud comprising a few to several hundred trackable fragments of varying mass and imparted velocity [see e.g., Johnson, 1989, 1999a; Tan and Ramachandran, 2005]. Similar events have occurred involving satellites themselves, typically caused by electrical faults and battery malfunctions [see e.g., Tan et al., 2017; Tan and Reynolds, 2019].

Collisions have taken place between a variety of cooperative and uncooperative objects, spanning the full range of trackable (and indeed untrackable) sizes. Spacecraft are routinely impacted by small particulates like paint flecks and micrometeorites in the sub-mm range. Over 1500 impact craters were identified on windows of the NASA Space Shuttle Orbiter across fifty sampled missions, 98 of which were large enough to warrant a replacement [Christiansen et al., 2004]. Fortunately, collisions between larger objects are much rarer, though far more catastrophic, resulting in thousands of new fragments to track and catalogue [see e.g., Kelso, 2009].

Concerningly, some of the largest fragmentation events have happened intentionally. Multiple nations have conducted anti-satellite (ASAT) tests, employing so-called "kinetic kill vehicles" to destroy a satellite in orbit and demonstrate defence capabilities on a global stage. While some ASAT tests have been conducted out of necessity and with care to minimise the adverse effects of the insuing clouds of debris [see e.g., Mackey, 2009], others have shown a disregard for the safety of surrounding satellites [see e.g., Akhmetov et al., 2019b].

- *General deterioration* — The harsh conditions of the space environment can degrade the exterior surfaces and components of a satellite over time. Ultraviolet, electron and proton irradiation, and exposure to atomic oxygen can induce erosion and bring about thermal degradation [Sharma and Sridhara, 2012]. Among other things, this can result in the shedding of paint flakes, flecks of surface coating and strips of thermal blanket.

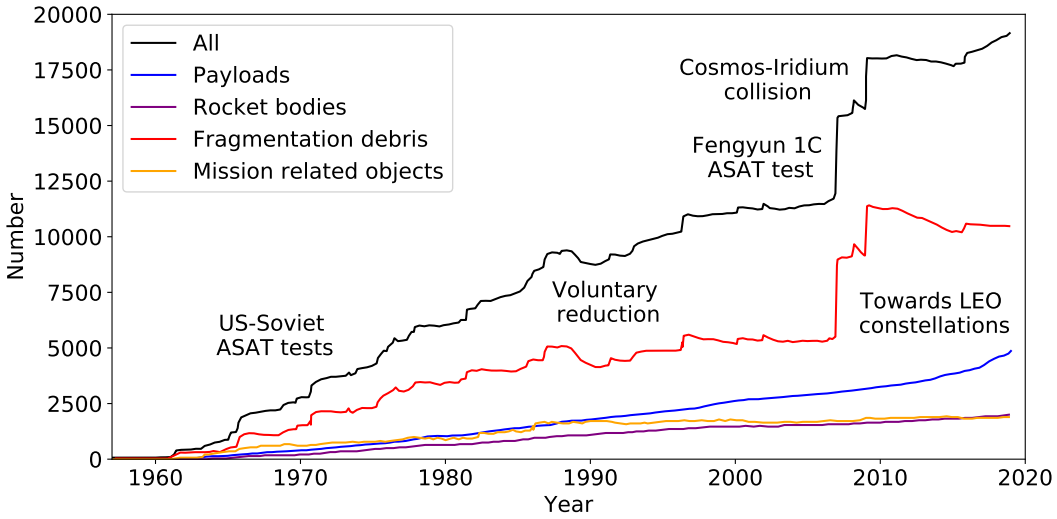

Figure 1.4: The temporal evolution of the USSPACECOM catalogue, which nominally maintains a record of orbital status for objects larger than around 10 cm and 1 m in the LEO and GSO regions, respectively. The comprehensive line profile for all tracked objects is shown in black, while subsets of the catalogued population are given in blue (payloads), purple (rocket bodies), red (fragmentation debris) and orange (MROs). Labels highlight key features of interest. Information sourced from Liou [2020b].

1.2.1 A brief history of events

A significant proportion of the catalogued debris population can be accounted for by appealing to known events that have taken place since the launch of Sputnik 1. The line profile in Fig. 1.4 shows how the number of objects in orbit being tracked has evolved over the past six decades, separated into sub-categories of interest. A previously steady rise in the number of payloads has transitioned to accelerated growth in recent years, as carrier vehicles become more powerful and deposit higher numbers of payloads per launch. The rise in the number of fragmentation debris shows a more eclectic history, as individual events have shaped the catalogue over the years.

1957-1990

The first unintentional break-up event took place in 1961, when a Thor-Ablestar upper stage exploded shortly after depositing its payload, the US Transit 4A satellite. Producing nearly 300 trackable fragments, the break-up more than tripled the number of catalogued objects at the time, with the majority remaining in orbit for

several decades [Portree, 1999; Johnson, 2010].

From the late-1960s to the mid-1980s, the US and Soviet Union frequently demonstrated their ASAT capabilities, conducting tens of tests between them [Liemer and Chyba, 2010]. The tests typically contributed in excess of 100 fragments to the orbital debris environment, many taking place at altitudes high enough to necessitate several decades of decay time prior to re-entry [Portree, 1999]. The last successful US ASAT test to take place before a congressional ban was conducted in 1985, involving the Solwind P78-1 gamma ray solar physics satellite at an altitude of 525 km [Tan et al., 1996]. Roughly half of the resulting debris cloud re-entered within a period of 4 years [Badhwar and Anz-Meador, 1989], with the majority of remaining fragments following suit within the decade. While Soviet ASAT tests typically made use of an interceptor satellite that would detonate when proximate to its target, the US Solwind test was the first to successfully deploy a so-called "kinetic kill vehicle"; namely, a heat-seeking homing missile that would destroy the target via kinetic impact [Tan and Reynolds, 2019].

In light of the 1986 US Space Shuttle Challenger disaster, NASA undertook a reexamination of its space safety policies, including those concerning orbital debris generation and mitigation. These initial steps kickstarted a series of policy reviews by key actors such as the US Air Force (USAF) and the US Department of Defence (DoD). The USAF Scientific Advisory Board, for example, published a report in 1987, the first to consider the orbital debris problem from a military perspective [Portree, 1999]. The Interagency Group (Space), established by President Reagan's administration to facilitate debris-related discussions between relevant US federal agencies, released an important report in 1989 [Kessler, 1989]. The Interagency Group report brought together the views of its constituent agencies and developed a US government consensus on orbital debris. Published at a time of political change across a number of spacefaring nations, this was pivotal in paving the way to a new era of international cooperation regarding the space domain. Around this time, Working Groups on Orbital Debris were established organisationally between NASA and ESA, and later nationally between the US and the Soviet Union. Collaborations within these Working Groups would result in a period of voluntary reduction in space activity, in an attempt to curtail the generation of further orbital debris. The timing was fortuitous, as a higher than normal solar activity in the years 1989-90 helped to accelerate the orbital decay of fragmentation debris within the LEO region, leading to a rare net decrease in the catalogued population [Johnson, 2010].

1990-present

In the early 1990s, the major space agencies came together to establish the Inter-Agency Space Debris Coordination Committee (IADC), to facilitate the sharing of technical experience and foster international collaboration [Portree, 1999]. As part of the early work undertaken by the IADC, NASA representatives investigated a large population of ∼cm-sized spherical pellets that had been uncovered by radar measurements, orbiting at altitudes in the range 850–1000 km, with inclinations around 65° [Kessler et al., 1997]. The tens of thousands of pellets have since been associated with leaked droplets of sodium–potassium (NaK) coolant liquid from nuclear-powered Russian Radar Ocean Reconnaissance Satellites (RORSATs) [Rossi et al., 1997; Settecerri et al., 1999; Stokely et al., 2009]. The droplets are thought to have leaked during the decommissioning phase of several RORSATs: the satellite's orbit would be raised to a LEO "graveyard", residing at a sufficiently high altitude to avoid commonly utilised bands for the foreseeable future; the reactor core would then be ejected, a process that would involve opening the coolant circuit, in turn releasing the NaK [Wiedemann et al., 2005]. Soonafter, the IADC drafted an early form of its Space Debris Mitigation Guidelines in response to the growing threat imposed by the orbital debris environment, later revised in 2007 [IADC, 2007]. The guidelines comprising this document are discussed in Section 1.2.4.

Despite a growing tendency for upper stages to be passivated upon abandonment, propulsion-related explosions have continued to occur as the orbits of many previously unpassivated stages are yet to decay. Of particular note are the nine Delta second stages that suffered break-ups between 1973 and 1991, alongside the more than fifty Proton Block-DM *Sistema Obespecheniya Zapuska* ullage motors that have exploded in the LEO, MEO (GLONASS transfer orbits) and GTO regimes [Pardini, 2005; Anz-Meador et al., 2018; NASA, 2020]. The latter series of explosions constitutes almost a half of the known propulsion-related fragmentation events, according to the classifications in Anz-Meador et al. [2018]. In 1996, a Pegasus Hydrazine Auxiliary Propulsion System exploded, producing over 750 trackable fragments and consequently becoming the most severe break-up on record at the time [Matney et al., 1997; Anz-Meador et al., 2018].

Though comparatively rare, accidental collisions have also taken place in orbit: Cosmos 1934 collided with a piece of debris from Cosmos 926 in 1991; the French Cerise satellite collided with an Ariane rocket body explosion fragment in 1996, tearing through its gravity-gradient stabilisation boom; a Thor 2A upper stage collided with a Chinese CZ-4 rocket body explosion fragment in 2005 [Alby et al., 1997; Kessler et al., 2010; Anz-Meador et al., 2018]. All three events resulted in

non-catastrophic break-ups, contributing fewer than ten new trackable fragments between them [Pardini and Anselmo, 2014]. The first and only accidental collision to involve two intact satellites thus far took place in 2009, proving to be catastrophic in nature. At an altitude of 790 km, the then-active commercial satellite, Iridium 33, collided with the inactive Russian satellite, Cosmos 2251, with an impact velocity in excess of 11.5 kms^{-1} [Kelso, 2009; Wang, 2010; Pardini and Anselmo, 2014]. The two satellites fragmented into 1668 and 628 trackable pieces, respectively [Anz-Meador et al., 2018]. The collision occurred in a LEO altitude–inclination band already densely populated with spacecraft, and so has been responsible for a large proportion of collision avoidance manoeuvres over the past decade. In some years, fragments from the 2009 collision have accounted for over half of the close approaches encountered by ESA spacecraft [Braun et al., 2016]. Furthermore, the ISS has been forced to carry out manoeuvres to avoid Cosmos–Iridium fragments on multiple occasions [see e.g., NASA, 2011, 2015a,b]. While some of the 2009 collision debris cloud has passed through the operational altitude band of the ISS and re-entered the Earth's atmosphere, over half of the catalogued population remain in orbit as of March 2021[4] [Anz-Meador et al., 2018].

Undeterred by the hiatus in ASAT testing recognised by the major space powers since the close of the Cold War era, China carried out tests of its own ASAT capabilities in the early 2000s. In 2007, a direct-ascent ASAT weapon successfully impacted the defunct meteorological satellite Fengyun-1C, which had previously operated in a polar sun-synchronous orbit, with an altitude of 850 km and an inclination of 98.6° [Kelso, 2007]. Following sixteen months of searching, around 2800 fragments had been tracked by the SSN [Liou and Johnson, 2009]. Roughly a thousand more fragments have been associated with the event since, and over half of the total catalogued population remains in orbit [Lambert, 2018]. The debris cloud has evolved to span the full LEO altitude band, and has spread unevenly across the full longitudinal range around the Equator. In the following year, the US destroyed a failed reconnaissance satellite using a ship-launched missile [Stansbery et al., 2008; Mackey, 2009]. Orbiting at an altitude of around 250 km, the target satellite USA-193 was suspected to have retained a significant quantity of highly toxic hydrazine fuel that could survive re-entry and cause harm on-ground. Numerous steps were taken to demonstrate an increased level of situational awareness relative to the Chinese test: the US announced their intention to carry out the ASAT test in advance, making it much more transparent for other agencies and operators with a vested

[4]Inferred from element sets sourced from https://celestrak.com/NORAD/elements/ (accessed March 2021)

interest; and the interception was conducted at a time most favourable to optical tracking, optimizing the SSN's ability to detect, track and catalogue fragments from the resulting break-up. Furthermore, owing to the low altitude of the interception, a large proportion of the ensuing debris cloud is thought to have re-entered immediately, while the remaining fragments were left in short-lived orbits [NASA, 2008]. With China having demonstrated its prowess in the ASAT domain, India began to rethink its stance on the militarisation of space [Rajagopalan, 2011]. A resulting investment in kinetic weaponary culminated in the recent destruction of the polar sun-synchronous Microsat-R satellite in March 2019, making India the fourth nation in history to successfully demonstrate ASAT capabilities [Akhmetov et al., 2019a]. Despite the low $\sim$ 260 km altitude of Microsat-R at the time of interception, the suspected head-on collision boosted several fragments to high apogee orbits, with around 80 % of initially catalogued debris possessing apogees above the operational altitude of the ISS and some extending to the boundary of the LEO region [Tan and Reynolds, 2019; Oltrogge et al., 2019].

Meanwhile, the threat of a second accidental catastrophic collision has loomed in recent years. The decommissioned Infrared Astronomical Satellite (IRAS), for instance, experienced a near-miss with USAF's Gravity Gradient Stabilization Experiment GGSE-4 in January 2020[5]. Similarly, the defunct Russian navigation satellite Cosmos 2004 narrowly avoided a collision with an abandoned Chinese CZ-4C rocket body in October 2020[6].

1.2.2 Sources of information

As the population of orbital debris has grown over time, so too has the need to reliably track and catalogue the objects orbiting the Earth. The US DoD has maintained a catalogue of artificial objects in space since the launch of Sputnik 1. Originally overseen by the North American Aerospace Defence Command (NORAD), the satellite catalogue is currently maintained by the US Space Command (USSPACECOM), which recently regained independence from the US Strategic Command (USSTRATCOM) in 2019[7]. Though other nations and agencies are known to harness their own space surveillance capabilities [see e.g., Dicky et al., 1993; Vallado and Griesbach, 2011; Peldszus and Faucher, 2020], the USSPACECOM catalogue

[5]The final miss distance calculated by LeoLabs prior to the IRAS–GGSE-4 conjunction was 47 m: https://twitter.com/LeoLabs_Space/status/1222650724347252736 (accessed November 2020)

[6]The final miss distance calculated by LeoLabs prior to the Cosmos–CZ-4C conjunction was 11 m: https://twitter.com/LeoLabs_Space/status/1317166964805111808 (accessed November 2020)

[7]Gen. John W. Raymond was nominated as commander of the newly reinstated USSPACECOM in March 2019, announced via https://www.spacecom.mil/MEDIA/NEWS-ARTICLES/ (accessed November 2020)

is widely regarded as the most comprehensive from a global perspective, receiving regular state updates from a wide array of ground- and space-based sensors.

Space Surveillance Network

The orbital state information available from the USSPACECOM catalogue is generated using observational data acquired by the US SSN, comprising over 30 ground-based radar and optical sensors, alongside 6 satellites in orbit [Weeden, 2019]. Observations taken by the SSN are continually forwarded to the Combined Space Operations Center (CSpOC), overseen by the US Air Force Space Command (AFSPC) via the 18$^{\text{th}}$ Space Control Squadron (18 SPCS) at the Vandenberg Air Force Base in California, US. The catalogued states are then distributed in the form of mean orbital elements [Hoots et al., 2004]; a 'basic' version of the catalogue is made publicly available via the Space-Track website[8], used extensively for civilian and scientific research, while operators can gain access to an advanced version containing more sensitive information. According to the latest boxscore[9], the SSN has tracked and catalogued over 47000 objects, with 21900 of these remaining in orbit at the time of writing.

Despite offering the best coverage of global space assets, the USSPACECOM catalogue is far from complete. The SSN is able to reliably track objects down to roughly 10 cm in size at LEO altitudes, and around 50–100 cm when observing the higher altitude GSO region. Smaller objects are monitored sporadically at best, due to the limited availability of sufficiently sensitive sensors. In the LEO region, relative velocities of 10–15 kms^{-1} are commonplace; in this hypervelocity regime, collisions with debris fragments as small as 1 cm can prove mission-fatal, while even mm-sized objects can inflict a disruptive amount of damage to solar panels and other external hardware. For example, in 2016, ESA's sun-synchronous Sentinel-1A satellite experienced an anomaly that was attributed to a sub-1 cm piece of orbital debris impacting a solar panel [Krag et al., 2017]. The collision resulted in notable attitude changes and a permanent partial power loss. Too small to be tracked by the SSN, the characteristics of the colliding fragment were instead fortuitously inferred from images of the resulting impact crater acquired using onboard cameras.

[8] A publicly-available version of the USSPACECOM catalogue of objects orbiting the Earth is accessible via https://www.space-track.org/

[9] The SATCAT Boxscore maintains a record of objects tracked and catalogued by the US SSN, and is updated daily via the CelesTrak website: https://celestrak.com/satcat/boxscore.php (accessed March 2021)

Two-line element sets

Catalogued orbital states have historically been distributed in the format of NORAD two-line element (TLE) sets. For a particular reference epoch, the TLE encodes a selection of mean orbital elements determined for an object orbiting the Earth. The two lines of information, each containing 69 characters, can be used in conjunction with Simplified Perturbations (SP) models to propagate the orbital state of the object in an Earth-centred inertial coordinate frame, akin to the geocentric equatorial frame discussed in Section 1.1. Development of the SP model series began in the 1960s [Lane, 1965]; Simplified General Perturbations (SGP) models are appropriate for propagating the orbital state of a LEO satellite, while Simplified Deep Space Perturbations (SDP) models are designed for spacecraft in high altitude orbits such as those of the GSO region. These early efforts culminated in the development of SGP4, the most commonly used model in conjunction with TLEs, which incorporated a more rigorous treatment of atmospheric drag [Hoots and Roehrich, 1980; Hoots et al., 2004]. In a series of papers, Vallado et al. [2006] and Vallado and Crawford [2008] have provided a comprehensive overview of the physics contained within the latest manifestations of the SGP4 source code, including the process of obtaining the orbital state in TLE format from observational data.

TLEs and SP propagators have been in regular operational use for decades, though several limitations are associated with them. The mathematical formalism of the SGP4 model, for instance, only takes into account the largest perturbations affecting a satellite: J_2 to J_5 zonal harmonics (see Section 1.3.1), alongside simplified drag, radiation pressure and three body gravitational effects [Vallado and Cefola, 2012]. As aerodynamic perturbations are intrinsically linked to the solar activity cycle, their influence is inherently challenging to predict, consequently resulting in large propagation uncertainties. With other poorly modelled perturbations contributing further uncertainty, TLEs must be regularly updated to ensure that custody of tracked objects can be maintained. A number of studies have sought to improve upon the SGP4 algorithm: Ziebart et al. [2005] and Li et al. [2018] explore more detailed treatments of SRP and thermal effects using box-wing models of spacecraft and ray tracing techniques, while Abdel-Aziz [2013] incorporates albedo and earthshine effects, and relativistic corrections, to achieve reportedly longer-lasting accuracy in the propagation phase.

In addition, the TLE format offers no way of encoding *a priori* knowledge regarding spacecraft manoeuvres, which often prove necessary to counter the effects of perturbative forces and preserve the desired orbit. Hence, if a manoeuvre is undersampled by observations feeding into the orbit determination procedure, this can

Table 1.2: The components of a two-line element set[†]. ID numbers correspond to the labels found in the supplementary figure. The three-line (name + TLE) or "3LE" format is shown for completeness. Red boxes encompass the relevant cells for each component.

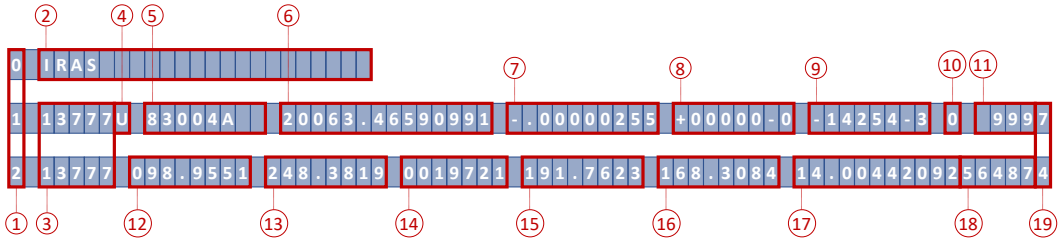

ID	Component name	Line(s)	Cell(s)	Comments
1	Line number	All	01	
2	Object name	0	01–24	
3	Catalogue ID	1, 2	03–07	
4	Classification	1	08	U if unclassified, C if classified, S if secret
5	Int'l designator	1	10–11	Last two digits of launch year
			12–14	Launch number of the year
			15–17	Piece of the launch
6	Epoch	1	19–20	Last two digits of epoch year
			21–32	Fractional year day for epoch
7	First derivative of mean motion	1	34–43	Ballistic coefficient
8	Second derivative of mean motion	1	45–52	Decimal point assumed
9	Drag term	1	54–61	Radiation pressure coefficient
10	Ephemeris type	1	63	Always zero for distributed data
11	Element set number	1	65–68	Counter of TLEs generated
12	Inclination	2	09–16	[degrees]
13	RAAN	2	18–25	Right ascension of the ascending node [degrees]
14	Eccentricity	2	27–33	Decimal point assumed
15	Argument of perigee	2	35–42	[degrees]
16	Mean anomaly	2	44–51	[degrees]
17	Mean motion	2	53–63	Revolutions per day
18	Revolution number	2	64–68	Revolution count up to epoch
19	Checksum	1, 2	69	Modulo 10

[†]Definitions sourced from https://www.space-track.org/documentation#/tle (accessed March 2021)

lead to significant inaccuracies in the resulting TLE. Indeed, propagation of a TLE is rendered meaningless if the spacecraft's motion becomes non-Keplerian in the interim between TLE generation and the epoch of interest, for example if the orbit has been influenced by propulsive forces that are not accounted for by SP models. This was highlighted as a prevalent issue in the recent Phantom Echoes campaign to monitor the Mission Extension Vehicle-1 (MEV-1) from launch to rendezvous [George et al., 2020]. During MEV-1's orbit-raising and circularisation phase, angular offsets between the observed positions and those predicted by propagating day-old Space-Track TLEs were frequently found to be as high as 5 degrees, making it difficult to track the spacecraft with narrow-field sensors.

Typically, TLEs are not published with covariance information or any other measure of uncertainty [Thompson et al., 2019], though numerous studies have investigated the projection accuracy of TLEs and the SGP4 propagator [see e.g., Boyce, 2004; Flohrer et al., 2008; Geul et al., 2017]. It is important to remember that TLEs derive from observational data, the quality of which will depend on sensor characteristics, observing conditions, post-acquisition processing, and so on. The type of sensor employed will also have a part to play: active sensors such as radars can typically measure the range and its rate of change; observations of high altitude targets with optical telescopes instead provide angles-only information, necessitating the estimation of the range, a key parameter for orbit determination (recall Section 1.1). The challenges associated with maintaining custody of an object using angles-only data are explored further in Chapter 5.

Originally designed with brevity in mind, at a time of low bandwidth and storage, the format of the TLE itself imposes a number of limiting constraints. The most pressing of these is the fact that TLEs cap identification numbers at 5 digits. With more advanced sensing technologies coming online (see below), waves of new satellites licenced and scheduled for launch (see Section 1.2.4), and a very real threat from future accidental catastrophic collisions, satellite catalogues will soon encroach on this limit. To address this issue, and provide the scope for imparting additional information available for a given object, Space-Track have recently started to distribute orbital states in the form of Orbit Mean-Elements Messages (OMMs), available in a range of file formats to ensure future interoperability[10].

Radar and optical measurements

The majority of space surveillance observations utilise radars or optical telescopes. As the sensitivity of a radar drops steeply with the fourth power of the range, where

[10] https://celestrak.com/NORAD/documentation/gp-data-formats.php (accessed March 2021)

range is the observer–target distance, they are most effective at monitoring the LEO region. Observations of high altitude orbits typically employ the use of optical sensors, with sensitivities that drop less steeply with the square of the range.

The SSN makes use of both conventional radars with steerable and immobile antennas, and wide-field phased-array radars comprising several thousand elements that allow the antennas to be electronically steered. Key contributors to the SSN have included the AN/FPS-85 phased-array radar at Eglin Air Force Base, Florida [Settecerri et al., 2004], and the Air Force Space Surveillance System "Space Fence", a series of 3 transmitters and 6 receivers spanning the width of the US that was decommissioned in 2013[11]. The latter system has recently been replaced by the new S-band US Space Fence [Haimerl and Fonder, 2015] which became operational in March 2020[12]. The Space Fence, which operates at much higher frequencies than its predecessor, is expected to significantly bolster the existing satellite catalogue with many thousands of objects in the LEO region smaller than the current 10 cm cut-off, whilst also supporting operations for MEO and GSO satellites.

The main optical component of the SSN is the Ground-Based Electro-Optical Deep Space Surveillance (GEODSS) system [Henize et al., 1993; Wootton, 2016]. GEODSS is made up of three geographically distanced sites (Socorro, New Mexico; Maui, Hawai'i; Diego Garcia, British Indian Ocean Territory), each comprising three 1 m electro-optical (EO) detectors. This series of optical telescopes has historically served as the SSN's primary source of information for objects in high altitude orbits, and will soon be supplemented by NASA's 1.3 m Eugene Stansbury Meter Class Autonomous Telescope (ES-MCAT) on Ascension Island [Lederer et al., 2013, 2019]. With ES-MCAT, NASA aim to conduct a survey of the GSO region down to objects roughly 20 cm in size, pushing below the SSN's nominal cut-off of 1 m at high altitudes and filling a longitudinal gap in the GEODSS network. Several optical surveys of the GSO region and other high altitude orbital regimes have taken place in the past few decades, and a summary is provided in Section 1.3.3.

The reflected light from an orbiting body contains information about its shape and attitude, but is also affected by sensor characteristics, atmospheric interference and the viewing geometry at the time of the observation. Though a difficult task, the disentanglement of these components affords the observer an opportunity to investigate the nature of the object itself and, perhaps of greater interest, in-

[11] https://www.af.mil/News/Article-Display/Article/466832/air-force-space-command-to-discontinue-space-surveillance-system/ (accessed November 2020)

[12] Lockheed Martin's Space Fence has achieved initial operational capability, and will soon significantly increase the number of objects being tracked and catalogued by the SSN: https://www.spaceforce.mil/News/Article/2129325/ussf-announces-initial-operational-capability-and-operational-acceptance-of-spa/ (accessed November 2020)

fer its intentions. Consequently, light curve characterisation, namely the process of characterising an object based on measurements of its apparent brightness over time, remains a very active area of research. Several studies have developed techniques to extract shape and attitude information from light curves [see e.g., Hall et al., 2007; Wetterer and Jah, 2009; Hinks et al., 2013; Hinks and Crassidis, 2016; Piergentili et al., 2017; Yun and Zanetti, 2020], and classify objects based wholly or partially on their photometric signatures [see e.g., Scott and Wallace, 2008; Dao et al., 2018; Furfaro et al., 2018; Kelecy et al., 2019]. Yanagisawa and Kurosaki [2012] derive a tri-axial ellipsoidal model for a Cosmos 2082 rocket body in LEO, probing its physical and rotational properties using optical light curve data. Linares et al. [2014] utilise a data fusion technique, combining optical light curve and angles-only measurements to enhance the sensitivity of their algorithm and recover shape, orientation and trajectory information for sparsely sampled orbital arcs. Fan and Frueh [2020] carry out a successful two-step light curve inversion in the presence of measurement noise for two different geometric shapes, while Kelecy et al. [2020] make use of information theory techniques to classify simulated box-wing satellite models as active, passive (debris), dormant (potential threat) or transitioning, given a range of both *a priori* and *a posteriori* sources of information.

Numerous groups have accrued large databases of optical light curves: the Astronomical Institute of University of Bern (AIUB) have obtained in excess of a thousand light curves for LEO, MEO and high altitude objects with the 1 m ZIMLAT telescope at the Zimmerwald Observatory, Switzerland [see e.g., Schildknecht et al., 2008b, 2015; Šilha et al., 2017b]; the Faculty of Mathematics, Physics and Informatics at Comenius University in Bratislava, Slovakia, have observed 226 objects in GSO, GTO, Molniya and GNSS orbits using a 0.7 m optical telescope [see e.g., Zigo et al., 2019; Šilha et al., 2020]; the Astronomical Observatory of Odessa National University, Ukraine, have acquired high resolution light curves for over 500 defunct satellites in LEO, using their 0.5 m KT-50 telescope [see e.g., Shakun and Koshkin, 2014; Schildknecht et al., 2015; Koshkin et al., 2017]; preliminary observational campaigns undertaken by the University of Warwick, UK, gathered light curve measurements for 350 GSO objects using a 36 cm robotic astrograph, and 550 LEO targets with the repurposed SuperWASP instrument, both situated at the Roque de los Muchachos Observatory in La Palma, Canary Islands [Chote et al., 2019].

Defunct satellites, abandoned rocket bodies and debris fragments are uncontrolled, thus their attitude will freely evolve under the influence of the natural perturbative forces acting upon them. Objects that are not actively stabilised to

counter these external torques are often found to be tumbling with high spin rates (typically of the order of seconds to minutes), and many studies have made use of photometric light curves to estimate tumbling rates and monitor their temporal evolution [see e.g., Papushev et al., 2009; Read et al., 2012; Santoni et al., 2013; Binz et al., 2014; Cognion, 2014; Ryan and Ryan, 2015; Kudak et al., 2017; Benson et al., 2020]. Precise, high cadence light curve measurements can reveal finer rotational signatures (such as sharp glints) that can, in principle, be matched with high fidelity models of possible target body geometries. For example, Earl et al. [2018] estimate the spin axis orientation of Echostar-2, a defunct GSO satellite, by comparing sharp, bright glints in high resolution light curve measurements to those generated using a specular reflectance model. Šilha et al. [2018] provide an overview of rotational properties derived from light curves in the AIUB database, finding over half of the observed GSO objects to be rotating, as opposed to only 3 % of targets sampled in the LEO region. Tumbling GSO satellites are of particular interest from an environmental modelling perspective; the dominant perturbative force aside from gravity in high altitude orbits is SRP, which remains poorly understood and contributes significantly to uncertainties in orbital propagation. Rotational properties extracted from photometric light curves enable the effects of SRP (alongside other forces) to be probed, and help refine models of the perturbative forces that feed into orbit propagators [see e.g., Ojakangas et al., 2011; Früh et al., 2013; Albuja et al., 2015, 2018]. More generally, an understanding of the tumbling states of objects in any orbital regime will be key to the success of future disposal and servicing missions (see Section 1.2.4).

The optical brightness of an object orbiting the Earth is inversely proportional to the square of its distance from the observer. Predominantly governed by the reflection of light from the Sun, an object's brightness is also a function of its physical characteristics, surface properties and the viewing geometry at the time of observation. In its simplified form, the visual magnitude m_{V} of an orbiting body may be expressed as [McCue et al., 1971]

$$m_{\mathrm{V}} = m_{\mathrm{sun}} - 2.5 \log \left[\frac{\rho S}{R^2} f\left(\psi\right) \right], \tag{1.2}$$

where $m_{\mathrm{sun}} = -26.74$ with no atmospheric corrections, ρ is the reflectivity, S is the cross-sectional (illuminated) area of the object and R is the observer–object distance. The solar phase angle ψ (observer–object–Sun) gives the angle between light from the Sun that is incident on the object and light reflecting off of it along the observer's line of sight. The choice of phase function, $f\left(\psi\right) = f_{\mathrm{spec}}\left(\psi\right) + f_{\mathrm{diff}}\left(\psi\right)$,

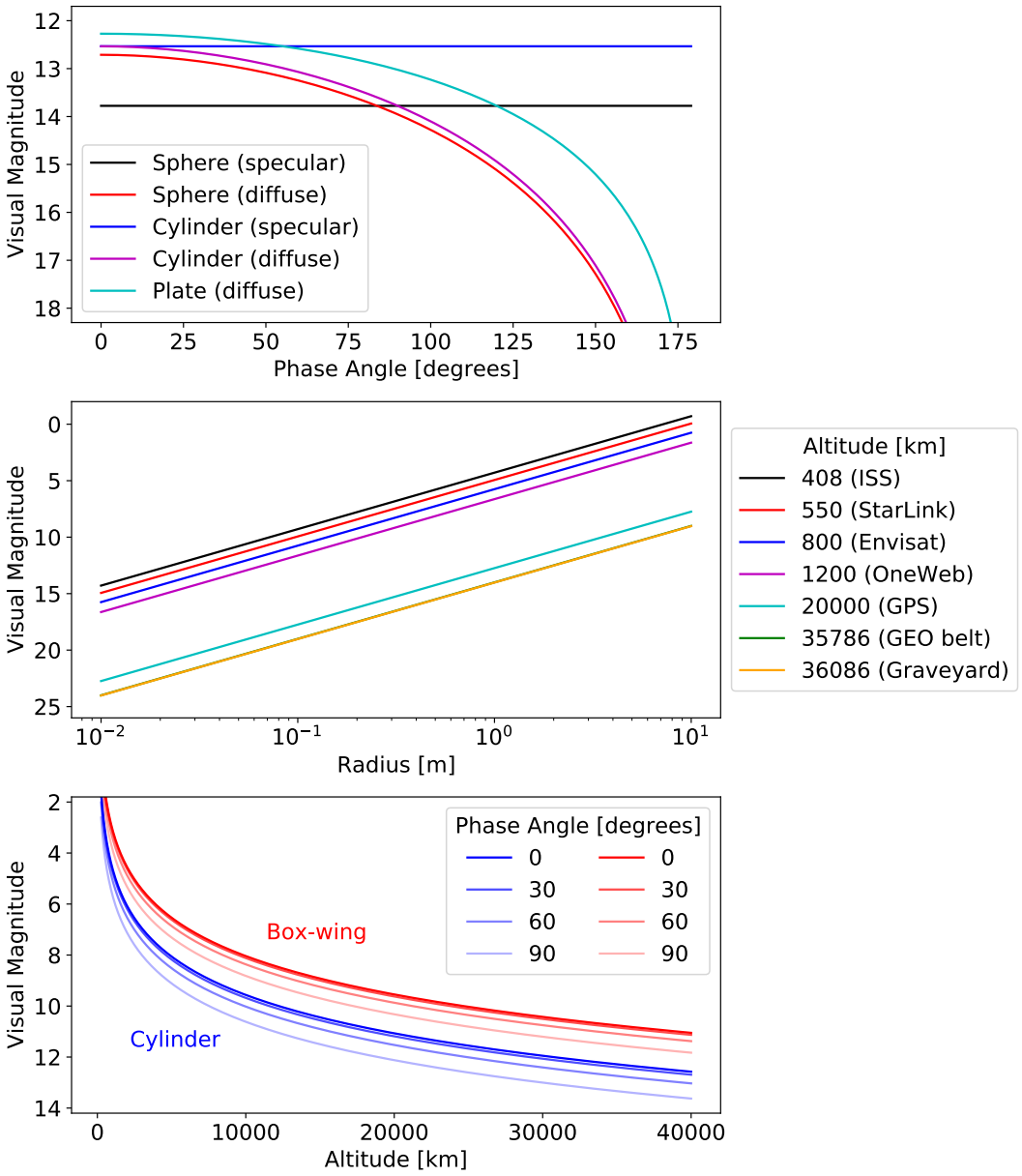

Figure 1.5: Top) Expected brightness as a function of phase angle for a selection of simple geometric shapes, orbiting at the geostationary altitude $R = Z_{\rm GEO}$ with $\rho S = 1\,{\rm m}^2$. Middle) Simulated brightness as a function of object radius for a diffuse (Lambertian) sphere with $\rho = 0.1$, orbiting at a selection of key altitudes with a phase angle $\psi = 15°$. Note that the 'GEO belt' case (green) is concealed by the nearby 'Graveyard' case (orange) on this scale. Bottom) Simulations of brightness as a function of orbital altitude and phase angle for two composite examples: a cylindrical bus with a circular antenna; and a 'box-wing' satellite with solar panels extending from either side of its central, cylindrical bus. A reflectivity $\rho = 0.1$ was assumed for all components. Further details relating to the composite models are provided in the main text.

depends on the type of surface reflecting light, typically comprising specular and diffuse components. In the case of a metallic sphere with a smooth, mirrored surface, the reflection will be predominantly specular, such that the light scatters in one direction only and the function $f_{\text{spec}} = \frac{1}{4\pi}$ is constant. On the other hand, diffuse or Lambertian reflection will result from rough (e.g., painted) surfaces, whereby light is scattered in many directions. The phase function for a sphere then takes the form,

$$f_{\text{diff}}(\psi) = \frac{2}{3\pi^2}\left[\sin\psi + (\pi - \psi)\cos\psi\right]. \tag{1.3}$$

While the specular and diffuse phase functions above are appropriate for spherical approximations, simple forms also exist for cylindrical and plate-like geometries [see Table 1; Krag, 1974]. For reference, the visual magnitude is simulated for a variety of configurations in Fig. 1.5. In the top panel, the phase angle dependence is illustrated for purely diffuse/specular examples, orbiting in the GEO belt with a reflectivity–area product $\rho S = 1\,\text{m}^2$. The diffuse cases show a gradual decline in brightness from a maximum apparent magnitude (outside of shadow) at $\psi = 0°$, through the low phase angle regime that is typical of GSO surveys (see e.g., Chapter 3), before fading steeply as larger phase angles are reached. For the specular cylinder and diffuse plate examples, the phase functions are more complex, dependent on additional factors such as the temporal extent of glints and the object's orientation relative to the observer [McCue et al., 1971]. In these cases, the extremal (maximum) brightness is taken, though a relatively weak glint is considered for the specular cylinder for clarity; the maximum brightness for a strong glint would be several magnitudes brighter. Evidence of specular glinting in real photometric light curves will be explored in Chapters 3 and 4.

In the middle panel of Fig. 1.5, the visual magnitude is given as a function of object size for Lambertian spheres with $\rho = 0.1$, placed at a number of key orbital altitudes. The geostationary case (green) is employed in Chapter 3 to provide primitive estimates of object size based on extracted brightness measurements. The dominance of R in the governing equation is clear from the simulated examples, with identical spheres differing by 10 magnitudes when separated by the ISS–GEO distance.

The final panel of Fig. 1.5 shows brightness as a function of R for two composite models at selected phase angles. The 'Cylinder' model combines a diffuse cylindrical bus (length 4 m, diameter 2 m), covered in solar panels, with a circular antenna (diameter 2 m) and a rod-like antenna (length 50 cm, diameter 5 cm), where both antennas are modelled as diffuse plates. The chosen configuration is based on

the cylindrical Hughes HS-376 bus that is later discussed in Chapter 3. The 'Box-wing' model comprises a diffuse cylindrical bus (length 4 m, diameter 2 m), between two sets of large solar panels (length 5 m, width 2 m) and two sets of smaller solar panels (length 4 m, width 2 m), treated as diffuse plates. The central bus is considered to be side-on relative to the observer's line of sight, such that the visible surface is that of the circular cap, where antennas would reside. This second model is representative of the Russian Gorizont and Raduga series, based on the box-wing KAUR-3 satellite bus that features in the discussion of Chapter 3. For the purposes of these illustrative simulations, only diffuse components of the reflected light are considered. Contributions from specular cylinders and plates depend strongly on viewing geometry and orientation, varying from negligible (no glint) to several magnitudes (strong glint) in certain configurations. Specular glints, as their name suggests, are transient in nature, while the diffuse reflection gives a good estimate of the baseline brightness for a given object.

Environmental models

Turning attention to objects below the size cut-offs of the USSPACECOM catalogue, comparatively very little is known about the small debris population. While small fragments make up a tiny proportion of the overall mass of catalogued objects (payloads and rocket bodies constitute over 98 % of the total tracked mass in orbit, according to latest figures from ESA [2020]), their numerical abundance remains a critical consideration, owing to the high risks that even mm-sized particles can pose to active satellites and crewed missions.

The 1–10 cm bracket in LEO has been probed by a number of collateral sensors over the past few decades, which are typically carrying out SSA observations as a secondary purpose, rendering it impossible to routinely track and catalogue the small objects they uncover. Observations carried out by NASA using the Haystack [Stansbery et al., 1995; Settecerri et al., 1999], Haystack Auxiliary [Stansbery and Settecerri, 1997] and Goldstone [Goldstein et al., 1998; Matney et al., 1999] radars have detected LEO objects down to a few mm in size. Similar observations have been conducted by ESA, making use of the Tracking & Imaging Radar system in Germany [Mehrholz et al., 2002]. These experiments have accrued statistical information by operating the radars in "beam-park" mode, whereby the beam is pointed in a fixed direction relative to the Earth's rotation, and candidate objects are registered via their back-scattered signal as they pass through the radar's FOV. *In situ* methods have been used to investigate the population of sub-mm orbital debris, via examination of impact features on spacecraft such as the

European Retrievable Carrier, Long Duration Exposure Facility and Hubble Space Telescope [see e.g., Love et al., 1995; Drolshagen et al., 1996; Graham et al., 2001; Drolshagen, 2008]. LEO objects $\sim$ 1–3 mm in size lie within an observational 'gap'; too small to be detected by the most sensitive radars, yet too rare to have caused a statistically informative number of craters on surfaces that have been analysed using *in situ* techniques. In the GSO region, the population of debris smaller than roughly 10 cm remains unprobed by any technique.

Satellite operators are thus forced to appeal to environmental models when assessing the overall risk posed by small debris to their payloads. The latest releases of the ESA Meteoroid and Space Debris Terrestrial Environment Reference (MASTER) model [Flegel et al., 2009] and the NASA Orbital Debris Engineering Model (ORDEM) [Krisko, 2014] incorporate the current state-of-the-art knowledge held by the respective agencies relating to the status of the orbital debris environment. Both models are deterministic, with empirical frameworks that take into account existing archives of source events (launches, fragmentations, and so on), alongside the available observational data (as above) in order to verify and refine the output debris flux distributions [see e.g., Braun et al., 2019]. Owing predominantly to the different source datasets that act as input to the models, MASTER and ORDEM are known to differ significantly in their output [Krisko et al., 2015]. Most notably, flux estimates within the 1 mm–1 cm bracket exhibit discrepancies that exceed an order of magnitude in places; unsurprising, given the lack of observational constraint afforded by the aforementioned data gap in this size range. The MASTER model predicts that the number of objects larger than 1 cm orbiting the Earth is approaching 1 million, while the ORDEM output is around a factor of two fewer; both estimates nevertheless highlight the inadequacies of current space surveillance catalogues.

Recent efforts to improve environmental models have looked to incorporate more accurate representations of the objects themselves. An object's physical characteristics, such as its shape and material composition, are key considerations when modeling the risk it poses to other satellites, the evolution of a fragmentation cloud if the object were to explode or collide with another, and its observability with respect to ground- and space-based surveillance sensors. Cowardin et al. [2020] are in the process of cataloguing and characterising nearly 200000 debris fragments greater than 2 mm in size that were generated by the laboratory-based DebriSat hypervelocity impact experiment. Selected fragments have undergone further analysis using bidirectional reflectance measurements to aid in the refinement of phase functions for size estimation models, while pre-impact spectral measurements are being used

as a baseline for material characterisation. Many studies have acquired laboratory- or ground-based multi-colour photometric [see e.g., Seitzer et al., 2010; Hejduk et al., 2012; Cardona et al., 2016; Lu et al., 2017; Cordelli et al., 2018] or time-resolved spectroscopic [see e.g., Seitzer et al., 2012; Bédard et al., 2014; Vananti et al., 2017] measurements, in efforts to probe the material properties of objects orbiting the Earth. Other laboratory-based experiments have simulated aging of common spacecraft materials (metals, multi-layer insulation, and so on), typically finding that space-like conditions can have a significant effect on observational features [see e.g., Sznajder et al., 2015; Engelhart et al., 2019; Beisecker et al., 2020].

1.2.3 The current picture

In the top row of Fig. 1.6, the number of objects penetrating the LEO and GSO regions are provided, according to recent figures from ESA [2020]. Though still far from complete, the populations quoted are slightly bolstered compared to those of the publicly available USSPACECOM catalogue alone, as the authors make use of additional data sources, such as ESA's Database and Information System Characterising Objects in Space[13] (DISCOS) and a catalogue maintained by the Russian Keldysh Institute of Applied Mathematics (KIAM). By number, the vast majority of objects in both regions are uncontrolled, thus lacking any form of collision avoidance capability. In the LEO region, fragmentations (break-ups, collisions, and so on) are responsible for around 89.5 % of entries labelled as debris, while MROs make up the remainder. A large proportion of objects intersecting the GSO region are unidentified, that is to say their nature and launch origin remain unclear. There are a number of reasons for this: historically, the GSO region has received far less attention from an orbital debris perspective, and it is likely that numerous anomalous events took place without any real-time follow-up; substantial populations of HAMR objects exist in high altitude orbits, which have been highly perturbed by SRP and other poorly modelled forces, rendering it impossible to associate them with a launch [Kelecy and Jah, 2011]; thought to hail from payloads in the GSO region, the uncorrelated HAMR objects now reside in highly eccentric orbits that necessitate bespoke observational strategies which have only been employed in the past couple of decades [see e.g., Schildknecht et al., 2003; Früh and Schildknecht, 2012].

The second row of Fig. 1.6 shows the number of payloads launched to the LEO and GSO regions by year. Here, the greater expense of launching to high altitudes shines through; the vast majority of payloads launched to the GSO region since the

[13] DISCOSweb is available via https://discosweb.esoc.esa.int/ (accessed November 2020)

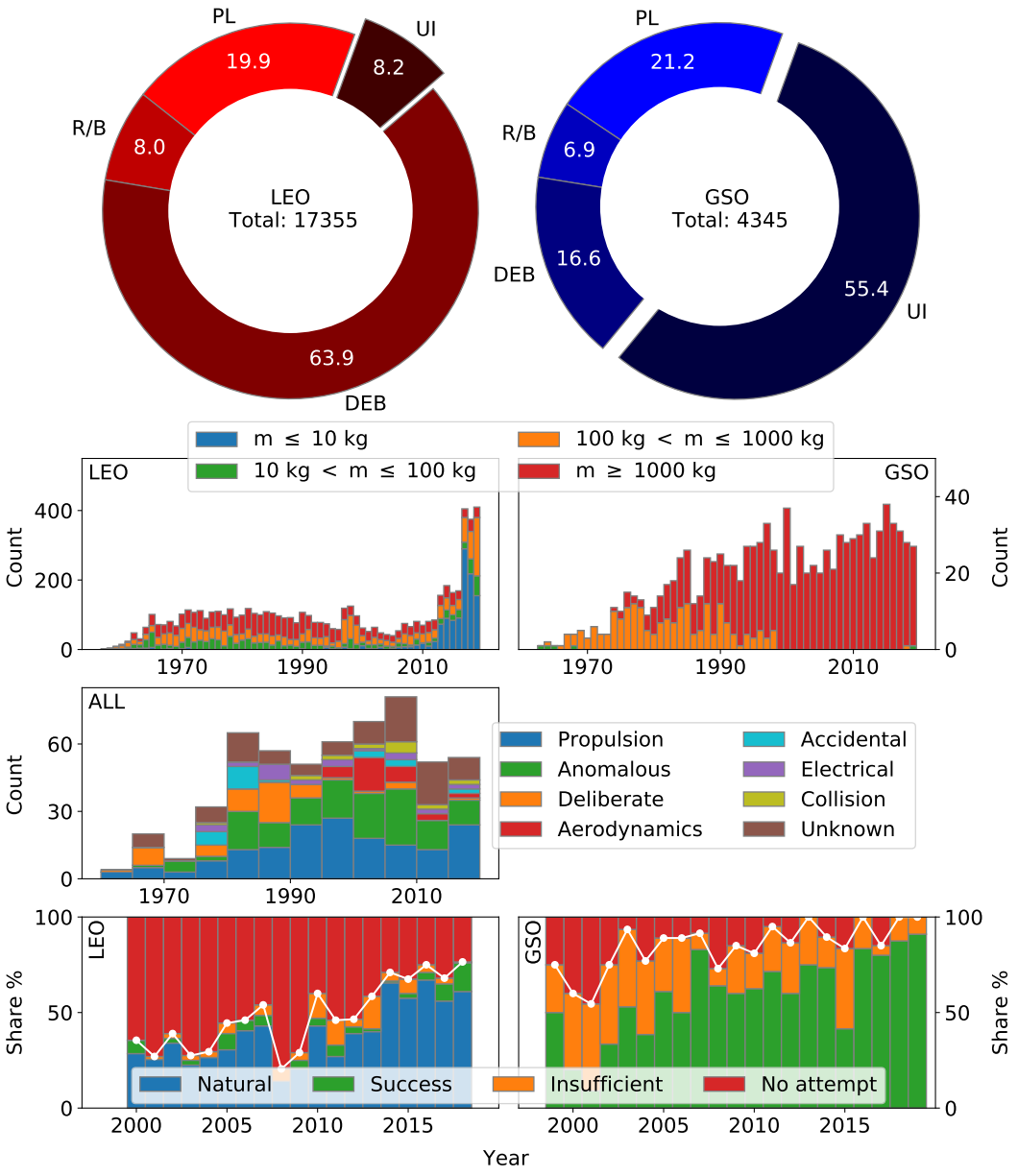

Figure 1.6: Top row) Number of objects penetrating the LEO (left) and GSO (right) regions, categorised by object type: payload (PL), rocket body (R/B), debris (DEB) or unidentified (UI). Second row) Payload launch traffic into the LEO (left) and GSO (right) regions, categorised by mass m. Third row) Number of fragmentation events, categorised by cause. Bottom row) Adherence to mitigation guidelines (see Section 1.2.4) for the LEO (left) and GSO (right) regions, with clearance attempts categorised as naturally compliant, successful, insufficient or not performed. White lines give the proportion of cases where an attempt was made to adhere to the guidelines. Information sourced from ESA [2020], correct as of the end of 2019.

1980s have exceeded 1000 kg. Driven primarily by cost, though more recently by a desire to mitigate the problem of orbital debris, operators have opted to make more efficient use of a given launch, loading each satellite bus with multiple functionalities. The opposite trend can be seen for LEO payloads. With the emergence of private launch companies in recent years, even small businesses and academic institutions can now obtain access to space. The growing tendency to launch small, compact "CubeSats" and other nanosatellites has accelerated, as planned LEO constellations (see Section 1.2.4) start to take shape.

1.2.4 Future outlook and proposed solutions

Many groups and agencies have developed models for projecting the future evolution of the orbital debris environment [see e.g., Lewis et al., 2001; Walker et al., 2001; Liou et al., 2004; Rossi et al., 2009; Dolado-Perez et al., 2013; Radtke and Stoll, 2016]. A number of these environmental models have been used to inform studies undertaken by the IADC in the development of their debris mitigation guidelines, which have since been adopted by the United Nations Committee on the Peaceful Uses of Outer Space (UNCOPUOS). The third row of Fig. 1.6 gives the number of fragmentation events to occur in five year bins since the early 1960s, categorised by the event cause. Historically, the most common type of fragmentation event has been the accidental break-up of an orbiting body due to the explosion of propulsion- or electrical-related subsystems onboard. To address this, the IADC guidelines encourage the passivation of a satellite or upper stage, namely that remnant sources of energy are depleted as soon as they are no longer needed for an operational or disposal-based purpose. While passivation has since become commonplace, numerous unpassivated satellites and rocket bodies remain in orbit, so explosions will likely continue to occur unless these abandoned objects can be deorbited in some way.

Post-mission disposal (PMD) is another important form of debris mitigation. Certain altitude–inclination bands within the LEO region are already unstable; even with no future launch activities, the debris population is projected to exhibit a nett increase [see e.g., Liou and Johnson, 2008; Kessler et al., 2010; Liou et al., 2013]. The "Kessler Syndrome" [Kessler and Cour-Palais, 1978] refers to the process whereby debris fragments generated from accidental collisions themselves become significant sources of future debris, ultimately leading to an exponential growth in the population regardless of efforts to curtail the problem. For objects penetrating the LEO region, the IADC guidelines recommend that operators ensure disposal via atmospheric re-entry within 25 years of the EOL. Objects in orbits below an altitude of 600–700 km will typically be naturally compliant with the so-called "25

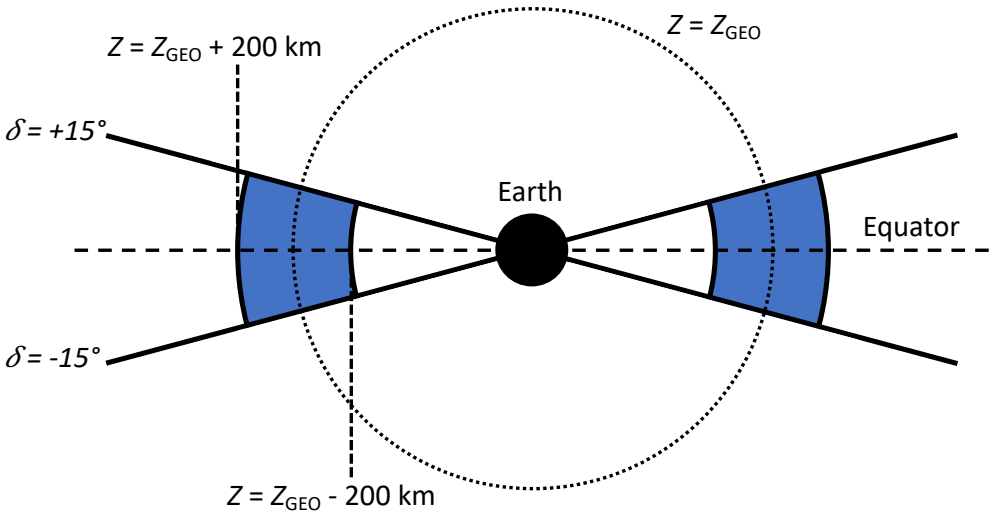

Figure 1.7: An illustrative sketch of the GSO Protected Region (in blue), as defined by the IADC Space Debris Mitigation Guidelines [IADC, 2007]. Extending 200 km above and below the geostationary altitude $Z_{\mathrm{GEO}} = 35786\,\mathrm{km}$, the Protected Region is a segment of a spherical shell spanning $\pm 15°$ in declination relative to the equatorial plane of the Earth. Note that the scale of the Protected Region has been exaggerated for clarity.

year rule", owing to orbital decay induced by atmospheric drag. Operators with LEO payloads in higher altitudes can either accelerate orbital decay using propulsion or non-propulsive alternatives (e.g., dragsails), or raise their craft into a stable, non-intrusive graveyard orbit.

The GSO region is too high altitude for atmospheric drag to provide a mechanism for orbital decay, thus there is no natural 'sink' for objects residing there. Orbital lifetimes for GSO debris are thus rendered infinitely long from an operational perspective [Yasaka et al., 1999; Anderson and Schaub, 2014]. At such high altitudes, mitigation is currently the only realistic option for minimizing the risk posed to active GSO satellites, as the cost of a manoeuvre to deorbit the craft would be exorbitent. Consequently, the IADC guidelines advise that decommissioned GSO payloads undergo an EOL manoeuvre to place them in a supersynchronous graveyard orbit above the GSO Protected Region (GSOPR), depicted in Fig. 1.7. Specifically, the recommended increase in perigee altitude ΔH for a satellite to safely clear the operational zone is given by [Jehn et al., 2005; IADC, 2007]

$$\Delta H\,[\mathrm{km}] = 235\,\mathrm{km} + \left(1000 \cdot C_r \cdot \frac{S}{m}\right)\,\mathrm{km}, \tag{1.4}$$

where C_r is the SRP coefficient, S $\left[\mathrm{m}^2\right]$ is the averaged cross-sectional area of the satellite and m [kg] is its dry (hardware; excluding propellant) mass.

The bottom panels of Fig. 1.6 provide recent statistics on the levels of adherence to mitigation standard practices exhibited by LEO and GSO satellite operators since their inception in the late 1990s. Excluding cases that were already naturally compliant with the 25 year rule, adherence to this recommendation remains concerningly low, with fewer than 30 % of non-compliant payloads making an attempt to become so across the period 2010–18. Clearance rates for GSO payloads have been much higher, with over 80 % of decommissioned satellites successfully conducting the recommended EOL manoeuvre into a suitable graveyard orbit. However, it is important to keep in mind the GSO residents that reached EOL prior to the issuance of guidelines, existing in an uncontrolled and likely unpassivated state ever since. These defunct satellites are typically in drift orbits or librating about one or both of the geopotential wells that result from the non-spherical shape of the Earth (see Section 1.3.1), in either case with the potential to intersect the operational regions of the GEO belt and pose a direct risk to active satellites. Recent efforts to encourage operators to minimize their 'footprint' in space and adhere to mitigation standard practices have culminated in the development of a "Space Sustainability Rating" [Letizia et al., 2020].

An IADC study by Liou et al. [2013] employed six of the leading environmental models, finding that the simulated population of orbital debris would continue to increase by a factor of ~ 30 % over the next 200 years, even with a 90 % mitigation compliance rate and no future explosions in orbit; of course, these assumptions are incredibly optimistic, and the actual population growth in this period will undoubtedly be worse. Several studies have identified active debris removal (ADR) as a way to reduce the likelihood of a Kessler-like collisional cascade and thus control the orbital debris population [see e.g., Liou et al., 2010; Bonnal et al., 2013; White and Lewis, 2014]. In the context of ADR, Liou [2011] used NASA's LEO-to-GEO Environment Debris model to investigate the effects of target selection and implementation epoch on the long-term evolution of the orbital debris environment. The study found that the removal of five high impact targets per year could be sufficient to stabilise the population, if combined with a 90 % mitigation compliance rate and launch traffic representative of the period 2003–11. On average, the addition of ADR to this scenario reduced the predicted number of catastrophic collisions from 24 to 14 across the 200 year projection, highlighting the importance of removing high risk targets from the near-Earth environment. Both Liou [2011] and McKnight et al. [2019] identify several clusters of derelict rocket bodies in the LEO region that

pose a high risk of generating debris and contributing to collisional cascading, thus making them sensible targets for future ADR missions. Another high priority target is ESA's defunct eight-tonne satellite, Envisat, residing in a high density altitude band around 760 km. Like many potential ADR candidates, Envisat is known to exhibit signs of complex tumbling [Pittet et al., 2018], and a number of studies have explored the observational and operational challenges of rendezvousing and capturing a spinning, uncooperative target [see e.g., Nishida and Kawamoto, 2011; Kanzler et al., 2015; Gómez and Walker, 2015].

Owing to the high costs and technical challenges associated with ADR concepts, a number of studies have investigated the feasibility of removing multiple targets within a single mission [see e.g., Braun et al., 2013; Bérend and Olive, 2016; Shen et al., 2018]. A wide variety of mechanisms have been proposed for capturing and removing target spacecraft: prospective capture methods include the deployment of nets [see e.g., Botta et al., 2017; Shan et al., 2019], harpoons [see e.g., Dudziak et al., 2015], robotic arms [see e.g., Reintsema et al., 2010] and tentacles [see e.g., Wormnes et al., 2013]; removal concepts appeal to a variety of techniques, such as drag augmentation [see e.g., Underwood et al., 2019], electrodynamic tethering [see e.g., Nishida et al., 2009; Pardini et al., 2009], propulsion [see e.g., DeLuca et al., 2013; Olympio and Frouvelle, 2014] and laser ablation [see e.g., Phipps et al., 2012; Ebisuzaki et al., 2015]. A more extensive review of ADR concepts is provided by Shan et al. [2016]. ADR techniques remain largely untested in orbit: the RemoveDebris mission, led by Surrey Space Centre, carried out successful captures of planted debris using net and harpoon systems, prior to the partial deployment of a dragsail device [Forshaw et al., 2016; Aglietti et al., 2020]; having successfully launched in March 2021, Astroscale's ELSA-d mission aims to conduct the first capture of a tumbling client in orbit, using a magnetic docking system [Blackerby et al., 2019]; ESA's ClearSpace-1 mission[14] will likely be the first to remove an existing item of debris from orbit, and is currently due to target a Vespa upper stage in LEO when it launches in the mid-2020s. The pioneering ADR missions will target debris objects in the LEO region, where the risk of collisional cascade is highest. Remediation missions targeting higher altitudes remain technologically and financially infeasible, though the GSO region provides an excellent testbed for in-orbit servicing concepts [see e.g., Xu et al., 2011; Flores-Abad et al., 2014; Medina et al., 2017]. For example, Northrop Grumman's MEV servicers have successfully rendezvoused and docked with two GSO communications satellites, Intelsat-901 (February 2020) and Intelsat-1002 (April 2021), with the aim of extending their operational lifetime by

[14]Latest updates via: https://www.esa.int/Safety_Security/Clean_Space/ (accessed March 2021)

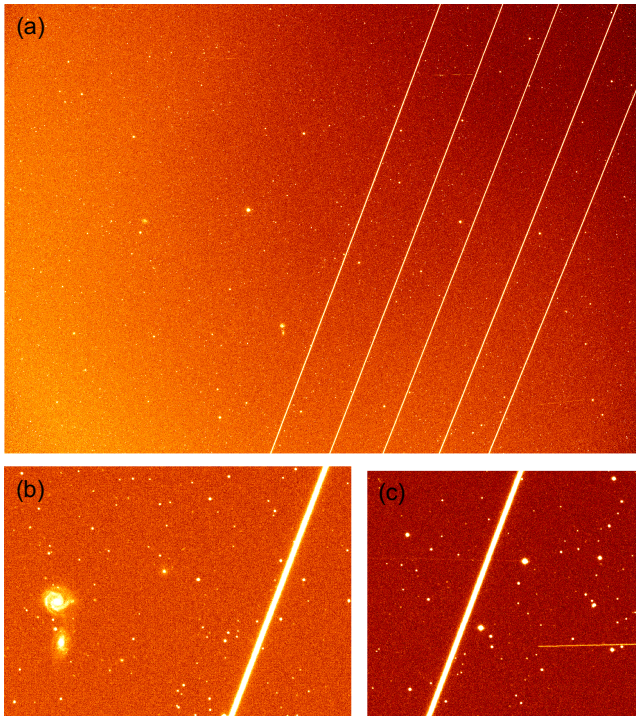

Figure 1.8: Examples of survey images acquired by the Gravitational wave Optical Transient Observatory in La Palma, Canary Islands. The telescope was tracking sidereally, so stars are point-like within the images. A full frame image is shown in (a), contaminated by the trails of five satellites belonging to the Starlink constellation. In (b) and (c) close-up views of individual trails are provided, highlighting their superior brightness relative to a galaxy and a higher altitude satellite, respectively.

five years[15].

To place even further strain on surveillance and tracking systems, launch traffic to LEO has risen sharply in recent years, owing to the proliferation of small satellite technology (as evidenced in the second row of Fig. 1.6). Of particular concern are the large constellations of satellites that are under development, offering innovative solutions in providing global observational coverage and ubiquitous access to communications. Many private companies have already received permission from licensing authorities to launch thousands of new satellites into a variety of LEO altitude–inclination bands [Muelhaupt et al., 2019; Curzi et al., 2020]. Efforts to simulate the effects of injecting large constellations into the LEO environment have collectively agreed that the impact will depend heavily on the success rate of PMD [see e.g., Bastida Virgili et al., 2016; Radtke et al., 2017; Pardini and Anselmo,

[15] https://www.northropgrumman.com/space/space-logistics-services/ (accessed March 2021)

2020]. For example, Bastida Virgili et al. [2016] find that a 50 % PMD success rate leads to an exponential increase in the projected population, driven predominantly by collisional cascading between undisposed members of the constellation itself. A recent update to the US Orbital Debris Mitigation Standard Practices (ODMSP) has specified that large constellation operators should aim for PMD success rates greater than 90 % [Liou, 2020a]. It remains to be seen whether this level of adherence will be achievable.

Moreover, a number of studies have highlighted the negative impact that planned constellations are likely to have on astronomical observations across a range of wavelength bands [see e.g., Dai et al., 2019; Hainaut and Williams, 2020; McDowell, 2020]. Satellite streak contamination in astronomical imaging is by no means a new issue, but the vast numbers and low altitudes involved in maintaining a LEO constellation are sure to make the problem particularly prevalent. An example of streak contamination by a collection of SpaceX's Starlink satellites is provided in Fig. 1.8. While the lowest altitude constellations are likely to be the brightest, those in higher altitude bands (e.g., as proposed for OneWeb) will perhaps be of greater concern to astronomers; low altitude satellites will spend much of the night eclipsed in the Earth's shadow (see Section 2.2.2), while members of the OneWeb constellation will remain visible for the majority of a given night. Seitzer [2020] has recommended that constellation operators take precautions to keep their satellites faint, and opt for altitude bands below $\sim 600\,\mathrm{km}$, in order to best combat the issue.

1.3 The geosynchronous region

1.3.1 Orbital characteristics

The gravitational environment surrounding the Earth can be described by appealing to the geoid, an equipotential surface whose shape arises from the Earth's uneven mass distribution. Capderou [2014] derives the expanded form of the geopotential U, given by

$$U(r,\lambda,\phi) = \frac{\mu}{r}\left[1 - \sum_{l=1}^{\infty}\left(\frac{R}{r}\right)^{l} J_l P_l\left(\sin\phi\right) + \sum_{l=1}^{\infty}\sum_{m=1}^{l}\left(\frac{R}{r}\right)^{l}\left(C_{lm}\cos m\lambda + S_{lm}\sin m\lambda\right) P_{lm}\left(\sin\phi\right)\right]. \quad (1.5)$$

Here, the potential is expressed in terms of the spherical coordinates (r, λ, ϕ), representing the geocentric radius, longitude and latitude, respectively, while μ is the

standard gravitational parameter. The first term in the square brackets (1) represents the familiar form of the central potential, while the term in P_l and J_l describes the contribution of zonal (latitudinal) harmonics. The third and final term in C_{lm}, S_{lm} and P_{lm} encodes the contribution of sectoral (longitudinal) and tesseral (checkered) harmonics. The term of degree $l = 2$ corresponds to a flattening of the Earth into an ellipsoid, while terms of higher degree account for deviations between this ellipsoidal approximation and the geoid itself.

The shape of the geoid has important consequences for the dynamical behaviour of GSO satellites. Most notably, the oblate spheroidal shape of the Earth results in two geopotential wells, situated at 75° E and 105° W [McKnight and Di Pentino, 2013]. Hence, uncontrolled objects in the GSO region will migrate to the nearest well, before oscillating about its center indefinitely. To prevent this happening for operational satellites, east–west (E–W) station-keeping manoeuvres are used to keep the payload "on station". Owing to the limited space within the GEO belt, satellite operators are allocated specific longitudinal slots in which to place their payloads; E–W station-keeping is thus used to ensure the satellites remain at their assigned longitudes. Objects in libration orbits that are 'trapped' in either or both of the geopotential wells pose a disproportionate risk to active satellites. For example, McKnight [2010] found that $\sim 80\,\%$ of the total collisional risk to operational GSO satellites could be attributed to librating objects, despite these comprising a mere $\sim 15\,\%$ of the catalogued population at the time of publication. This is unsurprising, considering that trapped objects sample a range of longitudes as they go about their 1–10 year oscillatory cycle within a geopotential well [McKnight and Di Pentino, 2013]. Objects that are trapped in both wells are of particular concern, sampling almost every longitude as their orbital state evolves over time. A second perturbation is induced by the gravitational interaction of the Earth with the Moon and the Sun. This causes a 53 year precessional cycle of the satellite orbit, oscillating between 0° and 15° inclination [Anderson et al., 2015]. Most operational satellites in the GEO belt will counter for this using north-south (N–S) station-keeping manoeuvres.

Many of the GSO satellites that reached EOL prior to the emergence of debris mitigation guidelines have existed in an uncontrolled state ever since, and are consequently either librating or drifting in the vicinity of the GSO region. According to McKnight and Di Pentino [2013], a derelict object will be trapped in a libration orbit, regardless of its longitude, provided the condition $\xi = (Z_a - Z_{\mathrm{GEO}}) - (Z_{\mathrm{GEO}} - Z_p) < 40\,\mathrm{km}$ is satisfied, where $Z_{\mathrm{GEO}} = 35786\,\mathrm{km}$ is the geostationary altitude, while Z_a and Z_p are the apogee and perigee of the object's orbit, respectively. Higher values

of ξ can still lead to entrapment if the object's longitude is proximate to that of a geopotential well. Objects that have attempted an EOL manoeuvre to reach a graveyard orbit are typically drifting relative to the GEO belt; those below Z_{GEO} will exhibit an easterly drift, while those above are drifting westerly. Many of these drift orbits intersect the operational zones of the GSOPR, while some remain within its bounds for an entire revolution. HAMR objects, typically fragments of debris, are also susceptible to SRP perturbations, which can significantly alter their orbital eccentricities and inclinations.

1.3.2 Fragmentation events

Remarkably few fragmentation events have been confirmed to have taken place within the GSO region, in spite of the significant population of faint debris that has been uncovered by optical surveys over the past few decades (see Section 1.3.3). The addition of several unconfirmed, or indeed completely artificial, fragmentation events to ESA's MASTER-2009 model proved necessary to recreate observations of the GSO debris environment [Krag et al., 2009]. Recent updates to the reference population for NASA's ORDEM list a total of seven confirmed break-ups in the GSO region: two Titan 3C Transtage rocket bodies (NORAD 3432, 21/02/1992; NORAD 3692, 28/02/2018), three Ekran satellites (NORAD 10365, 23/06/1978; NORAD 11561, 23/04/1981; NORAD 13554, 23/12/1983), a Breeze-M rocket body (NORAD 41122, 16/01/2016) and a BeiDou satellite (NORAD 34779, 29/06/2016) [Manis et al., 2019]. While the causes remain unclear, it is highly likely that the fragmentations listed arose due to residual sources of stored energy onboard, such as batteries, propellants and high pressure subsystems. Owing to the SSN's sensitivity limitations, only a few tens of fragments have been catalogued from these events [see e.g., Cowardin et al., 2017; Anz-Meador et al., 2018], though break-up models predict hundreds of fragments that are too small to be reliably tracked [see e.g., Ikeda et al., 2008; Petit et al., 2018]. Other candidates have previously been identified via abrupt changes in their orbital elements [see e.g., Rykhlova et al., 1997], though the majority of these anomalies have since been attributed to either propellant venting or collisions with small debris particles that are unlikely to have generated significant quantities of fragments [Johnson, 2001].

In spite of a curtailment over the past couple of decades, significant populations of abandoned rocket bodies and apogee kick motors remain in and around the GSOPR [Johnson, 1999b; McKnight and Di Pentino, 2013]. Many of these derelict stages are likely orbiting in an unpassivated state, each carrying a high risk of exploding and injecting a few hundred fragments of debris into the GSO environment,

the majority of which would not be visible to the SSN. A recent study by Oltrogge et al. [2018] found that relative velocities as high as 4 kms^{-1} can be encountered between objects crossing the GSO region; following from this, the authors posit that debris fragments in the 1–10 cm bracket could cause mission-fatal damage to an active GSO satellite, while impacts with objects larger than 20 cm could generate large tertiary fragments with the potential to seed a collisional cascade. As observational efforts can currently probe the GSO region to 10–20 cm at best (see Section 1.3.3), and knowledge of GSO fragmentation history is far from complete, studies rely on extrapolation techniques to estimate the small GSO debris population. For instance, Murray-Krezan et al. [2015] used data from the NASA Wide-Field Infrared Survey Explorer telescope, estimating there to be 1036–3060 objects larger than 10 cm in the GSO region, and 35458–157956 greater than 1 cm. Using this extrapolated GSO catalogue, Oltrogge et al. [2018] determined a collision rate of once every four years when considering the active residents against objects 1 cm and above.

Objects residing in HEOs can further add to the risk, with recent observations uncovering a number of fragmentation clouds that are partially penetrating the GSOPR [Schildknecht et al., 2019]. Four significant break-ups of abandoned GSO/HEO upper stages were observed in the period 2018–19. Collectively, these events produced over 1000 fragments, a few hundred of which cross the GSOPR. It is also possible that collisions with small debris were responsible for the heavily-publicised anomalies involving the GEO satellites, Intelsat 29e (NORAD 41308, 10/04/2019), Telkom 1 (NORAD 25880, 25/08/2017) and AMC-9 (NORAD 27820, 17/06/2017) [Cunio et al., 2017, 2019].

1.3.3 Optical surveys

Optical measurements have played a critical role in investigating the high altitude orbital debris environment. Surveys of the GSO region and nearby regimes have been conducted since the mid-1990s for a variety of purposes, from tracking and cataloguing unknown fragments, to collating statistical information for environmental modeling. An overview of past and ongoing optical surveys of the GSO region is provided in Table 1.3.

The first extensive GSO survey was conducted by NASA's Charge-Coupled Device (CCD) Debris Telescope (CDT), a portable instrument that could detect $\sim$ 60 cm-sized GSO objects [see e.g., Jarvis et al., 2001; Barker et al., 2005]. The CDT campaigns highlighted the incompleteness of the USSPACECOM catalogue, motivating the development of more sensitive surveys that followed. Over the past couple of decades, ESA and the AIUB have made use of a 1 m telescope on Tener-

Table 1.3: Optical surveys of the GSO region. Instrumental FOVs are listed as narrow (N) if FOV < 0.5 deg^2, medium (M) if $0.5 <$ FOV < 1 deg^2, wide (W) if $1 <$ FOV < 10 deg^2 and ultra-wide (UW) if FOV > 10 deg^2. Survey depths are denoted m_X for a given photometric band X, and M for cases where the band is not specified or absolute magnitudes have been quoted [see Africano et al., 2005].

Survey	Instr. size [m]	Instr. FOV	Survey depth	Reference
NASA CDT	0.32	W	$M \sim 16$	Barker et al. [2005]
MODEST	0.61	W	$m_R \sim 18$	Seitzer et al. [2004]
TAROT	0.18–0.25	W–UW	$m_R \sim 15$	Alby et al. [2004]
ESA-AIUB	1.00	M	$m_V \sim 20$	Schildknecht [2007]
ISON	0.22–0.70	N–UW	$M \sim 18$	Molotov et al. [2008]
ISON (faint)	1.00–2.60	N	$M \sim 20$	Molotov et al. [2009]
Pan-STARRS	1.80	UW	$m_V \sim 21$	Bolden et al. [2011]
Magellan	6.50	N	$m_R \sim 19$	Seitzer et al. [2016]
FocusGEO	(3×)0.18	UW	$M \sim 15$	Luo et al. [2019]
NASA MCAT	1.30	N	TBD	Lederer et al. [2019]
DebrisWatch I	2.54	N	$m_V \sim 21$	Blake et al. [2021]

ife, Canary Islands, and a collection of follow-up instruments at the Zimmerwald Observatory, Switzerland, to carry out surveys and targeted observations of a variety of high altitude objects, uncovering previously unknown populations in the GSO, GTO, MEO and HEO regimes [see e.g., Schildknecht et al., 2004, 2008a; Šilha et al., 2017a]. Although the ESA 1 m has a relatively narrow $0.7° \times 0.7°$ FOV, the instrument is sufficiently sensitive to detect GSO objects down to ~ 15 cm in size. Early ESA campaigns to observe GSO debris revealed a bimodal brightness distribution, with a bright-end peak corresponding to large, intact satellites, and a faint-end peak spanning from roughly the sensitivity limit of the SSN down to that of the ESA 1 m itself. Since 2002, NASA and the IADC have conducted a series of observational campaigns using the Michigan Orbital DEbris Survey Telescope (MODEST) in Chile [see e.g., Seitzer et al., 2004; Abercromby et al., 2011]. The MODEST campaigns would typically gather around 20–40 nights of data per year, and detect GSO objects larger than ~ 20 cm [Šilha et al., 2020]. Geographically, MODEST resides in a favourable location, in sight of the geopotential well at 105° W, an important part of the GSO region to probe when investigating the debris population. The Russian KIAM maintains an extensive catalogue of high altitude objects, using data acquired by the International Scientific Optical Network (ISON), comprising 100 telescopes across 17 countries, as of 2019 [Molotov et al.,

2019]. Large components of the ISON have been used to investigate the faint GSO debris environment, and the network continuously tracks a population of objects that fall below the 1 m size cut-off of the SSN [Molotov et al., 2009].

Fragments at the 5–20 cm level remain poorly characterised, as they are typically straddling or below the sensitivity limits of the 0.2–1 m-class telescopes that are frequently employed to survey the GSO region, instead calling for the superior collecting area of larger aperture telescopes. The 6.5 m Magellan telescope has been used for a small number of GSO spot surveys, targeting known fragmentation events [see e.g., Seitzer et al., 2016, 2017]. These deep observations, alongside those acquired with the Panoramic Survey Telescope and Rapid Response System (Pan-STARRS) 1.8 m [Bolden et al., 2011] and the 2.54 m Isaac Newton Telescope (INT) [Blake et al., 2021], have provided insight into the behaviour of this elusive population of faint GSO debris. The latter survey formed the basis for much of the work presented herein, and a discussion of its findings is reserved for Chapter 3.

1.4 Thesis outline

This thesis explores a number of ways in which optical imaging can contribute to enhanced levels of SSA, using datasets acquired by a variety of instruments at the Roque de los Muchachos Observatory on La Palma, Canary Islands. Chapter 2 introduces the sources of data, strategies and techniques that are frequently employed throughout the thesis. Photometric results from the aforementioned INT survey of faint GSO debris are presented in Chapter 3. Targeted observations of catalogued spacecraft in the LEO and GSO regions are described in Chapter 4, acquired in the early phases of two light curve surveys performed using the SuperWASP-North array and a robotic astrograph, respectively. Orbital arcs extracted from the light curve surveys are used as test cases in Chapter 5, where an overview of the development and testing of a custom orbit refinement algorithm is provided. Chapter 6 presents a preliminary analysis of a supplementary dataset obtained using a robotic astrograph, which was slaved to the INT during its survey of the GSO region. Finally, a summary of the main body of the thesis is given in Chapter 7, alongside a brief commentary on the future outlook for SSA. Further details related to the algorithms presented in Chapter 5 are provided in Appendices A to C.

In addition to the overall declaration at the start of this thesis, each chapter begins with a section that briefly summarises collaborative elements of the work contained therein.

Chapter 2

Methods

This chapter introduces the sources of data, observational strategies and analysis techniques that are frequently employed or referenced throughout the thesis.

2.1 Data sources

Much of the work presented herein relies upon image data from optical telescopes, acquired internally by myself or other members of the Astronomy and Astrophysics Group at the University of Warwick. Occasionally, external sources of information are used to either match untargeted observations to known objects that have been catalogued, or simulate the predicted motions of spacecraft using archival orbital state data.

2.1.1 Catalogues

Owing to its superior coverage on a global scale, the USSPACECOM catalogue (see Section 1.2.2) is used wherever the need for TLE (orbital state) or other archival information arises. Specifically, the publicly available version of the catalogue is queried using `spacetrack`[1], a Python client for the Space-Track website. As part of the study to be outlined in Chapter 5, the Python package `tlemcee`[2] has been developed, comprising a variety of routines for manipulating and propagating TLEs. The package is built around existing `skyfield` routines [Rhodes, 2019] that channel the SGP4 model [Hoots and Roehrich, 1980; Vallado and Crawford, 2008] to interpret the TLE format and predict the positions of Earth-orbiting objects at desired epochs.

[1] https://github.com/python-astrodynamics/spacetrack (accessed March 2021)
[2] https://github.com/jblake95/tlemcee (accessed March 2021)

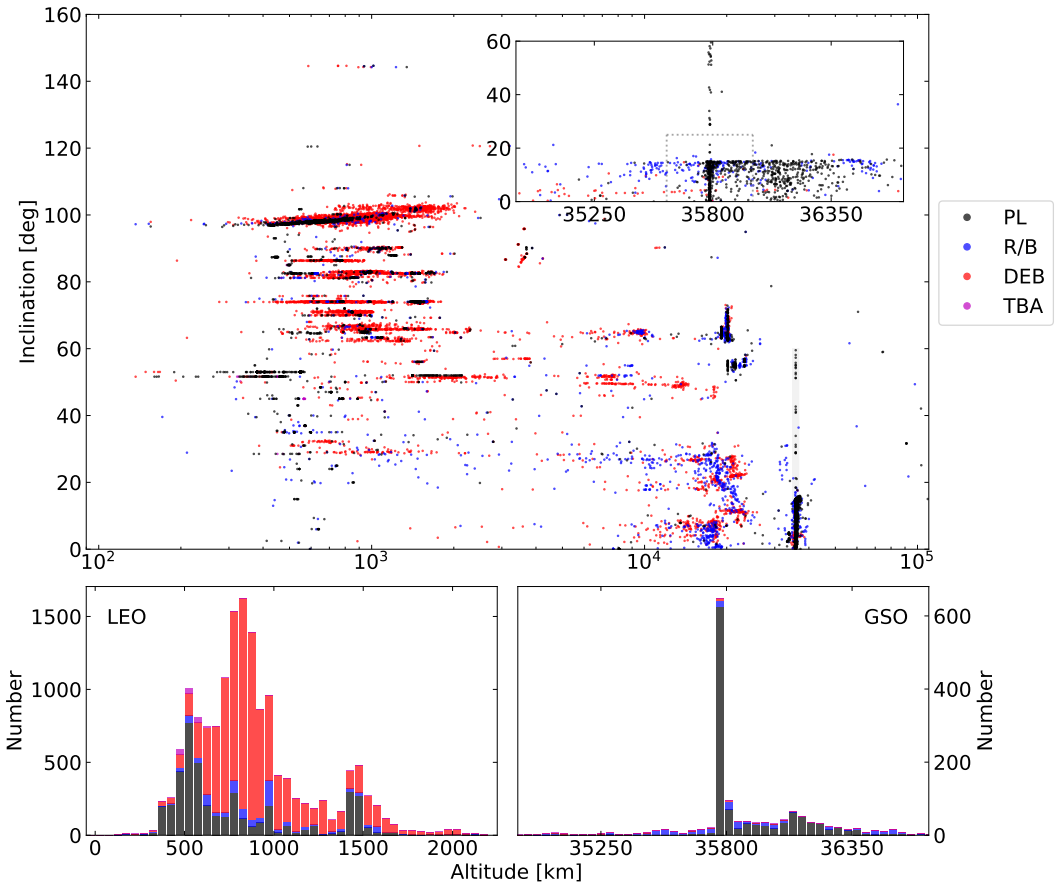

Figure 2.1: Altitudes and orbital inclinations for objects in the publicly available USSPACECOM catalogue, as sourced from the Space-Track website. Altitude is computed as the average of an object's orbital apogee and perigee. Top) Altitude–inclination space for objects in all catalogued regimes. A zoomed-in view (inset) shows the altitude band surrounding the GSO region, indicated by the grey dotted box specifying the boundaries defined in ESA [2020]. Bottom) Altitude histograms for objects in the LEO (left) and GSO (right) regions, as highlighted by the shaded sections in the top panel. In all panels, objects are separated into four categories: payloads (PL, black), rocket bodies (R/B, blue), debris (DEB, red) and "to be assigned" (TBA, pink).

In the top panel of Fig. 2.1, orbital altitudes and inclinations are given for the full range of catalogued objects in near-Earth space, as a function of object type. Histograms are provided in the bottom panels for the LEO and GSO regions, of most relevance to this work, highlighting the most populous altitude bands. In LEO, the 700–900 km band is particularly crowded, where many polar orbiting satellites coexist with fragments from the Fengyun-1C ASAT test and the Iridium–Cosmos collision (see Section 1.2.1). The large spike at $\sim$ 550 km corresponds to the several hundred Starlink satellites that have been launched in the past couple of years. Unsurprisingly, the most densely populated altitude band in the vicinity of the GSO region is that which encompasses the operational GEO belt, though a secondary peak can be seen $\sim$ 350 km above this, where defunct satellites reside in supersynchronous graveyard orbits.

2.1.2 Telescopes

The works presented in Chapters 3–6 make use of observational data acquired by three optical telescopes, based at the Roque de los Muchachos Observatory on La Palma, Canary Islands. A brief overview of the activities carried out by each instrument is given below.

SuperWASP-N

The SuperWASP-North (SuperWASP-N) telescope, alongside its southern counterpart in South Africa, conducted what remains the most successful ground-based exoplanet survey to date [Pollacco et al., 2006]. Over the past couple of years, SuperWASP-N has been repurposed by Paul Chote to observe objects much closer to home. The extensive coverage afforded by its array of eight co-mounted 200 mm f/1.8 camera lenses, each imaging an $8^\circ \times 8^\circ$ FOV with a platescale of $14''$ per pixel, has been exploited in a number of different ways to observe objects in near-Earth space.

Preliminary observation runs in late 2017 and early 2018 focused on scanning the accessible regions of the GEO belt. Since late 2018, however, SuperWASP-N has primarily been used to amass a database of light curves for relatively bright LEO targets. In support of this latest campaign, the camera footprint has been reconfigured to achieve an overlapping $\sim$ 200 deg^2 FOV, and an external timing module has been fitted to facilitate GPS-timestamped triggering of simultaneous exposures. Early contributions to the LEO light curve database are presented in Chapter 4, alongside a discussion of the observational strategies employed.

RASA

In the summer of 2018, a 36 cm f/2.2 Rowe Ackermann Schmidt Astrograph (RASA) was commissioned by Paul Chote and members of the Warwick Satellites Group, as a robotic commercial-off-the-shelf (COTS) instrument for imaging orbital debris. Paired with an FLI ML50100 camera, the RASA was temporarily installed on a Paramount ME mount, and controlled using adapted software from the Warwick 1 m Telescope. The RASA imaged over a $3.6° \times 2.7°$ FOV, with a platescale of $1.57''$ per pixel. As for SuperWASP-N, the RASA was fitted with a custom GPS timing module for precise measurement of start- and end-of-exposure times. The instrument specification is explored further in Chapter 6.

Following a series of manual and partially automated test observations of the GSO region, the RASA was used to acquire a supplementary dataset during a survey of faint GSO debris conducted with the INT. Analysis of the resulting dataset is presented in Chapter 6, alongside a more detailed consideration of the instrument's capabilities. From July–August 2019, the RASA system was used to conduct a fully automated survey of derelict GSO objects, building a database of high cadence light curves. Preliminary observations are outlined in Chapter 4, alongside a discussion of the observational strategies employed.

INT

In September 2018, eight nights of dark–grey time on the 2.54 m INT were used to conduct a survey of faint GSO debris. Observations were carried out using the prime focus Wide Field Camera (WFC), which nominally provides a $33'$ diameter FOV, with a platescale of $0.33''$ per pixel. The larger aperture of the INT supplies a higher collecting area for photons of light, improving the signal-to-noise ratio (SNR), thus making the instrument more sensitive to fainter targets. The results of this survey are presented in Chapter 3.

2.2 Observational strategies

Observational strategies are a key consideration when attempting to detect objects orbiting the Earth. In this section, a brief overview of CCD astronomy is provided, alongside an outline of the strategies that are typically employed to optimise the manifestations of target objects in CCD images for detection algorithms in post-acquisition processing.

2.2.1 CCD astronomy

All observations presented herein make use of optical telescopes paired with CCD detectors. Comprising an array of pixels, a CCD can detect and capture incident photons of light by exploiting the principles of semiconductor physics. The so-called "water bucket" analogy is often used to paint a picture of the inner workings of a CCD [see e.g., Fig. 2.1 of Howell, 2006]. In this analogy, an array of buckets (pixels) in a field (CCD chip) collects rain (photons) during a storm (exposure). Following the storm, a metering procedure (readout) is carried out for each row of buckets in turn, ultimately resulting in a two-dimensional map of the water collected across the field.

In reality, photons of light cannot be stored directly over the course of an exposure. Instead, photons of a suitable energy (wavelength) will be absorbed upon striking a pixel, exciting one or more valence electrons to the conduction band. Sub-pixel 'gates' are used to apply voltages and trap the excited electrons in potential wells during the integration. Upon readout, the voltages are cycled to electronically shift the charge stored within each pixel to a serial shift register, row by row. The selected row is subsequently shifted to an output amplifier, where the charge in each pixel is measured as a voltage and converted to a digital number in analog-to-digital units (ADU) by an analog-to-digital converter (ADC). The gain of a CCD is the amount of voltage or number of electrons required to produce an output of 1 ADU.

At their inception, CCDs revolutionised astronomy, owing primarily to the high quantum efficiencies (QEs) they can achieve, alongside their impressive linearity relative to alternative imagers. The QE gives the ratio of incident photons to those detected by the CCD. Linearity in this context refers to the relationship between the incoming photon intensity and the digital output of the CCD. Beyond a certain threshold intensity, the response of a CCD becomes non-linear, until the maximum ADU set by the dynamic range of the ADC, or indeed the potential well depth, is reached. The FLI ML50100 camera that was paired with the RASA instrument (see Section 2.1.2), for example, hosts a 16-bit ADC, with a maximum output of $2^{16} - 1 = 65535$ ADU. In practice, CCD pixels can reach saturation even below the non-linear regime, and charge can 'bleed' into neighbouring pixels, resulting in bright streaks extending in opposite directions from the saturated pixel.

The SNR for a source of interest within a CCD image is given by

$$\mathrm{SNR} = \frac{N_S}{\sqrt{N_S + n\left(N_B + N_D + N_R^2\right)}}. \tag{2.1}$$

Here, N_S is the number of photons collected for the source, n is the number of pixels associated with the source, N_B is the number of photons contributed by the sky background per pixel, N_D is the number of dark current electrons per pixel, and N_R is the number of read noise electrons per pixel. Dark current arises from thermal noise in the detector, though its contribution is very small for modern devices that are cooled; indeed, subtraction of the dark current is overlooked for the analyses presented herein. The read noise amounts from the non-repeatable nature of the ADC conversion and spurious electrons introduced by the readout electronics themselves. The SNR of a target object, and thus its detectability in post-acquisition processing, will be strongly influenced by the observational strategies employed. Before exploring this further in Section 2.2.3, it is important to understand the key constraints that must be taken into account when conducting any form of optical imaging for SSA.

2.2.2 Observational constraints

A number of factors can affect the ability of an optical telescope to observe an object orbiting the Earth:

- *Visibility above the horizon and weather conditions* — As with any astronomical observation, the target must be visible above the observer's horizon. Sky fields with high elevation angles are preferable, owing to reduced levels of atmospheric extinction. Inclement weather conditions can further obscure the field of interest, and even render the observations unsafe from an instrumental perspective.

- *Earth's shadow and viewing geometry* — Target objects that have passed into the projection of the Earth's shadow cone (accounting for parallax relative to the observer's location) will be eclipsed, and therefore not visible. For this reason, the majority of LEO objects that are visible to ground-based telescopes can only be observed during twilight hours before sunrise and after sunset, as the shadow's projection covers most of the night sky at such low altitudes. For comparison, the shadow's projection at the GEO altitude has an angular radius of around 10°. It is favourable to observe high altitude objects as near to the longitude of the anti-solar point as possible, whilst avoiding the shadow. By minimising the solar phase angle, the apparent brightness of the target is maximised as more sunlight reflects off of the external surfaces along the observer's line of sight, thus improving object detectability in post-acquisition processing.

- *Galactic plane* — When searching for objects of interest in CCD images, it is common practice to mask the stellar background in some way. For instance, the ESA-AIUB processing pipeline applies a slightly enlarged mask relative to the expected stellar morphology for a given series of survey frames, in order to account for windshake or telescope jitter during the exposures [Schildknecht, 2007]. Crowded fields like those in the vicinity of the galactic plane thus render an unfavourably large proportion of the CCD frame unusable. Astrometric calibrations (see Section 2.3.2) are also complicated by the high levels of source blending associated with crowded fields, an issue that can be exacerbated by certain observational strategies.

- *Moon and other bright sources* — Light from the Moon increases the sky background and thus degrades the sensitivity of the observations, making it more likely for faint objects to be lost in the noise floor of the CCD. As a result, care must be taken to maintain a large separation between the field of interest and the Moon. Other bright sources like planets and prominent stars can obscure large regions of the CCD through saturation, and introduce numerous 'distractors' for object detection algorithms to deal with.

- *Telescope and enclosure limitations* — Further elevation constraints can be imposed by the telescope enclosure itself. In the case of SuperWASP-N, for example, the visibility of northerly and, to a lesser extent, southerly fields is severely hindered; Chote et al. [2019] circumvent this issue by observing northerly targets with the southern-most cameras of the SuperWASP-N array, and vice versa for southerly targets. Certain telescope manoeuvres can prove costly from a time perspective and result in large amounts of dead time between successive exposures. The so-called 'meridian flip' undertaken by German equatorial mounts (like that of the RASA system) for collision avoidance serves as an illustrative example.

2.2.3 Optimising observations

While the considerations above are relevant to all activities involving optical imaging, a number of additional factors may be taken into account to optimize a set of observations to search for objects in particular orbital regimes. It is important to gain an appreciation for the ways in which an instrument's properties and modes of operation can work to complement the orbital characteristics of the targets being imaged and aid object detection algorithms in post-acquisition processing.

For most optical SSA observations, targeted or untargeted, image processing algorithms are tasked with searching for sources moving relative to the stellar background. In this sense, strategies for observing orbital debris are very similar to those employed in the search for asteroids and near-Earth objects (NEOs) [see e.g., Rykhlova et al., 2001; Schildknecht, 2007; Micheli et al., 2018]. Main-belt asteroids typically exhibit angular rates of fractions of a degree per day, while NEOs can reach several degrees per hour. Orbital debris span a much larger range of angular rates owing to their proximity to the Earth; high altitude objects like those in the GSO region have comparable rates to the most extreme NEOs, while LEO objects traverse arcs of tens of degrees in the space of minutes. Observations of Earth-orbiting objects can therefore prove very demanding, often requiring large fields of view, high pixel resolutions and rapid readout times.

The manifestation of a target object within the resulting CCD image will depend strongly on the tracking rate employed, and the intrinsic motion of the object itself; the optimal rate will in turn depend on the desired output of the observations. When conducting a survey to probe faint debris, for example, care must be taken to maximize the SNR by tracking at the expected rate of the target objects, thus ensuring that photons of light from a given object will integrate over the same pixels of the CCD. Exposure time is also an important consideration here. In the ideal case of a perfectly matched tracking rate, a longer exposure time will be beneficial as the SNR continues to grow. In practice, however, slight rate offsets can lead to trailing across pixels in the image, and the sky background will consequently become the limiting factor. Stars will also trail across the CCD when tracking non-sidereally, thus increasing the exposure time will result in longer star trails. The negative impacts of star streaking are two-fold: longer streaks make it more difficult to accurately determine the stellar positions in the image space, a key step for both astrometric and photometric calibration of the frame (see Section 2.3.2); star trails can be viewed as distractors when searching for objects of interest, so streak elongation serves to further contaminate the frame and encroach on the regions that are useful for detection. Schildknecht et al. [1995] find that relatively short exposure times of a few seconds achieve a sufficient SNR when tracking at the expected rate of the target object, though longer exposures may be appropriate when optimizing the duty cycle of a particular instrument.

In surveys of the GSO region, the telescope will often be operated in 'stopped' or 'untracked' mode, with tracking disabled. Station-kept satellites in the GEO belt maintain a fixed position above a select longitude and latitude on Earth, and so appear as point sources within CCD frames acquired using this mode of operation.

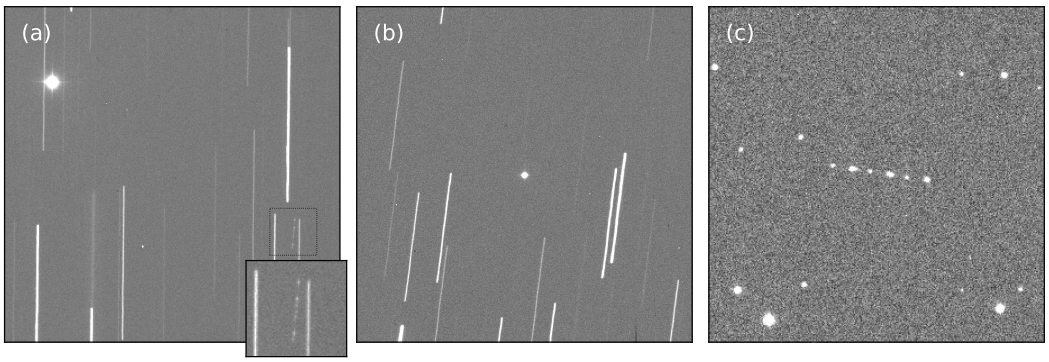

Figure 2.2: Different observational strategies employed to observe objects orbiting the Earth. An untracked INT frame is shown in (a), with stars trailing vertically in the image. A station-kept GEO satellite is visible in the top left-hand corner, while a much fainter, uncatalogued GSO object is shown inset, in the bottom right-hand corner. Other small, point-like features in this panel are single frame detections attributed to cosmic ray events. In (b), differential tracking rates were applied to integrate light from a Titan 3C transtage rocket body (NORAD 5589) onto the same pixels of the INT frame. The stars trail diagonally in the image owing to the non-sidereal rates in both right ascension and declination, while the tracked object is visible as a point source in the centre of the window. A sidereally tracked RASA exposure is given in (c), with background stars visible as point sources and the long trail of the Sirius 3 satellite (NORAD 25492) visible in the centre. Short-duration glints become apparent along the otherwise faint trail in this mode of operation.

Uncontrolled objects in the GSO region will instead manifest as trails, shorter than the star streaks in the image and typically oriented in the north–south direction, owing to the inclined nature of their orbits (see Section 1.3.1). Panel (a) of Fig. 2.2 shows part of a CCD frame acquired with the INT operating with tracking disabled. The morphologies described above are nicely illustrated by the two non-stellar objects in view: a bright and consequently saturated GEO satellite, visible as a point source in the top left-hand corner; a much fainter, uncontrolled object that is drifting relative to the fixed GEO satellite, apparent as a trail with multiple glints in the bottom right-hand corner. A detailed discussion of glinting and other forms of brightness variation is reserved for Chapters 3 and 4, where high cadence light curves are extracted and analysed for a range of trailing GSO and LEO detections.

Surveys of the GSO region, in particular those focused on probing faint debris, are often limited by narrow fields of view. It is therefore important to carry out the observations efficiently, while still obtaining a sufficient level of information for each object detected. Multiple observations of a given detection are necessary

to discern it from false positives like cosmic rays, and also to have any chance of gaining insight into its orbital characteristics, photometric behaviour, and so on. The ESA-AIUB surveys of the GSO region that have taken place over the past couple of decades have predominantly made use of a 1 m Zeiss telescope in Tenerife, which achieves a 0.7° diameter FOV [Schildknecht, 2007]. The ESA-AIUB observations utilize the untracked mode of operation outlined previously when targeting the GSO region, imaging an appropriate field based on the considerations outlined in Section 2.2.2, and following this field for a series of exposures. As the stars drift during the exposure, the telescope is subsequently corrected to image over the same field every time, so that ultimately a strip of declination is scanned from east to west for the duration of a given set of exposures. Scanning a declination strip in this way affords the Zeiss telescope roughly 2.8 minutes in which to image a given GSO object; this is the time it would take for a star to traverse the FOV if the pointing correction were not applied, or equivalently, the time it would take a purely GEO object to cross the field if the telescope were tracking sidereally. There is thus a limit placed on the number of times the object can be observed, which will depend on both the exposure time and the deadtime between exposures.

By way of comparison, it takes around 2.2 minutes for stars to cross the $33'$ diameter field of the INT WFC, and 14.4 minutes for the wider field of the RASA. As will be discussed further in Chapter 3, a variation of the declination strip scanning strategy proved necessary when conducting a survey of GSO debris with the INT, owing to a relatively slow readout time. With the INT stopped, the selected field was allowed to drift for a set of seven exposures, prior to the application of a corrective slew. In this configuration, the frame crossing time for a candidate GSO object is no longer governed by the sidereal rate, and is instead dictated by the rate of the target objects themselves. The analyses presented herein make use of the rate limits defined in Seitzer et al. [2011] when limiting attention to circular orbits in the GSO regime:

$$|\text{Hour Angle rate}| < 2'' \, \text{s}^{-1} \text{ and } |\text{Declination rate}| < 5'' \, \text{s}^{-1}. \tag{2.2}$$

Taking the extremal rate in declination, the minimum crossing time is extended to 6.6 minutes with this strategy in place, ensuring that multiple observations of a detected object can be made in spite of the large amount of deadtime between exposures. If an instrument's combined exposure and readout time is sufficiently low, it may be possible to scan multiple strips at once. Another common approach to enhance the efficiency of a survey and combat a narrow FOV is to target regions

of space that are known to be densely populated, thus making the reasonable assumption that debris will trace the known catalogued population. For reference, an evolutionary view of the GSO region over the course of a sidereal day is provided in Fig. 2.3, illustrating zones of comparatively high density for the catalogued population, accompanied by views of the analemma-like signatures mapped out by GSO objects in different coordinate frames. Unsurprisingly, the highest concentrations in right ascension and declination (α, δ) space are found along the GEO belt which, from the topocentric viewpoint of La Palma, sits in the range $-5° < \delta < -4°$. Nafi and Geller [2019], for example, explore the benefits of targeting the so-called 'pinch points' where numerous uncontrolled objects pass through their ascending or descending nodes, supplementing the density of the operational zone.

Angular rates for GTO objects are higher than for those in circular GSO orbits, typically in the range 5–10$''\,\mathrm{s}^{-1}$. When targeting the GTO regime, it is therefore more appropriate to track at a rate within this bracket. An example of a CCD frame acquired with the INT in differential tracking mode is provided in panel (b) of Fig. 2.2; the star trails are slanted diagonally on account of the predominantly north–south motion of the uncontrolled GSO target, while the tracked object itself manifests as a point source in the resulting image. LEO objects can exhibit angular rates in excess of several hundred arcseconds per second. Very short exposure times are thus critical when tracking LEO targets, in order to prevent unreasonable levels of star streak coverage, alongside short readout times to maintain an efficient duty cycle. Scientific Complementary Metal-Oxide Semiconductor (sCMOS) devices are well suited to this task, achieving high QEs, low read noises and fast readout times, though a detailed discussion of these detectors falls outside the scope of this thesis. If the state (position, velocity) vector of the target object is poorly known, as can often be the case when tracking based on aged TLE information, a large FOV can also be necessary.

When carrying out targeted observations of a bright satellite, it may be beneficial to track at the sidereal rate and allow the target to trail across pixels of the CCD frame, imposing an additional $\sim 15''\,\mathrm{s}^{-1}$ motion in the right ascension direction. In sidereal tracking mode, the stars manifest as point sources in the frame, as illustrated in panel (c) of Fig. 2.2, thus making them minimally invasive in the object search phase. Longer exposure times have the effect of elongating the target's trail, presenting the observer with an opportunity to extract high cadence photometric information, a procedure that is outlined further in Section 2.4.5. Spreading the integrated light across a trail can reveal finer temporal features such as glints, emulating the process of taking many short exposure frames in quick succession (say,

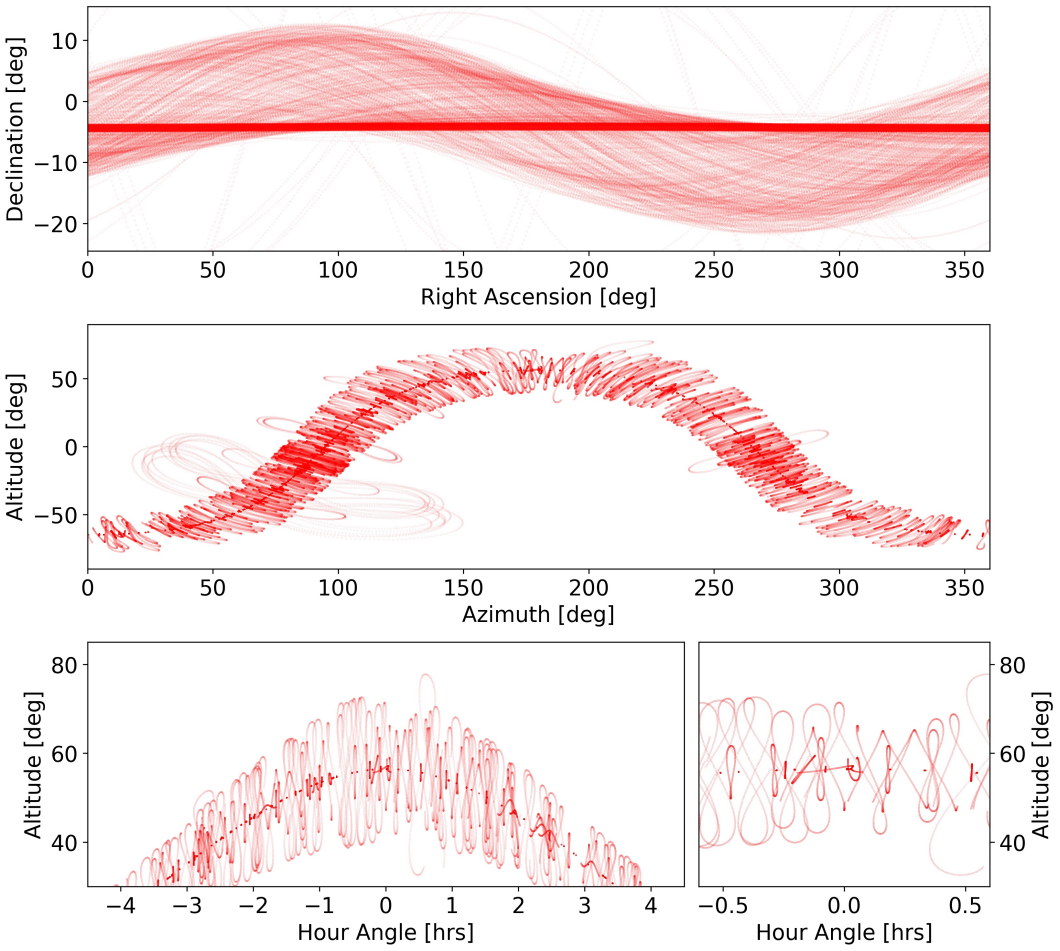

Figure 2.3: Evolution of the GSO region over the course of a sidereal day, depicted in different coordinate frames. Object positions are propagated from a starting epoch of 2020-12-20T19:00:00.00 UTC using the SGP4 algorithm, with latest TLEs extracted from the publicly available USSPACECOM catalogue, accessed via the Space-Track website. Positions are computed relative to an observer on the Canary Island of La Palma (longitude 28.7603135° N, latitude 17.8796168° W, elevation 2387 m). Top) Evolution in topocentric right ascension and declination space. The GEO belt, as visible from La Palma, sits between −4° and −5° declination. Surrounding sinusoids correspond to objects in inclined orbits, mostly uncontrolled (see Section 1.3.1). Middle) The horizontal (Altitude–Azimuth) coordinate system is fixed to a location on Earth, not the stars, and so provides a clearer sense of the analemma-like ground tracks of GSO objects relative to a ground-based observatory. Bottom left) GSO ground tracks in hour angle and altitude space, visible from La Palma with an elevation exceeding 30° above the horizon. A zoomed-in view is provided (bottom right), more clearly illustrating the different analemmas (e.g., figure-of-eight) traced by GSO objects over the course of a sidereal day.

with an sCMOS detector) with a single, long exposure CCD frame. The extremely high angular rates of LEO targets call for ultra-wide fields of view if tracking sidereally, or sufficiently short exposure times, in order to capture the full extent of the object's trail.

2.3 Data reduction

Optical imaging can provide a wealth of information for SSA, typically stemming from two key data products: angles-only positional information, from which a target's state vector can be derived (see Section 2.5); and photometric light curves, providing an insight into the target's attitude and physical properties. Prior to the extraction of this information, a number of steps must be carried out to calibrate the raw CCD image frames and search for the target object(s) of interest.

2.3.1 Standard astronomical calibrations

The analysis pipelines presented in Chapters 3, 4 and 6 each carry out bias and flat field corrections in the initial stages of image processing. A bias frame is a 0 s exposure acquired with the camera shutter closed. Bias voltages are constant offsets that are applied to avoid negative pixel counts, which cannot be represented by the ADC. With no exposure time, bias frames are devoid of photoelectrons and thermally excited electrons, and so specifically probe the bias level and read noise. Typically, several bias frames are median combined to form a master bias, as each pixel may differ from the true bias level owing to read noise, cosmic rays, and so on. The master bias can then be subtracted from all other frames (including flat fields) to remove the bias level from each pixel.

Flat field frames are used to correct for pixel-to-pixel variations, vignetting and non-uniform illumination across the CCD. Owing to the wavelength dependence of the latter two, such frames must be taken with the same filter used for observations. In particular, the wide field images captured by the SuperWASP-N array suffer from severe circular vignetting that arises from baffles in the lenses. Flat fields are obtained by exposing the CCD to a uniform light source, typically the twilight sky at dusk or dawn. When acquiring the flat fields, different regions of the twilight sky are imaged to facilitate the simple removal of stars when combining to create a master frame. After bias subtracting and subsequently normalizing each flat field by its mean flux, several are median combined to form a master flat. Bias subtracted science frames can then be divided by the resulting master flat to carry out the flat field correction.

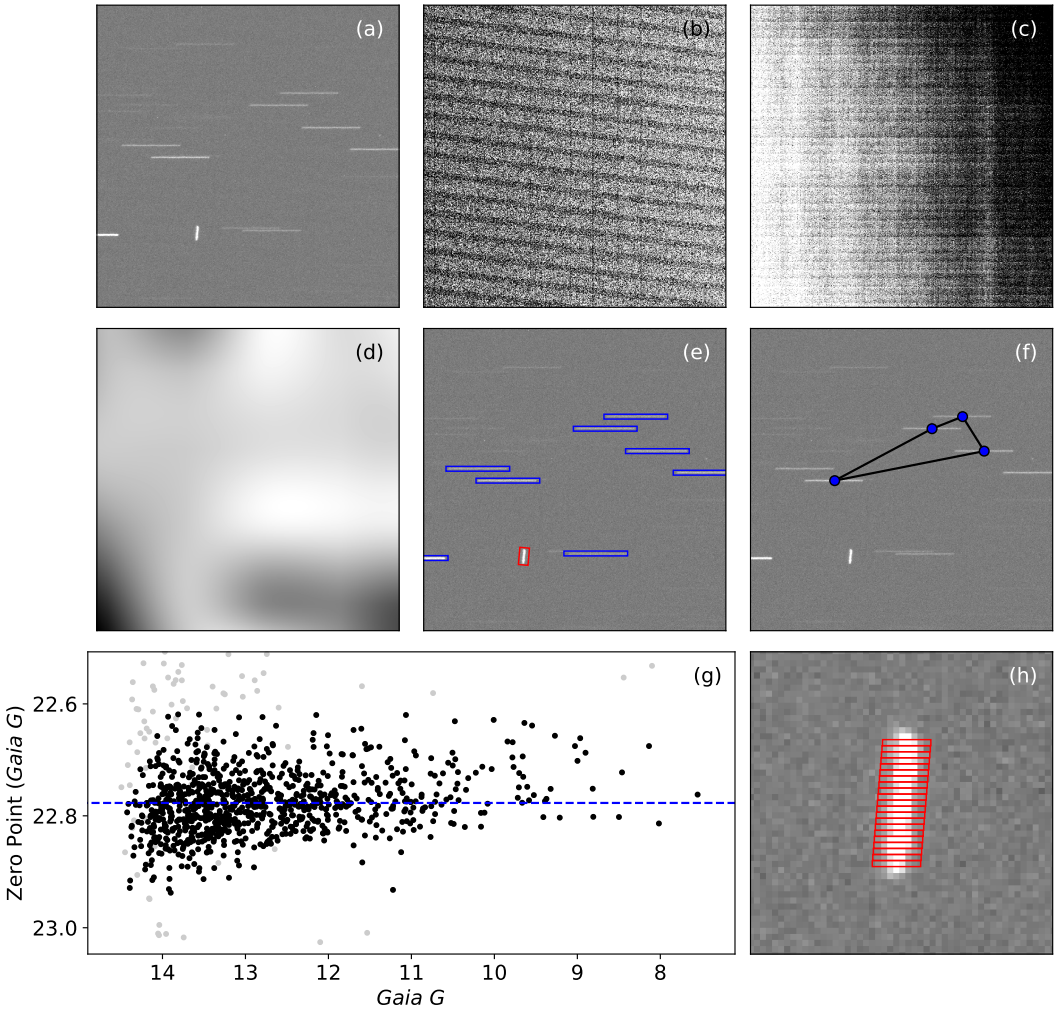

Figure 2.4: Stages of the image processing pipeline used to reduce RASA frames in Chapter 6, largely representative of all the analysis pipelines deployed throughout this thesis. (a) A 400×400 square-pixel window sampled from a raw 10 s exposure acquired with the RASA. The telescope was operated with tracking disabled, such that stars trail horizontally in the image and objects in the GSO region manifest as shorter trails or points. A GSO satellite can be seen in the bottom left-hand corner. The corresponding windows in the master bias and flat field frames are provided in (b) and (c), respectively, while (d) shows a map of the sky background. (e) Source detection techniques (see Section 2.4) are used to identify star trails (blue) and candidate objects of interest (red) within the image. (f) An astrometric calibration is carried out using the known star trail positions. (g) A photometric calibration is performed by comparing the measured brightnesses of stars in the image to those in a standard catalogue, and the zero point of the frame (blue line) is estimated. (h) Rectangular apertures (red) placed along the trails of candidate objects of interest are used to extract photometric light curves.

Following the bias and flat field corrections, it is important to model and subtract the spatially-varying sky background from each calibrated science frame. Modelling of the background is carried out using `SEP` [Barbary, 2016], a Python library for source extraction and photometry, built around the core algorithms of Source Extractor [Bertin and Arnouts, 1996]. An example window of a raw RASA science frame, the corresponding regions within the master bias and flat field frames, and the 2D background map for the window are provided in panels (a)–(d) of Fig. 2.4.

2.3.2 Astrometric and photometric calibrations

A source extraction procedure, making use of `SEP` and the filtering techniques outlined in Section 2.4.1, can be carried out to identify stellar sources within the background subtracted science frames. In order to convert the positions of stars from pixel (x, y) to celestial (α, δ) coordinates, an astrometric calibration must be performed to map the image using known catalogued stars. The `Astrometry.net` tool is used frequently throughout to perform blind solving of astronomical images, pattern-matching subset quadrilaterals of stars against existing sky catalogue grids to determine accurate World Coordinate System (WCS) solutions [Lang et al., 2010]. With the resulting WCS metadata, it is simple to convert between image and sky coordinates using `astropy` WCS routines [Robitaille et al., 2013; Price-Whelan et al., 2018]. In Chapter 6, an iterative procedure that can be performed in order to refine the WCS solution determined by `Astrometry.net` is outlined. Panel (e) of Fig. 2.4 shows the results of a source extraction procedure carried out for the example RASA frame; the methods used to discern between stars and target objects within the image are discussed in Section 2.4. An example of a subset quadrilateral of detected star trails is provided in panel (f) of Fig. 2.4.

Photometry is the technique of measuring the flux or intensity of light, and is the source of a key diagnostic product when carrying out optical observations for SSA. Prior to the extraction of brightness information for candidate objects of interest, the CCD frame must be photometrically calibrated. The photometric calibration is achieved by cross-matching the WCS coordinates of the detected star trails with those of known stars in standard catalogues. Care must be taken to filter out stellar detections that are blended on the image pixel scale. The photometric zero point for the frame is determined by comparing the standard magnitudes of the catalogued stars in an appropriate filter band against their instrumental counterparts, derived by summing rectangular apertures placed over the extracted star trails. The zero point measures the brightness of a source that would produce one count (ADU) per second on the CCD, and thus is a function of the instrument

properties and the sky transparency.

2.4 Object detection

Objects of interest can exhibit a variety of morphologies depending on their orbital characteristics and the observational strategies employed, as evidenced in Fig. 2.2. A robust source extraction procedure is therefore required, in order to:

- detect point sources and trails within the image, corresponding to candidate stars or objects of interest;
- distinguish between the two, while filtering out spurious detections such as cosmic rays, detector artefacts, and so on;
- refine positional estimates for the sources that survive filtering to ensure accurate placement of apertures for brightness measurements.

The following sections give an overview of the key techniques employed by the analysis pipelines presented in Chapters 3, 4 and 6 to perform the above tasks.

2.4.1 Thresholding

The `SEP` library features a threshold-based extraction tool, which can be used to obtain a preliminary inventory of sources in the CCD frame. As part of the extraction process, the image is convolved with a matched filter to improve the SNR of detections. Photons from a stationary, unresolved source (i.e. far smaller than a pixel, the maximum resolution of the imager) will spread across an area described by the point spread function (PSF) of the image. The structure of the PSF is shaped by atmospheric turbulence, alongside diffraction and aberration effects from the telescope optics themselves. Matched filters afford the opportunity to extend the concept of a PSF to account for trailing sources within the frame, though their implementation can significantly increase the computational expense of source extraction algorithms. Prior information regarding the observational strategies employed can be incorporated by substituting the default convolution filter[3] for one that more closely represents the expected morphologies of target objects within the image. For example, star trails in an untracked CCD frame can be represented by a trailed gaussian PSF, with an estimated length and orientation inferred from the telescope alignment, exposure time and plate scale of the detector. This approach is adopted

[3]The default convolution filter for the `SEP` extraction tool is a 3×3 array with weights $[[1, 2, 1], [2, 4, 2], [1, 2, 1]]$, appropriate when searching for point sources in an image.

in Chapter 6 to extract stellar sources from survey frames, and future development will look to incorporate it when detecting the target objects themselves.

Subsequent thresholding returns an array of sources with a sufficiently strong convolution response. Typically, the deblending functionality of the `SEP` extraction routine is bypassed in an effort to avoid the splitting of trailed sources into multiple detections; a particularly prevalent issue for candidate objects that exhibit significant brightness variation over the course of an exposure. Stars can be distinguished fairly robustly by exploiting their common morphological properties, namely their length and orientation in image space. The extracted positional information for the stellar subset of detections can then be parsed to the solve-field routine of `Astrometry.net`, in order to determine a preliminary astrometric solution, as described in Section 2.3.2.

2.4.2 Mathematical morphology

After astrometrically and photometrically calibrating the CCD frame, the star trails serve no further purpose other than to distract object search algorithms with false positives, thus making it beneficial to remove their signal from the frame. Taking inspiration from Laas-Bourez et al. [2009], this is achieved by applying mathematical morphological operations. Mathematical morphology is a technique for analysing geometrical structures in binary and greyscale images. Here, a brief overview of the relevant formalism is provided; for further detail, the reader is referred to the extensive body of literature available on the subject [see e.g., Breen et al., 2000; Matheron and Serra, 2002; Serra and Soille, 2012].

By applying some combination of morphological operations, it is possible to probe an image $f(x)$ using a structuring element B. The structuring element is a simple pixel structure that can be used to match or miss shapes within the image. A morphological transformation is achieved by conducting a pixel-by-pixel scan of the image with B. For a given step of the scan, B is centred on the pixel of interest, encompassing a set of neighbouring pixels that are fed as input to the desired operation, generating a value that is assigned to the corresponding pixel in the transformed image. The simplest morphological operations are erosion ϵ and dilation δ, which can be expressed as

$$\epsilon^B(f(x)) = \inf\left[f(x-b) : b \in B\right] \quad \text{and} \quad \delta^B(f(x)) = \sup\left[f(x+b) : b \in B\right]. \quad (2.3)$$

The erosion operation yields the minimum pixel value within the neighbourhood defined by the scanning structuring element, while the dilation instead returns the

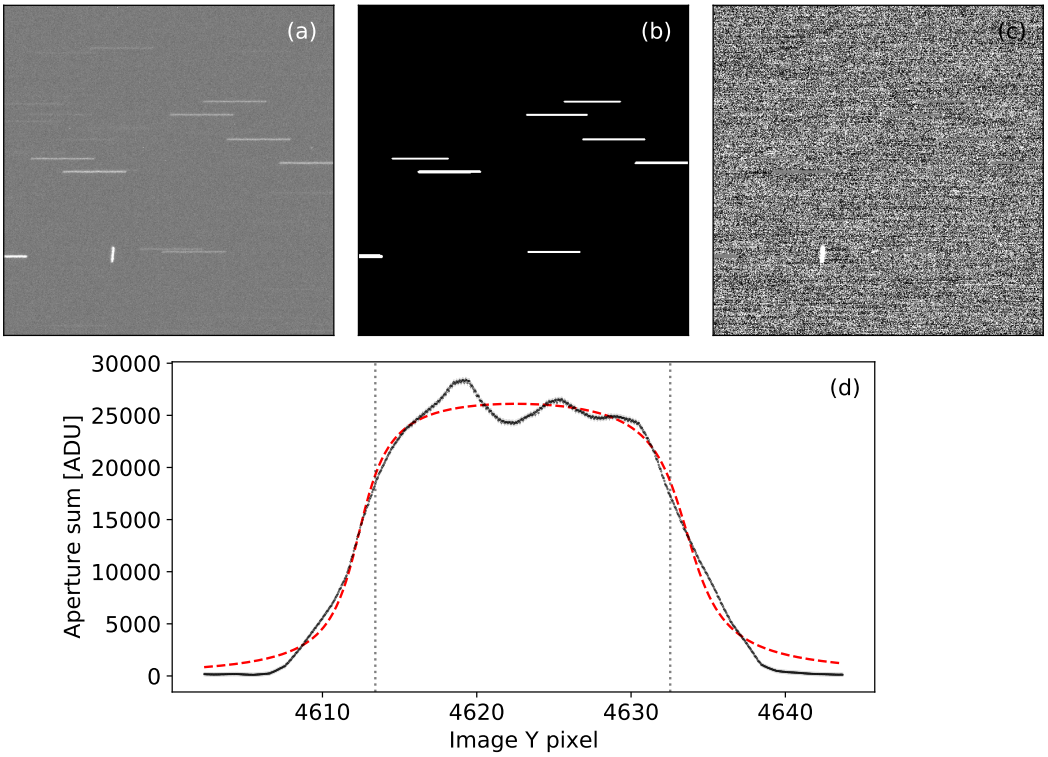

Figure 2.5: Key steps of the detection algorithm carried out as part of the image processing pipeline used to reduce RASA frames in Chapter 6, largely representative of all the analysis pipelines deployed throughout this thesis. (a) A 400×400 square-pixel window sampled from a raw 10 s exposure acquired with the RASA. The telescope was operated with tracking disabled, such that the stars trail horizontally in the image and objects in the GSO region manifest as shorter trails or points. A GSO satellite can be seen in the bottom left-hand corner. A stellar mask obtained using mathematical morphology techniques (see Section 2.4.2) is shown in (b), while the star-subtracted frame is given in (c). Masked pixels in the latter panel have been replaced by the mean pixel value for clarity. The along-trail profile (black) for the detection is provided in (d), fitted with a Tepui function (red). Resulting estimates for the start- and end-of-exposure y positions are marked (grey).

maximum pixel value. Erosions act to reduce peaks and spread dark regions within the image, while dilations widen peaks and diminish dark regions. When applied sequentially, these operations give the opening O and closing C of an image. The opening operation $O^B\left(f\left(x\right)\right) = \delta^B\left(\epsilon^B\left(f\left(x\right)\right)\right)$ acts to remove small peaks, while the closing operation $C^B\left(f\left(x\right)\right) = \epsilon^B\left(\delta^B\left(f\left(x\right)\right)\right)$ has the effect of removing small dark regions.

The object detection stages of the analysis pipelines presented in Chapters 3 and 6 follow the lead of Laas-Bourez et al. [2009], making use of the Spread TopHat transformation η, given by

$$\eta^B(f(x)) = f(x) - O^B(C^B(f(x))). \tag{2.4}$$

In this transformation, the opening of the closing is subtracted from the original image, acting to remove sources that contain the structuring element, while limiting remnant noise in the resulting image. The `scipy` morphology routines [Jones et al., 2001] are employed to carry out the transformation, with rectangular structuring elements of dimensions $1\times\frac{1}{2}l_{ST}$ pixels and $1\times\frac{1}{6}l_{ST}$ pixels for the opening and closing operations, respectively, where l_{ST} is the expected length of star trails in the CCD frame. The chosen dimensions ensure that both elements are contained within even the fainter star trails, leading to their removal from the image. Panels (a)–(c) of Fig. 2.5 provide an example of the Spread TopHat transformation in action, culminating in the star-subtracted frame shown in (c). The candidate GSO source is retained, as it does not contain either of the structuring elements. A `SEP` source extraction can subsequently be performed using the transformed frame, detecting any sources above a set threshold that survive the morphological transformation. Remnant false positives, such as star trail edges, cosmic rays and detector artefacts are filtered out using morphological cuts, alongside previously refined knowledge of the stellar positions from the calibration stages of processing.

2.4.3 Position refinement

In the case of trailed detections, it is necessary to accurately determine the start and end points, as they will correspond to the object's angular positions at the start- and end-of-exposure, respectively. The source extraction carried out on the star-subtracted frame makes use of the default convolution filter, owing to the wide range of possible target morphologies. The resulting positional estimates are thus sufficiently accurate for point-like detections (station-kept GEO satellites in the untracked frames), though poorly determined for trailed candidates (uncontrolled

objects in the untracked frames).

One method that can be used to refine the initial positional estimates is to fit the intensity profiles measured along and across the detected trail. Typically, a gaussian model is appropriate for the across-trail fit, while a good approximation of the along-trail profile is given by a "Tepui" function, of the form

$$I(x) = A\left[\arctan\left(b_1\left(x - c - x_0\right)\right) - \arctan\left(b_2\left(x + c - x_0\right)\right)\right]. \tag{2.5}$$

Here, A is the normalised amplitude, b_1 and b_2 are related to the profile tilt, c gives the half-width and x_0 is a translational offset. Numerous studies have made use of the Tepui function when fitting streaks in astronomical images [see e.g., Montojo et al., 2011; Park et al., 2016; Lacruz et al., 2018]. In Chapter 3, the relevant intensity profiles are obtained by summing circular apertures placed along and across the trail, using the initial `SEP` positional estimates to inform aperture placement. An example of a Tepui fit applied to the along-trail profile of an uncontrolled GSO object observed with the RASA is provided in panel (d) of Fig. 2.5.

Alternatively, the initial `SEP` extraction can be used to narrow the search window, allowing a more targeted extraction to be performed using a matched filter with a structure informed by the preliminary estimates of length and orientation in image space. The use of a more representative filter strengthens the convolution response, refining the initial estimates of the target's morphology. The matched filtering approach is explored further in Chapter 6.

2.4.4 Arc correlation

A correlation of detections between frames allows for additional vetting of remnant false positives that survive the preceding rounds of filtering. This is particularly important for surveys of faint debris, where detection thresholds have to be set as close to the noise floor as possible, raising the number of spurious detections that need to be flagged. When observing the GSO region with tracking disabled, frame-to-frame correlation within a given pointing of the telescope can be carried out simply, yet fairly robustly, by fitting and sequentially updating a linear trajectory in hour angle and declination space. This method assumes a constant angular velocity for the target; a reasonable assumption to make for the short observation windows, and consequently short arcs, that are typical of faint GSO surveys. In Chapter 3, the frame-to-frame correlation is carried out manually 'by-eye', while the aforementioned procedure is automated for the analyses presented in Chapter 6. The approach of generating and updating a rolling fit across successive frames can

easily be extended to objects in other orbital regimes, provided the observer has a reasonably precise handle on the expected motion of the target.

Trails with one or more saddle points in their profiles that have split into multiple detections within a single exposure can be identified at this stage and combined to form a single detection. For these cases, additional vetting is carried out 'by-eye'. Typically, candidates must be detected in two or more frames to be considered real, though objects with fewer than three correlated detections have been manually inspected for the analyses presented herein. Isolated detections are discarded as false positives.

2.4.5 Aperture photometry and light curve extraction

Aperture photometry entails the summing of pixel values within a two-dimensional aperture placed at the centroid of a source. For cases involving stars or known, tracked objects orbiting the Earth, aperture placement can be guided by catalogued information, subject to a successful astrometric calibration. In the latter case, the necessary orbital state information is typically derived from TLEs (see Section 1.2.2), thus care must be taken to account for positional offsets arising from inaccuracies and shift apertures accordingly; a method for dealing with this problem is discussed further in Chapter 4. TLE information will be lacking for uncatalogued objects, such as those encountered by a dedicated survey, and so aperture placement will instead rely on centroiding in image space carried out as part of a source extraction procedure.

For stationary, point-like sources in an image, circular apertures are most appropriate, with a radius encompassing as few surrounding background pixels as possible, in order to minimise the contribution of read noise. Rectangular or pill-like apertures are more suitable for trailed detections. In the analyses to follow, the `SEP` library is utilised when summing circular apertures, the `photutils` routines [Bradley et al., 2016] are employed for rectangular cases and the `TRIPPy` package [Fraser et al., 2016] is used for pill photometry. Background-subtracted frames can be used for the aperture summation; alternatively, an annulus can be placed around the aperture and summed to give an estimate of the sky background, though care must be taken to avoid contamination from other sources nearby, a common issue for crowded fields. The background-corrected aperture sum gives an estimate of the flux received from the target over the course of the exposure. The instrumental magnitude m_{instr} of the target can be derived from its flux f, as $m_{\mathrm{instr}} = -2.5 \log_{10} (f \,/\, t_{\mathrm{exp}})$, where t_{exp} is the exposure time. It is common for brightness measurements in astronomy and the space sciences to be measured on a logarithmic scale in this way, with base 2.5.

The so-called magnitude scale is such that brighter stars have lower magnitudes. The instrumental magnitude can be summed with the photometric zero point of the frame to give the calibrated magnitude in a particular pass band.

An advantage of operating the telescope with a slight discrepancy between the tracking rate and the expected rate for target objects is that high cadence photometric information can be extracted from each individual frame. As mentioned previously, this is the case for uncontrolled GSO objects when observed using the untracked mode of operation, or bright targets in any near-Earth regime when tracking sidereally. In order to extract light curves from trailed detections, appropriate aperture centroids are computed using the refined start and end positions. These can be assigned a timestamp, either by assuming a constant velocity throughout the exposure such that the target spends an equal amount of time in each aperture (necessary if the detection is uncatalogued, see Chapter 3), or by informing aperture placement with a TLE (possible if the object is catalogued, see Chapter 4). When extracting light curves, background contamination (e.g., blending with star trails) is corrected by placing equivalent apertures in a reference frame. The process of selecting, or indeed acquiring, an appropriate reference frame varies depending on the observational strategy employed, thus further detail is reserved for the relevant chapters to follow. For accurate aperture placement, the images must be aligned to ensure that their respective fields overlap; typically, an initial alignment is carried out using the astrometric solutions, and remnant offsets are accounted for with the `DONUTS` package [McCormac et al., 2013]. With the reference apertures in place, an aperture-by-aperture subtraction can be performed to apply the correction.

2.5 Orbit determination

Though so-called "angles-only" (right ascension, declination) measurements have many uses in their raw form, their conversion to an orbit is critical for a number of applications: identifying or gaining "custody" of the object on future nights of observations; tracking and cataloguing the object, keeping its orbital state up-to-date; correlating separate arcs and combining those that belong to the same object, a common task when conducting surveys. This section briefly outlines two orbit determination methods that are used in analyses to come.

2.5.1 Gauss Method

For preliminary or initial orbit determination (IOD), the Gauss Method is employed. The algorithm takes as input three observations at times (t_1, t_2, t_3), the position

vectors of the observer at those times ($\mathbf{R}_1$, $\mathbf{R}_2$, $\mathbf{R}_3$) and the corresponding direction cosine vectors ($\hat{\boldsymbol{\rho}}_1$, $\hat{\boldsymbol{\rho}}_2$, $\hat{\boldsymbol{\rho}}_3$). The slant ranges ($\rho_1$, ρ_2, ρ_3) are then estimated in order to compute the object's geocentric position vectors [Curtis, 2013]

$$\mathbf{r}_j = \mathbf{R}_j + \rho_j \hat{\boldsymbol{\rho}}_j, \tag{2.6}$$

where $j = 1, 2, 3$. By estimating the Lagrange coefficients for the object, it is possible to compute the velocity vector for the second (middle) observation, $\mathbf{v_2}$. For reference, a step-by-step outline of the algorithm is provided in Appendix A, alongside an iterative procedure that can be used to improve upon the initial orbit. With knowledge of the state vector ($\mathbf{r_2}$, $\mathbf{v_2}$), the orbital elements (semi-major axis a, eccentricity e, inclination i, right ascension of the ascending node Ω, argument of perigee ω and true anomaly θ) can be determined using the algorithm outlined in Appendix B. The sensitivity of the Gauss Method to a variety of input variables, such as the time interval between observations, is explored in Chapter 5.

2.5.2 Markov Chain Monte Carlo

In Chapter 5, a TLE-driven orbit fitting package is developed, making use of a Markov Chain Monte Carlo (MCMC) method. The MCMC is a powerful numerical technique for estimating model parameters and their uncertainties, incorporating prior information that would otherwise be ignored with alternative methods (e.g., a least-squares fit). In MCMC algorithms, models are generated by sampling from the posterior probability distribution $P(\theta \mid \Delta)$ for model parameters θ, and compared against the available dataset Δ. The posterior probability gives the distribution of parameters that is consistent with the dataset, and can be found using Bayes' Theorem,

$$P(\theta \mid \Delta) = \frac{P(\Delta \mid \theta)\, P(\theta)}{P(\Delta)}. \tag{2.7}$$

The posterior probability is governed by: the prior function $P(\theta)$, which encodes any prior knowledge that is available for the parameters, such as fundamental limits or expected ranges based on previous investigations; the likelihood function $P(\Delta \mid \theta)$, which gives the probability of observing the dataset as generated by the given set of model parameters; the evidence $P(\Delta)$, which is the probability of observing the dataset given the model itself, accounting for all possible values of the model parameters in a weighted fashion. It can be computationally expensive to determine the evidence; fortunately, in many MCMC algorithms, the term cancels when drawing samples from the posterior distribution, and so can be ignored.

Though a number of algorithms exist [see e.g., Section 29, MacKay, 2003], the discussion here is limited to the Metropolis-Hastings (M-H) algorithm [see e.g., Chib and Greenberg, 1995], a variant of which is employed by the `emcee` package [Foreman-Mackey et al., 2013] that features in Chapter 5. The algorithm initiates with an ensemble of "walkers", derived from preliminary guesses for the model parameters; at every step of the Markov chain, each walker will encode a different set of parameter values. The walkers undergo a random walk, exploring the parameter space, and ultimately drawing a representative sample from the posterior distribution. At each step, a new candidate set of model parameters is drawn. The posterior probability of the newly proposed model is compared to that of the previous step. If the probability is higher, such that a jump to the new step would be advantageous, then the new set of parameters is accepted. However, if the probability is lower, the new set of parameters is only accepted if the probability ratio exceeds a randomly generated number between 0 and 1. Otherwise, the previous set of parameters is retained as the chain progresses to the next step. Models that better fit the dataset are thus more likely to be accepted by the algorithm, and over time the walkers will climb *en masse* to the highest likelihood regions of the parameter space. The so-called "burn-in" phase, marked by a large-scale migration of walkers in the initial stages of the chain, is cut in order to retain only the maximum likelihood sample. Given a sufficient number of steps, the chain will converge upon a stationary set of samples from the posterior distribution, from which the 'optimal' set of parameters can be extracted.

The observational strategies and analysis techniques introduced are utilised in the remaining chapters to acquire and process optical datasets for a variety of SSA-driven activities. The following chapter provides an overview of photometric results from a survey of the GSO region conducted with the INT.

Chapter 3

A survey of faint GSO debris

This chapter provides an overview of a survey conducted with the INT to probe the faint GSO debris environment. The motivation for such a survey is explored in Section 3.1, while Section 3.2 outlines the observational strategy employed. The analysis pipeline developed to process the survey images and extract photometric information is described in Section 3.3. Key results from the survey are presented and discussed in Section 3.4, and a summary is provided in Section 3.5. The work forms part of DebrisWatch (DW), an ongoing collaboration between the University of Warwick and the Defence Science and Technology Laboratory (Dstl, UK) investigating the population of GSO debris.

Declaration — The following summarises elements of collaborative work that are included in this chapter. Telescope time on the INT was awarded upon the successful review of a proposal drafted by Don Pollacco (University of Warwick), with named collaborators: myself, Paul Chote, Tom Marsh, Dimitri Veras (University of Warwick); Stuart Eves (SJE Space Ltd); Chris Watson (Queen's University Belfast). Paul Chote and myself were accompanied by Will Feline and Grant Privett (Dstl) for the observing run, both of whom assisted with initial eye-balling of survey frames. The control script that was used to carry out observational sequences and synchronise the INT and RASA instruments was developed by Paul Chote. Will Feline and Nick Harwood (Dstl) performed the correlation between orbital arcs detected by the survey and known objects in the publicly available USSPACECOM catalogue. The analyses presented in Section 3.4.3 take inspiration from Chote [2020]; elements that are reproduced or extended from this work are clearly indicated in the section, and included with the author's permission. This chapter is based on findings that were presented in the 2019 AMOS technical proceeding, Blake et al. [2019], which was later adapted and published as the paper, Blake et al. [2021].

3.1 Motivation

Knowledge of the unique and desirable characteristics offered by orbits in the GSO region predates the dawn of the Space Age. Objects in the GSO region have an orbital period matching that of the Earth's rotation, and consequently trace simple, localised analemmas in an observer's sky over the course of a sidereal day (see Section 2.2.3). Station-kept satellites in the GEO belt remain stationary in the Earth-fixed frame, a property exploited for communications since the 1960s.

Though the LEO region has historically received more attention from an orbital debris perspective, owing to a much higher spatial density and the presence of crewed missions, there are nevertheless plenty of reasons why the GSO debris environment is a cause for concern:

- the GSO region is situated far above the outer layers of the atmosphere, and so lacks the natural 'sink' for debris that would otherwise be driven by atmospheric drag;
- manoeuvres to deorbit GSO spacecraft are both impractical and expensive, thus pioneering ADR missions currently have their sights set on LEO targets;
- the GEO belt is a narrow ring of orbits in the equatorial plane, and orbital slots are limited both latitudinally (0° inclination is desirable) and longitudinally (to prevent crowding and radio interference between payloads), hence the need to clear the operational zone upon reaching EOL;
- in spite of the upwards trend shown in the bottom right panel of Fig. 1.6 in Section 1.2.3, a 100 % success rate for existing EOL mitigation measures is yet to be achieved, thus many derelict objects continue to penetrate the GSOPR and pose a risk to active satellites;
- the orbits of GSO debris will evolve under the influence of perturbative forces acting in the region (see Section 1.3.1), and relative velocities can approach the hypervelocity (4–5 $\mathrm{km s^{-1}}$ and above) regime where even cm-sized debris could cause mission-fatal damage to an active satellite;
- rocket bodies in GTOs or other HEOs are often abandoned in elliptical orbits that cross the GSOPR, some of which continue to exist in an unpassivated state with a high risk of explosion;
- indeed, recent observations of anomalies and break-ups in the GSO, GTO and HEO regimes (see Section 1.3.2) have highlighted the growing population of faint debris penetrating the GSOPR.

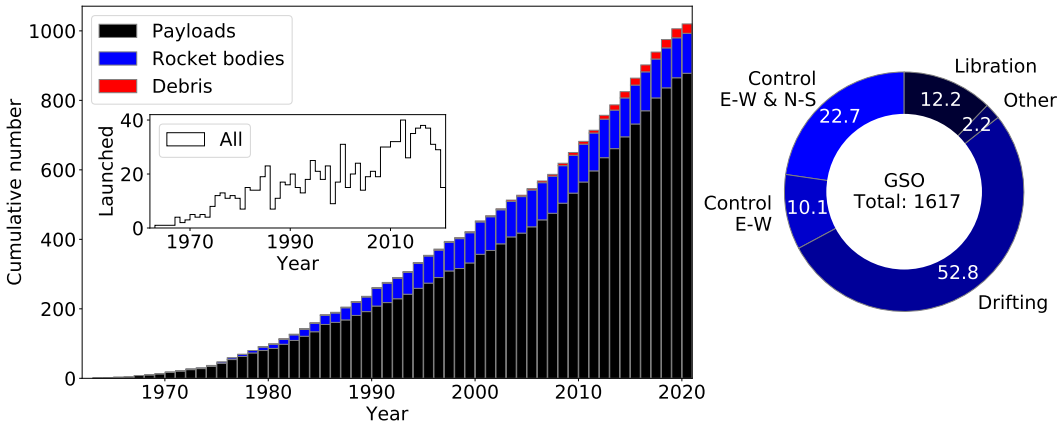

Figure 3.1: Left) The cumulative number of tracked objects in the GSO region, with objects separated into three categories: payloads (black), rocket bodies (blue) and debris (red). Debris fragments are binned by the year they were first tracked and catalogued. Left inset) The number of objects launched to the GSO region per year. Information sourced from the publicly available USSPACECOM catalogue, accessed via the GSO sub-catalogue from Space-Track as of May 2020. Right) The orbital status of tracked GSO objects in 2019, as provided by ESA [2020]. The latter figure is derived from ESA's DISCOS database, which combines the USSPACECOM catalogue with other sources of data, hence the disparity between the overall object counts.

To add weight to the factors listed above, GSO satellites represent some of the most expensive assets in space, often comprising several payloads on a single bus to counter the substantial costs of launching to such high altitudes. It is thus fairly typical for multiple parties to have vested interests in a given satellite's safety while the craft carries out its primary mission goal(s). Furthermore, with the upward trend evident in the left-hand panel of Fig. 3.1, showing the number of GSO objects tracked and catalogued by the SSN over time, it is clear that an imperfect disposal rate will result in fewer viable orbital slots and increased collision risk in the GSOPR.

Over the past couple of decades, a number of surveys have been conducted to probe the GSO debris environment (see Section 1.3.3). The majority have utilised optical telescopes with apertures of 1 m or less, with sensitivity limits in the range 15^{th}–20^{th} magnitude, corresponding to objects larger than ~ 20 cm in diameter (depending on the viewing geometry, assumed shape and reflectivity; see Eq. 1.2, Section 1.2.2). Comparatively few surveys have made use of larger telescopes to probe fainter. The 6.5 m Magellan telescope has been used for a small number of GSO spot surveys, targeting known fragmentation events to more efficiently search for debris with the instrument's narrow $30'$ diameter FOV [Seitzer et al., 2011]. Deep observa-

tions of the GSO region have also been conducted with the much wider-field 1.8 m Panoramic Survey Telescope and Rapid Response System (Pan-STARRS) [Bolden et al., 2011], alongside large aperture (0.5–2.6 m) components of the International Scientific Optical Network (ISON) [Molotov et al., 2009]. These more sensitive surveys have uncovered a number of faint debris that exhibit photometric signatures of rapid tumbling. Owing to the limited availability of time on large aperture telescopes, and the balance that must typically be struck between aperture size and FOV, knowledge of the very faint debris population remains sparse. It is important that large telescopes continue to probe the evolving population of faint GSO debris, in order to more accurately quantify the risk posed to active satellites and to better understand the behaviour of uncontrolled objects drifting in the vicinity of the GSO region.

3.2 Observational strategy

Deep surveys of the GSO region, and other high altitude orbital regimes, rely on passive optical sensors that collect photons of light from the Sun (and to a much lesser extent from earth/moonshine) that have reflected off the external surfaces of target objects along the observer's line of sight. Active sensors, like those employing radar or laser ranging techniques, transmit pulses of electromagnetic radiation and observe the backscatter that is received. The sensitivity of active sensors drops with the fourth power of the range, owing to the round trip undertaken by the outgoing radiation as it reflects back towards the receiver, while that of a passive sensor diminishes with the square of the range. Passive optical telescopes are thus a more appropriate tool for probing the faint end of the GSO debris population. While the SNR will be influenced by a number of factors (e.g., the presence of central obstructions like prime focus cameras, the filter throughput, the detector QE, and so on), it will scale to first order with the square of the aperture radius. Larger mirrors provide a more extensive collecting area for incident photons of light, improving the SNR and thus enabling the instrument to search for fainter targets. The detection limit will also be influenced by the site transparency and seeing; La Palma is a high quality astronomical site with a sub-arcsecond median seeing in the summer and autumn months[1]. With current technologies, large aperture ground-based optical telescopes in high quality sites are the most effective option when aiming to probe the population of faint debris in the GSO region.

[1]Further information regarding site quality at the Roque de los Muchachos Observatory can be found at http://www.ing.iac.es/astronomy/observing/conditions/ (accessed March 2021)

Table 3.1: Logistical details for the observation run. In total, 552 separate pointings of the telescope in hour angle and declination were achieved in the 58 hours of survey time. Approximately half the night of 5$^{\text{th}}$ September was lost due to weather and technical issues. The remaining time was dedicated to targeted observations that are outside the scope of this thesis.

Night	Survey time [hrs]	Telescope pointings
02/09/2018	8.5	65
03/09/2018	7.7	76
04/09/2018	6.4	71
05/09/2018	4.5	15
06/09/2018	7.0	77
07/09/2018	6.0	63
08/09/2018	8.5	86
09/09/2018	9.4	99
	58.0	552

To this end, eight nights of dark-grey time on the 2.54 m INT were used to conduct an untargeted survey of the GSO region visible from the Roque de los Muchachos Observatory on La Palma, Canary Islands. Logistical details for the survey are provided in Table 3.1. Observations were made using the prime focus WFC, consisting of four thinned 2k $\times$ 4k CCD chips, which combine to image over a $33'$ diameter FOV. One of the CCD chips was rendered unusable due to an issue with the readout electronics. The faulty chip is discarded for the following photometric analyses, reducing the effective FOV to $22' \times 33'$. Two-by-two binning was applied, resulting in a resolution of $0.66''$ pixel^{-1}. The observations were taken using a *Harris* V filter with a central wavelength of 5425 Å, a full width at half maximum of 975 Å and a peak throughput of 88 %. While the V passband is only reasonably well placed to capture the sunlight illuminating and reflecting off the surfaces of target objects, it provides a direct comparison with the brightness measurements quoted for the ESA-AIUB campaigns conducted in Tenerife, located a mere $\sim$ 100 km east of La Palma (see Section 1.3.3).

Steps were taken to optimise the observations for finding objects in the GSO region. The telescope was operated using the 'untracked' mode described in Section 2.2.3, pointing at a fixed hour angle and declination, and ensuring that photons from GSO candidates would integrate across fewer pixels to improve the SNR. In this observing mode, GSO objects manifest as point sources or short trails with different orientations in the resulting image, while background stars appear as longer trails,

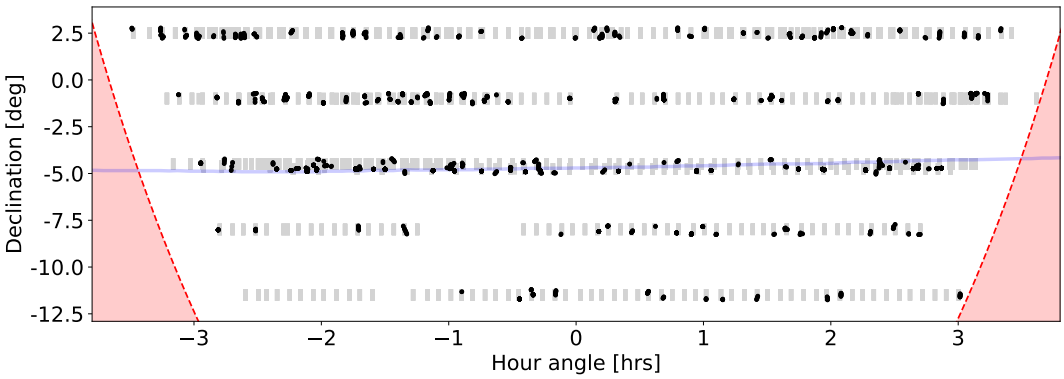

Figure 3.2: Telescope pointings for the DW-INT survey. Imaged fields are given by the grey boxes, while detections are overlaid as black dots. The approximate declination of the geostationary belt as visible from the vantage point of the INT is indicated by the blue line. Shaded red regions mark the altitude limits that constrained the accessible range in hour angle for a given declination strip.

streaking across at the sidereal rate. An exposure time of 10 s was chosen to provide a balance between streak coverage and duty cycle. Observations were taken by selecting a nominal field with a specific right ascension and declination, corresponding to a fixed solar phase angle (observatory–target–Sun), which was minimised whilst remaining outside of the Earth's shadow (see Section 2.2.2). This allowed for the detection of fainter objects by maximising their apparent brightness. The selected field would then be used to generate the telescope pointings for the given night, scanning a strip of fixed declination with each pointing directed at a separate hour angle.

A map of telescope pointings in hour angle and declination for the survey is provided in Figure 3.2. The INT telescope control system disables several important instrument features upon issuance of a telescope "stop" command. Instead, a differential tracking offset was applied upon reaching the chosen field, in order to counter the sidereal rate and freeze the hour angle for the duration of the given pointing. Each telescope pointing was observed for roughly four minutes, comprising seven 10 s exposures with a 25 s readout time per exposure. Multiple exposures were taken at each pointing to allow for the correlation of detections across frames. After each set of exposures, the telescope pointing was updated to retrieve the chosen field and the above procedure was repeated. This differs from the "declination strip" strategy employed by the ESA-AIUB GSO surveys, where a corrective slew is applied after every exposure to follow precisely the same field in right ascension and declination for the entire duration of the pointing. Opting to perform the cor-

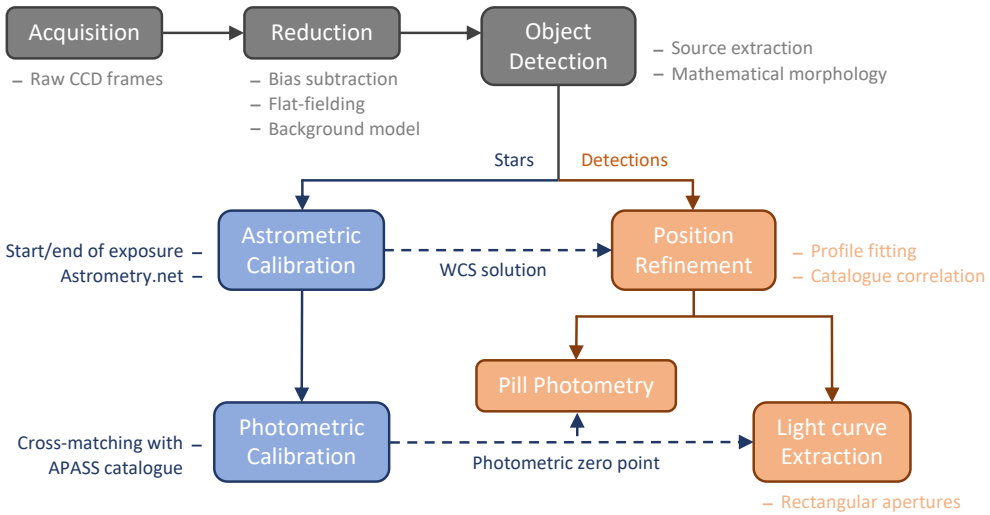

Figure 3.3: Flowchart outlining the analysis pipeline described in Section 3.3.

rective slew after each set of seven exposures afforded a more substantial temporal coverage for each candidate GSO object detected, an important consideration given the narrower field of the INT relative to that of the ESA 1 m. Survey operations began when the target field exceeded 30° elevation in the east and continued until it set below 30° elevation in the west, owing to enclosure limitations. Most aspects of the observing procedure were automated using a script, however limitations in the INT control system meant that operator input was required for each new pointing.

The observation script also sent commands to a second telescope on-site, the 36 cm RASA (see Section 2.1.2) assembled from COTS equipment, featuring a much larger $3.6° \times 2.7°$ FOV. The RASA remained slaved to the INT for the duration of the observation campaign. The additional dataset acquired by the RASA forms the basis for the work presented in Chapter 6, which compares the performance of the COTS instrument against that of the large aperture telescope in the context of GSO surveillance.

3.3 Analysis pipeline

The survey data were processed using a custom analysis pipeline, which is outlined in Fig. 3.3. Written in Python 3, the pipeline employs many of the techniques described in Chapter 2, and takes inspiration from a number of algorithms developed previously to search for artificial objects in astronomical images [see e.g., Laas-

Bourez et al., 2009; Levesque, 2009; Privett et al., 2017].

Prior to processing the raw CCD images in bulk, master bias and flat field frames were generated by combining the relevant calibrations acquired at the beginning and end of each night (see Section 2.3.1). A bad pixel mask was derived from a combination of appropriate flat fields, identifying defective pixels that were subsequently replaced with a sigma-clipped median of the surrounding pixel values. The raw frames could then be fed to the custom analysis pipeline, which processes a given image as follows[2]:

- *Reduction* — Standard bias and flat field calibrations are applied using the master calibration frames, and a model of the spatially-varying sky background is subtracted from the calibrated frame (see Section 2.3.1).

- *Astrometric and photometric calibrations* — A preliminary source extraction is carried out to identify stars in the image, exploiting their common morphologies and orientations. An astrometric calibration is performed using the centroids determined for the extracted star trails, and the resulting WCS solution is subsequently used to carry out a photometric calibration for the frame (see Section 2.3.2). The extracted star trails are cross-matched with known stars in the American Association of Variable Star Observers All-Sky Photometric Survey (APASS) catalogue [Henden et al., 2009, 2016]. The photometric zero point for the frame is found by comparing the standard magnitudes quoted in the APASS catalogue against their instrumental counterparts, derived by summing rectangular apertures placed over the matched star trails.

- *Object detection* — Many GSO residents are moving relative to the geostationary tracking rate and so are not fixed in the topocentric coordinate frame. The reflected light from these objects will spread over a trail of pixels mapped out by the angular path traversed during the exposure. Additional structure along the trails (e.g., glints, flares, gentle oscillations) can result from changes in the reflected light received from the object along the observer's line of sight. As a result, objects of interest exhibit a wide range of morphologies and orientations, examples of which can be seen in Fig. 3.4. Background star trails are removed from the image using the mathematical morphological Spread TopHat transformation (see Section 2.4.2). Additional checks are required to separate

[2]This section provides a top-level overview of the custom analysis pipeline developed to process raw CCD frames acquired using the INT; for low-level discussions of the individual tasks and techniques (including the various packages and libraries employed), the reader is referred to the appropriate sections of Chapter 2 highlighted throughout.

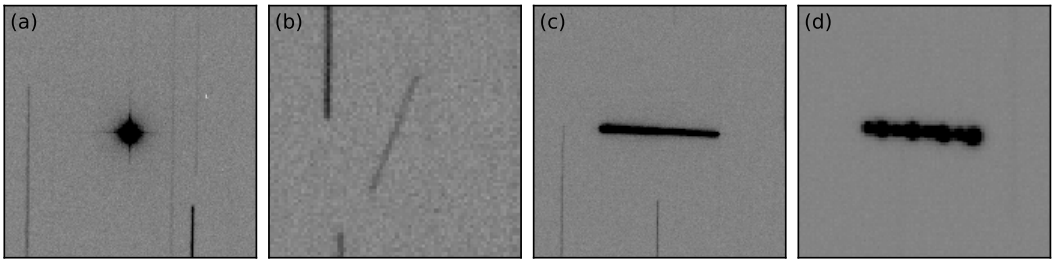

Figure 3.4: Examples of different morphologies for objects detected by the INT. With the telescope viewing direction fixed relative to the Earth, station-kept GEO satellites appear as point-like features in the acquired CCD frames, as illustrated by the saturated case in (a). Objects that are moving relative to the GEO tracking rate will manifest as trails. An example of a faint GSO trail with uniform brightness is given in (b). Other trails exhibit brightness variation, over timescales longer (c) and shorter (d) than the exposure time. Vertical lines in the background are stars streaking across the images.

the objects of interest from remnant 'distractors' that survive the transformation. Candidate cosmic rays are removed from the transformed image by running the `ccdproc` lacosmic routine [Craig et al., 2015], which employs a Laplacian edge detection technique [see Van Dokkum, 2001] to identify and mask cosmic rays by the sharpness of their intensity profiles. A 3σ threshold cut is applied to filter out the majority of additional spurious detections, with σ the global background root mean square (RMS). The remaining false positives are typically edges of star trails that are easily flagged using knowledge of the trail positions from the calibration stages of the pipeline.

- *Position refinement* — For trailed detections, the initial positional estimates obtained via the threshold extraction are refined by fitting the intensity profiles along and across the trail. A gaussian model is used to fit the across-trail profile, while a Tepui function is found to best approximate the along-trail profile (see Section 2.4.3). Using this refinement procedure, typical uncertainties in the trail start- and end-of-exposure positions amount to $\sim$1–2″, corresponding to a few hundred metres at GSO altitudes. Within the scope of the photometric analyses to follow, this level of uncertainty was deemed acceptable. An improved algorithm for joint astrometric and photometric calibration is presented in Chapter 6; future development of the DW-INT processing pipeline will look to incorporate this algorithm and further refine the positional estimates for objects detected in the survey frames.

- *Pill photometry* — The refined centroid and orientation estimates allow for more accurate placement of a pill-shaped aperture, the sum of which provides a measure of the total flux integrated over the course of the exposure (see Section 2.4.5). Trail morphologies are well approximated by pill shapes, so the contribution of background noise to the aperture sum is minimised. Uncertainties in the measured magnitudes consist of two parts: the first is a systematic uncertainty from the zero point measurement, which is based on the background stars and is typically $\sim$0.05 magnitudes for a given frame, while the second is the photometric uncertainty from the aperture sum, which is typically $\sim$0.001 magnitudes for bright objects ($V \sim 12$) and $\sim$0.05 magnitudes for faint objects ($V \sim 18$) in a 10 s exposure. That said, it should be noted that intrinsic brightness variability can often cause much larger scatter in short-timescale measurements extracted for trailed detections, as illustrated by the light curves provided in Section 3.4.2.

- *Light curve extraction* — In the final stage of the pipeline, light curves are extracted from the trailed detections (see Section 2.4.5). Rectangular apertures are placed along the trail, each covering a discrete pixel in width to avoid correlated noise injection. Constant rates of change in angular position throughout the exposure are assumed, such that a given source will spend an equivalent amount of time in each aperture placed along its trail. In order to correct for background contamination (e.g., blending with star streaks), equivalent apertures are placed in a reference frame containing the same field. Initially, the region of overlap is found using the astrometric solutions for the two relevant frames. In cases where the region of interest has exited the FOV, the detection cannot be paired with a reference frame and is discarded from the light curve extraction. Sections of the light curve that are too heavily blended with background stars are masked 'by eye' in a subsequent vetting procedure. Remaining alignment offsets are accounted for by feeding the regions of overlap to the DONUTS algorithm [McCormac et al., 2013]. With the reference apertures in place, an aperture-by-aperture subtraction is carried out. The corrected fluxes are converted to calibrated magnitudes using the photometric zero points determined in the calibration stages of the pipeline.

The refined centroid and orientation estimates are used to predict where the object will appear in subsequent frames within a given pointing, and a frame-by-frame correlation of detections is carried out (see Section 2.4.4). By fitting and sequentially updating a linear trajectory in hour angle and declination space, trails belonging to

the same orbital arc are identified and matched. A verification is carried out 'by eye' to ensure that the resulting arcs are not contaminated by spurious detections in the nearby vicinity of the corresponding objects of interest. In the photometric analyses that follow, single frame detections are discarded as false positives.

3.4 Results and discussion

3.4.1 Sampled population

A total of 226 orbital tracks spanning two or more exposures within a given pointing were detected. The brightness distribution for these detections is presented in panel (a) of Fig. 3.5. Rate cuts are applied as in Eq. 2.2 (Section 2.2.3) to reduce the sample to orbital tracks that are consistent with circular orbits in the GSO regime, namely those with |Hour Angle rate| $<$ $2''\,s^{-1}$ and |Declination rate| $<$ $5''\,s^{-1}$. Objects with rates exceeding these limits likely reside in GTOs or other HEOs with apogees near or beyond the GSO region. The resulting subset of circular GSO detections is represented by the black lines in Fig. 3.5. A correlation procedure is performed to match the INT detections to known objects in the publicly available USSPACECOM catalogue. Each detection (time, right ascension, declination) is correlated against every object in the catalogue, by computing the chi-square between the observed positions and those predicted by propagating TLEs to the observation epoch. Over 85 % of the observed tracks with $V < 15$ successfully match a known object in the catalogue, while ∼99 % of fainter detections fail to correlate. A brightness of 15^{th} visual magnitude corresponds to an object roughly 1 m in diameter (depending on the viewing geometry, shape and albedo; see Eq. 1.2, Section 1.2.2), thus the correlation appears to be consistent with the nominal size cutoff for the GEODSS network that feeds the USSPACECOM catalogue with observational data for high altitude targets.

The rate cuts reduce the sample size to 129 circular GSO tracks, giving a detection rate of $\sim 11\,\text{hour}^{-1}\text{deg}^{-2}$ for the survey. A similar detection rate was observed by the Magellan surveys in Chile [Seitzer et al., 2011], within sight of the geopotential well at a longitude of 105° W. Risk assessments have found that collision probabilities increase by a factor of seven in the vicinity of the potential wells [McKnight and Di Pentino, 2013], owing to the relatively high density of trapped objects in libration orbits. The vantage point of the INT (La Palma, ∼18° W) sits almost directly between the two wells, thus a lower detection rate would be expected. However, the limited time available on large aperture telescopes means that both surveys suffer from small number statistics, making it difficult to draw conclusions regarding

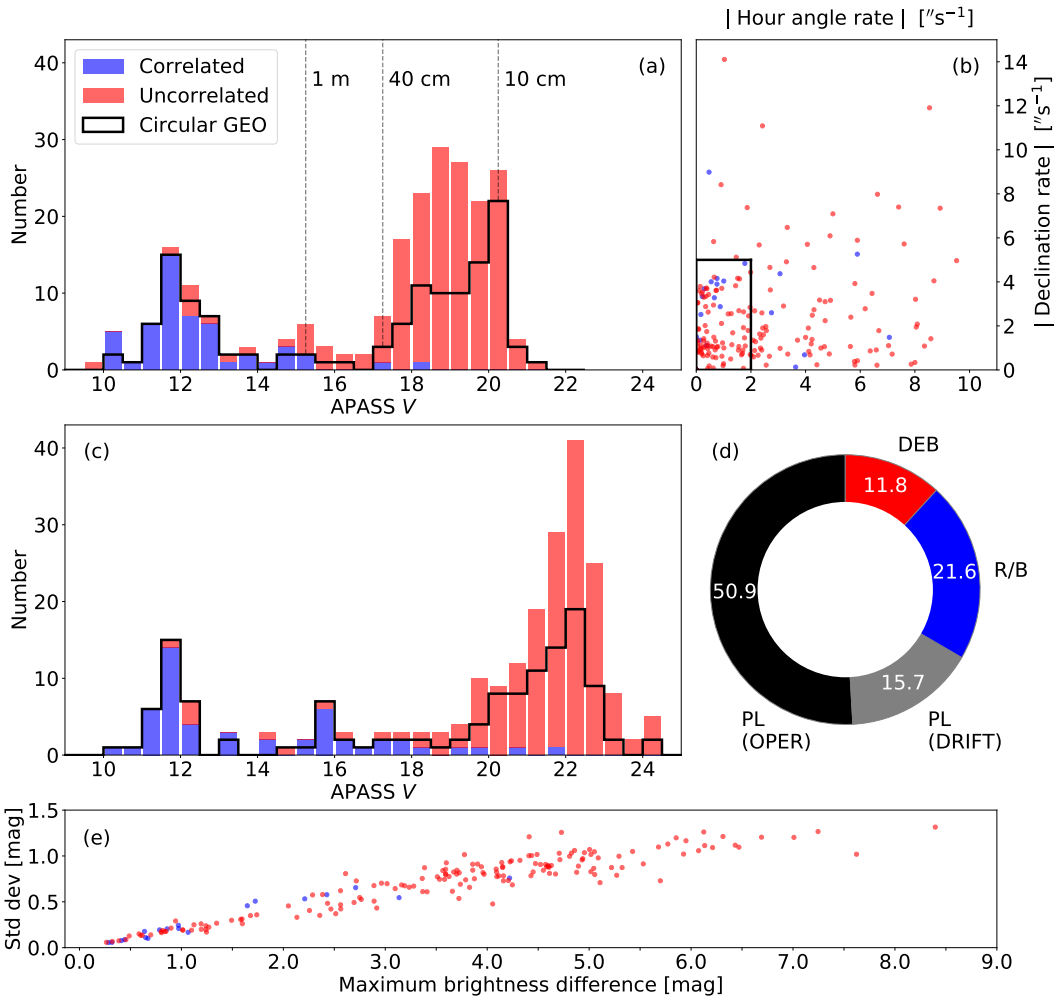

Figure 3.5: (a) Brightness histogram for the detected population. Tracks that correlate with the publicly available USSPACECOM catalogue are shown in blue, while those that fail to correlate are in red. The black line gives the sample of tracks which lie within the rate cut limits shown in (b). Labelled size estimates assume that the objects are Lambertian spheres with an albedo $A = 0.1$. (b) Rates in hour angle and declination for the tracks detected. The rate cuts applied in order to obtain the circular GSO sample are indicated by the black box. (c) Brightness histogram for the detected population, normalised by trail length. This normalisation determines the brightness of a geostationary source with the same peak flux for an equivalent integration time. (d) Object types for correlated detections in the overall sample, categorised as operational or drifting payloads (PL), rocket bodies (R/B) or debris (DEB). (e) Light curve statistics for the overall sample. For each detected object, the difference between the maximum and minimum brightness is plotted against the standard deviation.

detection rates at this early stage.

A bimodal brightness distribution is observed, consistent with the findings of previous GSO surveys. The bright end of the sample peaks at $V \sim 12$, in accordance with the population uncovered by the ESA-AIUB OGS observation campaigns in Tenerife that began in the late 1990s [see e.g., Schildknecht et al., 2004]. This is to be expected given that the majority of bright, correlated objects are geostationary and the two instruments sample the same segment of the GEO belt. For reference, the correlated detections are classified according to object type in panel (d) of Fig. 3.5. Complete logs of catalogue information for operational and non-operational objects that correlate with tracks detected in the DW-INT survey frames are provided in Tables 3.2 and 3.3, respectively. A steep rise is seen in the number of objects detected at magnitudes fainter than $V \sim 17$. The overall distribution appears to plateau between $V \sim 18$ and the sensitivity limit of the sensor at $V \sim 21$. The circular GSO sample continues to rise as the sensitivity limit is reached, suggesting that the modal brightness may be fainter still.

Assuming the objects are Lambertian spheres with an albedo $A = 0.1$, the DW-INT survey frames probe to sizes $d < 10\,\mathrm{cm}$ (see Section 1.2.2). These assumptions are nevertheless very uncertain, owing to the lack of *a priori* knowledge for any object that fails to correlate with the catalogue. Furthermore, the brightness of a given object is not always constant over the course of an observation. Indeed, from panel (e) of Fig. 3.5, it can be seen that over 45 % of uncorrelated tracks in the overall sample with successfully extracted light curves vary in brightness by more than four magnitudes across the observation window. In some cases, such brightness variation may manifest as sharp flares or glints, while other objects may exhibit smooth oscillations between successive minima and maxima. Photometric behaviour of this kind renders any generalisation regarding the albedo redundant. In general, uncorrelated detections appear to show a greater extent of brightness variation relative to their correlated counterparts within the sampled population.

Using the correlation results, it is possible to gain a very primitive estimate of the underlying population of faint GSO debris. Taking the circular GSO sample, the correlated to uncorrelated ratio stands at 4:9 for the tracks sampled by the survey frames. If this ratio is mapped to the 1022 objects in the publicly available USSPACECOM catalogue (recall Fig. 3.1), which was itself used for the correlation procedure, then an estimate of roughly 3300 objects is obtained. Taking a conservative limit of 10 cm as the smallest size probed by the DW-INT survey, this value can be qualified as an estimate of the GSO population greater than 10 cm in size. Of course, this is a very basic treatment of the results and many other factors would

Table 3.2: Catalogue information for operational satellites that correlated with tracks detected in the DW-INT survey frames. Objects are designated as payloads (PL), rocket bodies (R/B) or debris (DEB). Source abbreviations and radar cross-section (RCS) definitions can be found on the Space-Track website, from which this information was obtained.

Name	NORAD ID	Source	Launch Year	Type	Perigee [km]	Apogee [km]	Inclination [deg]	RCS
INTELSAT 806	25239	SES	1998	PL	36108	36140	1.47	LARGE
ASTRA 2B	26494	SES	2000	PL	35765	35810	4.41	LARGE
TDRS 9	27389	US	2002	PL	35679	35899	7.40	LARGE
HISPASAT 30W-4	27528	SPN	2002	PL	35761	35815	0.97	LARGE
NIMIQ 2	27632	CA	2002	PL	36036	36072	4.25	LARGE
EUTE HOT BIRD 13E	28946	EUTE	2006	PL	35771	35802	0.04	LARGE
SYRACUSE 3B	29273	FR	2006	PL	35764	35809	0.00	LARGE
INTELSAT 11	32253	ITSO	2007	PL	35781	35793	0.02	LARGE
ASTRA 4A	32299	SES	2007	PL	35775	35799	0.02	LARGE
EUTE 10A	34710	EUTE	2009	PL	35765	35809	0.07	LARGE
SICRAL 1B	34810	IT	2009	PL	35780	35808	0.00	LARGE
EUTE KA SAT 9A	37258	EUTE	2010	PL	35764	35808	0.03	LARGE
HISPASAT 30W-5	37264	SPN	2010	PL	35767	35807	0.06	LARGE
METEOSAT 10	38552	EUME	2012	PL	35784	35790	1.00	LARGE
SES 5	38652	SES	2012	PL	35779	35795	0.05	LARGE
GALILEO-FM4	38858	ESA	2012	PL	23211	23233	54.97	LARGE
SES 6	39172	SES	2013	PL	35779	35795	0.02	LARGE
EUTE 3B	39773	EUTE	2014	PL	35773	35800	0.07	LARGE
EUTE 8 WEST B	40875	EUTE	2015	PL	35768	35805	0.07	LARGE
EXPRESS AM-8	40895	CIS	2015	PL	35785	35788	0.02	LARGE
INTELSAT 29E	41308	ITSO	2016	PL	35618	35754	0.93	LARGE
EUTE 9B	41310	EUTE	2016	PL	35770	35803	0.10	LARGE
ECHOSTAR 21	42749	US	2017	PL	35778	35796	5.60	LARGE
BULGARIASAT-1	42801	BGR	2017	PL	35775	35798	0.02	LARGE
SES 14	43175	SES	2018	PL	35783	35790	0.01	LARGE
HISPASAT 30W-6	43228	SPN	2018	PL	35762	35812	0.05	LARGE

Table 3.3: Catalogue information for non-operational objects that correlated with tracks detected in the DW-INT survey frames. Objects are designated as payloads (PL), rocket bodies (R/B) or debris (DEB). Source abbreviations and radar cross-section (RCS) definitions can be found on the Space-Track website, from which this information was obtained.

Name	NORAD ID	Source	Launch Year	Type	Perigee [km]	Apogee [km]	Inclination [deg]	RCS
SYMPHONIE 2	8132	FGER	1975	PL	35846	35892	9.56	LARGE
NATO 3B	9785	NATO	1977	PL	37045	37455	12.72	LARGE
INTELSAT 4A-F3	10557	ITSO	1978	PL	35882	35896	13.05	LARGE
COMSTAR 3	10975	US	1978	PL	36014	36165	13.43	LARGE
TITAN 3C TRANSTAGE R/B	11147	US	1978	R/B	36511	38924	15.55	LARGE
SBS 3	13651	US	1982	PL	35829	35932	14.72	LARGE
RADUGA 13	14307	CIS	1983	PL	36300	36470	13.67	LARGE
SL-12 R/B(2)	15581	CIS	1985	R/B	35941	36123	13.47	LARGE
COSMOS 1687	16103	CIS	1985	PL	4796	35595	69.63	LARGE
SL-12 R/B(2)	16797	CIS	1986	R/B	36496	36569	14.58	LARGE
ARIANE 44P R/B	21223	FR	1991	R/B	410	35188	4.14	LARGE
GOES 8	23051	US	1994	PL	36138	36211	12.5	LARGE
SL-12 R/B(2)	23883	CIS	1996	R/B	36301	36601	15.02	LARGE
BLOCK DM-SL R/B	25938	SEAL	1999	R/B	2669	35742	0.68	LARGE
ATLAS 2A CENTAUR R/B	26053	US	2000	R/B	247	21460	25.93	LARGE
ARIANE 1 DEB	26787	FR	1985	DEB	973	35289	6.84	MEDIUM
TITAN 3C TRANSTAGE DEB	27790	US	1965	DEB	733	29623	26.55	SMALL
SL-12 R/B(2)	28119	CIS	2003	R/B	34897	36795	11.83	LARGE
BREEZE-M DEB (TANK)	29271	CIS	2006	DEB	285	15455	49.47	LARGE
FENGYUN 2D AKM	29642	PRC	2006	R/B	35575	36513	7.77	LARGE
ARIANE 5 R/B	32389	FR	2007	R/B	595	35064	5.29	LARGE
TITAN 3C TRANSTAGE DEB	33509	US	1968	DEB	35047	35529	3.82	SMALL
ARIANE 42P+ DEB	34198	FR	1992	DEB	557	27200	8.37	MEDIUM
FREGAT R/B	38859	CIS	2012	R/B	23650	23683	54.95	SMALL
CZ-3C DEB	40827	PRC	2010	DEB	631	35611	20.29	SMALL

need to be considered in order to gain a more reliable estimate from the available dataset. For instance, a degree of bias towards correlated objects, and a consequent underestimation of the total population, will have arisen from the near-fixed nature of active satellites along the GEO belt, which makes them very likely to be detected with the declination strip strategy employed, provided the appropriate declination is selected (as was the case for the DW-INT survey). Uncorrelated debris, on the other hand, typically sample a range of declinations in their inclined orbits and so are less likely to be uncovered on a given night by scanning a particular declination strip. If the geostationary belt (detected and catalogued) is discounted, the estimated total population of objects greater than 10 cm increases to roughly 4700. However, with the limited coverage afforded by the short survey time and narrow field of view, and the potential for multiple detections of a given object, it seems unlikely that the observed correlated to uncorrelated ratio would be truly representative of the overall population visible from La Palma at the time of the survey.

The primitive estimates above place towards the lower end of the bounds 1572–9515 derived by Murray-Krezan et al. [2019] for GSO debris greater than 10 cm in size, using a more intricate treatment of data from the NASA Wide-field Infrared Survey Explorer (WISE) [Liu et al., 2008] and MODEST [Seitzer et al., 2004] campaigns. It is important to remember, however, that La Palma is situated almost directly in-between the geopotential wells, thus the extrapolation of DW-INT statistics likely underestimates the total population.

Finally, the apparent sensitivity limit in panel (a) of Fig. 3.5 is not truly representative of the detection capability of the sensor, as intrinsic brightness will not be the only factor influencing this. As revealed by the circular GSO rate cuts, many objects have non-zero rates of change in angular position, placing a limit on the amount of time they will spend contributing flux to a given set of pixels, and therefore reducing the peak surface brightness. To highlight the effect of trailing, the total flux integrated for each of the detections is normalised by a factor x/l, where x is characteristic of the optical system's PSF and l is the extent of the angular path traversed by the object over the course of the exposure. The normalisation gives the brightness of a point-like detection that would possess an equivalent peak flux for the same integration time, resulting in the updated brightness histogram in panel (c) of Fig. 3.5. The faint end of the circular GSO distribution now peaks at $V \sim 22$, before dropping off as the sensitivity limit for 'stationary' objects is reached, implying that the modal brightness in this normalised regime could once again be even fainter. With the INT, a value of $x = 3.3$ px is achieved, meaning that an object moving at the maximum angular rate allowed by the circular GSO

rate cuts would take 0.4 s to cross each pixel. Exposing for longer than this time will weaken the ability of the pipeline to detect such an object, due to added noise from the sky background.

3.4.2 Light curves

The reflected light from an orbiting body contains information about its shape and attitude, but is also affected by the sensor characteristics, atmospheric interference and the viewing geometry at the time of the observation. Disentangling these components is a challenging task. Thus far, studies have focused on modelling the photometric signatures of large satellites by virtue of the relative ease in obtaining a useful dataset (see Section 1.2.2). However, understanding the attitude of faint debris will be a pivotal factor in predicting the long-term evolution of the GSO debris environment.

An example of a light curve extracted for a catalogued object can be found in panel (h) of Fig. 3.6. The corresponding orbital track correlates with SBS-3 (NORAD 13651), a decommissioned communications satellite that was moved to a graveyard orbit in 1995. Built on the Hughes HS-376 bus[3], the satellite consists of a cylindrical body with concentric solar panels and extended antennas. The satellite was spin-stabilised during its active lifetime, maintaining attitude by spinning a section of the platform at 50 rpm (0.83 Hz; 1.2 s period). The communications payload remained despun, ensuring steady pointing of the antennas and transponders. A periodic pattern can be seen in the light curve, indicating that the satellite is likely tumbling. Fourier analysis of the signal uncovers a 2.7 s period for the repeated pattern, though this could be a harmonic of the true tumbling rate given the geometric symmetry of the bus.

Panels (q) and (x) of Fig. 3.6 show two examples of light curves extracted for uncorrelated objects belonging to the faint end of the sampled population. Both tracks straddle the sensitivity limit of the INT, exhibiting significant brightness variation across the observation window. The first object oscillates in brightness with a period similar to the exposure time, peaking at $V \sim 16$ and otherwise fading into the background noise level. With such large variation in brightness, it is likely that the object is a small piece of highly reflective material tumbling in and out of the line of sight. Additional structure can be seen in the second light curve, possibly due to an asymmetry in the shape, or more complex tumbling dynamics.

[3]Historic and technical details regarding the structural and attitudinal properties of exemplar satellites referenced throughout the thesis are typically sourced from Gunter's Space Page, found via https://space.skyrocket.de/ (accessed March 2021)

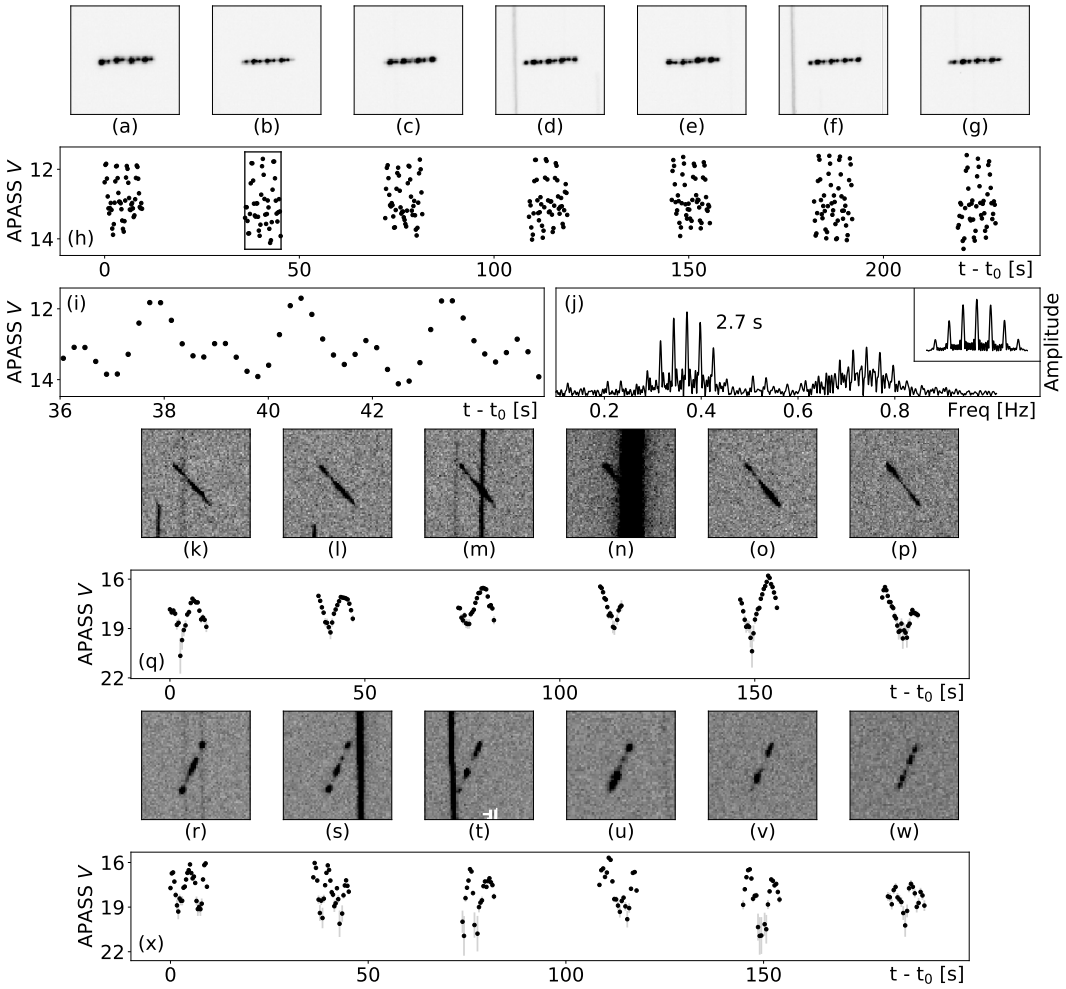

Figure 3.6: The top three rows present light curve analysis for a track correlated with the defunct satellite SBS-3 (NORAD 13651). Successive 10 s exposures are shown in (a)–(g), centered on the detected trails. The corresponding light curve is provided in (h), extracted using the analysis pipeline outlined in Section 3.3, while a zoom-in of the boxed region is given in (i). A 2.7 s period is uncovered by the Fourier amplitude spectrum in (j). The Fourier window function (inset) illustrates the effect of the readout-induced gaps in the light curve. The remaining rows present light curves for two uncorrelated tracks that exhibit significant brightness variation. Successive 10 s exposures are shown in (k)–(p) for the first object, while (q) gives the extracted light curve. Note that the 10 s exposure images provided in (r)–(w) for the second uncorrelated track are reflected in the horizontal direction, aligning each trail with its corresponding profile in (x).

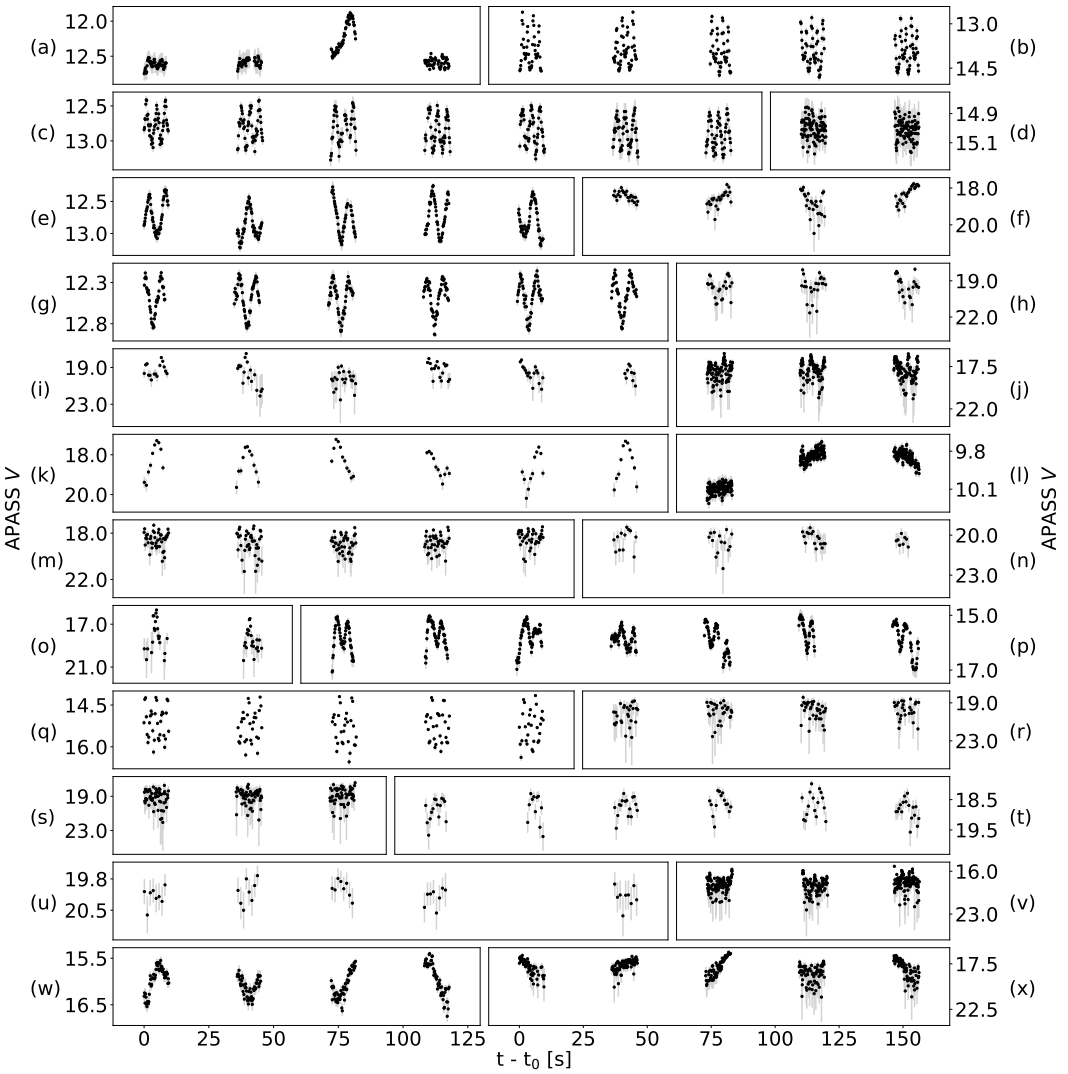

Figure 3.7: A montage of light curves for orbital tracks uncovered by the DW-INT survey, extracted using the analysis pipeline presented in Section 3.3.

A montage of further light curve examples is provided in Fig. 3.7. The light curve in panel (a) corresponds to a bright orbital track that correlates with Raduga 13 (NORAD 14307), a former Soviet communications satellite that was launched in 1983 and now resides in a drift orbit. The satellite is based on the KAUR-3 bus, a three-axis stabilised "box-wing" model with solar panels extending from both sides of the main body. A relatively flat light curve is seen at $V \sim 12.5$ across all but one exposure, which captures a clear glint where a highly reflective component enters the line of sight. The light curve in panel (b) is that of a track correlated with Intelsat 4A-F3 (NORAD 10557), a retired communications satellite that launched in 1978. Based on the Hughes HS-353 platform, the light curve unsurprisingly exhibits similar photometric signatures to those of SBS-3 presented in Fig. 3.6.

Panels (c), (e) and (g) of Fig. 3.7 give the light curves for three SL-12 rocket bodies (NORAD 16797, 15581 and 23883, respectively). Fourier analysis of light curve (c) uncovers a period of 3.4 s; the SL-12 appears to exhibit higher frequency brightness variations than expected from previous studies of such rocket bodies [see e.g., Cardona et al., 2016], though aliasing effects could be at play as a result of the object's geometric symmetry. The roughly 5 s period signals obtained from Fourier analysis of the other two SL-12 light curves are in better agreement with the findings of the cited study.

The remaining light curves in Fig. 3.7 correspond to orbital tracks that fail to correlate with catalogued objects. Light curves (f), (k), (l), (u), (w) and (x) all appear to be oscillating in brightness with a period exceeding the exposure time of 10 s. In these cases, it would be necessary to follow up with targeted observations of the object, preferably using an instrument with reduced dead time, in order to gain confidence in the true profile. The survey frames also revealed a number of uncorrelated objects that show structure in their light curves on a timescale shorter than the exposure time; this is the case for light curves (p), (q) and (t).

An interesting group of detections uncovered by the survey are only detectable as a result of sharp glints that can occur several times per exposure. Examples of this behaviour can be found in panels (h), (i), (j), (m), (o), (s) and (v). The extent of the brightness increase during a glint varies significantly case-by-case, with some objects climbing in excess of five magnitudes above the sensitivity limit, while others struggle to breach it. Finally, light curves (d), (n) and (r) show little variation in brightness within the window of observation. There are several explanations as to why this may be the case. The corresponding object could be uniformly reflective across its surface, or oriented in such a way that higher reflectivity components were hidden from the line of sight for the duration of the pointing. Alternatively,

the object may be stable in its motion (unlikely for the very faint examples) or tumbling faster than the sampling rate of the observations, such that its photometric signatures are unresolved. Noisy scatter could be due to small substructures upon the object's surface, though atmospheric fluctuations will also contribute to noise in all of the extracted light curves.

3.4.3 Brightness variability

This section moves on from the qualitative assessment above to consider more quantitative approaches for classifying tracks detected by the survey, based upon the different forms of brightness variability inherent in their light curves. When planning a survey of the GSO region, or indeed any orbital regime, estimates of mean brightness for prospective targets can inform the choice of instrumentation by calling for a particular level of sensitivity, resolution, and so on. Variability in brightness over time can impose further constraints on the observational strategies and post-acquisition processing algorithms employed. For instance, objects that exhibit sharp or rapid glinting in their brightness profile will require measurements to be taken at a high cadence in order to temporally resolve the fine structures in their light curves and avoid aliasing ambiguities. This can be achieved with short integration and readout times, or alternatively by optimising the search strategy to ensure prospective detections are trailing across pixels in the image frame (see Section 2.2.3). The latter strategy is discussed further in the context of targeted observations for LEO and GSO objects in Chapter 4. To cope with the continual growth in the number and diversity of spacecraft being launched into orbit, future data formats that replace the archaic TLE set should look to incorporate metrics that encode the brightness characteristics of an object, alongside other diagnostic information that is available, in order to generate a more reliable fingerprint for tracking and maintaining custody with surveillance instruments.

As evidenced in Section 3.4.2, the light curves extracted for tracks in the DW-INT dataset exhibit a wide variety of features: periodic oscillations on timescales shorter than the exposure time of 10 s; long timescale variability taking place over the course of the ∼few minute observation window; sharp glints, spanning ∼1–10 s, often rising from an otherwise flat profile; noisy scatter, particularly prevalent towards the faint end of the sampled population. Owing to the method of extraction (see Section 3.3), the time resolution for the light curves is governed by the angular rate of the detection as it traverses a path across the CCD pixels in each exposure of the given pointing. In the top panels of Fig. 3.8, trail rates are provided for the overall sample of detected tracks, as a function of mean calibrated brightness

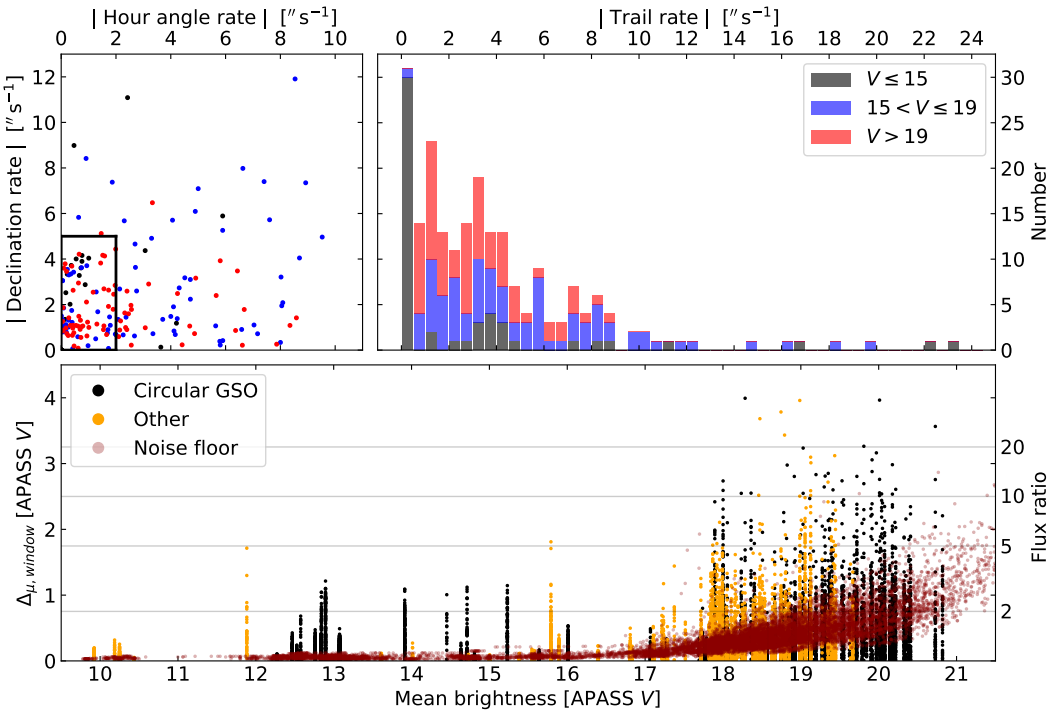

Figure 3.8: Top left) Rates in hour angle and declination for the detected tracks, given as a function of mean calibrated brightness in APASS V. Objects are coloured according to their brightness as follows: $V \leq 15$ (black); $15 < V \leq 19$ (blue); $V > 19$ (red). The rate cuts applied in order to obtain the circular GSO sample are indicated by the black box. Top right) A histogram of the trail rates (along trail) for the detected tracks, once again categorised by mean brightness. Bottom) A plot of the metric $\Delta_{\mu,window}$, where each spine of points corresponds to a separate track in the overall sample with a non-zero trail rate. For each track with an available light curve (extracted using the procedure outlined in Section 3.3), the difference between the individual brightness measurements and the mean brightness across the observation window is plotted. The height of a given spine thus indicates the maximal deviation from the mean brightness of the corresponding light curve, while the distribution of points comprising the spine characterises the brightness variability exhibited by the detected object. The metric is presented as a magnitude delta, though flux ratios are provided on the right-hand axis for reference. Where possible, the light curves are binned to 0.5 s intervals. Tracks belonging to the circular GSO sample are shown in black, while others are represented by the orange data points. The photometric noise floor illustrating the uncertainties determined for the individual measurements is provided in brown. Adapted from Chote [2020], with the author's permission.

in APASS V. All detections with $V > 15$, the majority of which corresponding to objects too faint to be catalogued by the USSPACECOM, are trailed with rates typically lower than $10'' \, \mathrm{s}^{-1}$. With no active station-keeping in place, the orbital states of the faint debris fragments will have evolved under the influence of natural perturbative forces in the GSO regime (see Section 1.3.1), hence their tendency to be drifting. The large peak at $0'' \, \mathrm{s}^{-1}$ (i.e. point-like in the survey frames) corresponds to the bright, station-kept GEO satellites that were observed. The time resolution for photometric measurements extracted from the point-like detections is 10 s, as set by the exposure time. In comparison, a resolution of ~ 130 ms is attainable for a circular GSO track with the maximal rate of $5'' \, \mathrm{s}^{-1}$ afforded by the imposed rate cuts.

For the analysis presented in the bottom panel of Fig. 3.8, the light curves for tracks with $\max(|\text{ Hour angle rate }|, |\text{ Declination rate }|) > 3'' \, \mathrm{s}^{-1}$ are binned to 0.5 s intervals in order to enhance the SNR. Every spine in the plot corresponds to a separate light curve in the overall sample, where the metric $\Delta_{\mu,window}$ has been plotted as a function of mean brightness. The metric evaluates the difference between each photometric measurement extracted from the available frames and the mean brightness across the observation window. It can be expressed for a given measurement j as

$$\Delta^{j}_{\mu,window} = |m_j - \mu_{window}| \, , \tag{3.1}$$

where $j = [1, n_{window}]$ for n_{window} measurements comprising the overall light curve, m_j is the calibrated magnitude for the measurement, and μ_{window} is the mean brightness across the observation window, given by

$$\mu_{window} = ZP - 2.5 \log \left(\frac{1}{t_{exp} n_{window}} \sum_{i=1}^{n_{window}} f_i \right) . \tag{3.2}$$

Here, ZP is the photometric zero point, f_i are the background-subtracted flux measurements and t_{exp} is the exposure time. Throughout this section, care is taken to carry out statistical evaluations and binning of the photometric data in linear flux space, as opposed to the logarithmic magnitude space.

Many objects at the faint end of the sampled population show significant levels of brightness variability, even accounting for the rising photometric noise floor. As discussed previously, this has important consequences for post-acquisition processing algorithms tasked with detecting objects in the survey frames. Extraction techniques need to be proficient at handling tracks that dip in and out of the noise floor over the course of a single exposure.

A primary aim for future processing algorithms (as eluded to by the literature review in Section 1.2.2) is to classify objects in orbit based on their observational characteristics. In the case of optical imaging, the objects must be grouped or clustered according to the photometric signatures exhibited by their light curves. Here, the level of clustering that can be achieved by applying a selection of primitive metrics to the DW-INT dataset is explored, taking inspiration from the work presented in Chote [2020].

Short period features that occur on timescales less than the exposure time can be examined by considering the variability on a frame-by-frame basis. Recall that the light curves extracted from the survey frames typically cover a 1–4 minute observation window, comprising 10 s segments (frames) of integration that are separated by 25 s of dead time. A segment-wise approach ensures that the metric remains isolated from global statistical properties that may be influenced by long timescale variability.

The top panel of Fig. 3.9 plots combinations of two metrics that probe the structure of short period features: $\Delta^{5}_{\mu,frame}$, which gives the median absolute frame-wise offset between the 5$^{\text{th}}$ percentile and mean brightness, thus indicating how far the segments dip below their means; $\Delta^{95}_{\mu,frame}$, which performs the same calculation for the 95$^{\text{th}}$ percentiles, thus providing a proxy for how far the segments peak above their means. More explicitly, the metric $\Delta^{l}_{\mu,frame}$ may be computed by evaluating the expression,

$$\left| P^{k}_{l,frame} - \mu^{k}_{frame} \right|, \tag{3.3}$$

and taking the median of values generated, with

$$P^{k}_{l,frame} = ZP - 2.5 \log \left[\frac{1}{t_{exp}} P_{l} \left(F^{k}_{frame} \right) \right], \tag{3.4}$$

$$\mu^{k}_{frame} = ZP - 2.5 \log \left[\frac{1}{t_{exp} n^{k}_{frame}} \sum_{i=1}^{n^{k}_{frame}} f_{i} \right]. \tag{3.5}$$

For a given segment $k = [1, n_{frames}]$, where n_{frames} is the number of segments comprising the light curve in question, the l^{th} percentile P_{l} is computed for the set of background-subtracted fluxes F^{k}_{frame} extracted from the corresponding frame. The mean brightness is calculated for the n^{k}_{frame} background-subtracted flux measurements comprising the segment. Following a conversion to calibrated magnitude, the absolute offset between the l^{th} percentile and mean brightness is determined, as in Eq. 3.3, and the metric $\Delta^{l}_{\mu,frame}$ is obtained by taking the median of values

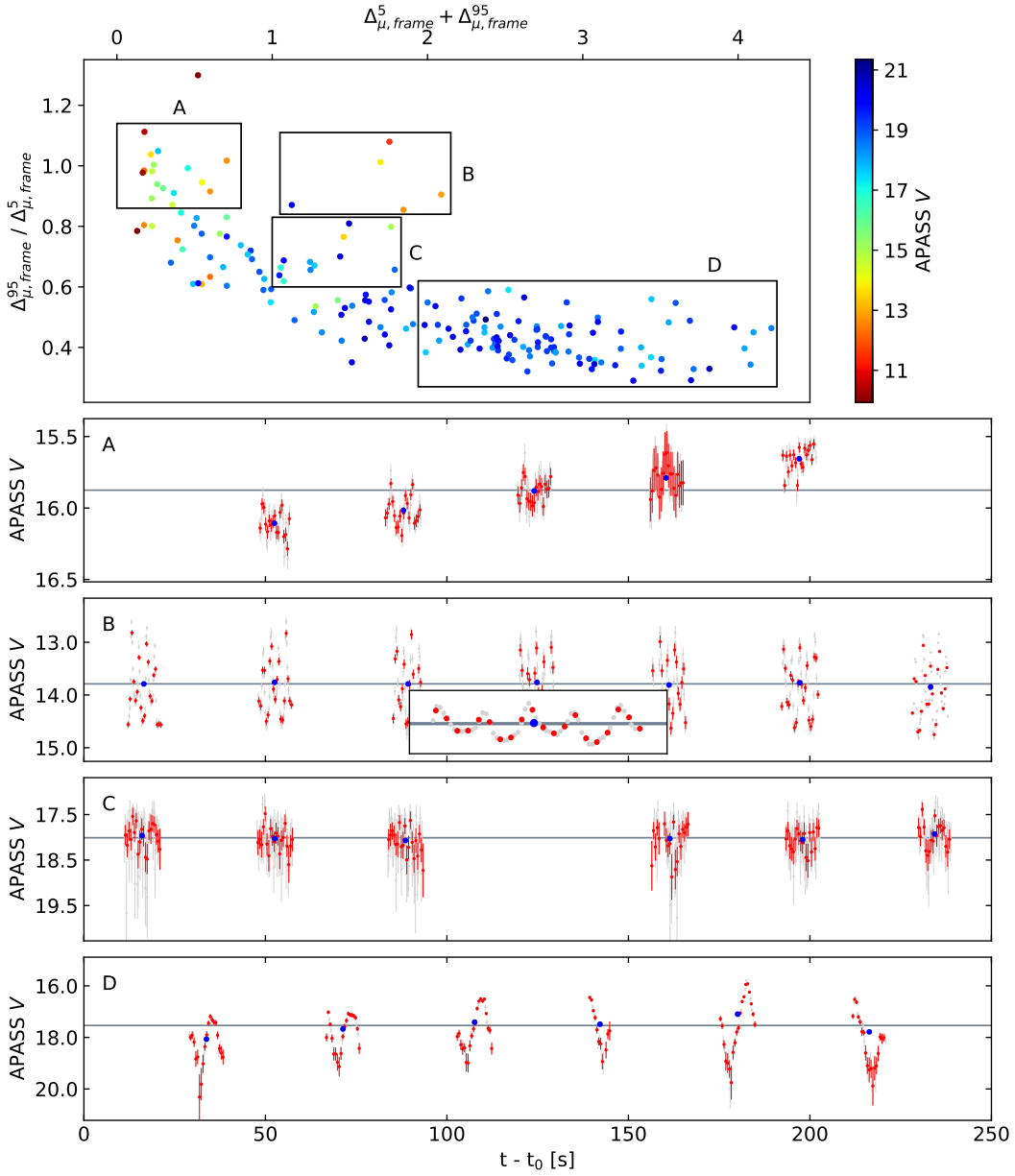

Figure 3.9: The metric sum $\Delta^5_{\mu,frame} + \Delta^{95}_{\mu,frame}$ and ratio $\Delta^{95}_{\mu,frame}/\Delta^5_{\mu,frame}$, plotted as a function of mean calibrated brightness in APASS V. Clustering of detected tracks exhibiting comparable short timescale brightness variability is achieved by plotting combinations of the absolute differences between the 5^{th}/ 95^{th} percentile and the mean brightness, computed on a frame-by-frame basis (see text). Exemplar light curves from regions 'A' to 'D' are provided, with a zoomed-in view of the oscillations in 'B' shown inset. The photometric measurements are given in their raw form (grey), and binned to 0.5 s intervals (red). The mean brightness for each frame is shown in blue, while the grey line marks the mean brightness across the full observation window. Extended from Chote [2020], with the author's permission.

generated for the n_{frames} segments.

When plotting the metric sum $\Delta^{5}_{\mu,frame} + \Delta^{95}_{\mu,frame}$ against the corresponding ratio $\Delta^{95}_{\mu,frame}/\Delta^{5}_{\mu,frame}$, tracks possessing similar short timescale structures in their light curves appear to cluster together in the parameter space. Representative examples from the regions 'A' to 'D' are provided in the remaining panels of Fig. 3.9. The objects in region 'A' have low values for both percentile metrics and near-unity ratios, typically exhibiting a low amplitude, yet even scatter about the mean brightness in each segment of their light curve. The exemplar light curve for region 'A' nicely demonstrates how the frame-wise percentile metrics are impervious to longer period variability extending across the observation window in its entirety. A similar structure is observed for tracks in region 'B' of the plot, which also have near-unity ratios but exhibit larger amplitude scatter above and below the mean brightness in each segment. Light curves in region 'B' of the parameter space typically exhibit near-sinusoidal oscillations that are equally weighted above and below the mean, though others with large scatter yet no discernible intrinsic variability are also present.

In region 'C' of Fig. 3.9, the metric ratio is slightly less than unity, and the scatter is consequently weighted below the mean. Bright objects with non-sinusoidal structure to their light curves are accompanied in this region by faint tracks that sit just above the noise floor, thus exhibiting noisy scatter that is weighted towards fainter magnitudes. Region 'D' of the metric space is populated exclusively by faint tracks with $V > 17$, which exhibit a large degree of scatter owing primarily to the rising photometric noise floor. That said, there are several cases where the large metric sum arises due to intrinsic variability from the object itself, as evidenced by the example provided for region 'D'. The tracks in this cluster are also characterised by a metric ratio much less than unity, indicating that the scatter is weighted strongly below the mean brightness for a typical light curve segment. As a result, region 'D' plays host to the group of tracks with sharp glints periodically breaching the noise floor discussed previously in Section 3.4.2.

To probe the long timescale variability in the DW-INT light curves, the following metrics are defined: $\Delta^{\mu,frame}_{\mu,window}$, which gives the median absolute offset between the mean brightness of each segment and that of the overall observation window, thus providing a measure of clustering about the overall mean; $\Delta^{\mu,frame(max)}_{\mu,frame(min)}$, which computes the maximum pair-wise offset between the mean brightnesses of the light curve segments, thus giving a sense of the maximal inter-frame variability. The

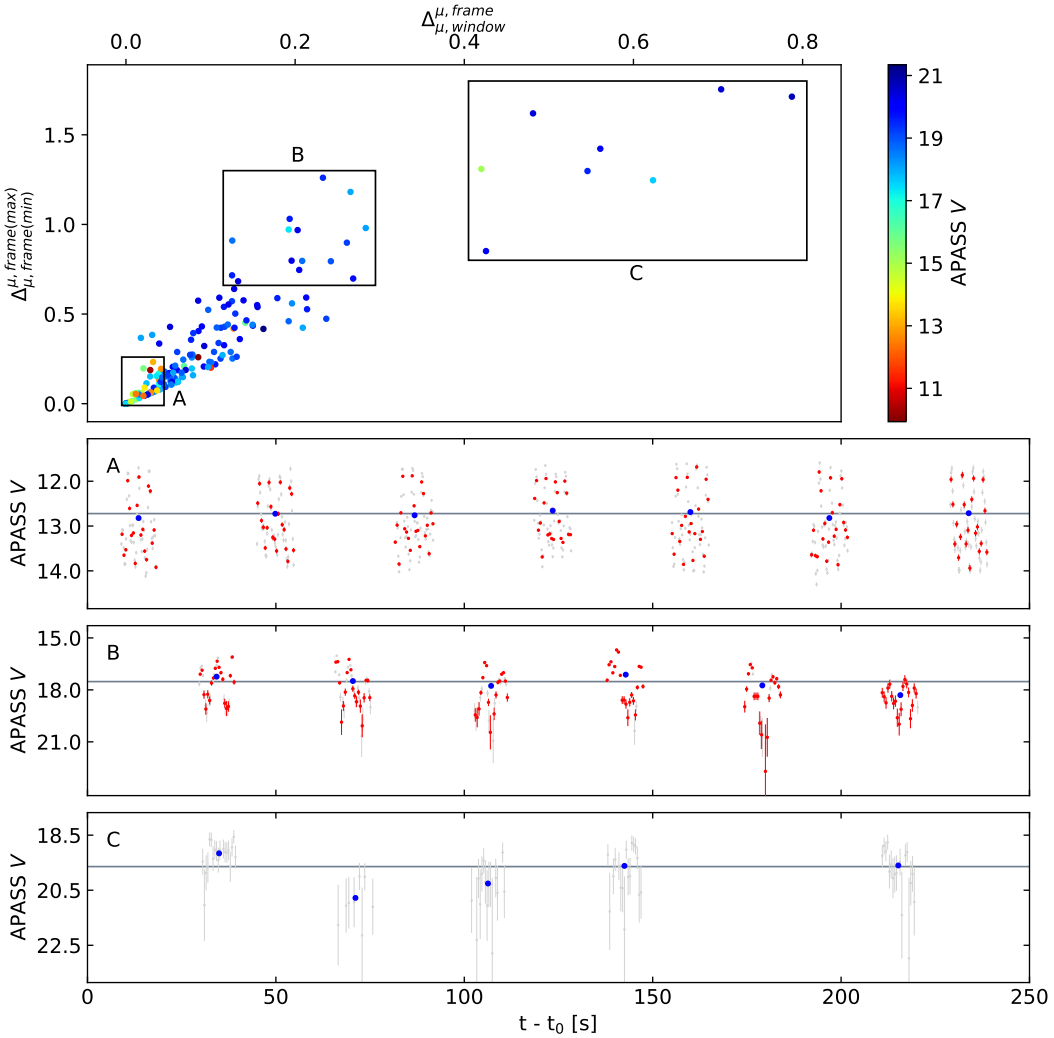

Figure 3.10: The metrics $\Delta^{\mu,frame}_{\mu,window}$ and $\Delta^{\mu,frame(max)}_{\mu,frame(min)}$, plotted as a function of mean calibrated brightness in APASS V. Clustering of detected tracks exhibiting comparable long timescale brightness variability is achieved by plotting the following against one another: the difference between the mean brightness computed on a frame-by-frame basis (see text) and the mean brightness determined across the full observation window; the difference between the maximum and minimum mean brightness computed on a frame-by-frame basis. Exemplar light curves from regions 'A' to 'C' are provided in the subsequent panels. The photometric measurements are given in their raw form (grey), and binned to 0.5 s intervals (red) where possible. The mean brightness computed on a frame-by-frame basis is shown in blue, while the grey line marks the mean brightness across the full observation window. Extended from Chote [2020], with the author's permission.

former may be found by taking the median of values generated by the expression,

$$\left|\mu^{k}_{frame} - \mu_{window}\right|, \tag{3.6}$$

with both terms as defined above for previous metrics. The latter metric is given by

$$\max\left(\mu_{frame}\right) - \min\left(\mu_{frame}\right), \tag{3.7}$$

where μ_{frame} is the collection of mean brightnesses μ^{k}_{frame} evaluated for the n_{frames} segments comprising the light curve in question.

When the two metrics are plotted against one another, as in the top panel of Fig. 3.10, tracks with similar long period features in their light curves appear to cluster in different regions of the parameter space. Light curves that fall within region 'A' of the plot have low values for both metrics, showing little to no long timescale brightness variability. While the shorter period intra-frame structure may influence the mean brightness of each light curve segment, the metrics used do little to discern between features that vary on timescales lower than the exposure time. In region 'B' of the metric space, light curves have relatively high maximal frame-to-frame offsets, yet fairly shallow differences between the frame means and the mean brightness across the observation window. This combination is typically indicative of brightness variability occurring over timescales comparable to the observational timespan, as appears to be the case for example 'B' in Fig. 3.10. Finally, light curves in region 'C' of the long timescale metric plot show some of the highest pair-wise offsets between frames, while also exhibiting large deviations from the mean brightness of the observation window. As is apparent for the example provided in the bottom panel of Fig. 3.10, this region of the metric space typically identifies variability with periods longer than the observation window, where the INT has moved on to a new pointing before the full cycle could be captured.

3.5 Summary

This chapter has presented photometric results from of an optical survey of the GSO region carried out using eight nights of dark-grey time on the 2.54 m INT on La Palma, Canary Islands. The survey was carried out as part of DebrisWatch, an ongoing collaboration between the University of Warwick and Dstl (UK) investigating the population of debris in the GSO region. Calibrated photometric light curves for candidate GSO objects were extracted from the survey image frames using a custom analysis pipeline, outlined in Section 3.3. Key findings from the survey are

briefly summarised as follows:

- a total of 226 orbital tracks are detected, 129 of which exhibiting rates of change in angular position consistent with circular orbits in the GSO regime;
- a detection rate of $\sim$11 hour^{-1}deg^{-2} for circular GSO objects is found, similar to rates observed by spot surveys of the GSO region undertaken using the Magellan 6.5 m telescope in Chile;
- a bimodal brightness distribution is observed, with the bright end centred around $V \sim 12$ and the faint end still rising at the sensitivity limit of $V \sim 21$, suggesting that the modal brightness may be fainter still;
- over 80 % of tracks with a mean brightness $V < 15$ (corresponding to a size larger than $\sim$1 m, assuming the objects are Lambertian spheres with an albedo of 0.1) correlate with known objects in the publicly available USSPACECOM catalogue, while the vast majority of fainter tracks fail to correlate;
- many faint, uncorrelated objects show optical signatures of tumbling, causing some to straddle the detection limit of the observations within a single exposure;
- over 45 % of uncorrelated tracks with successfully extracted light curves vary in brightness by more than four magnitudes across the window of observation;
- a degree of clustering is achieved by applying a selection of primitive metrics to the survey dataset, grouping together photometric light curves exhibiting similar short and long period brightness variability.

The GSO region is an important commodity with a limited number of orbital slots. Vacancies are set to become increasingly scarce with an imperfect disposal rate and an increase in orbital break-ups and anomalies observed in recent years. The latter have injected over a thousand new fragments into high altitude orbits since 2018, with a few hundred intersecting the GSOPR and posing a direct risk to active satellites. The majority of these fragments are too faint to be regularly tracked by the SSN, and thus remain unaccounted for in the publicly available USSPACECOM catalogue with its size cut-off of $\sim$50–100 cm at GSO altitudes. It is therefore essential that the faint end of the debris population continues to be probed in order to better understand the status of the GSO environment and how it will evolve both in the short- and long-term.

For the duration of the observation campaign, a 36 cm robotic astrograph was slaved to the INT, covering the same regions of sky with a larger FOV. The resulting dataset of simultaneous observations forms the basis for the work presented in Chapter 6. The next chapter, however, moves on to consider targeted observations of objects in the LEO and GSO regimes.

Chapter 4

Light curves of LEO and GSO targets

Since late 2018, members of the Satellites Group at the University of Warwick have been accruing databases of photometric light curves, extracted from targeted observations of LEO and GSO objects. This chapter provides an overview of early observations undertaken during the initial survey prototyping phase, which served to inform the observational strategies and scheduling procedures adopted as automated survey operations began in the summer of 2019. A motivation for the work is given in Section 4.1. The observational strategies employed by the survey instruments are discussed in Section 4.2, alongside a brief overview of the pipelines used to schedule and reduce the observations. Examples of light curves extracted for LEO and GSO targets from observations acquired during the protoyping phase are presented in Section 4.3. Finally, the current status of each survey is briefly discussed in Section 4.4 and a summary of the work is provided in Section 4.5.

Declaration — The following summarises elements of collaborative work that are included in this chapter. The presented observations were carried out remotely by myself, following training from Paul Chote, who spearheaded the light curve surveys. The scripts used to automate the generation of observational plan files and the reduction of survey frames were developed by Paul Chote. This chapter provides an overview of early contributions to the light curve surveys described in the 2019 AMOS technical proceeding, Chote et al. [2019], and associated poster.

4.1 Motivation

As discussed previously in Section 1.2.2, photometric light curves can impart a great deal of information regarding both the physical and behavioural characteristics of an object orbiting the Earth, and thus serve as useful diagnostic tools for SSA. The performance of algorithms designed to extract this information for the purposes of characterisation and classification will depend heavily on the quality and quantity of data available as input. The need for more data is fairly intuitive; the ability to classify an object based upon its photometric signatures will naturally require an understanding of the typical features that can arise across a wide and representative sample of objects. The term 'quality' has multiple meanings here: precise and accurate brightness measurements are important to ensure the algorithms are not led astray by spurious readings, for example those induced by source blending, bad pixels on the detector, and so on; the survey frames must be calibrated against a standard photometric catalogue to enable comparisons between light curves obtained by different instruments; the measurement cadence is also a key consideration, with instrumental constraints often resulting in sparsely sampled light curves that offer limited insight into the object's properties or attitude. High cadence measurements are sensitive to rapid changes in the target's brightness, revealing finer details that can be matched to more realistic geometric and attitudinal models (see Section 1.2.2 for a review of the relevant literature). The following sections present early contributions to two surveys accruing high cadence photometric light curves for target objects in the LEO and GSO regimes.

4.2 Strategies, scheduling and data reduction

For both the LEO and GSO light curve surveys, observations carried out in the initial prototyping phase were used to inform the strategies to be taken forward for automated operations, and to test early versions of the data reduction pipelines to be employed when extracting light curves from the survey frames. Further detail regarding the eventual automation of the tasks discussed herein for survey operations can be found in Chote et al. [2019].

The LEO observations made use of the ultra-wide FOV afforded by the eight cameras of the SuperWASP-N array, each imaging over an $8^\circ \times 8^\circ$ patch of sky. Owing to issues with two of the cameras during survey operations, the instrument's footprint was adjusted to cover a $\sim 200\,\mathrm{deg}^2$ region of sky, with much of the field imaged simultaneously by multiple cameras. With such a wide FOV, the LEO passes

could be observed with the telescope tracking sidereally (see Section 2.2.3), spreading integrated light from the target across pixels of the CCD frame and enabling the extraction of high cadence photometric information with an effective time resolution set by the angular speed of the target itself.

During the prototyping phase, the Heavens Above website[1] was used to inform a manual selection of bright LEO targets passing over La Palma in the twilight hours of the night in question. Care was taken when scheduling the observations to allow for sufficient time to complete a full observational sequence (outlined below) between each successive pass. The observational constraints listed in Section 2.2.2 were also taken into account when selecting targets, though an automated filter would later perform this more robustly in a way that would seek to minimise idle time during survey operations.

With a list of targets in place, plan files would be generated for each object, encoding the observational sequence to be run via the SuperWASP-N telescope control system (TCS). In each case, the target's latest TLE would be pulled from the Space-Track API and propagated using the `skyfield` SGP4 routines (see Section 2.1.1) to compute the pass start time, when the target would first become visible observationally. The TLE would then be propagated further until the target had traversed an angular path falling just short of the field width (allowing for uncertainties in the predicted positions). An average of the resulting start and end positions would guide the first pointing of the telescope. Scheduling of the following sequence could then take place:

1. slew to the pre-computed initial field;
2. start exposing shortly after the target enters the field;
3. end the exposure shortly before the target leaves the field, or when a maximum exposure time is reached (to limit background contamination from stellar blends);
4. slew to the next appropriate field, computed as above while allowing for a dead time of 15 s between exposures, during which the cameras are read out;
5. repeat steps 2–4 until the target sets below the horizon, gets eclipsed by the Earth's shadow, or enters the Moon's vicinity;

[1]The 'Daily predictions for brighter satellites' list available via the Heavens Above website [https://www.heavens-above.com/] was used to identify appropriate targets for early LEO observations undertaken by SuperWASP-N (accessed March 2021)

6. slew back to the initial field and repeat the sequence of exposures to obtain reference frames, allowing flux contamination from blended stars to be measured and subtracted.

The sequence would be run manually via the SuperWASP-N TCS prior to each pass, and the acquired frames stored for later processing.

Owing to the much slower angular rates associated with targets in the GSO region, the GSO light curve survey could make use of the more sensitive RASA instrument, still achieving a reasonably wide $3.6° \times 2.7°$ FOV. Early observations tested both the 'untracked' mode of operation, where station-kept GEO satellites appear as point sources in the resulting frames, and sidereal tracking as for the LEO sequences outlined above. The decision to adopt the latter for automated survey operations is discussed further in Section 4.3.2.

To facilitate manual target selection during the GSO survey prototyping phase, the inMySky[2] package was developed to enable the observer to browse through suitable candidates, visible at high elevation on the night in question. The script takes as input the latest GSO sub-catalogue pulled from the Space-Track API, propagates the constituent TLEs to the user-specified epoch and displays the computed positions in hour angle and altitude space. The observer can then select a point on the display, triggering the printing of a list in the terminal window that provides supplementary information for the corresponding object. As for the LEO survey, an automated filter would later conduct the target selection and scheduling procedures in a way that would minimise idle time during survey operations, while accounting for the observational constraints discussed in Section 2.2.2.

The selected target's TLE would be used to inform the initial pointing of the RASA instrument, which would thereafter be updated manually via a corrective slew in order to prevent the drifting target from exiting the FOV. Each GSO object selected as a target would typically be observed for a duration of around 30 minutes, a sufficient amount of time to sample the object's rotational characteristics in most cases (see Section 4.3.2), while ensuring that several targets could be observed on a given night. The observation window would comprise a series of 10 s exposures, separated by roughly 4 s of dead time for readout. On account of the more straightforward observational sequences afforded by the slow angular rates of GSO targets, it was possible to simply take an adjacent frame (either the previous or next frame in the series of exposures) as a reference, from which an estimate of the flux from background stars could be obtained.

[2] https://github.com/jblake95/inMySky (accessed March 2021)

Table 4.1: Catalogue information (1/3) for the LEO objects observed by the SuperWASP-N instrument in the period November–December 2018, as part of the initial prototyping phase of a survey to accrue a database of photometric light curves. Objects are designated as payloads (PL), rocket bodies (R/B) or debris (DEB). Source abbreviations and radar cross-section (RCS) definitions can be found on the Space-Track website, from which this information was obtained. Orbital states correct as of November 2020.

Name	NORAD ID	Source	Launch Year	Type	Perigee [km]	Apogee [km]	Inclination [deg]	RCS
IRAS	13777	US	1983	PL	879	905	98.96	LARGE
SL-8 R/B	8874	CIS	1976	R/B	963	1000	82.96	LARGE
COSMOS 1867	18187	CIS	1987	PL	777	799	65.01	LARGE
CZ-4 DEB	20855	PRC	1990	DEB	847	881	98.71	LARGE
DELTA 1 R/B	9786	US	1977	R/B	608	1217	28.01	LARGE
DUMMY MASS 2	24926	PRC	1997	PL	607	620	86.34	LARGE
SL-3 R/B	5918	CIS	1972	R/B	830	917	81.24	LARGE
SL-3 R/B	877	CIS	1964	R/B	645	745	65.08	LARGE
OAO 3 (COPERNICUS)	6153	US	1972	PL	695	705	35.01	LARGE
SL-8 R/B	19325	CIS	1988	R/B	947	998	82.95	LARGE
OAO 2	3597	US	1968	PL	735	744	34.99	LARGE
COSMOS 2327	23773	CIS	1996	PL	949	1018	82.99	LARGE
ENVISAT	27386	ESA	2002	PL	764	766	98.14	LARGE
IRIDIUM 73	25344	US	1998	PL	727	729	86.45	LARGE
SKYMED 1	31598	IT	2007	PL	622	623	97.89	LARGE
COSMOS 2082	20624	CIS	1990	PL	832	857	71.04	LARGE
SL-8 R/B	14241	CIS	1983	R/B	758	784	74.06	LARGE
MOS 1A (MOMO 1)	17527	JPN	1987	PL	878	891	99.14	LARGE
METEOR 2-1	8026	CIS	1975	PL	843	874	81.28	LARGE
COSMOS 1607	15378	CIS	1984	PL	910	993	64.99	LARGE
DELTA 1 R/B	15202	US	1984	R/B	544	3983	28.90	LARGE
SKYMED 3	33412	IT	2008	PL	622	624	97.89	LARGE
IRIDIUM 921	24873	US	1997	PL	522	532	86.40	LARGE
COSMOS 651	7291	CIS	1974	PL	892	945	64.97	LARGE
OAO 1	2142	US	1966	PL	773	784	35.05	LARGE
SL-8 R/B	17526	CIS	1987	R/B	945	1005	82.91	LARGE

Table 4.2: Catalogue information (2/3) for the LEO objects observed by the SuperWASP-N instrument in the period November–December 2018, as part of the initial prototyping phase of a survey to accrue a database of photometric light curves. Objects are designated as payloads (PL), rocket bodies (R/B) or debris (DEB). Source abbreviations and radar cross-section (RCS) definitions can be found on the Space-Track website, from which this information was obtained. Orbital states correct as of November 2020.

Name	NORAD ID	Source	Launch Year	Type	Perigee [km]	Apogee [km]	Inclination [deg]	RCS
SKYMED 4	37216	IT	2010	PL	622	623	97.89	LARGE
CZ-4B DEB	25733	PRC	1999	DEB	827	848	98.94	LARGE
SL-3 R/B	18961	CIS	1988	R/B	851	931	99.24	LARGE
SL-8 R/B	6324	CIS	1972	R/B	740	753	99.76	LARGE
METEOR 2-12	15516	CIS	1985	PL	933	955	82.53	LARGE
SL-8 R/B	10011	CIS	1977	R/B	991	2089	65.86	LARGE
SL-16 R/B	25407	CIS	1998	R/B	835	844	71.01	LARGE
COSMOS 44	876	CIS	1964	PL	581	782	65.06	LARGE
MONITOR-E/SL-19	27840	CIS	2003	PL	691	833	98.34	LARGE
SL-8 R/B	21088	CIS	1991	R/B	957	991	82.95	LARGE
COSMOS 773	8343	CIS	1975	PL	767	783	74.06	LARGE
FENGYUN 1C	25730	PRC	1999	PL	829	849	99.07	MEDIUM
SL-3 R/B	11289	CIS	1979	R/B	799	908	81.25	LARGE
SL-3 DEB	17755	CIS	1982	DEB	794	895	81.25	SMALL
NOAA 13	22739	US	1993	PL	844	856	98.46	LARGE
RADARSAT	23710	CA	1995	PL	788	790	98.57	LARGE
BREEZE-M DEB (TANK)	29649	CIS	2006	DEB	314	15732	49.55	LARGE
ATLAS CENTAUR R/B	6155	US	1972	R/B	630	682	35.00	LARGE
COSMOS 192	3047	CIS	1967	PL	700	714	74.01	LARGE
DELTA 2 R/B	25876	US	1999	R/B	493	1264	51.76	LARGE
ARIANE 42P R/B	22079	FR	1992	R/B	1299	1401	66.07	LARGE
MSX	23851	US	1996	PL	895	906	98.80	LARGE
SL-16 R/B	23405	CIS	1994	R/B	838	845	70.98	LARGE
CRYOSAT	36508	ESA	2010	PL	714	725	92.02	LARGE
BREEZE-M DEB (TANK)	27821	CIS	2003	DEB	259	13087	49.57	LARGE
SL-8 R/B	13034	CIS	1982	R/B	956	1005	82.94	LARGE

Table 4.3: Catalogue information (3/3) for the LEO objects observed by the SuperWASP-N instrument in the period November–December 2018, as part of the initial prototyping phase of a survey to accrue a database of photometric light curves. Objects are designated as payloads (PL), rocket bodies (R/B) or debris (DEB). Source abbreviations and radar cross-section (RCS) definitions can be found on the Space-Track website, from which this information was obtained. Orbital states correct as of November 2020.

Name	NORAD ID	Source	Launch Year	Type	Perigee [km]	Apogee [km]	Inclination [deg]	RCS
SMAP	40376	US	2015	PL	681	683	98.12	LARGE
SL-24 DEB	36510	CIS	2010	DEB	665	701	92.02	LARGE
SEASAT 1	10967	US	1978	PL	744	748	108.01	LARGE
SL-16 R/B	17974	CIS	1987	R/B	823	846	71.01	LARGE
METEOR 1-16	7209	CIS	1974	PL	818	874	81.23	LARGE
CZ-4C R/B	38355	PRC	2012	R/B	965	1208	100.14	LARGE
SL-16 R/B	24298	CIS	1996	R/B	839	863	70.84	LARGE
OPS 6182 (DMSP 5D-1 F3)	10820	US	1978	PL	767	781	98.53	LARGE
SL-3 R/B	8520	CIS	1975	R/B	836	890	81.29	LARGE
SL-14 R/B	14820	CIS	1984	R/B	605	631	82.54	LARGE
COSMOS 785	8473	CIS	1975	PL	887	1025	65.08	LARGE
FENGYUN 1D	27431	PRC	2002	PL	850	871	99.15	LARGE
SL-8 R/B	17526	CIS	1987	R/B	945	1005	82.91	LARGE
SL-8 R/B	21153	CIS	1991	R/B	957	999	82.93	LARGE
SJ-12	36596	PRC	2010	PL	570	584	97.67	LARGE
SL-8 R/B	18986	CIS	1988	R/B	937	1000	82.96	LARGE
IRIDIUM 46	24905	US	1997	PL	126	135	86.33	LARGE
NOAA 15	25338	US	1998	PL	798	812	98.71	LARGE
THOR AGENA B R/B	1807	US	1965	R/B	503	2649	79.84	LARGE
SL-16 R/B	23088	CIS	1994	R/B	842	845	71.00	LARGE
DELTA 1 R/B	10517	US	1977	R/B	476	1743	28.66	LARGE
SL-8 R/B	15032	CIS	1984	R/B	763	789	74.07	LARGE
SL-8 R/B	12150	CIS	1981	R/B	931	1017	65.82	LARGE
SL-8 R/B	13260	CIS	1982	R/B	954	1015	65.83	LARGE
SL-8 R/B	20528	CIS	1990	R/B	967	1012	82.94	LARGE

The data reduction pipelines employed to process image frames from the LEO and GSO surveys were developed by Paul Chote, and are largely similar to the analysis pipeline discussed in Chapter 3. For the photometric calibrations, comparison stars are queried from the *Gaia* DR2 catalogue [Gaia-Collaboration et al., 2016, 2018]. The *Gaia* G passband closely matches the white light response resulting from the RASA's lack of filter. The *Gaia* G_{BP} passband more closely matches the response curves of the broad-band 400–700 nm filters installed in the SuperWASP-N lenses, and would later be incorporated into the instrument's reduction pipeline for survey operations. Aperture placement for light curve extraction is driven by the target's TLE. Predicted positions for the trail's start and end points may be offset by several pixels from those observed, owing to the uncertainties associated with the TLE format and SP propagation models (see Section 1.2.2). The observed positions are identified via visual inspection (for the long LEO trails) or using a targeted `SEP` extraction (for the shorter GSO trails). Offsets are applied to the propagation epoch, inclination and right ascension of the ascending node (as defined in Appendix B), and a downhill optimisation is carried out to align the TLE-predicted trails with those observed. Further detail regarding the reduction, detection and light curve extraction procedures can be found in Chote et al. [2019].

4.3 Light curves from early observations

The following sections present a selection of light curves extracted from the LEO (Section 4.3.1) and GSO (Section 4.3.2) survey frames acquired as part of the initial prototyping phase. Comprehensive lists containing catalogue information for all the LEO and GSO targets that were observed during this period are provided in Tables 4.1–4.3 and Table 4.4, respectively. For reference, illustrations of the LEO and GSO spacecraft discussed qualitatively are presented in Fig. 4.1 and Fig. 4.8, respectively.

4.3.1 LEO light curves

In Fig. 4.2 and 4.3, light curves are displayed for a variety of LEO payloads observed by the SuperWASP-N instrument in the period November–December 2018. The diverse nature of the light curves is immediately clear, with each set of photometric measurements encoding a unique signature, fashioned from the physical and attitudinal characteristics of the spacecraft in question. While the brightness measurements have been photometrically calibrated in the *Gaia* G passband as above, it should be noted that additional corrections for viewing geometry and atmospheric

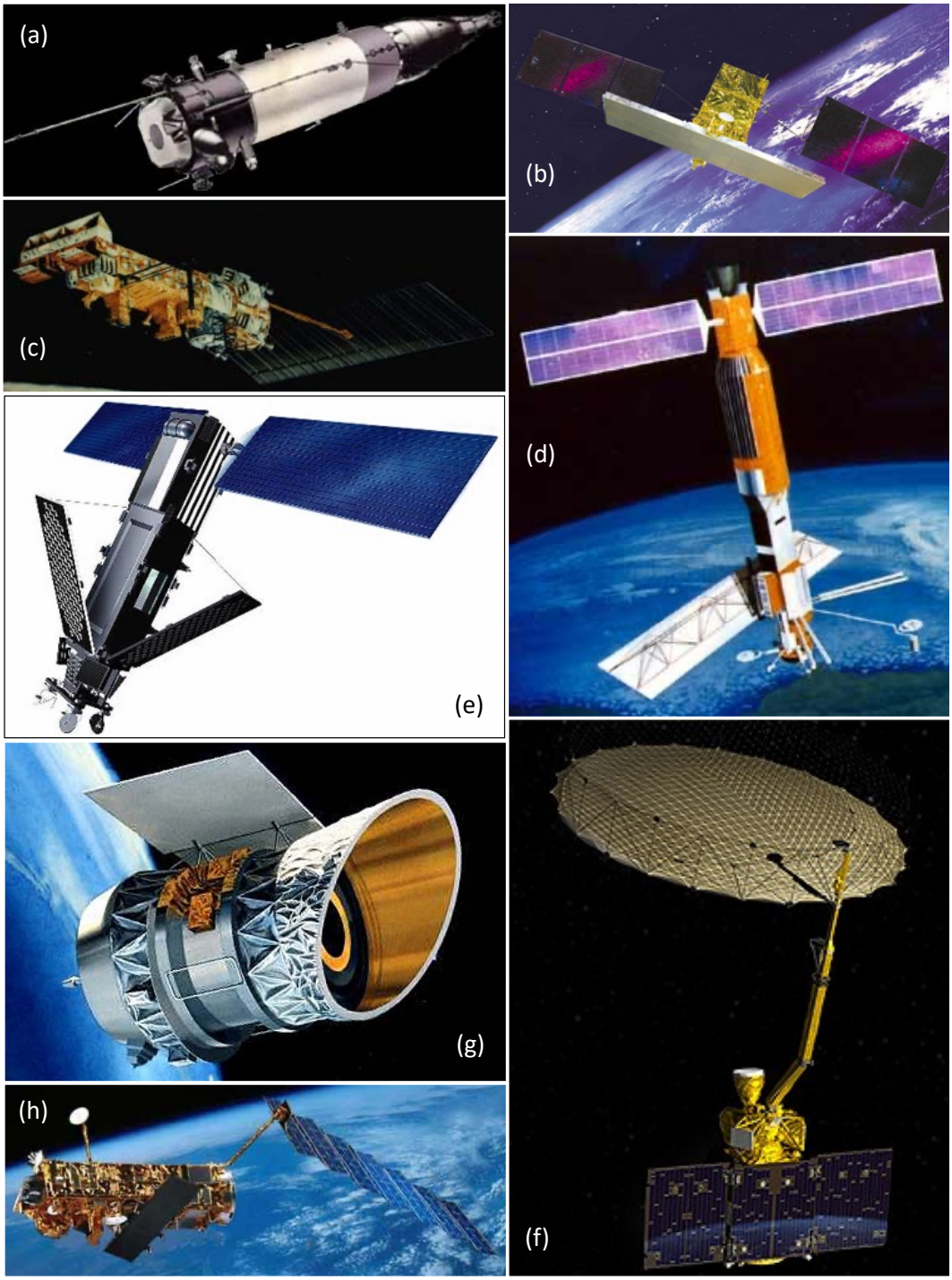

Figure 4.1: Illustrations of the various LEO spacecraft (or equivalent models) discussed in Section 4.3.1: (a) Cosmos 1867; (b) COSMO-SkyMed 1; (c) NOAA 13 (9); (d) Seasat 1; (e) Iridium 46 (1); (f) SMAP; (g) IRAS; (h) Envisat. Images sourced from Gunter's Space Page.

extinction are yet to be performed.

A sinusoidal pattern can be seen in the light curve for Cosmos 1867 in Fig. 4.2. The decommissioned Soviet/Russian craft is a nuclear powered *Plasma-A* satellite, based on the same bus as the problematic RORSATs discussed in Section 1.2.1. Cosmos 1867 suffered from a suspected impact event in early 2014 [NASA, 2014], and tens of fragments that are believed to be leaked NaK coolant have since been catalogued. The satellite has a cylindrical body with a cone-shaped nose, similar to that of a typical upper stage. Indeed, the smooth oscillations in brightness exhibited by the craft are akin to those observed for a number of LEO rocket bodies, as evidenced by the profiles in Fig. 4.4. Light curves for the COSMO-SkyMed satellites, 1 and 3, are also shown in Fig. 4.2. The two Italian satellites belong to a group of four space-based radar systems observing the Earth, residing in sun-synchronous polar orbits with a 97.9° inclination. The box-wing SkyMed satellites are known to flare in brightness, and a fairly long ($\sim 100\,\mathrm{s}$) example is observed during the SkyMed 1 pass, likely arising from the large phased-array radar antenna on the central platform of the bus. The satellite reaches a maximal brightness in the range $-2 < G < -1$ during the observation window, though the flare appears to peak in a data gap between the fourth and fifth exposure, while the telescope was slewing and the cameras were reading out. A much more rapid variation in brightness is observed for NOAA 13, in the fifth panel of Fig. 4.2. The US meteorological satellite suffered a failure soon after it launched in 1993, thought to be the result of a short circuit preventing the onboard batteries from recharging [Davis, 2007]. The NOAA 13 light curve exhibits a periodic glinting that appears to take place once every $\sim$1–2 s.

Sharp features are also observed in the light curve extracted from observations of the Seasat 1 satellite, shown in the third panel of Fig. 4.3. Seasat 1 possesses a complex structure: a long, cylindrical bus with two solar panel 'wings' at one end and five major instruments, including a synthetic aperture radar, at the other. The satellite's electrical system failed in 1978, yet it continues to orbit in an uncontrolled state at an altitude of $\sim 745\,\mathrm{km}$. Likely tumbling, the multiple peaks apparent in the Seasat 1 light curve result from highly reflective components moving into view along the observer's line of sight. As for the SkyMed satellites, members of the Iridium constellation are also known to produce impressive flares, often involving rapid changes in brightness by several magnitudes. An example is captured in the light curve acquired for Iridium 46, in the fifth panel of Fig. 4.3. Once again, the flare is not observed in its entirety, with only the ingress visible prior to a data gap. While partially due to dead time between exposures, the detector is also likely to

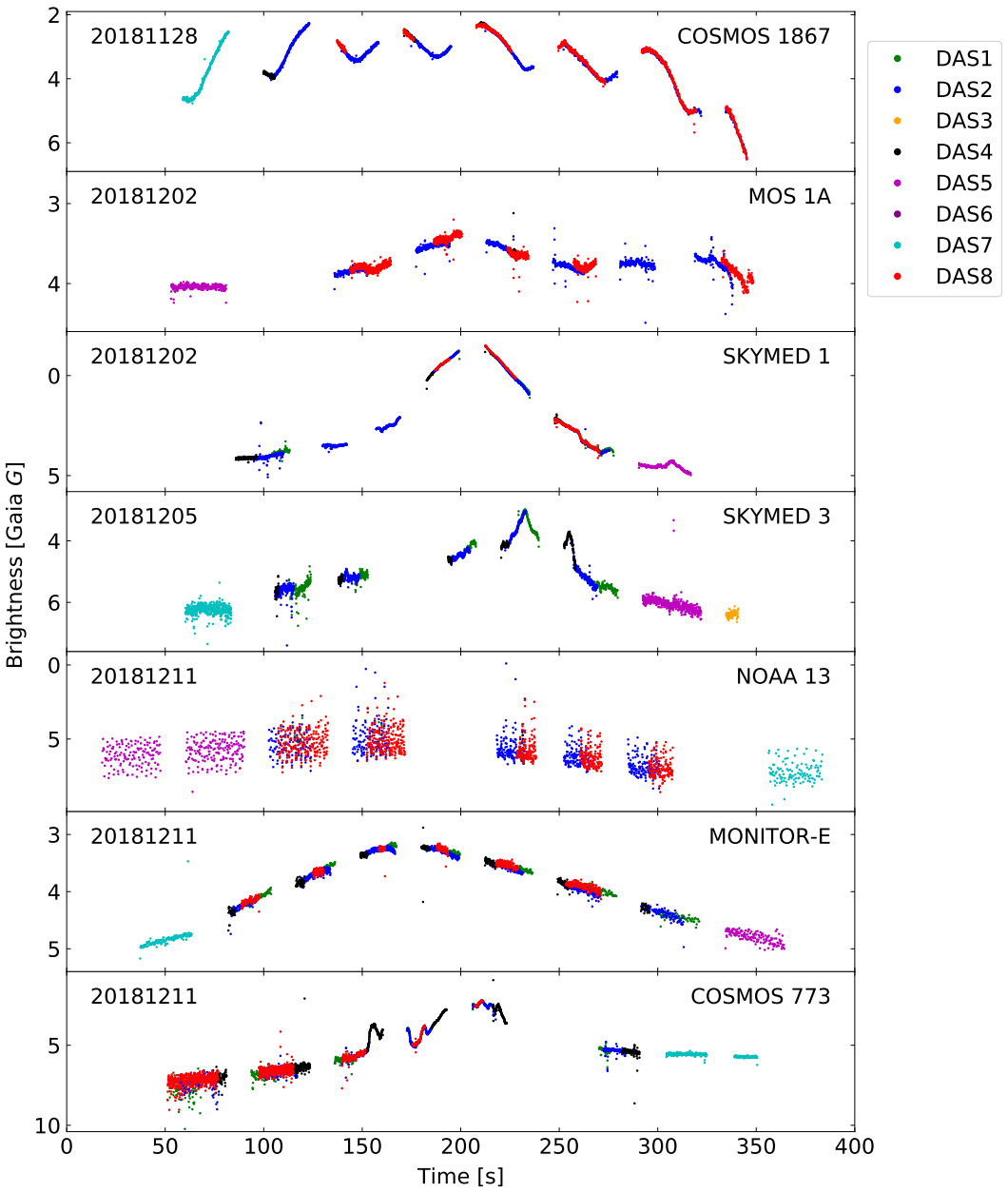

Figure 4.2: Photometric light curves for a selection of LEO payloads (1/2) observed by the SuperWASP-N instrument in the period November–December 2018. Timestamps and identifiers are provided in the top-left and top-right of each panel, respectively. Brightness measurements are colour-coded by camera according to the right-hand legend. Gaps in the data arise from the dead time between exposures, during which the cameras are read out and the telescope slews to the next appropriate field.

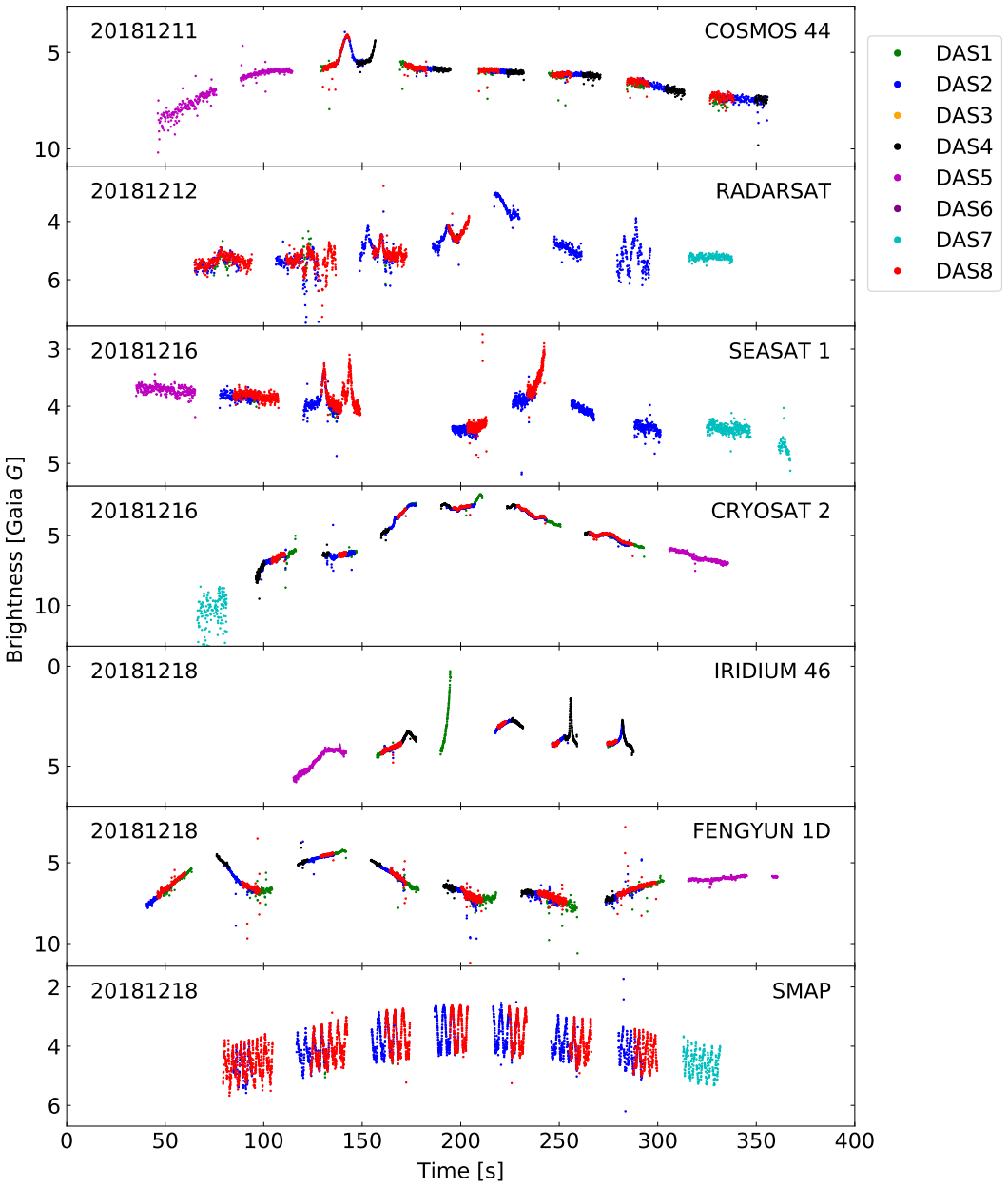

Figure 4.3: Photometric light curves for a selection of LEO payloads (2/2) observed by the SuperWASP-N instrument in the period November–December 2018. Timestamps and identifiers are provided in the top-left and top-right of each panel, respectively. Brightness measurements are colour-coded by camera according to the right-hand legend. Gaps in the data arise from the dead time between exposures, during which the cameras are read out and the telescope slews to the next appropriate field.

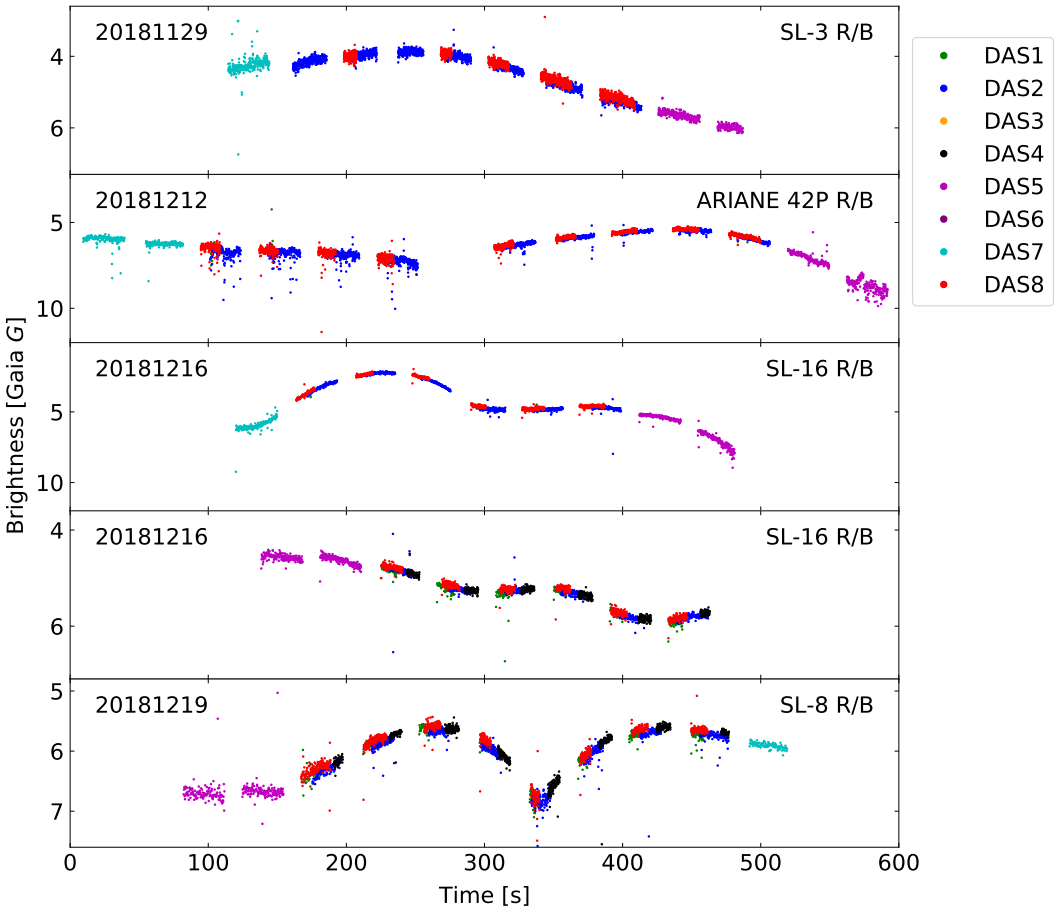

Figure 4.4: Photometric light curves for a selection of LEO rocket bodies observed by the SuperWASP-N instrument in the period November–December 2018. Timestamps and identifiers are provided in the top-left and top-right of each panel, respectively. Brightness measurements are colour-coded by camera according to the right-hand legend. Gaps in the data arise from the dead time between exposures, during which the cameras are read out and the telescope slews to the next appropriate field.

have saturated at the flare peak; the SuperWASP-N detectors are able to acquire useful photometric data for objects brighter than $G \sim 9$ (to penetrate the noise floor) and fainter than $G \sim -1$ (to avoid saturation). The SMAP Earth observation satellite consists of a box-wing bus with an extended antenna spanning 6 m in diameter[3]. The large antenna is offset relative to the plane perpendicular to the normal vector of the Earth's surface, and rotates about the latter with a rate of one revolution every ~ 4 s to conically scan the field below. Interestingly, this aligns with the periodicity seen in SMAP's light curve, given in the bottom panel of Fig. 4.3, suggesting that the rapid brightness oscillations arise from the reflective antenna repeatedly rotating in and out of view along the SuperWASP-N instrument's line of sight.

Prior to the implementation of an automated scheduling procedure, observational gaps that would otherwise be written off as idle time were often filled with LEO passes partially obscured by the Earth's shadow. Examples in Fig. 4.5 show a variety of LEO payloads and rocket bodies either entering or emerging from the eclipsing shadow at a rate governed by the object's altitude. An increased scatter in the raw photometric measurements can be seen as the targets are eclipsed, plunging the light curves into the noise floor. The examples highlight the importance of accounting for the shadow when scheduling observations of any object, irrespective of its brightness.

Some objects of particular interest were observed at multiple epochs. A collection of light curves extracted from early observations of IRAS, for instance, is shown in Fig. 4.6. Launched in 1983, the space-based observatory operated for less than a year before the onboard cryogenic coolant depleted and the mission was brought to a close. The decommissioned satellite has remained in its sun-synchronous polar orbit ever since, residing in a densely populated altitude band surrounding $\sim$ 890 km. Indeed, a 'near-miss' encounter between IRAS and another uncontrolled spacecraft took place in early 2020 (see Section 1.2.1). Multiple passes were also observed for the Envisat satellite over the course of the LEO survey prototyping phase, and the resulting series of light curves is shown in Fig. 4.7. Communications between ESA and Envisat were unexpectedly lost in 2012. Like IRAS, the defunct Earth observation satellite continues to orbit in a densely populated sun-synchronous polar band, and has been identified as a high priority target for future ADR missions (see Section 1.2.4). In both cases, the light curves show numerous short and long period glints arising from reflective components of the box-

[3]Further detail regarding the instrument specification for the SMAP satellite can be found via https://smap.jpl.nasa.gov/observatory/instrument/ (accessed March 2021)

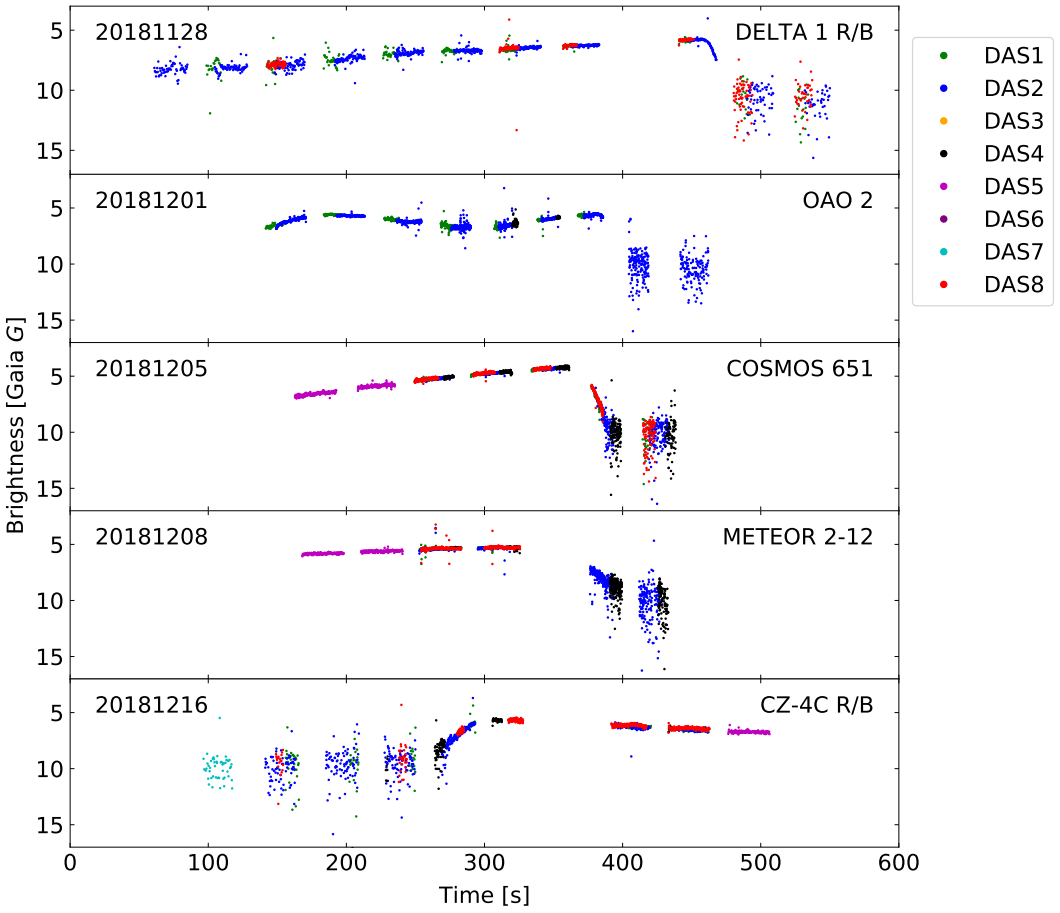

Figure 4.5: Photometric light curves for a selection of LEO payloads and rocket bodies observed by the SuperWASP-N instrument in the period November–December 2018. In each case, the object either starts or ends the pass eclipsed by the Earth's shadow. Timestamps and payload names are provided in the top-left and top-right of each panel, respectively. Brightness measurements are colour-coded by camera according to the right-hand legend. Gaps in the data arise from the dead time between exposures, during which the cameras are read out and the telescope slews to the next appropriate field.

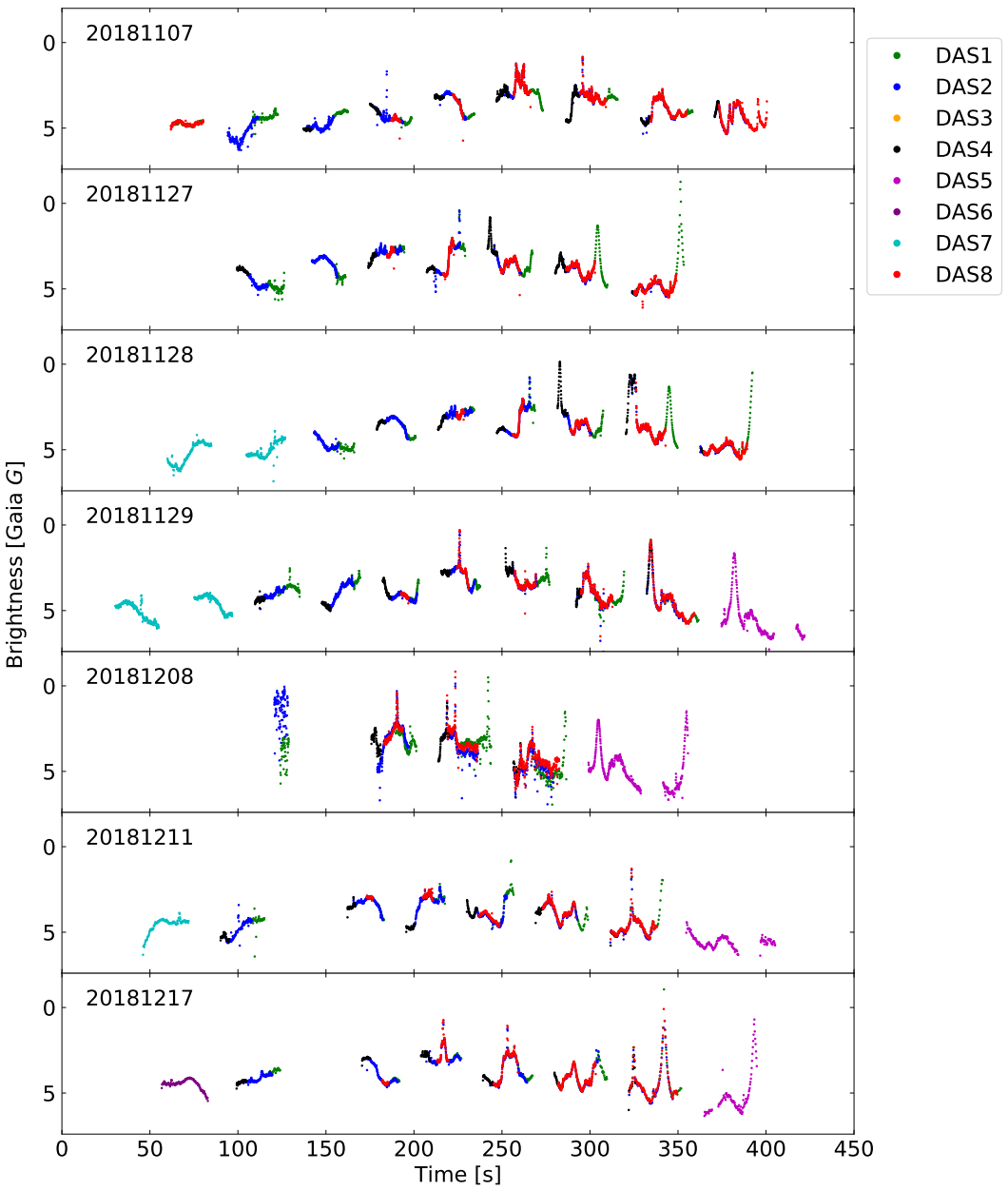

Figure 4.6: Photometric light curves for IRAS, a decommissioned space-based astronomical telescope in the LEO region. The satellite was observed by the SuperWASP-N instrument on multiple nights across the period November–December 2018. Timestamps are provided in the top-left of each panel. Brightness measurements are colour-coded by camera according to the right-hand legend. Gaps in the data arise from the dead time between exposures, during which the cameras are read out and the telescope slews to the next appropriate field.

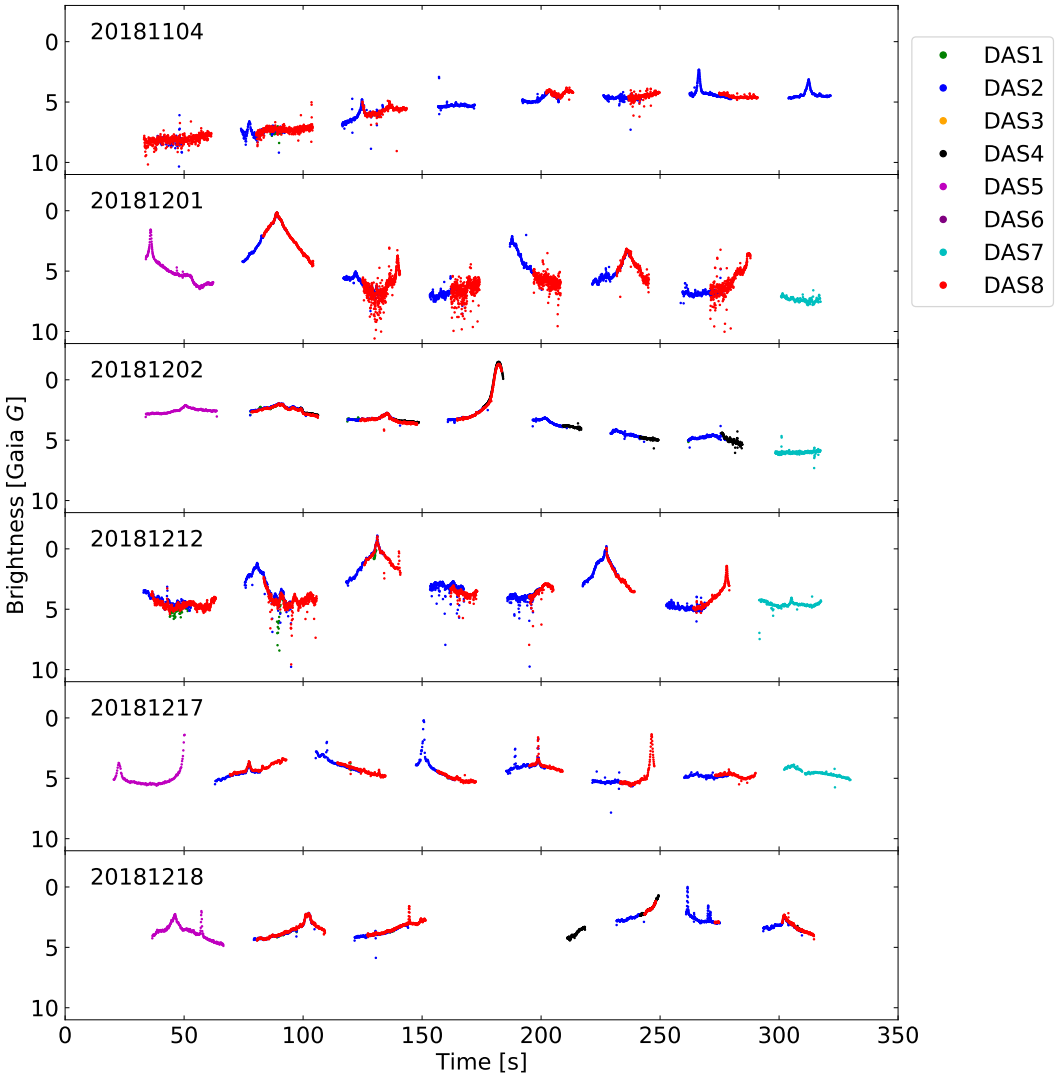

Figure 4.7: Photometric light curves for Envisat, a LEO polar orbit Earth observation satellite that has existed in an uncontrolled state since its failure in 2012. The satellite was observed by the SuperWASP-N instrument on multiple nights across the period November–December 2018. Timestamps are provided in the top-left of each panel. Brightness measurements are colour-coded by camera according to the right-hand legend. Gaps in the data arise from the dead time between exposures, during which the cameras are read out and the telescope slews to the next appropriate field.

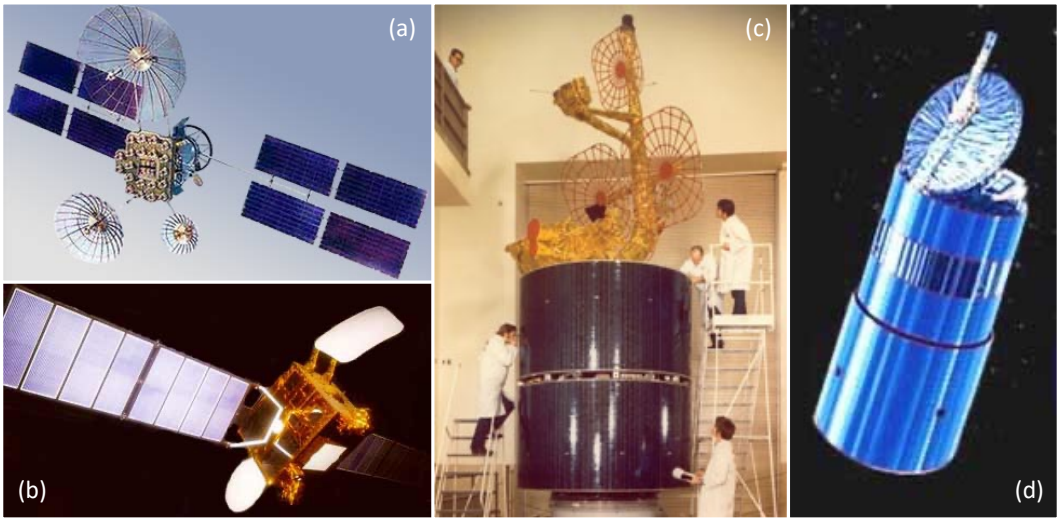

Figure 4.8: Illustrations of the various GSO spacecraft (or equivalent models) discussed in Section 4.3.2: (a) Cosmos 2054; (b) Arabsat 1A; (c) Intelsat 4A-F1; (d) Telstar 302 (301). Images sourced from Gunter's Space Page.

wing spacecraft. While similar features can be matched between different passes, it is clear that multiple epoch observations enable different attitudinal phases to be probed, acting to build a more complete understanding of both the target's behaviour and how it evolves over time. That said, the rapid nature of LEO passes makes this a very challenging endeavour, as the photometric information derived from a set of observations may often be too sparse to probe a full rotational cycle. Targets in the GSO region can be observed for much longer owing to their much lower angular rates, and thus pose less of a problem in this regard.

4.3.2 GSO light curves

In Fig. 4.9, examples of light curves extracted from early RASA observations of targets in the GSO region are provided. Each of the ∼5 minute segments shown is derived from an overall observation window of roughly 30 minutes, in order to more clearly illustrate the differing photometric signatures. The targets were imaged using two modes of operation: the 'untracked' mode, where tracking is disabled and the telescope remains fixed relative to the Earth; the 'sidereal' mode, where the telescope tracks sidereally, remaining fixed relative to the background stars. Both of the observational strategies appear to perform equally well when sampling long period features, where the target's brightness is evolving smoothly over timescales longer than the 10 s exposure time. Shorter period signatures such as sharp glints,

Table 4.4: Catalogue information for a selection of GSO objects observed by the RASA instrument in April 2019, as part of the initial prototyping phase of a survey to accrue a database of photometric light curves. All objects are designated as payloads (PL). Source abbreviations and radar cross-section (RCS) definitions can be found on the Space-Track website, from which this information was obtained.

Name	NORAD ID	Source	Launch Year	Type	Perigee [km]	Apogee [km]	Inclination [deg]	RCS
INTELSAT 4A-F1	8330	ITSO	1975	PL	35865	35895	12.09	LARGE
TELSTAR 302	15237	US	1984	PL	35911	35938	15.14	LARGE
ARABSAT 1A	15560	AB	1985	PL	35732	35744	14.18	LARGE
INTELSAT 515	19772	ITSO	1989	PL	36025	36211	15.04	LARGE
COSMOS 2054	20391	CIS	1989	PL	35803	35826	14.32	LARGE

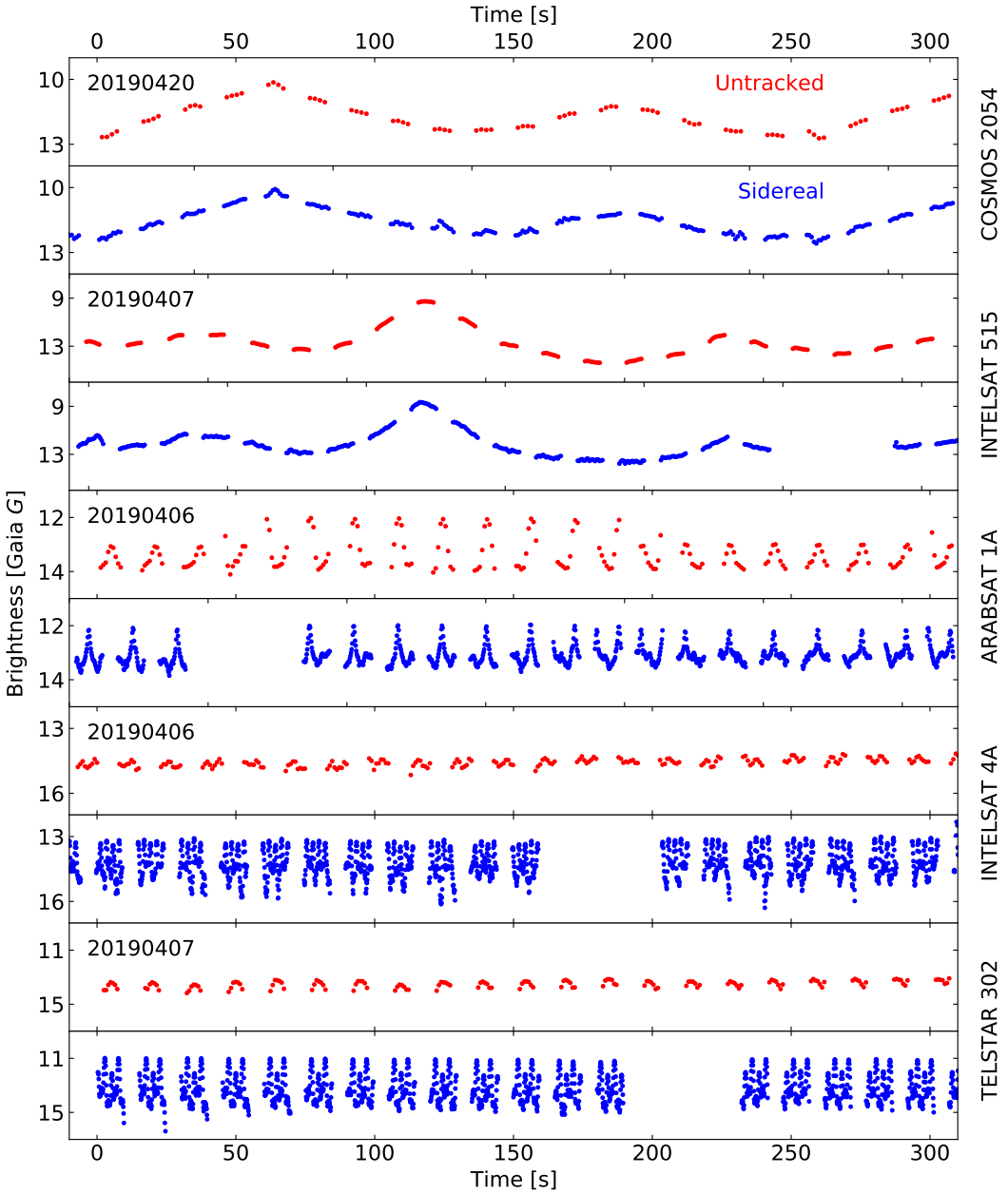

Figure 4.9: Photometric light curves for a selection of GSO payloads observed by the RASA instrument in April 2019. For each object, images were acquired with the telescope in 'untracked' mode (red), such that a station-kept GEO satellite would be point-like, and separately with the telescope tracking sidereally (blue), leading to a trailing rate of around $15'' \, \mathrm{s}^{-1}$ in the right ascension direction. Timestamps are provided in the top-left for each pair of panels corresponding to the objects identified on the right-hand side. Gaps in the data arise from the dead time between exposures, during which the cameras are read out and the telescope slews to the next appropriate field if necessary. Adapted from Chote et al. [2020] with the author's permission.

on the other hand, are often poorly resolved by the untracked observations. Targets in the GSO region manifest as longer trails in the sidereally tracked frames, owing to an additional $\sim 15'' \, \mathrm{s}^{-1}$ streaking along the right ascension axis. Longer trails facilitate the extraction of higher time resolution photometric information from the frames, thus allowing finer details in the light curve to be uncovered. The lower time resolution afforded by the shorter trails obtained with the RASA operating in the untracked mode has the effect of smearing shorter period signals and introducing sampling ambiguities via aliasing. For this reason, the sidereal tracking strategy was adopted when full survey operations began in the summer of 2019.

The light curves for Cosmos 2054, shown in the top two panels of Fig. 4.9, serve as excellent examples for illustrating the two strategies in action. Fourier analysis of the full dataset uncovers an underlying $\sim 250\,\mathrm{s}$ periodicity, which is preserved by both modes of operation. However, a number of short period glints along the otherwise smoothly oscillating profile are resolved by the higher cadence measurements extracted from the sidereally tracked frames. Launched in 1989, Cosmos 2054 is a decommissioned data relay satellite that provided communications to the MIR space station and other Soviet/Russian spacecraft. Based on the KAUR-4 bus model, the satellite features two pairs of solar panel 'wings' and multiple large antennas. The light curve exhibits similar features to those found in the INT observations of Raduga 13 presented in Chapter 3, a satellite based on an earlier version of the KAUR model. A relatively flat brightness profile for Raduga 13 was found within the bounds of the INT observation window (see Section 3.4.2), except for one ~ 0.5 magnitude glint that spanned a single 10 s exposure, closely resembling the short period glints visible in the Cosmos 2054 light curve. The RASA's shorter readout time reduces the amount of dead time between exposures, limiting the severity of data gaps and increasing the likelihood of capturing the short period features. Furthermore, the presented RASA light curves cover a much longer observation window relative to that afforded by the INT during its survey of faint GSO debris, allowing rotational cycles to be sampled fully in the majority of cases, and the associated periodicities to be inferred.

The different resolutions afforded by the two strategies are clearly illustrated by the latter three examples in Fig. 4.9, with dominant periods in the range 4–16 s. The smearing effect inherent in the untracked measurements acts to broaden the sharp repeating glints that are observed for Arabsat 1A, which appears to be tumbling with a period slightly longer than the exposure time. For the rapid oscillations in brightness exhibited by Intelsat 4A-F1 and Telstar 302, where multiple rotational cycles appear to take place in the time frame of a single exposure, the smearing

instead results in a greatly diminished amplitude where the apertures placed in the untracked frames have been wide enough to partially span neighbouring peaks and troughs in the light curve. The latter two spacecraft are based on cylindrical Hughes bus models, similar to that of SBS-3 discussed in Chapter 3. Owing to the lower plate scale of the INT detector, a given target in the GSO region will span a longer trail in image space when captured by the INT than it would if observed by the RASA. It was therefore possible to preserve the short period features in the extracted light curve for SBS-3, even with the INT operating in the untracked mode at the time of acquisition.

4.4 Status and future outlook

Following the initial prototyping phase, automated survey operations began in the summer of 2019. The RASA GSO survey ran for several weeks in the period July–August 2019, while the SuperWASP-N survey continued until November 2019. The resulting database of LEO light curves has since been supplemented by sporadic observations that took place in the latter months of 2020 after necessary maintenance work had been carried out. As of February 2021, over 3000 light curves have been amassed by the two surveys; around 600 profiles correspond to GSO targets observed by the RASA, while a database containing more than 2400 LEO passes has been accrued using the SuperWASP-N instrument.

The LEO light curve database is currently serving as a key data resource for a PhD project funded by the European Office of Aerospace Research and Development (EOARD), a detachment of the USAF Office of Scientific Research. Focused on the application of machine learning techniques, the project aims to classify LEO targets based upon the signatures in their photometric light curves.

The GSO light curves acquired by the RASA have played an important role in characterising the performance of the COTS instrument. In particular, the rotational properties of the targets observed have been used to inform a consideration of potential observational strategies in the conceptualisation and design of a GSO monitoring system, a project which also serves as motivation for the work presented in Chapter 5.

4.5 Summary

Over the past couple of years, the SuperWASP-N array and the COTS RASA instrument (see Section 2.1.2) have been accruing databases of high cadence photometric

light curves via targeted observations of objects in the LEO and GSO regions, respectively. Photometric measurements encode a wealth of information relating to the physical and attitudinal nature of the target object (see Section 1.2.2). Fine details such as sharp glints or other forms of rapid brightness variability can be revealed in an object's light curve by increasing the observational cadence and thereby boosting the time resolution. In principle, these additional signatures can be matched to more realistic models of the target's geometry and behaviour for the purposes of characterisation or classification.

This chapter has provided an overview of early observations undertaken during the initial prototyping phase for each of the surveys, which took place in late 2018 and early 2019. In Section 4.2, the partially automated procedures that were implemented to select suitable targets, schedule the observations and process the acquired image frames were discussed. The outlined procedures would later inform the strategies and techniques adopted as automated survey operations began in the summer of 2019. Further information regarding the evolution of the data acquisition and processing pipelines developed for the light curve surveys can be found in Chote et al. [2019]. A selection of light curves were presented, extracted from observations undertaken by myself during the prototyping phase, and a qualitative evaluation of the wide variety of photometric signatures uncovered for both LEO (Section 4.3.1) and GSO (Section 4.3.2) targets was conducted.

To date, a dataset in excess of 3000 light curves has been amassed by the two instruments, forming the basis for several ongoing or prospective projects that fall outside the scope of this thesis. The RASA observations have been used to inform the conceptualisation and design of a future GSO monitoring survey, which also serves as motivation for the work presented in Chapter 5.

Chapter 5

Orbital analysis of observational arcs

In this chapter, the issue of orbit determination is addressed in the context of maintaining a catalogue of objects for a future monitoring system. The ability to refine existing orbital information via the injection of new data is a key consideration that will ultimately inform the observational strategies employed by such a system, and indeed the final configuration of the system itself. The orbital accuracies attainable for a variety of observational sequences are explored, and a commentary on the strategies to keep in mind when finalising a design for the system is provided.

A motivation for the work is given in Section 5.1, briefly outlining the importance of orbit determination when performing SSA-driven surveillance activities. Section 5.2 concerns itself with the computation of a preliminary orbit estimate, investigating the effects of observational time intervals and arc sampling on the performance of the Gauss method for preliminary orbit determination (see Appendix A) when applied to a selection of simulated arcs. Section 5.3 outlines the development and testing of a custom orbit refinement algorithm, making use of observational arcs acquired by the RASA and SuperWASP-N instruments as part of the light curve surveys introduced in Chapter 4. Finally, a summary is provided in Section 5.4.

Parts of the work contributed to GEOMON, a Phase 1 Defence and Security Accelerator (DASA) project tasked with the conceptualisation and design of a cost-effective survey instrument, capable of performing deep observations of the GSO region with wide coverage. Deliverables for the GEOMON project were taken on by members of the Warwick Satellites Group, in contract with Harwell Associates Ltd.

Declaration — The following summarises elements of collaborative work that

are included in this chapter. The real (observational) orbital arcs that serve as test cases for the `tlemcee` orbit refiner were extracted from observations conducted by Paul Chote, as part of the light curve surveys presented in Chapter 4. The analysis pipelines described in Chote et al. [2019] were used to extract the orbital arcs and their associated light curves from the available observations. The work is based on the technical report, Blake et al. [2020b], which served as a deliverable for the aforementioned GEOMON DASA project.

5.1 Motivation

Orbit determination is a critical task that feeds directly into a number of vital activities for achieving safe and sustainable levels of SSA:

- establishing a catalogue of regularly tracked objects and updating orbital states when new information becomes available;
- maintaining "custody" of a given spacecraft and recovering it at a future epoch, for example on successive nights of a survey;
- carrying out targeted observations based on catalogued orbital states, as was necessary when conducting the light curve surveys introduced in Chapter 4;
- associating different arcs belonging to the same object and correlating with known objects based on catalogued information, as is necessary when faced with a sample of orbital tracks from an untargeted survey.

As discussed in Section 2.2, the properties of an orbital arc will depend heavily on the observational strategies employed, and care must be taken to optimise the detected arcs for subsequent orbit determination without encroaching on the primary goal(s) of the observations. This can be a difficult balance to strike when, for instance, conducting a survey of faint GSO debris, as evidenced by the short arcs presented in Chapter 3. The desire to cover a large area of sky and probe a more significant proportion of the visible GSO region from a particular ground site can compromise the orbital arc length sampled for a given object, owing to limitations imposed by instrument sensitivity and FOV [see e.g., Schildknecht, 2007; Blake et al., 2021]. Short arcs offer limited information regarding the curvature of an orbit, thus rendering their association a challenging and non-trivial task that has served as motivation for a large body of research [see e.g., the review provided by Pirovano et al., 2020a].

Table 5.1: Catalogue information for objects used as test cases in the form of simulated (SIM) or observed (REAL) orbital arcs in Chapter 5. All objects are designated as payloads (PL). Source abbreviations and radar cross-section (RCS) definitions can be found on the Space-Track website, from which this information was obtained.

Name	NORAD ID	Source	Launch Year	Type	Perigee [km]	Apogee [km]	Inclination [deg]	RCS	Orbit	Arc Type
GORIZONT 30	23108	CIS	1994	PL	35778	35805	14.8	LARGE	GSO	SIM
GALAXY 3	15308	US	1984	PL	35868	35963	15.2	LARGE	GSO	SIM
SKYNET 5C	33055	UK	2008	PL	35779	35808	0.1	LARGE	GSO	SIM
INTELSAT 905	27438	ITSO	2002	PL	35782	35805	1.2	LARGE	GSO	SIM
ASTRA 1KR	29055	SES	2006	PL	35788	35798	0.1	LARGE	GSO	REAL
ASTRA 1L	31306	SES	2007	PL	35779	35808	0.1	LARGE	GSO	REAL
ASTRA 1M	33436	SES	2008	PL	35782	35806	0.0	LARGE	GSO	REAL
ASTRA 1N	37775	SES	2011	PL	35770	35818	0.0	LARGE	GSO	REAL
GLOBALSTAR M051	25853	GLOB	1999	PL	1950	1951	51.98	LARGE	LEO	REAL

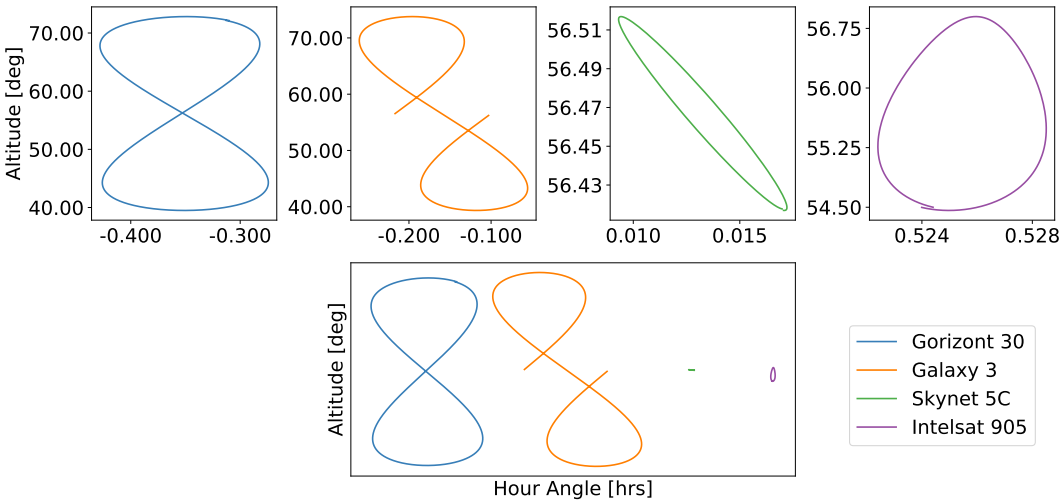

Figure 5.1: Simulated arcs for four GSO satellites: Gorizont 30 (blue), Galaxy 3 (orange), Skynet 5C (green) and Intelsat 905 (purple). The top four panels are scaled appropriately to convey the analemma morphologies mapped out by the satellites over the course of a sidereal day. The bottom panel shows the analemmas collectively to scale in hour angle and altitude space. The simulated arcs serve as test cases for the Gauss IOD method in Section 5.2.

A common approach when surveying the GSO region with multiple available sensors is to operate one or more in the familiar "survey" mode (e.g., the untracked, declination strip scanning method described in Section 2.2.3), and conduct "follow-up" observations with those that remain [see e.g., Abercromby et al., 2009]. The short arcs acquired in survey mode can be used to compute a circular approximation of the orbit, which can subsequently be propagated to reacquire the object with a follow-up instrument in order to elongate the overall arc observed. While a circular assumption may be reasonable for spacecraft in near-GSO orbits, it will be highly inaccurate for other objects of interest, such as those in the GTO/HEO regimes or the eccentric HAMR fragments. Follow-up observations must therefore be carried out in a timely fashion to ensure that the propagation accuracy is sufficient to allow for recovery of the object within the bounds of the follow-up sensor's FOV. An alternative solution which allows for more reliable follow-up of brighter targets is explored in Chapter 6. Here, the performance of a custom orbit determination algorithm is investigated, when applied to orbital arcs extracted from survey frames acquired by the RASA and SuperWASP-N instruments.

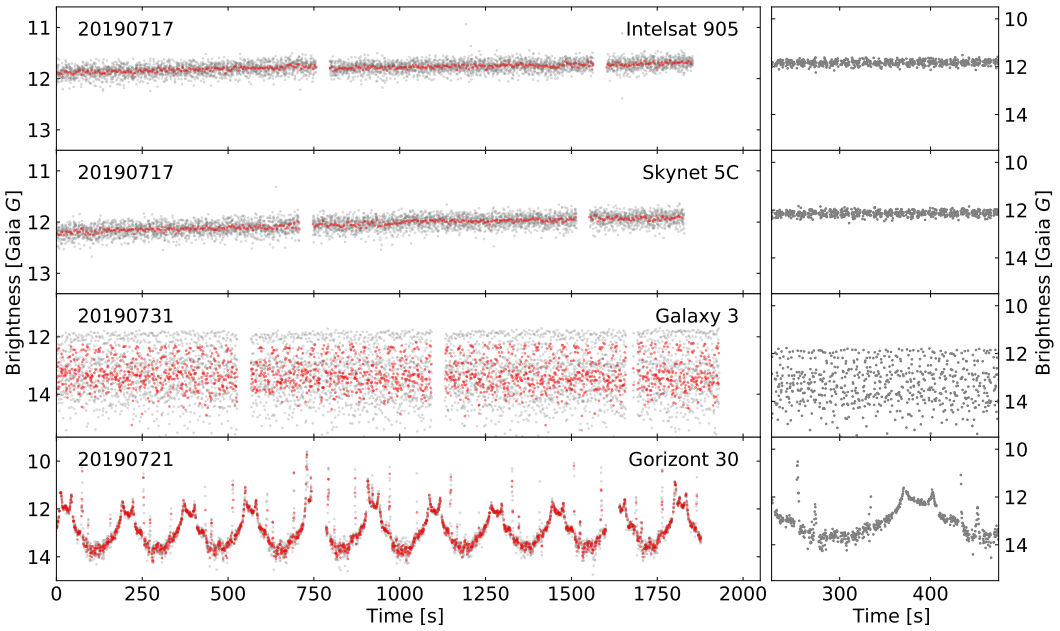

Figure 5.2: Photometric light curves for the four GSO satellites chosen as test cases for the Gauss IOD algorithm, acquired by the RASA instrument. The raw brightness measurements are shown in grey, while the red points are binned to 2 s intervals. The left-hand panels give the full temporal extent of the light curves, while the right-hand panels provide zoomed-in views on a fixed brightness scale to more clearly demonstrate the different levels of variability. Labels in the left-hand panels indicate the night of observation (left) and the satellite name (right).

5.2 Initial orbit determination

The preliminary task undertaken by the algorithm is to carry out an IOD and compute initial estimates of the orbital parameters. Numerous IOD methods have been developed for this purpose: the Laplace, Gooding's and Double r-iteration methods to name three [see e.g., Schaeperkoetter, 2012]. The suitability of an IOD method will vary significantly depending on the quality, quantity and nature of the input data. For the angles-only measurements that are typical of passive optical observations, the most commonly used is the Gauss method of preliminary orbit determination (see Appendix A), or some variant thereof. Consequently, the Gauss method is utilised for this work. The following section explores the effects of observational time intervals and arc sampling on the IOD performance. Estimates for the orbital parameters generated by the IOD are subsequently fed to an orbit refinement algorithm, which is introduced in Section 5.3.

5.2.1 Simulating arcs

Simulated orbital arcs are used to gain insight into the global behaviour of the Gauss method for IOD, generated by propagating TLEs of catalogued objects. The use of simulated arcs has the effect of removing biases from sensor noise, observational duty cycles, weather effects, and so on, which have the potential to skew the performance analytics of interest. The listed factors become more important to consider in Section 5.3, when the IOD solutions for real observational arcs are fed as input to a refinement algorithm.

Orbital arcs are simulated for four GSO satellites, namely Gorizont 30, Galaxy 3, Skynet 5C and Intelsat 905. Catalogue information is provided in Table 5.1 for the chosen satellites, alongside other spacecraft that are referenced throughout this chapter. The analemmas in hour angle and declination space that result from the simulation are shown in Fig. 5.1. The positions are computed with a 2 s cadence for times t in the range $\epsilon - \frac{\tau_{\mathrm{sd}}}{2} < t < \epsilon + \frac{\tau_{\mathrm{sd}}}{2}$, where ϵ is the reference epoch of the relevant TLE and τ_{sd} is one sidereal day ($23^{\mathrm{h}}56^{\mathrm{m}}04^{\mathrm{s}}$). For consistency, the observation site is taken to be La Palma[1] for all four simulated arcs. The TLEs are propagated using the `skyfield` SGP4 routines (see Section 2.1.1).

The four satellites were selected from a pool of objects satisfying the following criteria at the chosen simulation time:

- visible from the vantage point of La Palma, with $|\text{Hour Angle}| < 1$;
- visible above the horizon with Altitude $> 30^\circ$ for the duration of the simulation.

Skynet 5C and Intelsat 905 remain in operation as station-kept GEO communications satellites at the time of writing; the former is a military craft in use by the British Ministry of Defence, while the latter forms part of the commercial Intelsat fleet. On the other hand, Gorizont 30 and Galaxy 3 are decommisioned GSO communications satellites. While the Russian Gorizont payload lingers in a synchronous (yet inclined) orbit, the early member of Intelsat's Galaxy series retired to a supersynchronous graveyard orbit in the mid-1990s, as evidenced by the drifting nature of its analemma in Fig. 5.1. The uncontrolled satellites each map out the figure-of-eight path in hour angle and declination space that is characteristic of inclined GSO orbits, while the operational spacecraft are near-fixed in the sky, as expected. For reference, photometric light curves extracted from RASA observations of the four satellites are provided in Fig. 5.2, acquired as part of the GSO

[1] Observation site, La Palma: longitude 28.7603135° N, latitude 17.8796168° W, elevation 2387 m

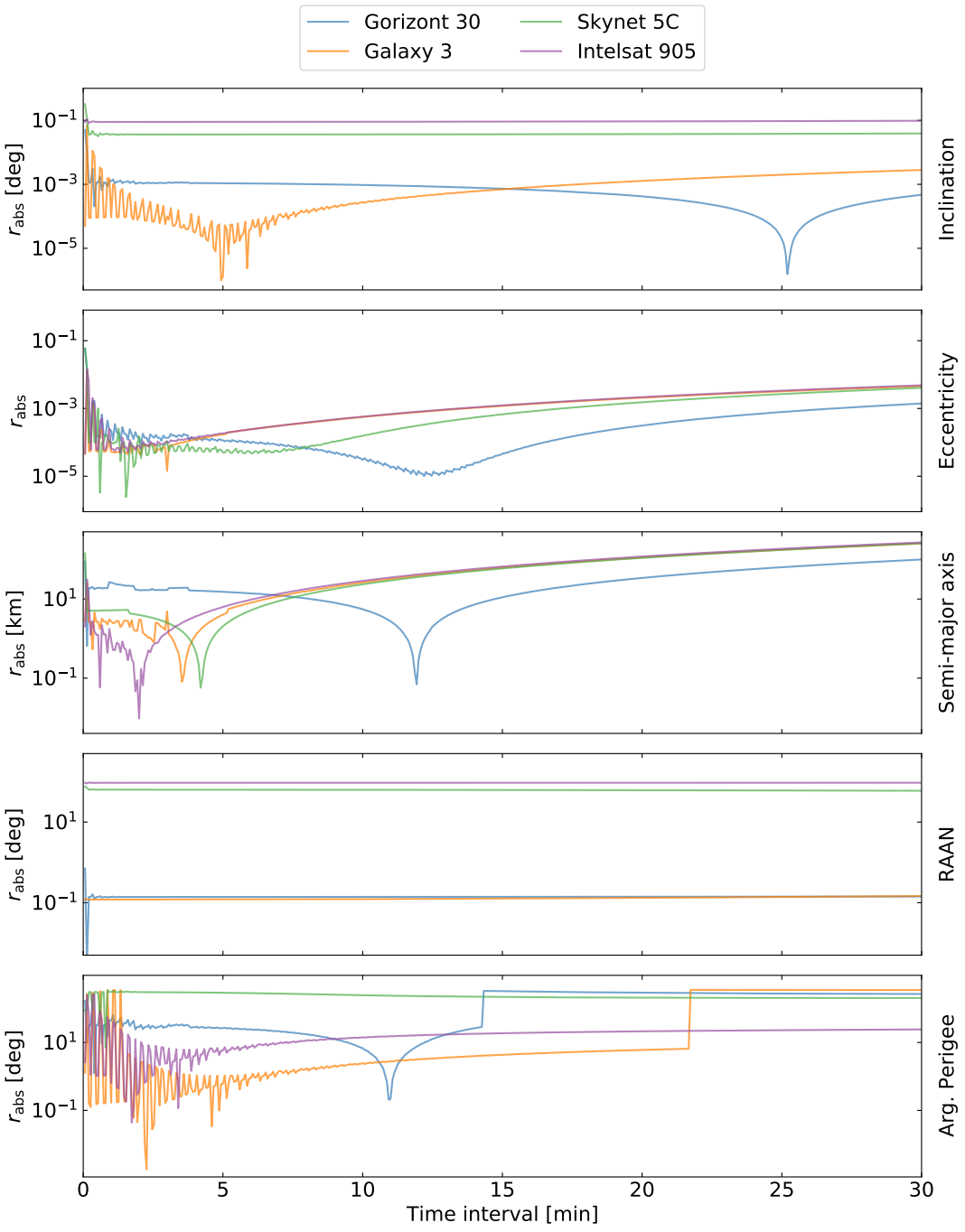

Figure 5.3: Performance of the Gauss IOD algorithm for varying time interval τ between the first and third observations, when applied to the simulated orbital arcs for Gorizont 30 (blue), Galaxy 3 (orange), Skynet 5C (green) and Intelsat 905 (purple). The absolute residual r_{abs} (see text) compares the IOD output to the TLE-informed 'truth' for each of the orbital parameters (labelled right).

survey described in Chapter 4. The controlled nature of the operational spacecraft is clear, with both showing little to no brightness variability across the window of observation. Conversely, the uncontrolled Gorizont and Galaxy satellites exhibit considerable variation of the order of several magnitudes. Rapid glinting can be seen for Galaxy 3, while Gorizont 30 appears to be tumbling at a much slower rate with a period in excess of 100 s. In both cases, periodic peaks in the light curves indicate that reflective components of the spacecraft are repeatedly passing in and out of view along the RASA's line of sight. It is important to note that the effects of viewing geometry have not been accounted for; the gentle changes in average brightness apparent in the top two panels of Fig. 5.2, for instance, arise due to a changing solar phase angle across the roughly 30 minute window of observation.

5.2.2 Effect of time interval on initial orbit

One of the key input variables to consider when assessing the performance of the Gauss algorithm is the time interval $\tau = t_3 – t_1$ between the first and third observations. To test the impact of τ on the quality of the IOD solution, the Gauss algorithm is performed for different observational "trios" extracted from the simulated arcs. For the analyses that follow, the TLE values for the orbital parameters Ψ_{TLE} are taken as the 'truth', and the absolute residual $r_{\mathrm{abs}} = \Psi_{\mathrm{TLE}} - \Psi_{\mathrm{IOD}}$ is used as a proxy for algorithmic performance, where Ψ_{IOD} are the orbital parameter estimates determined by the algorithm. The results of this test are shown in Fig. 5.3. It is apparent from the four test cases alone that the optimal time interval varies case-by-case and there is no 'one size fits all' approach. Time intervals in excess of 30 minutes are found to result in a severe degradation of the solution, a well-known effect of approximations that feed into the algorithm [Pirovano et al., 2020b]. In a like manner, time intervals of around 6 minutes or less lead to unstable solutions, owing to the geometry of the problem.

Very poor estimates of the right ascension of the ascending node (RAAN) are obtained for the station-kept GEO test cases. This is to be expected, as GEO satellites are near-equatorial, with inclinations close to 0°, approaching the regime where the RAAN becomes undefined. In such a configuration, the reference (equatorial) plane and the orbital plane are coplanar, thus the ascending node does not exist. An illustrative diagram depicting the orbital elements referenced throughout this chapter is provided in Appendix B. A similar issue arises from the circular nature of the simulated arcs, for both the GEO and GSO satellites. With close to zero eccentricity, the orbits of such satellites approach a regime where the perigee becomes undefined. The argument of perigee and true anomaly are therefore lack-

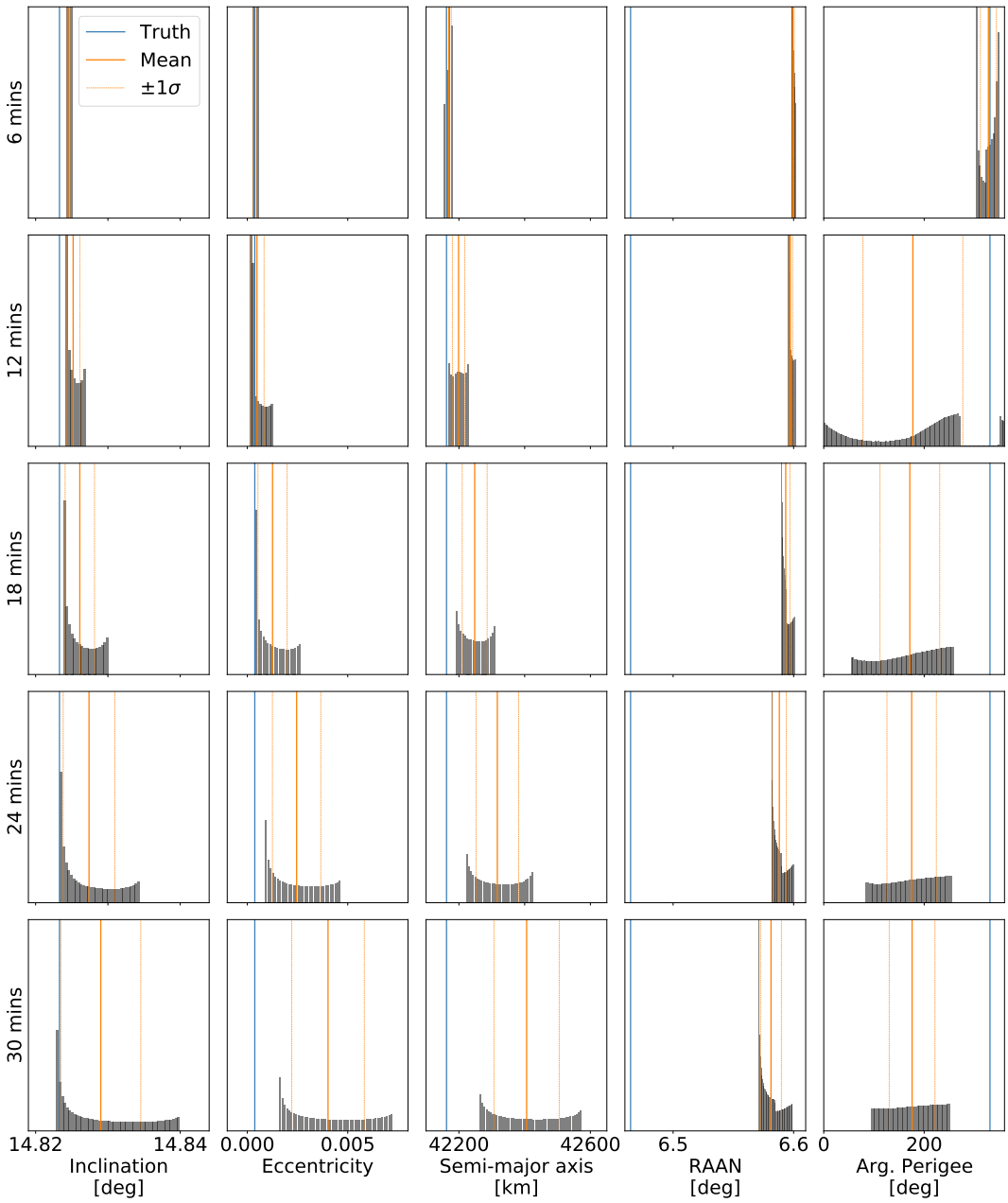

Figure 5.4: Batch performance of the Gauss IOD algorithm when applied to all available observation trios, with time intervals τ of 6, 12, 18, 24 and 30 minutes, respectively by row. The presented example makes use of a 10 hour segment extracted from the simulated Gorizont 30 orbital arc. Orange lines depict the mean and standard deviation for each of the resulting distributions, while the blue lines give the TLE-informed 'truth' for each of the orbital parameters.

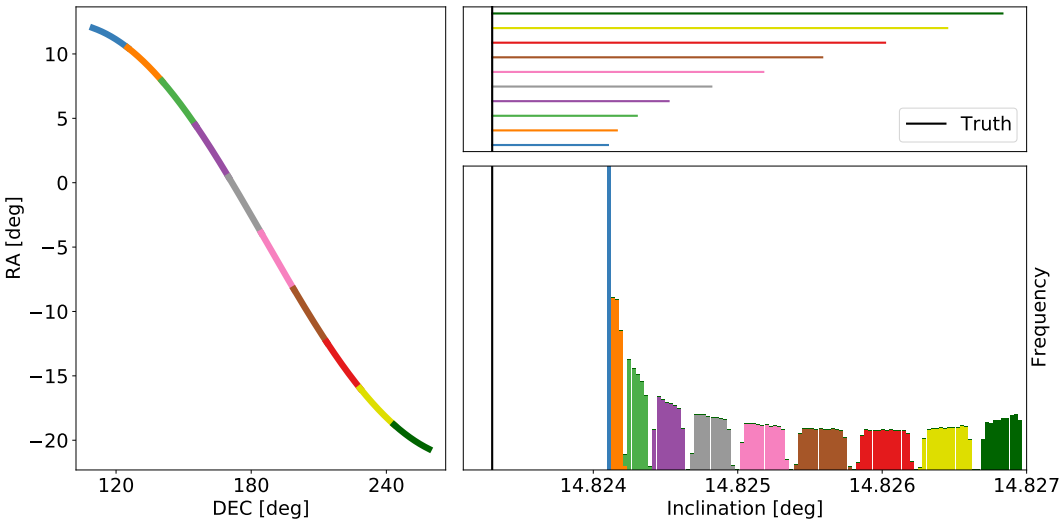

Figure 5.5: Batch performance of the Gauss algorithm for different 1 hour segments of the simulated Gorizont 30 arc (10 hours in total, shown left). The presented example makes use of all available observational trios with a time interval τ of 12 minutes. The inclination distributions obtained are given in the bottom right panel, while the top right panel depicts the median inclination for each segment relative to the 'truth' value from the TLE.

ing for a circular orbit, as both use the perigee as a reference. This explains the poor performance of the Gauss algorithm when estimating the argument of perigee for the four test cases. The Galaxy 3 satellite, with an eccentricity of 0.0012 (an order of magnitude greater than those of its counterparts), is the only object to achieve a reasonable solution for the argument of perigee. In the case of a circular, equatorial orbit (as is approximately true for the GEO test cases) it is necessary to collect the aforementioned angular parameters into a single, alternative element: the true longitude, representing the sum of the RAAN, argument of perigee and true anomaly.

Next, the effect of running the Gauss algorithm on all available observational trios that satisfy a given time interval is examined. The results of this test for the simulated Gorizont 30 arc are displayed in Fig. 5.4. Generally, a wider spread of solutions is observed for higher time intervals. This makes intuitive sense; a higher time interval will sample a larger segment of the orbital arc, making it more sensitive to the large-scale structure of the orbit's analemma and thus more sensitive to discrepancies in the initial orbit determined by the IOD algorithm.

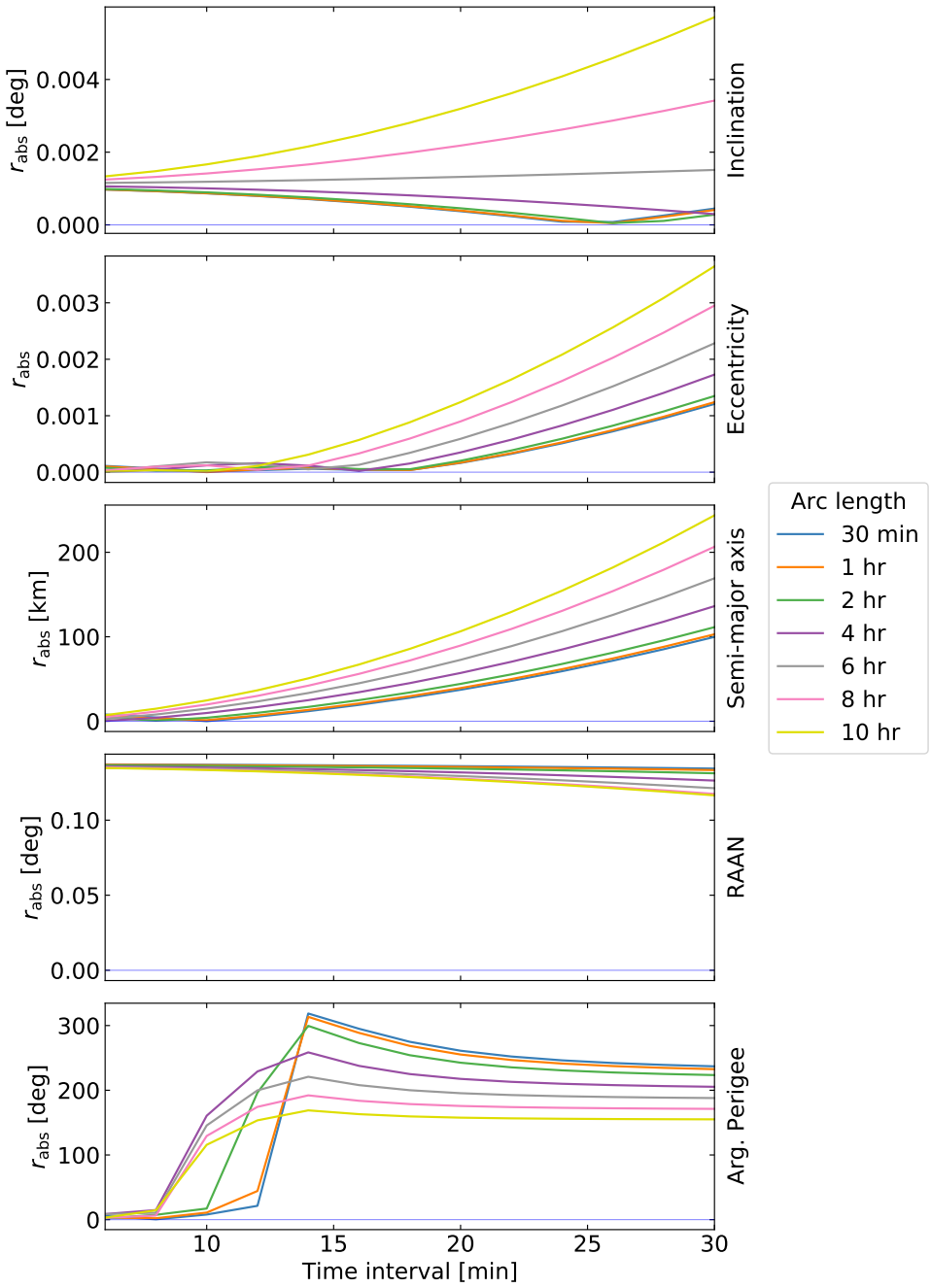

Figure 5.6: Batch performance of the Gauss algorithm for varying time interval and arc length. The presented example makes use of segments extracted from the simulated Gorizont 30 orbital arc. For each time interval, the mean solution obtained when applying the algorithm to all available observation trios within the bounds of the extracted arc segment is taken, as in Fig. 5.4. The absolute residual r_{abs} (see text) compares the IOD output to the TLE-informed 'truth' for each of the orbital parameters (labelled right).

5.2.3 Effect of arc length on initial orbit

To further clarify the above interpretation, the Gauss algorithm is carried out for batches of trios extracted from different segments of the simulated Gorizont 30 arc. The resulting distributions, shown in Fig. 5.5, demonstrate that the differing structure along the orbital arc leads to slight discrepancies in the IOD solutions obtained. It is important to keep in mind that the goal of running the Gauss algorithm is to provide an initial estimate of the orbital parameters, so the minor inconsistencies that result from the arc sampling are unlikely to pose a significant problem when refining the orbit.

Finally, the effect of arc length on the performance of the IOD algorithm is investigated. Batches of trios, grouped by time interval as above, are extracted from arc segments of differing length and fed as input to the Gauss algorithm. Resulting performance metrics for the simulated Gorizont 30 arc are displayed in Fig. 5.6. As shown previously, the performance will also depend on the segment of arc that is sampled. With this in mind, the arc length is found to have very little effect on the quality of the IOD solution. For example, while a 10 hour arc appears to result in a poorer solution for the inclination, the gap in performance is comparable to that induced by sampling the 30 minute segment at a time 10 hours later (as in Fig. 5.5). This is helpful from an observational perspective, as it means that an IOD solution of similar accuracy can be derived from a comparatively short arc.

Although the Gauss method can provide a reasonable estimate of an object's orbit in certain cases, it can fall far short for the circular, equatorial orbits that are commonplace in the GSO regime. The following section moves on to consider a robust approach for refining the initial orbit estimate, with the aim of obtaining sufficient accuracy to recover the object of interest at a future date.

5.3 Refinement of initial orbit

The procedure developed to refine the IOD solution makes use of a Bayesian approach, employing an MCMC technique to draw representative samples from the posterior distribution function,

$$p\left(\theta \mid x, y, \sigma\right) \propto p\left(\theta\right) p\left(y \mid x, \sigma, \theta\right), \tag{5.1}$$

where $p\left(\theta\right)$ encodes the relevant prior information and $p\left(y \mid x, \sigma, \theta\right)$ is the likelihood function. The technique was adopted primarily for its reliability and ease of implementation relative to alternative multi-parameter optimisation methods, though

the algorithm has also proved efficient when faced with fairly small parameter space dimensions (7 or less here). Past studies have utilised a similar approach for refining orbits derived from radar [see e.g., Palmer et al., 2017] and optical telescope [see e.g., Lederer et al., 2019] data; most notably in the latter case, the NASA ES-MCAT processing pipeline incorporates a TLE-driven MCMC algorithm for the refinement of an initial circular estimate of the orbit [Hickson, 2019].

Equation 5.1 retains the notation defined in Section 2.5.2, where a more in-depth discussion of MCMC algorithms is provided, though the dataset Δ is expressed in terms of the independent and dependent variables, respectively x and y, alongside the associated uncertainty σ. In the analyses that follow, the model parameters θ are: the orbital inclination, eccentricity, RAAN and argument of perigee, all as defined in Appendix B; the mean anomaly, which measures the hypothetical perigee–object angle along a circular approximation of the orbit, and can be converted to the familiar true anomaly; the mean motion, given by the reciprocal of the orbital period, and its first derivative (the ballistic coefficient). The MCMC is implemented as part of the software package `tlemcee`[2], developed to combine the IOD and refinement routines used throughout this work. The package makes use of `emcee` [Foreman-Mackey et al., 2013], a Python-based ensemble sampler used extensively within the astronomical community.

For initial testing, the likelihood computation is treated separately for right ascension α and declination δ, such that the independent variable x is time t, while the angular measurements form two distinct dependent variables y. Future development of the code will aim to combine the two to form a likelihood function in terms of the separation in spherical polar coordinates. The uncertainties σ in the angles-only measurements also feed directly into the likelihood calculation. By way of an example, the natural logarithm of the likelihood function for the right ascension can be expressed as

$$\ln p\left(\alpha \mid t, \sigma, \theta\right) = -\frac{1}{2} \sum_{n} \left[\frac{\left(\alpha_n - \text{model}\left(t_n, \theta\right)\right)^2}{\sigma_n^2} + \ln\left(2\pi\sigma_n^2\right) \right]. \tag{5.2}$$

Computationally, logarithmic probabilities are more manageable than the probabilities themselves, as the latter can be very large for substantial datasets. The likelihoods evaluated for both right ascension and declination are summed to obtain an overall estimate.

The prior function, as its name suggests, encodes any prior knowledge held regarding the model parameters that can be used to inform the sampler. Uniform

[2] https://github.com/jblake95/tlemcee (accessed March 2021)

priors are used for testing of the `tlemcee` package, enabling the MCMC to draw samples within a set range of values for each parameter, with a uniform or flat probability. For the inclination, mean motion and ballistic coefficient, the prior ranges are informed using distributions extracted from the GSO sub-catalogue available from the Space-Track website. As the following analyses focus on a constellation of station-kept GEO satellites, a narrower range for the eccentricity prior than that indicated by the GSO sub-catalogue is used, owing to its inclusion of uncontrolled GSO satellites, whose orbits may have evolved to become more eccentric. Finally, for the RAAN, argument of perigee and mean anomaly, the MCMC is allowed to explore the full parameter space, in light of the fact that these parameters are not constrained by the orbital regime in question. Further details regarding the prior information used in the analyses to follow are provided in Appendix C.

The model that is fed to each of the likelihood functions carries out the following two steps:

1. A rolling adjustable TLE is modified, setting the relevant elements to their value at the current iteration of the MCMC.

2. The Python `skyfield` routines [Rhodes, 2019] are used to propagate the modified TLE to the timestamps of the input dataset. These employ the SP models that are commonly used to propagate orbital states for low (SGP) and high (SDP) altitude objects (see Section 1.2.2). The resulting right ascensions and declinations are then fed to the likelihood function to progress the MCMC.

Stage 2 of the model initially proved to be markedly more expensive in terms of computational runtime. The issue with execution time was addressed by pre-computing the expensive attributes of the input time array, avoiding repetitive computation that would otherwise take place every time the model function is called. On average, the pre-computation led to a reduction in the execution time by a factor of around 30. Future development of the package will look to further reduce the computational expense by improving the efficiency of the TLE modification undertaken in stage 1 of the model.

To test the performance of the `tlemcee` orbit refiner, a rolling catalogue scenario is considered: angles-only measurements are obtained for a previously catalogued object, and the aim is to combine the new dataset with archival information to update the orbital state. It should then be possible to propagate the updated state and recover the object at a future epoch of observation. Section 5.3.1 outlines the observational dataset used to test the refiner, namely three consecutive nights of RASA observations imaging the Astra 19.2° E constellation, a group of four station-

Table 5.2: Summary of the observational dataset acquired with the RASA pointing at the station-kept GEO Astra 19.2° E constellation. Orbital arcs extracted from the observations are used as a test case for the `tlemcee` orbit refiner. The dataset comprises a series of 10 s exposures, separated by gaps resulting from the readout procedure, slewing and other hardware- or weather-related interruptions.

Night	Arc length [mins]	Measurements
20180618	241	237
20180619	285	657
20180620	155	1009
	681	1903

kept GEO satellites. To best simulate the rolling catalogue scenario and assess the performance of `tlemcee` when fitting real observational arcs, the refinement procedure is carried out using the first two nights of available data (20180618, 20180619), and propagation to the third night (20180620) is employed as a proxy for algorithmic success. For the refinement itself, two separate approaches are examined:

1. An IOD is carried out using the Gauss method, averaging over all observational trios with time intervals between 6 and 10 minutes. The results from Fig. 5.3 are used to inform this choice, with the relatively short arcs in this range performing well for the station-kept GEO test cases. The IOD provides reasonable estimates for the inclination, eccentricity and mean motion. As discussed in Section 5.2.2, the RAAN, argument of perigee and mean anomaly are poorly determined owing to the circular, equatorial nature of the orbits in question. This is accounted for by performing a preliminary run of the MCMC, fixing the well determined parameters to their IOD values for the duration, and allowing the three poorly determined angular parameters to vary. The initial values for the variable parameters are set to 180° and allowed to explore the full parameter space [0°, 360°]. Finally, a second run of the `tlemcee` refiner is performed, this time allowing all the parameters to vary, setting initial values to those determined by the IOD, or the first run of the MCMC, as appropriate.

2. The catalogued TLE with a reference epoch closest to the start time of the first night of observations is pulled from Space-Track, and its elements are used directly as seed values for the MCMC.

The first approach, hereafter 'IOD input', represents the worst-case scenario

where the `tlemcee` orbit refiner effectively starts from scratch to obtain an estimate of the orbital parameters. The second approach, hereafter 'TLE input', offers a more realistic demonstration of the rolling catalogue capability, where the orbital solution merely requires slight adjustment each time a new night of data becomes available.

5.3.1 Observational dataset

The analyses that follow utilise three nights of RASA observations capturing the station-kept GEO 19.2° E Astra constellation. A logistical summary of the dataset is provided in Table 5.2. The four satellites making up the constellation (Astra 1KR, 1L, 1M and 1N) are closely separated in space at any given time. The paths mapped out by the satellites in right ascension and declination space over the course of a sidereal day intersect one another, as evidenced in Fig. 5.7. At these points of intersection, non-resolved images will show only three members of the constellation, where two have morphed to become one. The chosen dataset thus represents a challenging test case for orbit determination and custodial algorithms. Catalogue information for the four Astra satellites is provided in Table 5.1 at the beginning of the chapter.

Adapted versions of the analysis pipelines described in Chote et al. [2019] were used to extract the necessary positional information from the raw RASA frames, comprising the following steps:

1. The standard reduction procedures involving bias and flat field corrections are carried out as before. Astrometric and photometric calibrations are performed using an iterative algorithm that is discussed further in Chapter 6.

2. Difference images are created for each frame against the previous or next frame to subtract the background stars.

3. A source extraction is performed on each frame. Sources are iteratively correlated to the previous detection based on their proximity to a predicted position, found by sequentially updating a linear trajectory in hour angle and declination space.

The extracted arcs are correlated against the expected positions for the four Astra satellites, using the archival TLEs with reference epochs closest to the observational timestamps in question. The results of the correlation procedure are shown in Fig. 5.7.

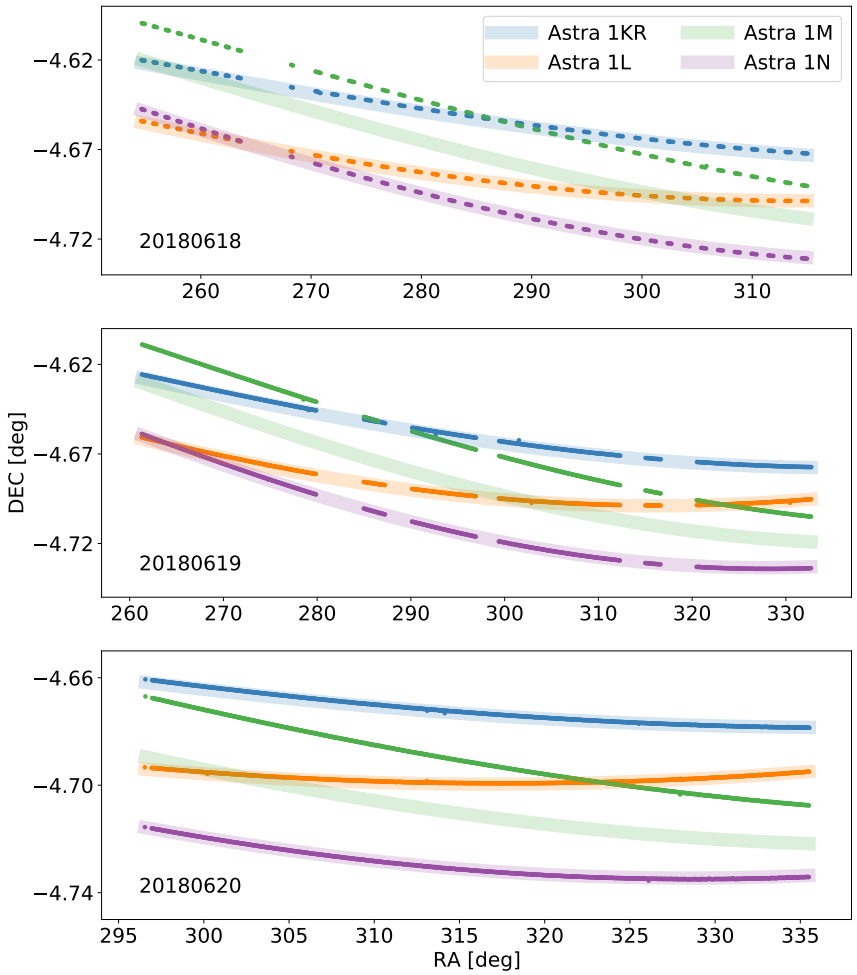

Figure 5.7: Observed orbital arcs for the 19.2° E Astra constellation, comprising Astra 1KR (blue), Astra 1L (orange), Astra 1M (green) and Astra 1N (purple). The arcs were extracted from three nights of observations undertaken by the RASA instrument, dates for which are labelled in the bottom left of each panel. The positional measurements (points) in right ascension and declination space have been correlated against the TLEs (bands) with the most proximate reference epoch to the given observational timestamp. Potential explanations for the poor agreement between the predicted Astra 1M positions and their observational counterparts are discussed in Section 5.3.3.

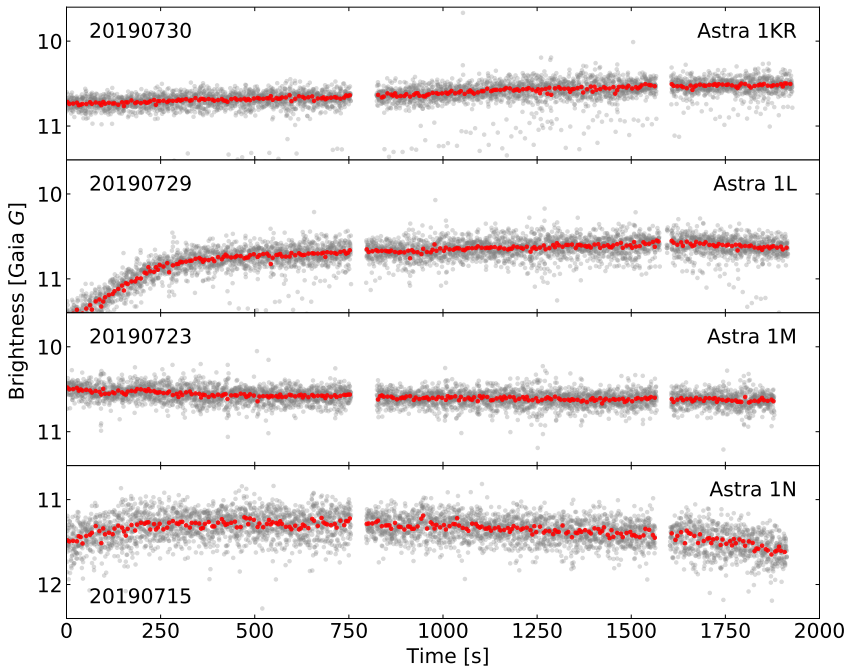

Figure 5.8: Photometric light curves for the four station-kept GEO satellites comprising the Astra 19.2° E constellation, acquired by the RASA instrument as part of the GSO light curve survey described in Chapter 4. The raw brightness measurements are shown in grey, while the red points are binned to 2 s intervals. Labels in each panel indicate the night of observation (left) and the corresponding satellite name (right).

For reference, photometric light curves for the relevant Astra satellites are provided in Fig. 5.8. As for their simulated counterparts, the controlled nature of the station-kept Astra satellites is clear, with very little brightness variation exhibited throughout the window of observation. Note that the effects of viewing geometry have not been accounted for. While some of the gentle variations in brightness may be attributed to a changing solar phase angle over the course of the observations, more significant features (e.g., the steep rise in brightness during the first few hundred seconds of the light curve extracted for Astra 1L) are instead the result of aperture misalignment, an issue to be addressed in future development of the pipelines.

5.3.2 Orbit fitting with `tlemcee`

In Fig. 5.9, an example of the `tlemcee` orbit refiner in action using the 'IOD input' approach is provided, fitting a pair of 4 hour orbital arcs extracted from the first

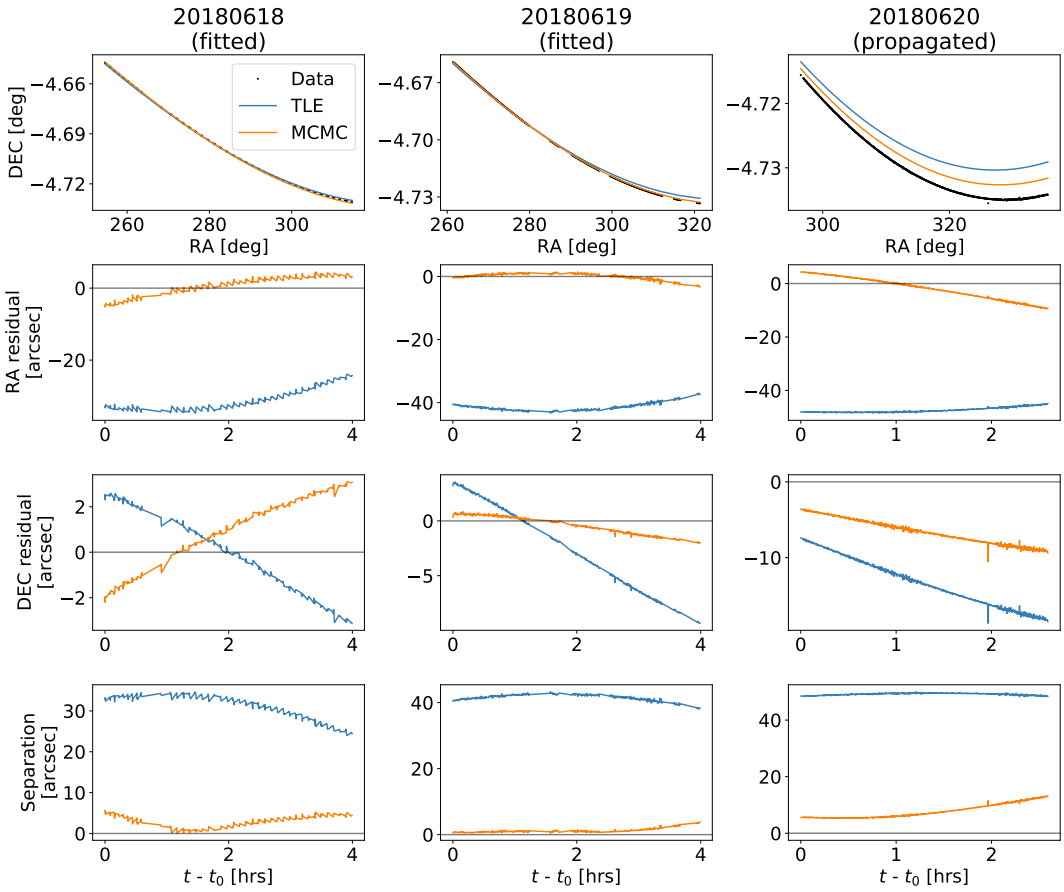

Figure 5.9: Performance of the `tlemcee` orbit refiner when fitting a pair of 4 hour orbital arcs for Astra 1N, extracted from two consecutive nights of RASA observations (20180618, 20180619). The first two columns show the fit quality for the two input arcs, while the third column shows the fitted model propagated to the third night of observation (20180620). The refined orbit (orange) determined by `tlemcee` shows roughly a factor of four improvement over the propagated TLE solution (blue).

two nights of RASA observations available for Astra 1N. The arcs are first pruned of significant anomalies, most likely resulting from blending with nearby sources (e.g., a star, or another member of the constellation), though otherwise all available measurements are utilised. For the fitted nights, the maximal angular separation between the model and observed positions is around $5''$, significantly lower than those predicted by the catalogued TLE. When propagated to the third night, the fit degrades by around 5–$10''$ in separation, roughly consistent with the degradation exhibited by the TLE solution. For reference, the plate scale of the RASA is approximately $1.6''\,\text{pixel}^{-1}$, so a degradation of roughly 5 pixels is observed for the above case. A more in-depth discussion of the Astra 1N case study is provided in Appendix C, alongside a selection of diagnostic plots showing the inner workings of the `tlemcee` orbit refiner.

5.3.3 Effect of arc length on fitted orbit

It is important to consider the effects that observational strategies can have on the quality of the fitted orbit. One factor that is likely to have an impact is the length of the observed arc that is fed as input to the MCMC. In Fig. 5.10, the performance of `tlemcee` is illustrated for orbital arcs of varying length, extracted from the first two nights of RASA observations available for the Astra 19.2° E constellation, as for the example above.

As is to be expected, the 'TLE input' cases generally perform better, owing to the vastly superior initial estimates supplied by the TLEs. A more eclectic response is observed for the 'IOD input' runs, typically exhibiting higher levels of scatter. This could be due to degeneracies in the orbital solutions. The IOD-informed runs facilitate a more extensive exploration of the parameter space, in particular for the RAAN, argument of perigee and mean anomaly. It is therefore more likely that the MCMC will encounter 'distractor' solutions residing in localised regions of high likelihood, that fit the observations relatively well but propagate poorly. A similar issue has been found when testing `tlemcee` for LEO arcs, discussed further in Section 5.3.5. With a couple of exceptions, the performance of `tlemcee` appears to improve as longer arcs are fed as input to the orbit refiner. This makes intuitive sense, as the availability of more data should help to more effectively constrain the orbital solution. The refinement procedure results in a notably poor fit for the Astra 1M arcs. This may be due to additional forces at play (e.g., a manoeuvre of the craft via propulsion) that remain unmodelled as part of the `skyfield` SDP routines employed by `tlemcee` [see e.g., Vallado and Cefola, 2012]. The comparatively poor performance of the TLE for the Astra 1M case adds weight to this theory. Limiting

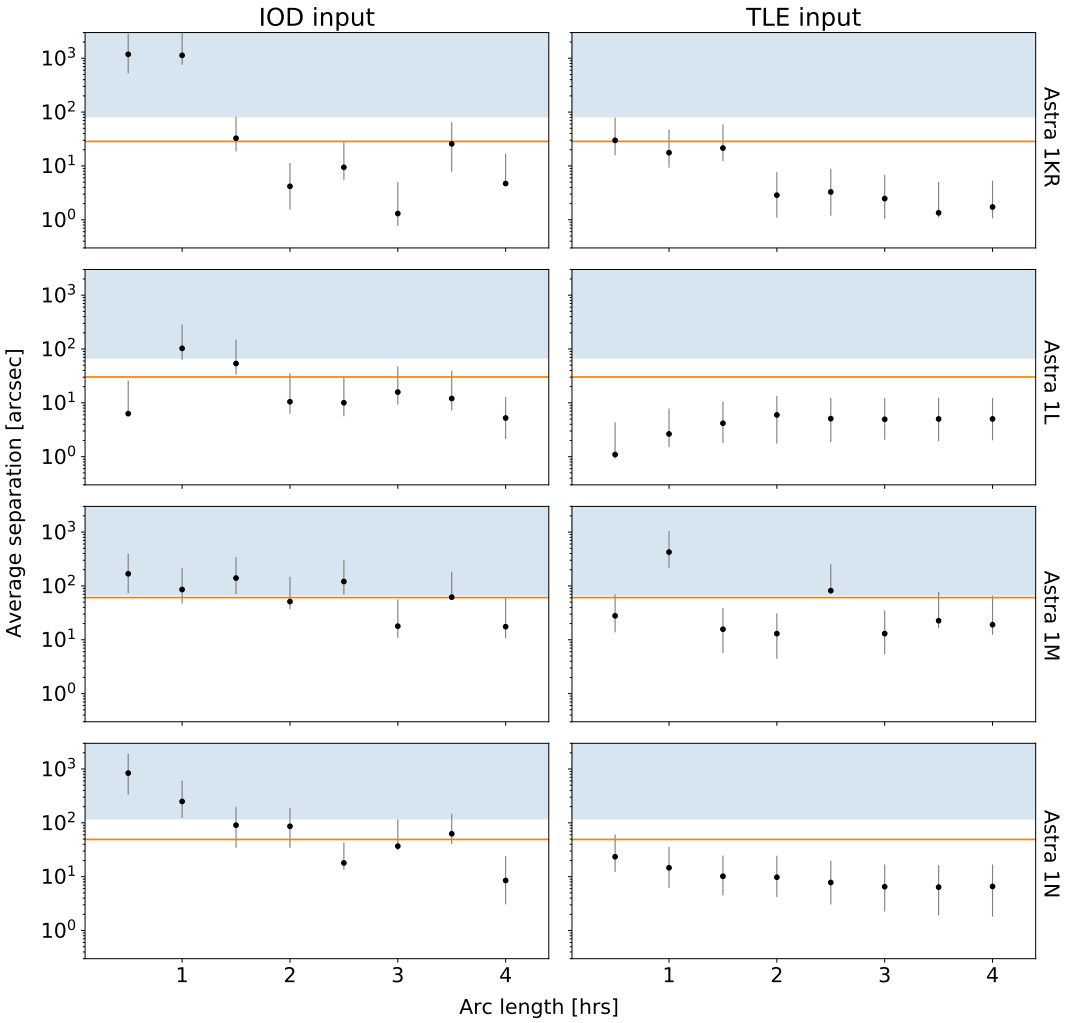

Figure 5.10: Performance of the `tlemcee` orbit refiner for orbital arcs of varying length, extracted from the first two nights of RASA observations (20180618, 20180619) available for the Astra 19.2° E constellation. The fits make use of all data comprising the observed arcs for each night that survive pruning (removal of suspected blends, and so on). The left column shows results for the 'IOD input' cases, while those in the right column stem from the 'TLE input' approach (see text). Average separations are used as a proxy for the fit quality when propagated to the third night of observation (20180620). The orange lines mark the analogous average separations achieved by propagating catalogued TLEs pulled from the Space-Track website, with reference epochs closest to the start of the first night of observations in each case. The blue shaded regions show the average separation between each satellite and its closest neighbour in the constellation, as informed by the third night of observations.

attention to the other three satellites, arc lengths within the range 2–4 hours are typically found to result in a reliable fit, with solutions sufficiently accurate to discern the target from its nearest neighbour on the following night of observation. Shorter arc lengths offer less predictable performance.

5.3.4 Effect of cadence on fitted orbit

A second feature of the observational strategy that could affect the performance of the `tlemcee` orbit refiner is the cadence of the observations. Here, the term "cadence" refers to the time between collective groups of exposures. In the following analyses, for instance, groups of exposures are considered that span a window of 1 minute, with each group separated by the given cadence. In other words, the RASA observes the target for 1 minute, typically comprising four or five 10 s exposures given its fast readout time, then ceases observations for the specified cadence, before carrying out another 1 minute batch of exposures. Naturally, it is impossible to precisely replicate this strategy with the real observational Astra arcs, given their susceptibility to data gaps induced by source blending and hardware-related interferences. Consequently, a 'minimum cadence' is applied, whereby the batches of exposures are separated by at least the cadence.

The results of testing `tlemcee` for different cadences are shown in Fig. 5.11. As before, the performance is generally better for the 'TLE input' approach, with the 'IOD input' cases exhibiting a higher degree of scatter. For the majority of cases, a degradation in fit quality is observed towards sparser arcs (longer cadence), as would intuitively be expected. That said, in certain cases a reasonable performance is observed all the way up to a cadence of 180 minutes. For the most part, cadences within the range 0–100 minutes exhibit the most reliable performance. Indeed, for TLE-informed fits, the arc cadence appears to have very little effect even beyond that range. This is useful from an observational perspective, as longer cadences allow for a higher number of targets to be observed within a given time frame; the monitoring instrument would be free to slew from one target to the next, filling the cadence with successive observation batches for multiple objects. The fact that the observational cadence appears to have a very limited impact on the quality of the fitted orbital solution for 'TLE input' cases is promising from the perspective of maintaining a rolling catalogue with such an instrument. From testing of the `tlemcee` orbit refiner, it seems that observing long arcs with long cadences strikes an optimal balance between the efficiency of the observational strategy and the performance of the initial orbit refinement.

The panels in Fig. 5.12 show how arc length and cadence maps to percentage

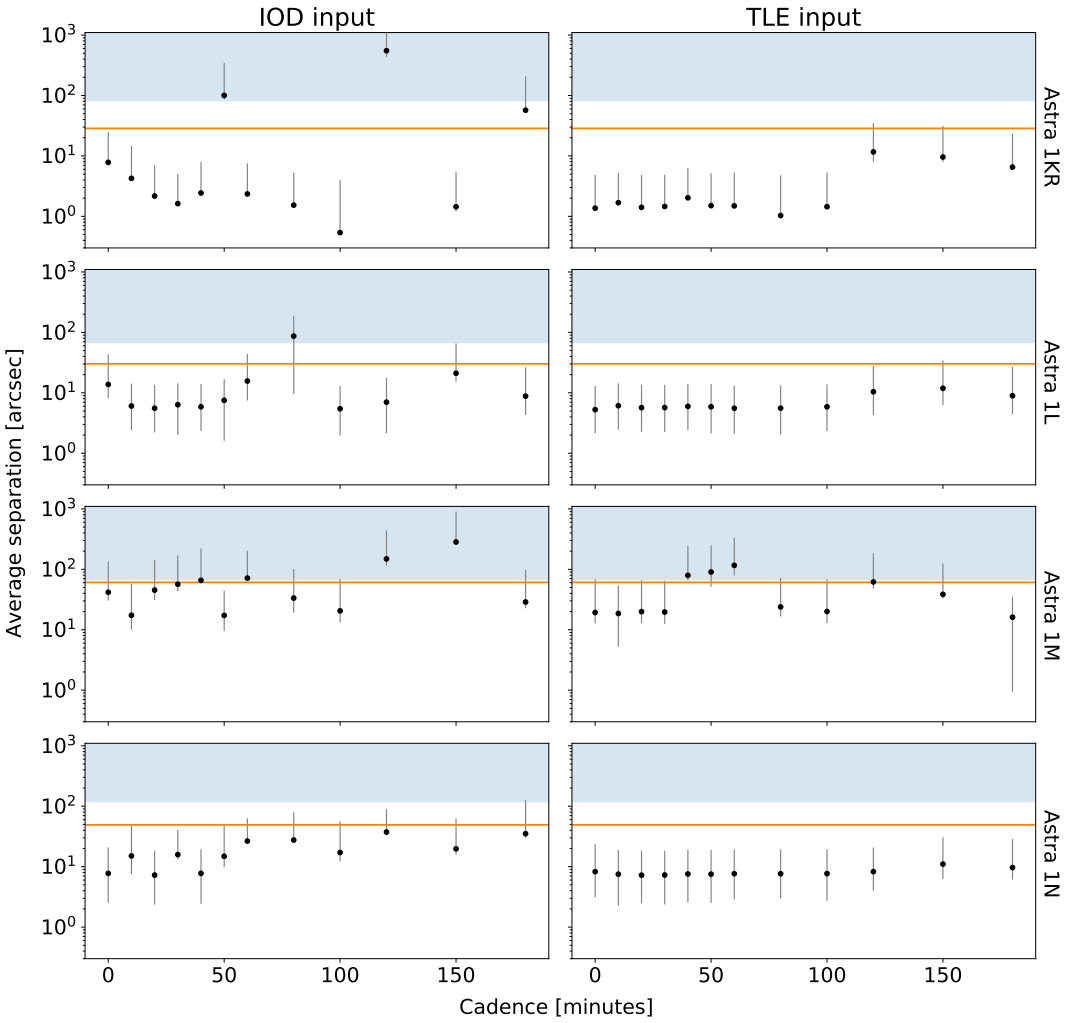

Figure 5.11: Performance of the `tlemcee` orbit refiner for arcs of varying cadence, with fixed lengths of 4 hours, extracted from the first two nights of RASA observations (20180618, 20180619) available for the Astra 19.2° E constellation. The fits make use of all data comprising the observed arcs for each night that survive pruning (removal of suspected blends, and so on) and that satisfy the chosen cadence. The left column shows results for the 'IOD input' cases, while those in the right column stem from the 'TLE input' approach (see text). Average separations are used as a proxy for fit quality when propagated to the third night of observation (20180620). The orange lines mark the analogous average separations achieved by propagating catalogued TLEs pulled from the Space-Track website, with reference epochs closest to the start of the first night of observations in each case. The blue shaded regions show the average separation between each satellite and its closest neighbour in the constellation, as informed by the third night of observations.

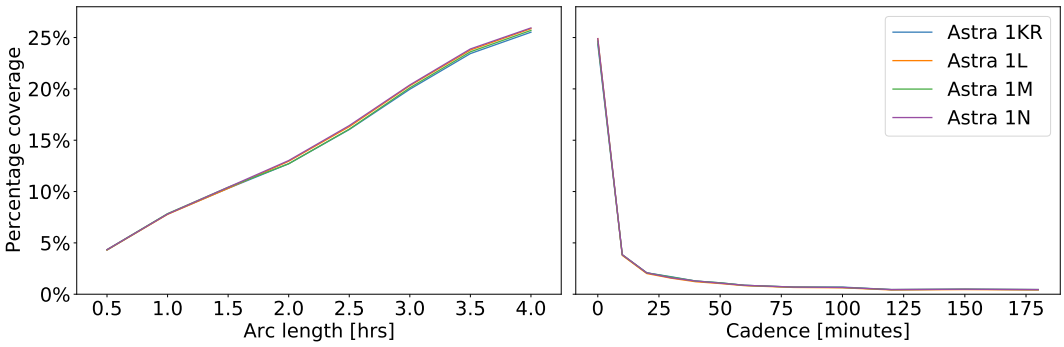

Figure 5.12: Percentage coverage as a function of arc length (left) and cadence (right) for the Astra 19.2° E dataset acquired by the RASA. All exposures are assumed to be 10 s in duration.

Table 5.3: Summary of the observational dataset acquired with the SuperWASP-N telescope pointing at Globalstar M051, a decommissioned LEO satellite. Orbital arcs extracted from the observations are used as a test case for the `tlemcee` orbit refiner.

Night	Arc length [mins]	Measurements
20190806	3.5	5
20190807	4.8	6
20190808	4.8	6
20190809	2.9	4
	16.0	21

coverage for the Astra 19.2° E dataset. This metric refers to the proportion of time spent observing relative to the overall time available, amounting to two arcs spanning 4 hours each. Slight discrepancies are observed between the four satellites owing to object-specific factors such as blending, and so on, which can render individual frames unusable.

5.3.5 Extension to the LEO regime

The work presented in this chapter thus far has focused on orbital arcs for objects in the GSO region, owing to the conceptual goals of the GEOMON project that served as the primary motivation for the development of `tlemcee`. That said, the rolling TLE model that is adjusted at each step of the MCMC is sufficiently general to handle orbital arcs from any Earth-centred regime. By way of an example, a dataset

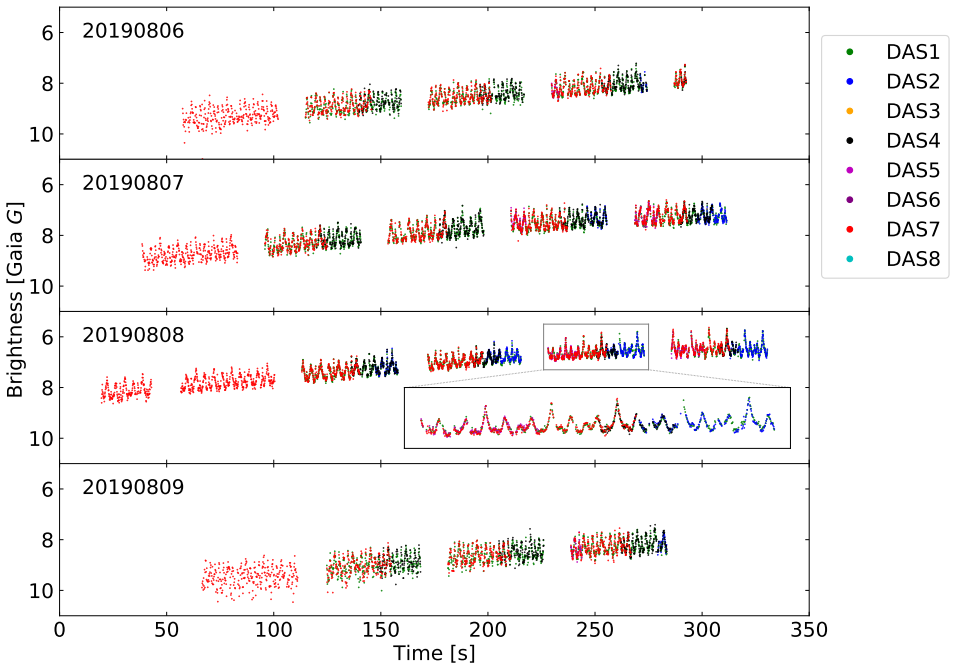

Figure 5.13: Photometric light curves for Globalstar M051, acquired by the SuperWASP-N array. Brightness measurements are colour-coded by camera according to the right-hand legend. Inset, a zoomed-in view of a single exposure is provided, highlighting the glinting nature of the spacecraft. Gaps in the data arise from the dead time between exposures, during which the cameras are read out and the telescope slews to the next appropriate field. Further detail regarding the extraction of light curves from the survey frames can be found in Chapter 4. Labels in each panel indicate the night of observation (top left).

comprising four separate passes observed for Globalstar M051, a decommissioned LEO satellite, is considered. The dataset was acquired using the SuperWASP-N array as part of the LEO light curve survey introduced in Chapter 4. Logistical details for the four passes, which took place on consecutive nights, are given in Table 5.3.

For reference, photometric light curves for Globalstar M051 are provided in Fig. 5.13, extracted from the corresponding SuperWASP-N survey frames. The periodic glinting exhibited by the satellite is clear, suggesting that the craft is tumbling and reflective components upon its exterior are repeatedly passing in and out of the telescope's line of sight. Note that the light curves and corresponding orbital arcs for the LEO satellite are temporally much shorter than those of its GSO counterparts. During a pass, the average LEO satellite will take roughly 5–10 minutes to rise above the horizon, traverse a path across an observer's sky, and set once more

below the horizon. As a result, the time available to observe an object in the LEO region is severely limited in comparison to that afforded by the near-fixed nature of GSO objects relative to the field of a ground-based sensor. Observations of LEO targets are further constrained by the Earth's shadow cone, the projection of which limits optical monitoring of the lower altitude bands to the twilight hours after sunset and before sunrise. When combined with the other observational constraints listed previously in Section 2.2.2, alongside the instrumental dead time necessitated by the camera readout and slewing of the telescope, sampling of LEO orbital arcs with ground-based optical systems can be challengingly sparse. In terms of temporal coverage, the Globalstar M051 arcs used as a test case here are fairly typical of those accrued during the LEO light curve survey described in Chapter 4.

In order to test the performance of `tlemcee` when fitting the Globalstar M051 arcs, a variation of the 'IOD input' approach outlined previously is carried out, using the middle two sets of available observations (20190807, 20190808) as the input dataset. As for the GSO test cases, preliminary estimates for the model parameters are obtained by carrying out an IOD using the Gauss algorithm. For the LEO case, an observational trio is extracted from the third night (20190808), with a time interval τ spanning close to the full extent of the selected pass. Owing to the inclined nature of the Globalstar's orbit ($i \sim 52^{\circ}$), the IOD is able to determine a reasonable estimate for the RAAN, one of the problematic angular parameters for the equatorial GSO arcs. This proves sufficient to render the preliminary 'angles-only' run of the MCMC unnecessary, in spite of the poor estimates that are obtained for the argument of perigee and mean anomaly as a result of the circular nature of the prospective orbit. Initial values for the `tlemcee` refiner can therefore all be derived from the IOD solution. For the MCMC, the following limits on the uniform priors are imposed: the RAAN, argument of perigee and mean anomaly are allowed to explore the full parameter space, as before; the inclination is given equivalent freedom, reflecting the wide variety of inclination bands populated by spacecraft in the LEO region (recall Fig. 2.1, Section 2.1.1); the limits for eccentricity and mean motion are set to representative values for the LEO region, respectively $[0.00, 0.25]$ and $[8.0, 15.0]$; the ballistic coefficient limits are expanded generously in comparison to those applied in the GSO test cases, owing to the more significant effects of atmospheric drag at LEO altitudes. Otherwise, the procedure is largely identical to that employed for the Astra 1N case study, a detailed description of which can be found in Appendix C.

The performance of the `tlemcee` refinement algorithm when fitting the Globalstar M051 dataset is depicted in Fig. 5.14. The resulting model is propagated to

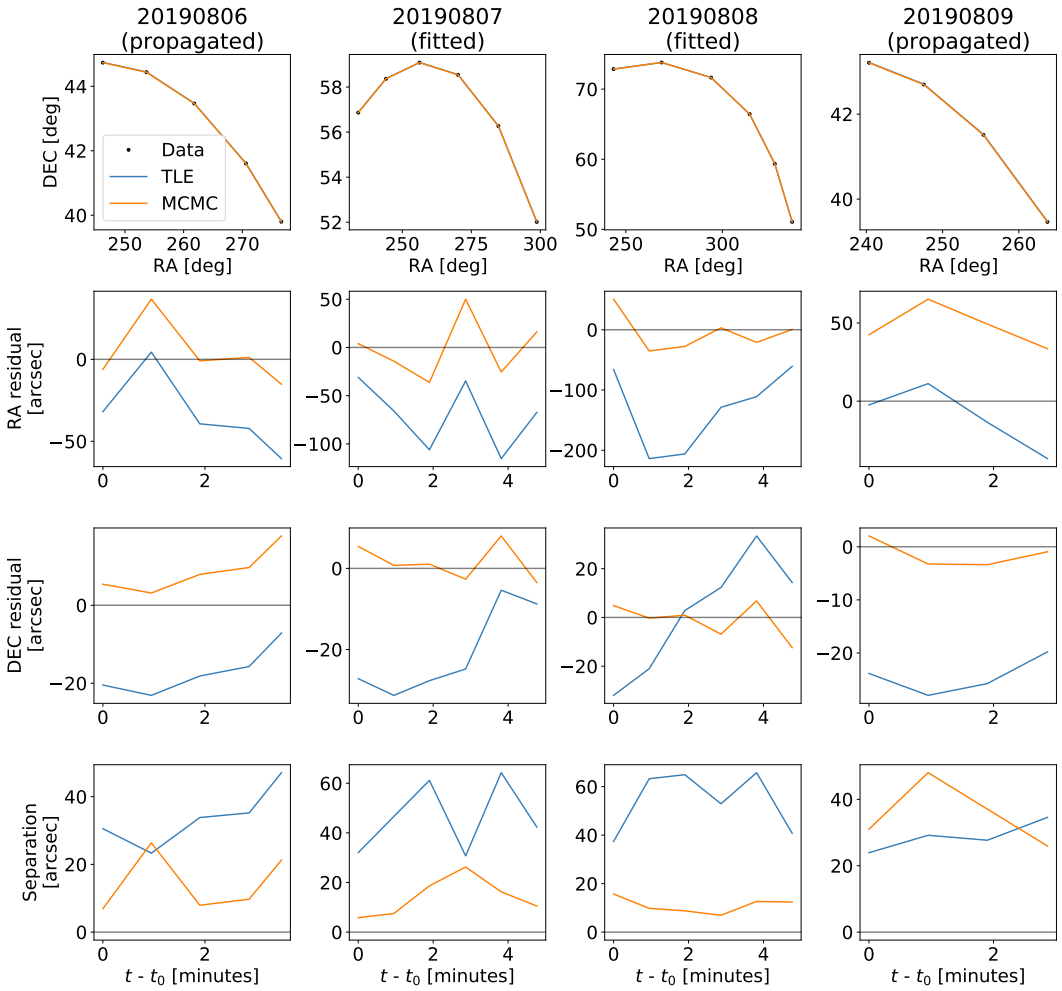

Figure 5.14: Performance of the `tlemcee` orbit refiner when fitting a pair of roughly 5 minute orbital arcs for Globalstar M051, extracted from two consecutive nights of SuperWASP-N observations (20190807, 20190808). The middle two columns show the fit quality for the two input arcs, while the outer two columns show the fitted model propagated to the previous (20190806) and following (20190809) nights, respectively. The refined orbit determined by `tlemcee` is shown in orange, while the propagated TLE solution is given in blue.

the observational timestamps of the other two arcs acquired one night either side of those fitted by the refiner. The predicted positions in right ascension and declination space are compared against those observed, alongside analogous positions predicted by the Space-Track TLE with reference epoch closest to the start of the first night of observations. In general, discrepancies between the observed and predicted positions are larger in scale for the Globalstar fit compared to those observed for the GSO test cases. There are a number of explanations for this: most notably, the camera pixel scale for SuperWASP-N is much larger than that of the RASA camera, so the inherent uncertainties in the extracted positional measurements are greater for the LEO example; moreover, the unpredictable and insufficiently modelled nature of atmospheric drag can reduce performance of TLE propagators when considering objects in the LEO regime. In spite of this, the `tlemcee` refiner improves upon the TLE prediction for the fitted arcs, and propagates to the other nights with a similar degree of accuracy.

5.4 Summary

This chapter has tested the performance of `tlemcee`, a Python package featuring a custom orbit determination and refinement algorithm. Developed primarily to inform possible observational strategies for a future GSO monitoring system as part of a Phase 1 DASA project, the orbit refiner is nevertheless sufficiently general to handle orbital arcs from any Earth-centred regime. The package employs an MCMC technique to draw representative samples from the posterior probability distribution for a set of model parameters, namely the elements of a rolling, adjustable TLE that is propagated to the observational timestamps of the dataset in question. Prior information is derived from an IOD, carried out using the Gauss method (see Appendix A).

Section 5.2 explored the global behaviour of the IOD algorithm using simulated orbital arcs for a selection of station-kept GEO and uncontrolled GSO satellites, investigating the effects of observational time interval and arc length on the IOD performance. Subsequently, the `tlemcee` refinement algorithm was tested, utilising multiple datasets acquired as part of the light curve surveys described in Chapter 4: three nights of RASA observations targeting the station-kept GEO Astra 19.2° E constellation; and four passes of the LEO Globalstar M051 satellite observed by the SuperWASP-N array across consecutive nights. The effects of arc length and observational cadence on the algorithmic performance were examined, and a commentary on the implications for potential survey strategies was provided.

Key findings from the work may be summarised as follows:

- The optimal time interval when using the Gauss method to carry out an IOD varies case-by-case. In general, it is best to avoid intervals outside the range 5–30 minutes; degradation beyond the upper limit arises due to approximations that feed into the algorithm, while intervals shorter than 5 minutes result in unstable solutions, owing to the geometry of the problem. Station-kept GEO cases seem to favour shorter time intervals. Arc length appears to have an insignificant effect on the initial orbit obtained, helpful from an observational perspective.

- The Gauss method provides a reasonable estimate for the inclination, eccentricity and mean motion, but very poor estimates for the argument of perigee and mean anomaly (if the orbit is circular), and RAAN (if the orbit is equatorial). A preliminary MCMC can be used to address this issue, enabling the problematic angular parameters to explore the parameter space with their counterparts fixed at the IOD estimates.

- In general, observing long orbital arcs with a long cadence is likely to strike the optimal balance between observational efficiency (i.e. observing a large number of targets over a given time frame) and orbit refinement performance (i.e. obtaining an accurate orbital solution). The `tlemcee` orbit refiner is found to perform most effectively in a rolling catalogue scenario, where archival orbital states are updated as new information becomes available. That said, the algorithm has also been used to determine orbital parameters 'from scratch' when fitting arcs across multiple nights of observation, performing similarly to the equivalent Space-Track TLE when recovering objects at a future epoch.

Overviews of the algorithms employed by `tlemcee` to generate IOD solutions and convert orbital state vectors to familiar TLE-friendly elements are provided in Appendices A and B, respectively. The inner workings of the `tlemcee` orbit refiner are demonstrated in Appendix C, using a dataset acquired by the RASA instrument for the station-kept GEO Astra 1N satellite as a case study.

The following chapter moves on to explore simultaneous observations of the GSO region that were undertaken using the robotic RASA during the DebrisWatch survey, introduced previously in Chapter 3. The wide field of the COTS instrument presented an opportunity to extract longer orbital arcs for bright detections, and the supplementary dataset helped alleviate some of the major issues that are typically associated with surveys of faint GSO debris.

Chapter 6

Simultaneous observations of the GSO region

Previously, Chapter 3 presented photometric results from an optical survey of the GSO region conducted using the 2.54 m INT on La Palma, Canary Islands. In addition to these primary observations, an additional dataset was obtained by slaving the 36 cm RASA instrument to the larger aperture telescope for the duration of the survey. This chapter presents a preliminary analysis of the resulting simultaneous dataset, alongside a commentary on the relative performance of the two instruments when tasked with surveying the GSO region.

A motivation for the pairing of a small aperture COTS instrument with a large telescope is given in Section 6.1. The specifications for both instruments are compared in Section 6.2, where a brief overview of the observational strategies employed is provided. The analysis pipeline used to process the RASA survey frames is outlined in Section 6.3, highlighting a number of improvements made to the DW-INT pipeline described in Section 3.3. Key results from analysis of the simultaneous dataset are presented and discussed in Section 6.4, and a summary is provided in Section 6.5. The work was carried out as a second instalment of the DebrisWatch collaboration between the University of Warwick and Dstl (UK), introduced in Chapter 3; note that the terms 'DW-INT' and 'DW-RASA' are used throughout to distinguish between the two sets of survey frames.

Declaration — The following summarises elements of collaborative work that are included in this chapter. The control script that was used to synchronise the INT and RASA instruments was developed by Paul Chote. The RASA light curves discussed in Section 6.4.2 were extracted by Paul Chote and presented previously

in Chote [2020]. Parts of the discussion are also explored in the GEOMON DASA technical reports, Chote et al. [2020]. The chapter is based on work presented in the 2020 AMOS Conference technical proceeding, Blake et al. [2020a], and associated poster.

6.1 Motivation

Artificial satellites in the GSO region continue to play an integral role in service provision for a whole host of applications (see Section 1.1.2). Unique properties of GSO satellites, such as the localised nature of their ground tracks and their ability to provide expansive coverage, have been exploited for telecommunications, weather monitoring and navigation since the formative years of the Space Age. The high cost associated with manufacturing, launching and operating a GSO satellite, coupled with the limited number of viable orbital slots, warrants a more comprehensive understanding of the region's debris environment.

As corroborated by the DW-INT findings presented in Chapter 3, the majority of debris fragments that reside in the GSO region are too faint to be routinely tracked and monitored by the SSN. This is particularly concerning given that many of the fragments generated by explosions, anomalies and general deterioration in recent years (see Section 1.3.2) penetrate the GSOPR, posing a direct risk to active satellites. Many surveys [see e.g., Alby et al., 2004; Seitzer et al., 2004; Barker et al., 2005; Schildknecht, 2007; Luo et al., 2019] of the GSO region have been conducted using optical telescopes with diameters of 1 m or less, typically achieving a sensitivity limit in the range 15^{th}–20^{th} Magnitude. The cited surveys have uncovered a few thousand fragments of sub-1 m debris in high altitude orbits, in some cases probing to the 15–20 cm level (depending on the assumed phase angle, shape and albedo). A few surveys [see e.g., Molotov et al., 2009; Seitzer et al., 2016; Blake et al., 2019, 2021] have probed deeper with larger telescopes, which typically have a small FOV. This can act to the detriment of the survey in one of two ways: targeted observations of known fragmentation events can be performed at the expense of poor sky coverage, or wider-reaching pointing strategies can be employed, resulting in sparse or limited positional information for the objects detected. The latter was true for the DW-INT survey that took place in late 2018. The following sections present a preliminary analysis of a supplementary dataset obtained with the COTS RASA instrument, which remained synchronised to the INT for the duration of the survey. The ways in which the paired COTS instrument acts to alleviate some of the limitations associated with deep GSO surveys are explored, and plans for a wider

comparative analysis of the two available datasets are discussed.

6.2 Observational strategy

Simultaneous observations were carried out using the 2.54 m INT and a robotic COTS instrument, both situated within the Roque de los Muchachos Observatory on the Canary Island of La Palma. Further detail regarding the observational strategies employed can be found in Chapter 3, where photometric light curves extracted from the DW-INT survey frames are presented. The COTS instrument made use of the 36 cm RASA and an FLI ML50100 camera. The RASA was temporarily installed on a Paramount ME mount for the duration of a separate survey accruing light curves for catalogued GSO targets; early contributions to this survey are described in Chapter 4. The RASA system featured a custom GPS timestamping unit enabling precise start- and end-of-exposure times to be measured [Chote et al., 2019]. Specifications of interest for the INT and RASA instruments are provided in Table 6.1.

The observations span eight nights of dark-grey time from 2$^{\text{nd}}$–9$^{\text{th}}$ September 2018. Target fields were selected based on their proximity to the Earth's shadow, leading or trailing it in order to minimise the solar phase angle (observatory–target–Sun) and thus maximise the apparent brightness of candidate GSO objects. Other constraints (see Section 2.2.2) were taken into account to ensure that the observations were optimised for detecting the faintest objects possible with the available instrumentation. Images were acquired using the untracked mode of operation (see Section 2.2.3), with the telescopes fixed in the topocentric coordinate frame (i.e. 'stopped'), ensuring that photons from potential GSO candidates would integrate over fewer pixels during the integration. An exposure time of 10 s was chosen as a compromise on the observational duty cycle, and also to limit star coverage in the CCD frames, as the stars streak across pixels at the sidereal rate when imaging with the untracked mode of operation.

A map of the declination strips scanned by the RASA pointings over the course of the survey is provided in Fig. 6.1. Multiple exposures were taken per pointing to allow for detections to be correlated between successive DW-RASA frames. The reduction in dead time afforded by the shorter readout and slew times of the RASA allowed for more exposures to be acquired at each pointing. For every sequence of seven images taken by the INT, typically 20–25 could be obtained with the RASA instrument.

Table 6.1: Specifications of interest for the INT and RASA instruments. Note that the quoted FOV for the WFC is lower than its achievable 34 square arcminutes, owing to severe pickup noise that rendered one of its CCD chips unusable.

Instrument	**Aperture [m]**	**CCD(s) [px]**	**FOV**	**Resolution [$''$px^{-1}]**	**Readout time [s]**	**Filter**
INT WFC	2.54	4×2k×4k (mosaic)	$33' \times 22'$	0.66 (binned, 2×2)	25	Harris V
RASA	0.36	8k×6k	$3.6° \times 2.7°$	1.57 (unbinned)	4	None

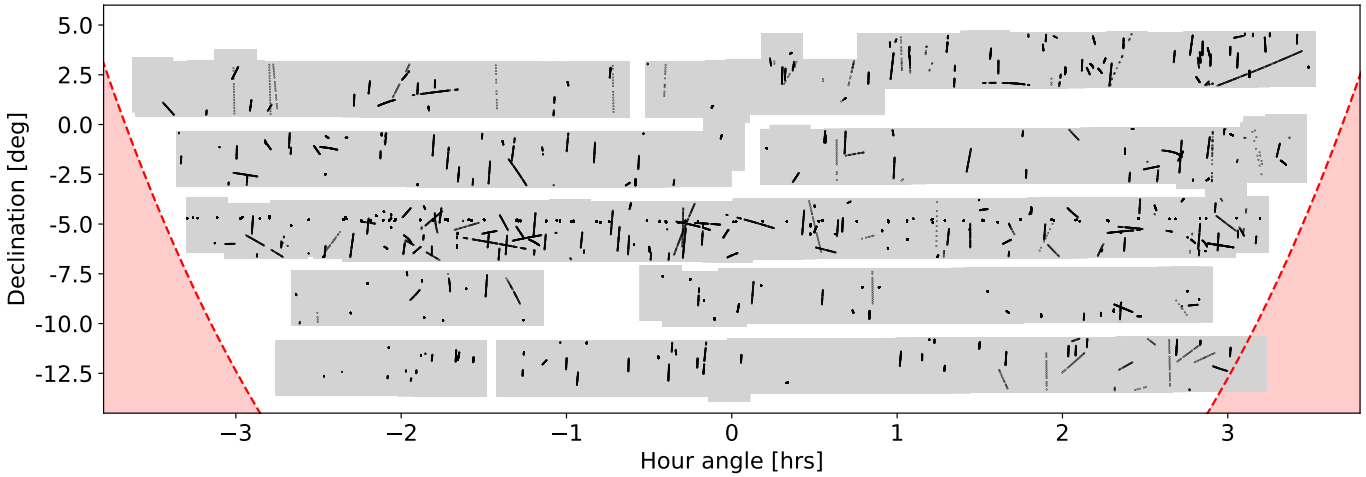

Figure 6.1: Telescope pointings comprising the DW-RASA dataset. Imaged fields are shaded in grey, while the black dots map out detections of candidate GSO objects uncovered by the analysis pipeline outlined in Section 6.3. The regions shaded in red denote the 30° altitude limits constraining the telescope pointings.

6.3 Analysis pipeline

The custom analysis pipeline presented in Chapter 3 is adapted and improved to process the raw DW-RASA CCD frames. A brief overview of the steps performed is provided below, highlighting the key developments. The updated pipeline employs a number of existing astronomical and scientific packages, including `SEP` [Bertin and Arnouts, 1996; Barbary, 2016], `Astrometry.net` [Lang et al., 2010], `astropy` [Robitaille et al., 2013; Price-Whelan et al., 2018], `astroquery` [Ginsburg et al., 2019], `scipy` [Jones et al., 2001] and `photutils` [Bradley et al., 2016]. Prior to the frame-by-frame processing, master calibrations are generated from bias and flat field frames taken at the start and end of each night. The available metadata for each frame of a given night is used to ascertain an appropriate search box for a bulk query to the *Gaia* DR2 catalogue, resulting in a local database of comparison stars for photometric calibration. The RASA frames are calibrated in the *Gaia* G passband, in order to best approximate its filterless response.

Each frame is subsequently processed as follows:

1. Bias and flat field calibrations are applied, and a model of the spatially varying sky background is subtracted from the calibrated frame.

2. Star trails are extracted from the frame by applying a matched filter that encodes their common morphological and orientational properties, and estimates of their centroids are subsequently used to obtain a preliminary astrometric solution.

3. Comparison stars are queried from the local database and filtered to reject those that are blended or saturated. The star trails in the frame are then cross-matched with the surviving comparisons to obtain a photometric zero point. A 10 pixel positional cut is applied, alongside a 3σ brightness cut, where σ is the standard deviation derived from the zero point calculation, to filter out anomalous matches.

4. The astrometric solution is refined using an adaptation of the algorithm described in Chote et al. [2019]. A custom 2D distortion map is fitted and an iterative improvement of the cross-match is carried out. As shown in Fig. 6.2, the implementation of this technique has greatly improved the quality of the resulting astrometric solution. The algorithmic performance for the bottom-left region of the DW-RASA frames is somewhat diminished as a result of miscollimated optics, which led to a blurring of the PSF, thus making it more challenging to determine accurate centroids for sources in that corner.

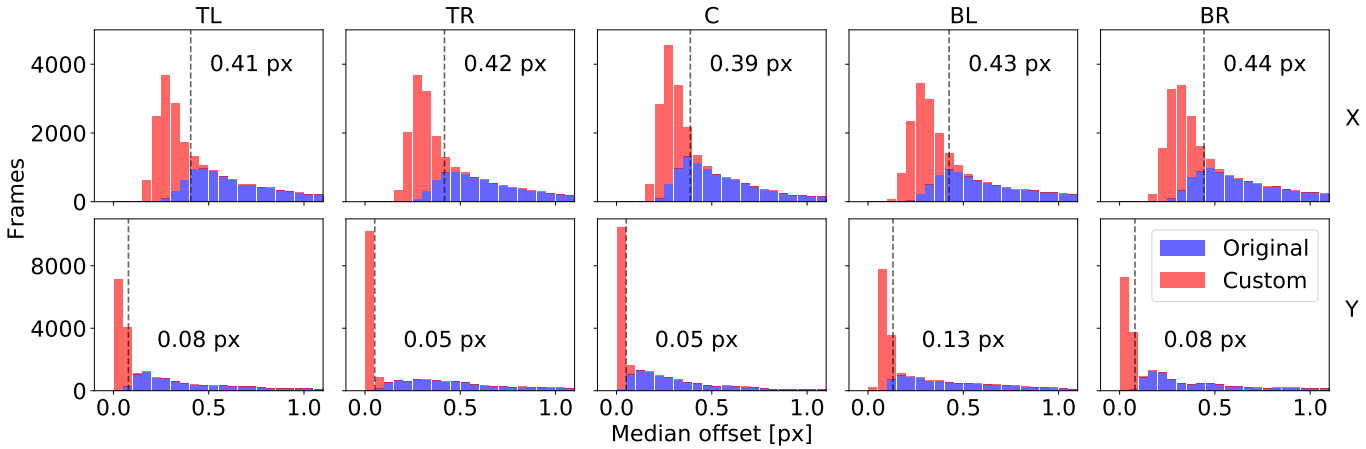

Figure 6.2: Astrometric accuracies achieved using `Astrometry.net` (blue) and the custom algorithm described in Section 6.3 (red). The top panels show median offsets in the X (right ascension) direction between the detected star trails and their matched comparisons, while those in the bottom panels correspond to the Y (declination) direction. The median offset for matched stars is evaluated within a 2044 px×2044 px tile situated in the top-left (TL), top-right (TR), centre (C), bottom-left (BL) and bottom-right (BR) regions of a given frame. In each panel, the 95^{th} percentile achieved by the custom algorithm is labelled (black). Owing to the trailed nature of stars in the DW-RASA frames, a higher accuracy is achieved in declination (across the trail) than in right ascension (along the trail). A similar analysis was performed as part of Chote et al. [2020], on a separate analysis pipeline.

5. Mathematical morphology techniques (see Section 2.4.2) are applied to remove the star trails. A threshold-based source extraction is carried out for the star-subtracted frame. The 'known' positions of the *Gaia* comparison stars are mapped to the image space using the astrometric solution and a proximity check is performed, filtering out common false positives that survive the star subtraction procedure.

6. Aperture photometry is performed for the surviving detections. An estimate of total brightness is obtained by summing the contents of a circular aperture if the detection is point-like (as for station-kept GEO satellites) or those of a rectangular aperture if the detection is trailed (as for uncontrolled GSO objects and those in other orbital regimes) in the image.

After processing the raw DW-RASA frames as above, the following tasks are performed using the resulting ensembles of positional measurements for candidate GSO detections:

1. Candidate objects of interest are correlated between the individual frames of a given pointing of the telescope, by fitting and sequentially updating a linear trajectory. Trails comprising multiple detections within a single exposure, for example those that appear to be tumbling in and out of the background noise floor, are identified at this stage and combined to generate an estimate of the overall centroid. These cases undergo additional vetting by eye. Remaining false positives are discarded as single detections; candidate objects were required to have been found in two or more frames to be considered in the analyses that follow.

2. Light curves are extracted for trailed cases by placing rectangular apertures along the trail, making use of the fitted trajectory to map spatial position to time. Reference images (typically the previous or next frame in the sequence of exposures) are used to subtract out contaminating background sources (e.g., star trails).

6.4 Results and discussion

6.4.1 Supplementing the sampled population

In the top left panel of Fig. 6.3, brightness histograms are given for the orbital arcs extracted from the DW-INT and DW-RASA frames. The higher detection rate for the RASA is immediately clear, owing to the wider coverage afforded by its larger

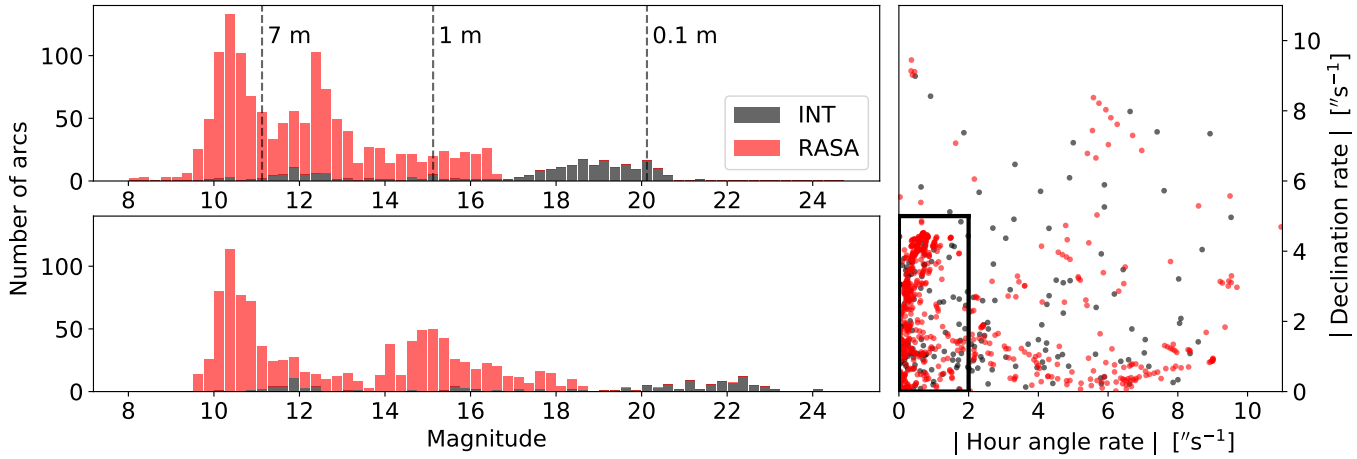

Figure 6.3: Top left) A histogram of brightness measurements for the full sample of orbital arcs detected by the INT (black) and the RASA (red) over the course of the survey. It is important to note that separate pass bands were used to calibrate the brightness measurements for each instrument, in light of the different filters used (see Table 6.1). The term 'Magnitude' thus refers to calibrated APASS V magnitude for the INT detections, and calibrated *Gaia* G magnitude for the RASA detections. The translational offset attributed to this colour term is approximately +0.5 magnitudes for the RASA measurements (towards fainter magnitudes), and is not applied here. Annotated size estimates are provided as a rough guide, and assume that the corresponding objects are Lambertian spheres with an albedo of 0.1. Right) Angular rates in hour angle and declination for the objects detected by the INT (black) and the RASA (red). Rate cuts (black box) are applied to reduce the sample to objects that likely reside in circular GSOs (see Section 2.2.3). Bottom left) A histogram of brightness measurements for the circular GSO sample of orbital arcs detected by the INT (black) and the RASA (red), normalised by trail length (see text).

FOV. A total of 1205 arcs comprising two or more detections within a given pointing are extracted from the RASA observations using the custom pipeline outlined in Section 6.3, compared to the 226 arcs from those of the INT that are analysed and discussed in Chapter 3. However, the inferior sensitivity of the RASA drops off at $G \sim 16.5$, so only the bright end of the sampled population is supplemented by the COTS instrument.

The bright end of the RASA distribution is found to split into two peaks. The first, centred around $G \sim 10.5$, corresponds to station-kept GEO satellites that are point-like in the DW-RASA frames. Objects with such a high brightness were found to easily saturate in a typical 10 s INT exposure, owing to the instrument's superior sensitivity. The RASA observations offer a chance to correct for the resulting skew at the extreme bright end of the distribution. A second peak is visible around $G \sim 12.5$, consistent with several other surveys of the GSO region undertaken at a similar longitude [see e.g., Schildknecht, 2007]. This peak likely corresponds to former GEO satellites that have been retired to graveyard orbits, as per the recommended mitigation guidelines (see Section 1.2.4). Owing to a lack of attitude control beyond decommisioning, many of these satellites exhibit a tumbling motion that is dependent on the perturbative forces acting within the GSO region. Satellites that are tumbling in this way will brighten and fade as highly reflective components (e.g., solar panels) pass in and out of the observer's line of sight, hence the discrepancy in average brightness between the two peaks.

As shown in the right-hand panel of Fig. 6.3, rate cuts are applied to obtain a sample of orbital arcs corresponding to objects in the GSO region that likely reside in circular orbits. The rate cuts reduce the sample size to a total of 956 circular GSO arcs for the RASA, and 129 for the INT. An additional histogram for the circular GSO sample is plotted in the bottom left panel of Fig. 6.3, having normalised the brightness measurements by a factor x/l, where x is characteristic of the optical system's PSF and l is the length of the path traversed over the course of the exposure. This gives the brightness of a point-like source possessing an equivalent peak flux for the same integration time, and so provides a clearer representation of the detection capabilities of the sensor. In the normalised regime, the peak centred on $G \sim 10.5$ remains largely unchanged, reinforcing the interpretation that it corresponds to station-kept GEO targets that are point-like and consequently unaffected by the normalisation. Conversely, the majority of orbital arcs comprising the second peak appear to exhibit off-GEO motion, as they shift towards fainter magnitudes, reinforcing the interpretation that they correspond to objects that are drifting in graveyard orbits. Uncontrolled debris will manifest as trails in survey frames ac-

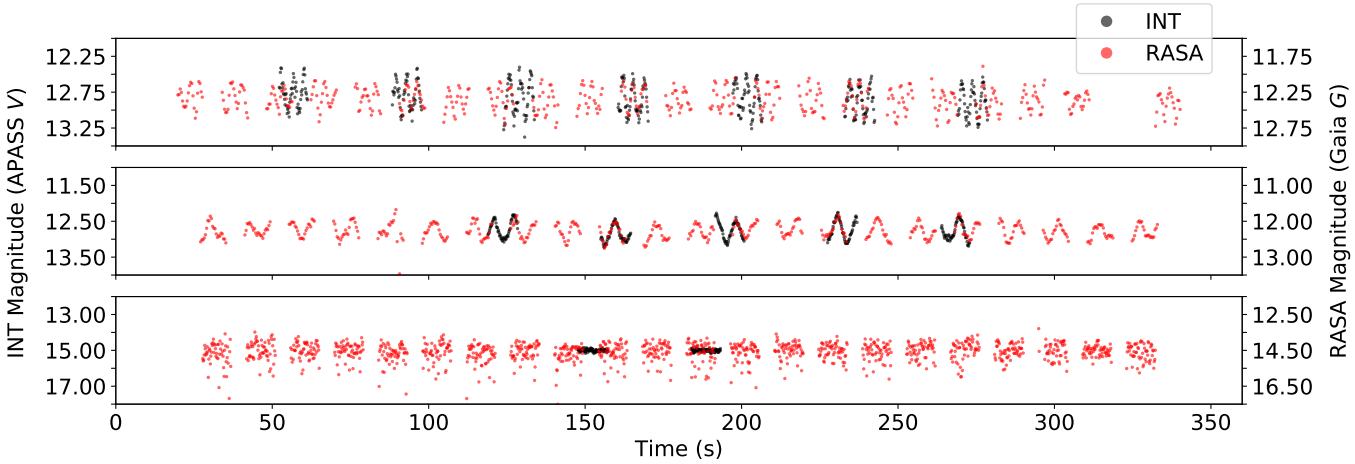

Figure 6.4: Examples of simultaneous light curves acquired by the INT (black) and the RASA (red). An offset of roughly 0.5 magnitudes is found between the two sets of brightness measurements, a colour term attributed to the different pass bands used for photometric calibration. Both the APASS V magnitude (INT, left-hand axis) and the *Gaia* G magnitude (RASA, right-hand axis) scales are provided. The light curves given in the top and middle panels correspond to orbital arcs correlated with SL-12 rocket bodies NORAD 16797 and NORAD 15581, respectively. The bottom panel shows the light curve extracted for an orbital arc that failed to correlate with the publicly available USSPACECOM catalogue. Adapted from Chote [2020] with the author's permission.

quired with the telescope in 'untracked' mode, owing to the inclined or eccentric nature of their orbits, and so will often spend a fraction of a second contributing flux to a given pixel of the CCD. For instance, an object with the maximal declination rate of $5'' \, s^{-1}$ afforded by the cuts imposed above would trail across 32 pixels of the detector in a 10 s RASA exposure, consequently spending roughly a second traversing the PSF. An exposure time longer than this will only serve to increase the noise contribution from the sky background, as the surface brightness spreads across multiple pixels instead of a localised group. By striking an accord between the exposure time and the expected PSF crossing time, an equivalent SNR can be achieved with a much lower observational cadence. As is the case for many surveys, however, the comparatively long readout times of the CCD detectors rendered such a low exposure time impractical. The use of sCMOS cameras (see Section 2.2.3) with their negligible readout times would alleviate this issue, though further discussion of these detectors would lie outside the scope of this thesis.

6.4.2 Simultaneous light curves

In Fig. 6.4, examples of simultaneous light curves extracted from the DW-INT and DW-RASA observations are provided. Photometric light curves form a useful by-product of GSO surveys, and contain information pertaining to the shape, reflectivity and attitude of the corresponding object. The development of techniques to deconvolve this information from measurements of an object's brightness over time is a very active area of research (see Section 1.2.2), with some surveys dedicating their efforts to acquiring high quality data for testing [see e.g., Chote et al., 2019; Šilha et al., 2020].

The top two panels of Fig. 6.4 display light curves extracted for two SL-12 rocket bodies: NORAD 16797 and 15581, respectively. A superb agreement can be seen between the INT and RASA photometry when considering brightness variability, accounting for the roughly 0.5 magnitude offset attributed to a colour term that is introduced by the differing filter response curves. Although the RASA was scripted to observe the same fields as the INT, the exposure sequences themselves were not synchronised. As a result, the RASA observations act to fill gaps in the light curves extracted from the DW-INT frames. The more efficient observational duty cycle afforded by the RASA's reduced dead time (required for readout and field acquisition overheads) is clearly beneficial, allowing measurements to be made across a larger proportion of the observation window, and resulting in an extension of the window for each individual pointing.

The light curve in the bottom panel of Fig. 6.4 corresponds to an orbital

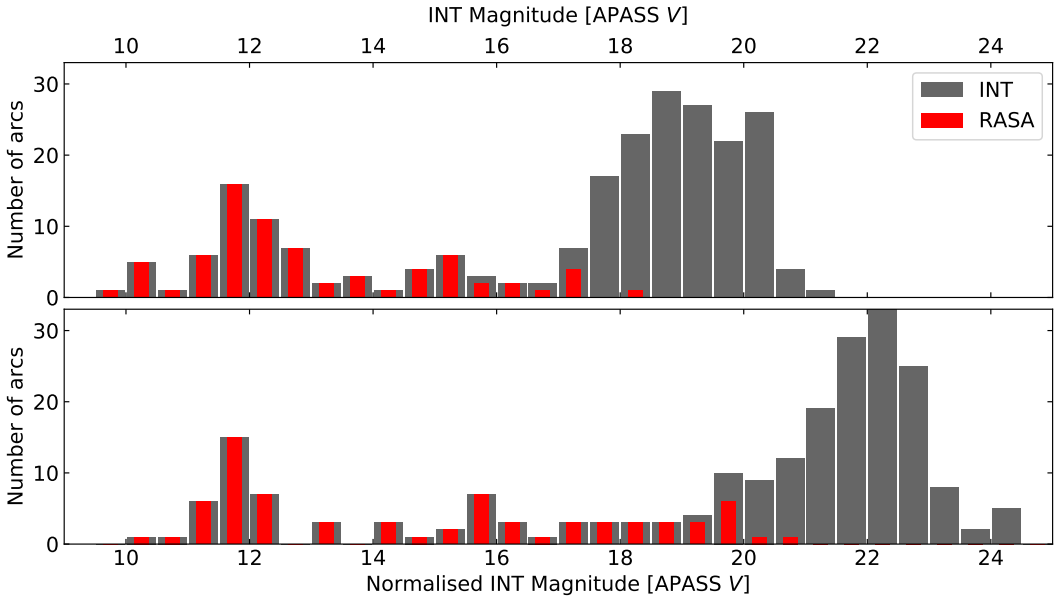

Figure 6.5: Histograms showing the recoveries achieved by the RASA instrument when performing a targeted search for tracks detected in the DW-INT survey frames. The overall population sampled by the INT observations is shown in black, while the RASA recoveries are indicated in red. The recovered detections are binned according to their mean brightness in the INT frames (top) and the mean brightness normalised by trail length (bottom, see text).

arc which failed to correlate with a known object when cross-matched against the publicly available USSPACECOM catalogue. Here, the limitations of the RASA's inferior sensitivity become apparent. A higher degree of scatter can be seen in the RASA brightness measurements compared to those extracted from the DW-INT frames, owing to the lower SNR of the corresponding sources. The SNR can be improved by binning data in the time domain, though this is naturally subject to a trade-off with time resolution. In the top panel, the effect of the RASA's larger pixel scale on time resolution can be seen, acting to diminish the amplitude of oscillations in the light curve.

6.4.3 Recovery of INT detections

This section moves on to investigate the recovery success achievable with the RASA when performing a targeted search for objects detected in the DW-INT frames. After identifying the group of DW-RASA exposures corresponding to the relevant pointing, positional estimates are obtained using the trajectory in hour angle and declina-

tion space determined using the DW-INT analysis pipeline, presented in Chapter 3. A $2\sigma_b$ source extraction is carried out within a search box of width $5l$ centred on the expected position in RASA image space, where σ_b is the global background RMS and l is the trail length as determined from the INT trajectory. A visual inspection of the resulting detections is used to assess the recovery performance, requiring the object to be found in two or more DW-RASA frames as a success criterion.

Histograms showing the successful RASA recoveries relative to the overall population of orbital arcs sampled by the DW-INT observations are provided in Fig. 6.5. All arcs with a mean INT brightness $V < 15$ are recovered well using the method outlined above, corresponding to objects exceeding roughly 1 m in diameter with a SNR safely above the noise floor. Recoveries of tracks fainter than this are typically aided by significant brightness variability, where glints in the object's light curve have penetrated the sensitivity limit in two or more of the DW-RASA frames. Glints and other boosts in brightness that can uncover objects hovering around the sensitivity limit are more likely to be captured by the DW-RASA observations, owing to the superior duty cycle afforded by its lower readout time relative to that of the INT WFC. In order to gain a clearer perspective of the RASA's intrinsic detection capabilities, the recovery is plotted as a function of mean INT brightness, normalised by trail length (as in Section 6.4.1). All objects with a normalised brightness $V < 18.5$ are successfully recovered using the outlined search method, consistent with the sensitivity limit found for the overall population sampled by the DW-RASA survey frames. As expected, however, the RASA instrument is not sensitive to the vast majority of faint, uncorrelated tracks detected by the larger aperture INT when using primitive search methods of this kind. Future efforts will look to employ more sophisticated techniques to uncover fainter tracks in the DW-RASA images, for example by applying matched filters using prior morphological and orientational information from the DW-INT baseline, or by stacking consecutive frames to enhance the SNR of targets.

6.5 Summary and future work

This chapter has presented a preliminary analysis of a simultaneous dataset from a survey of the GSO region, carried out using the 2.54 m INT and the 36 cm COTS RASA instrument, both situated on La Palma, Canary Islands. The observations were acquired across eight nights of dark-grey time in September 2018. An adapted version of the pipeline presented in Chapter 3 was used to process the raw DW-RASA survey frames, incorporating an iterative algorithm for refining the preliminary as-

trometric solution, originally developed for the light curve surveys introduced in Chapter 4. Key findings from a joint analysis of the two sets of survey frames are briefly summarised as follows:

- a total of 1205 orbital arcs comprising two or more detections within a given pointing are extracted from the DW-RASA frames, 956 of these exhibiting angular rates characteristic of objects in circular GSO orbits;
- two dominant populations are uncovered, the first centred around *Gaia* $G \sim 10.5$, corresponding to station-kept GEO satellites, and the second centred around *Gaia* $G \sim 12.5$, which likely corresponds to spacecraft that are drifting in graveyard orbits;
- the RASA is more efficient at surveying bright targets, owing to the more extensive coverage afforded by its wider FOV, and so acts to supplement the bright end of the sampled population;
- the RASA's wider FOV also facilitates an extended coverage for each INT field, enabling the extraction of longer orbital arcs for bright objects;
- the lower readout time of the RASA allows for more extensive and complete light curves to be extracted from trailed detections, though the larger pixel scale acts to reduce the time resolution compared to the DW-INT light curves;
- all tracks with trail-normalised APASS $V < 18.5$ are successfully recovered by the RASA, though the vast majority of the faint, uncorrelated detections uncovered by the INT fall below the instrument's sensitivity limit.

Overall, the simultaneous observations prove complementary in a variety of ways, and the use of a small aperture, wide FOV COTS instrument is found to alleviate several limitations that are typically associated with large telescopes when conducting surveys of the GSO region.

Future development of the project will aim to carry out a correlation between successive pointings to combine individual arcs belonging to the same object. Owing to its wider field, objects are likely to remain in view of the RASA for multiple pointings as it slews in accordance with the INT. This will, in principle, extend the orbital arcs to cover 10–12 minutes, compared to the 3–4 minutes achievable when extracting arcs from the DW-INT frames. It should then be possible to perform an IOD for the resulting collection of objects using short arc techniques [see e.g., Pirovano et al., 2020b], allowing the number of unique objects surveyed to be determined.

Chapter 7

Conclusion

> [Interviewer:] *Several songs on the album, like "Keep Talking" suggest that all problems can be solved through discussion. Do you believe that?*
> [Gilmour:] *It's more of a wish than a belief.* [laughs]
>
> –David Gilmour, Pink Floyd - *"Sounds of Silence" interview* by *Guitar World*, 1994

7.1 Summary

This thesis has explored a variety of ways in which optical imaging can contribute to enhanced levels of space situational awareness (SSA), applying a range of tools and techniques that are commonly used in astronomical surveys. The projects presented throughout have focused on two orbital regimes of particular interest: the low Earth orbit (LEO) region, with a high spatial density and a rapidly growing population; the geosynchronous (GSO) region, with a limited number of viable slots and a comparatively uncharacterised debris field. With an overarching goal of investigating and optimising search strategies for surveys of orbital debris, the projects have relied heavily on observational datasets acquired by three instruments based at the Roque de los Muchachos Observatory on the Canary Island of La Palma:

- the ultra-wide field SuperWASP-North (SuperWASP-N) telescope, with its array of eight co-mounted 200 mm camera lenses;
- a 36 cm robotic Rowe Ackermann Schmidt astrograph (RASA), commissioned exclusively using commercial-off-the-shelf (COTS) components;
- the 2.54 m Isaac Newton Telescope (INT), paired with its Wide Field Camera.

Recent break-ups and anomalies involving satellites and rocket bodies in high altitude orbits have highlighted the existence of a largely uncharacterised population of faint orbital debris, in many cases penetrating the geosynchronous Protected Region. With no atmospheric drag to provide a removal mechanism at such high altitudes, fragments of debris will remain in the vicinity of the GSO region indefinitely, their orbits and attitude evolving solely under the influence of natural perturbative forces like solar radiation pressure. Relative velocities in the GSO region can be sufficiently high to render even decimetre-sized debris a significant threat to active satellites, and so it is essential that the small (faint) end of the high altitude debris environment continues to be probed with large telescopes, in order to better understand the behaviour of uncontrolled objects and the risk they pose.

Chapter 3 presented photometric results from a survey of the GSO region conducted using eight nights of dark-grey time on the large aperture INT in September 2018. The survey was carried out as part of DebrisWatch, an ongoing collaboration between the University of Warwick and the Defence Science and Technology Laboratory (UK) investigating the GSO debris environment. A custom analysis pipeline was used to process the raw DebrisWatch-INT survey frames, performing the following tasks: standard bias and flat field corrections; astrometric and photometric calibrations; source extraction and filtering to separate candidate objects of interest from false positives; and extraction of high cadence light curves for off-geostationary (trailed) detections.

The brightness distribution for the population of orbital tracks sampled by the survey is consistent with findings from previous efforts to probe the faint end of the GSO debris environment. A bimodal distribution is observed, with a 'bright' peak associated with known, catalogued satellites and rocket bodies, and a 'faint' peak that appears to still be rising at the sensitivity limit of the INT, corresponding to uncatalogued fragments of debris. Reassuringly, the bright peak appears to be in accordance with observations carried out using the ESA 1 m Telescope in Tenerife [see e.g., Schildknecht et al., 2004], which samples from the same segment of the GSO region, and thus has sight of the same geostationary satellites that make up a large proportion of the brighter end. Owing primarily to its superior collecting area, the INT was able to perform a deeper search than those of the ESA campaigns, albeit over a much shorter timescale due to the limited time available on the large telescope. Similarly short surveys conducted with the 6.5 m Magellan Telescope in Chile [see e.g., Seitzer et al., 2011] have observed comparable detection rates to those of the DebrisWatch-INT survey, despite the Magellan's advantageous proximity to the 105° W geopotential well, though it is important to remember that both sur-

veys are consequently blighted by small number statistics. That aside, both surveys have uncovered intriguing populations of GSO debris that exhibit significant levels of brightness variability, motivating further study in future.

While the ESA campaigns, alongside efforts by the Astronomical Institute of Bern (AIUB) and more broadly the International Scientific Optical Network (ISON) [see e.g., Molotov et al., 2009], have vastly improved our understanding of the GSO debris environment, many limitations remain. Few nodes of these networks are able to track objects fainter than around 18^{th} visual magnitude, making real-time coverage of faint debris on a global scale extremely challenging. Furthermore, while the aforementioned agencies and institutes maintain their own catalogues of GSO debris, the widely-used US Space Command (USSPACECOM) catalogue remains severely incomplete in spite of its global coverage, limited by the inferior sensitivities of optical telescopes in the Space Surveillance Network. Other networks with global coverage of the GSO region exist, such as those deployed by ExoAnalytic Solutions and Numerica, however they predominantly comprise COTS-grade equipment that cannot probe as deep as the larger telescopes discussed. Moreover, limited reference to these networks can be found in the literature, as their observations are commercially sensitive and proprietary in nature. From a researcher's perspective, sporadic observations with large telescopes like those of the DebrisWatch and Magellan surveys are currently the most effective way of probing the GSO region at the decimetre level.

For the duration of the survey, a custom control script was used to synchronise the COTS RASA instrument to the INT. A preliminary analysis of the resulting simultaneous dataset was carried out in Chapter 6, exploring the benefits and limitations of pairing a large telescope with a smaller aperture COTS instrument when surveying the GSO region. The DebrisWatch-RASA survey frames were processed using an adapted version of the DebrisWatch-INT pipeline, incorporating an iterative algorithm for refining the initial astrometric solution. With its lower sensitivity, the RASA was able to image geostationary (GEO) satellites without saturating, resolving the bright end of the sampled population into two separate peaks. After normalising brightness by trail length, it became clear that the brightest peak corresponded to station-kept GEO satellites, while the second peak can be associated with decommissioned spacecraft that are drifting (and perhaps tumbling) in super-synchronous graveyard orbits. Owing to the more extensive coverage afforded by its wider field of view, the RASA was able to survey the region for brighter objects more efficiently than its larger counterpart, acting to supplement the bright end of the sampled population uncovered by the INT. However, the RASA's lower sensitiv-

ity meant that the vast majority of the faint, uncatalogued debris uncovered by the INT could not be recovered using a threshold-based source extraction. The lower readout time of the RASA reduced the dead time between exposures, thus allowing for more extensive and complete light curves to be extracted from a given pointing of the telescope. Generally, objects detected in the DebrisWatch-RASA frames were imaged for longer on account of the instrument's wide field of view, which enabled the extraction of longer orbital arcs, thus alleviating a common limitation associated with deep surveys of the GSO region.

The remaining chapters of this thesis have focused on two key by-products of optical surveys searching for debris: measurements of brightness (light curves) and position (orbital arcs) over time. Photometric light curves encode a wealth of information regarding an object's physical and attitudinal characteristics, thus serving as useful diagnostic tools for SSA. Precise, high cadence measurements can reveal fine rotational signatures, for example glints that occur as highly reflective components pass rapidly in and out of the observer's line of sight.

Chapter 4 presented early contributions to two remote surveys utilising the SuperWASP-N and RASA instruments to accrue high cadence light curves for targets in the LEO and GSO regions, respectively. The partially automated procedures used to select targets, schedule observations and process acquired frames during the initial prototyping phase for the surveys were discussed. With its ultra-wide field, the SuperWASP-N array is able to observe the rapid passes of bright LEO objects whilst tracking sidereally, allowing reflected light from the target to integrate across an elongated trail of pixels, and thus facilitating the extraction of high resolution light curves. Observations of GSO targets were acquired with the RASA instrument tracking sidereally, and separately with the telescope stopped (the 'untracked' mode of operation), the latter strategy aiming to match the expected motion of station-kept GEO satellites (as employed for the DebrisWatch survey). Exemplar light curves for a selection of LEO payloads and rocket bodies were presented, alongside observations undertaken across multiple epochs for two case studies of interest: the Infrared Astronomical Satellite (IRAS), which experienced a 'near-miss' conjunction with an uncontrolled spacecraft in 2020; and the environmental satellite, Envisat, identified as a high priority target for future active removal missions. The chapter moved on to discuss the benefits and limitations of the two observational strategies employed to image GSO targets with the RASA; both appear to perform equally well when sampling long period features, while glints that take place over timescales shorter than the exposure time are often poorly resolved by the untracked observations. Indeed, the sidereal strategy would later be adopted as full survey op-

erations began in the summer of 2019. The more than 3000 light curves amassed by the SuperWASP-N and RASA instruments over the past two years will feed into a number of prospective projects that fall outside the scope of this thesis.

Orbit determination is vital for a wide variety of SSA-driven activities, from establishing and maintaining a catalogue of tracked objects to carrying out targeted observations based on archival orbital states. Chapter 5 outlined the development and testing of `tlemcee`, a custom orbit determination and refinement algorithm, making use of observational arcs acquired by the SuperWASP-N and RASA instruments as part of the light curve surveys above. The presented work investigated the algorithmic performance in the context of maintaining a rolling catalogue of objects for a future monitoring system, providing a commentary on the observational strategies to keep in mind when finalising a design. The algorithm computes initial estimates for the orbital parameters using the Gauss method of preliminary orbit determination (see Appendix A). The performance of this initial orbit determination method was investigated using simulated orbital arcs, derived from archival two-line element (TLE) sets for a selection of station-kept GEO and uncontrolled GSO payloads, exploring the effects of observational time interval and orbital arc length. The optimal time interval was found to vary on a case-by-case basis, with intervals outside the range 5–30 minutes resulting in unstable or severely degraded solutions. Conversely, arc length was found to have an insignificant effect.

The initial orbit is fed as input to a Markov Chain Monte Carlo (MCMC) implementation, which draws representative samples from the posterior probability distribution for a set of model parameters, namely the elements of a rolling, adjustable TLE that is propagated to the observational timestamps of the input dataset. The `tlemcee` orbit refinement algorithm was tested using three nights of RASA observations tracking the station-kept GEO Astra 19.2° E constellation, alongside four passes of the decommissioned LEO Globalstar M051 satellite observed by SuperWASP-N across consecutive nights. Owing to the circular, equatorial nature of the Astra arcs, a preliminary run of the MCMC proved necessary to account for very poor initial estimates of the right ascension of the ascending node, the argument of perigee and the mean anomaly. The effects of orbital arc length and observational cadence on the algorithmic performance were investigated, using both the Gauss initial estimates and the archival TLE values as input to the MCMC. In general, it was found that observing long orbital arcs with a long cadence is likely to strike the optimal balance between observational efficiency (observing a large number of targets within a given timeframe) and orbit refinement performance (obtaining an accurate orbital solution). The `tlemcee` refiner proved most effective

in a rolling catalogue scenario, where archival orbital states are updated as new information becomes available.

Looking ahead, future developments will aim to incorporate more sophisticated techniques that are capable of handling the short orbital arcs synonymous with deep surveys of the GSO region [see e.g., Pirovano et al., 2020a]. This should allow a more complete orbital analysis to be conducted for the DebrisWatch datasets, in particular for the brighter objects detected by the RASA, with arcs 2–3 times the length of their INT counterparts.

7.2 Future outlook

The future evolution of the orbital debris environment will depend heavily on the actions undertaken by space-faring nations in the coming years and decades. What appears certain is that a failure to act could very quickly result in the operational loss of several key orbital regions for the future generations of space flight. When it comes to action, however, many unanswered questions persist as we approach the 64$^{\text{th}}$ anniversary of the Sputnik 1 launch, ranging from the technical feasibility, reliability and effectiveness of active removal concepts that are currently under development (see Section 1.2.4), to the establishment of an all-encompassing agreement between space-faring nations regarding the safe and sustainable use of the space domain.

Resolving the latter issue will be an essential step towards improving levels of adherence to mitigation guidelines, which fall far below where they need to be for LEO operators (see Section 1.2.3), especially given the hordes of constellations that are primed for launch over the next decade. Current guidelines that have been established on the international stage[1] are non-binding, and thus it remains the prerogative of individual space-faring nations to adopt them as part of their national laws and doctrines. Achieving a 'one size fits all' set of rules and regulations is, and will continue to be, an incredibly complex undertaking. A certain degree of flexibility and compromise will be necessary to accommodate the wide array of priorities across different sectors. With the militaries of major space powers still at the forefront of activity, both in terms of usage and technological capability, a cross-sector dialogue will be of paramount importance to ensure that all actors can strive towards a single goal of sustainability. Furthermore, the setting of standard guidelines and practices for future use of space must cater not just to the interests of

[1]The interested reader is referred to the AMOS Conference keynote given by Verspieren [2020], which features a more detailed discussion calling for the inclusion of military actors and representatives of emerging space nations when establishing standards and 'norms of behaviour' for the sustainable use of space.

current space-faring nations, but also those that may look to access the space domain in future. Efforts by so-called "emerging" space nations to launch and operate in Earth orbit may warrant additional leniency, owing to the relative inexperience of the agencies and/or institutions in question. However these obstacles are addressed, it is clear that transparency and cooperation will be pivotal factors in achieving success from a policy-based perspective.

Returning to the technical side of SSA, what challenges lie ahead? The shift towards smaller, light-weight spacecraft in the LEO region (see Section 1.2.3) has opened up the possibility of launching many tens of payloads on a single carrier vehicle. The resulting increase in launch efficiency, coupled with the projected injection of the many thousands of constellation nodes that have been licenced, has led to a rapid population growth that will likely continue to accelerate as more commercial entities enter the arena. Further strain will be placed on the archaic infrastructures of the SSN and other leading surveillance networks. This will likely necessitate either an (expensive) upgrade to the existing hardware, or the development of more sophisticated data fusion techniques, to combine information from a variety of sensors and sources. While the latter would, in principle, go a long way to solving the logistical challenge, it would serve to highlight another: how would information be shared, and to what extent? Even if the required infrastructure already exists, the above conundrum is likely to introduce a political stalemate that could take several years to disentangle.

In addition to the logistical challenges associated with a sky that is getting busier every year, surveillance networks may soon be tasked with tracking objects far beyond the 'high altitude' bounds of the GSO region, namely those in cislunar orbit (see Section 1.1.3). As we have seen from the DebrisWatch-INT survey, presented in Chapter 3, our knowledge of the faint debris population remains incredibly sparse, even at the GSO altitudes that are comparatively close to home. Objects in cislunar space will ultimately push fainter still, and observational lines of sight will often be obstructed by the Moon itself, or eclipsed in shadow. The development of more sophisticated object detection algorithms will be important, building on previous efforts to push deeper using single frame techniques [see e.g., Levesque, 2009; Zimmer et al., 2013; Hickson, 2018; Nir et al., 2018; Do et al., 2019] and multi-frame stacking [see e.g., Yanagisawa et al., 2005, 2012]. These efforts will need to be paired with bespoke sensor architectures that serve to aid the search algorithms both in terms of sensitivity and observational strategy, in order to further develop our understanding of the GSO debris environment, and to have any hope of performing informative observations of the cislunar regime from the ground. Similarly bespoke

instrumentation and strategies will be necessary to provide real-time monitoring of future rendezvous missions, both for the onboard servicing and active removal of spacecraft. The growing population of trackable objects is already necessitating the development of new and improved data formats (recall the inadequacies of TLEs, discussed in Section 1.2.2), as advancements in instrumentation and computation begin to unveil fainter fragments and supplement catalogues.

While awareness of the orbital debris problem has increased over the past couple of decades, the following goals remain a long way from being realised: the attainment of safe and sustainable levels of space situational awareness, ensuring the safety of active satellites, and indeed other spacecraft that are at a high risk of seeding collisional cascades in key orbital regimes; the identification and characterisation of all debris fragments that pose a threat to mission operations; the mitigation of future debris generation, via sufficient levels of adherence to internationally recognised and binding standard practices; and remediation of the issue, via the deployment of reliable and repeatable active removal technologies. Optical imaging will play a key role in achieving most, if not all, of the listed goals, while international cooperation will be integral to building our understanding of the ever-changing debris environment. As new technologies develop, and challenges are overcome, it is essential that we keep a watchful eye on the sky to protect the satellites that we, as a society, have come to rely on.

Appendix A

Gauss method of preliminary orbit determination

Given three observations at times t_1, t_2 and t_3, the Gauss method can be used to carry out a preliminary orbit determination for an orbiting body. As can be seen in Fig. A.1, the geocentric position vector $\mathbf{r}_i$ at time t_i is related to the observer's position vector $\mathbf{R}_i$, the slant range ρ_i and the topocentric direction cosine vector $\hat{\boldsymbol{\rho}}_i$ by the vector sum,

$$\mathbf{r}_i = \mathbf{R}_i + \rho_i \hat{\boldsymbol{\rho}}_i. \tag{A.1}$$

The position vector of the observer can be written as

$$\mathbf{R}_i = \left[\frac{R_\mathrm{E}}{\sqrt{1-(2f-f^2)\sin^2\phi_i}} + H_i \right] \cos\phi_i \left(\cos\theta_i \hat{\mathbf{I}} + \sin\theta_i \hat{\mathbf{J}} \right) + \left[\frac{R_\mathrm{E}\left(1-f^2\right)}{\sqrt{1-(2f-f^2)\sin^2\phi_i}} + H_i \right] \sin\phi_i \hat{\mathbf{K}}, \tag{A.2}$$

where f is the oblateness, given by

$$f = \frac{R_\mathrm{E} - R_\mathrm{P}}{R_\mathrm{E}}. \tag{A.3}$$

Here, R_E is the equatorial radius of the Earth, while R_P is the polar radius. The local sidereal time θ_i, geodetic latitude ϕ_i and elevation H_i collectively specify the observer's location at time t_i. Note that $i \in [1, 3]$ throughout this appendix.

For a given observation, the local sidereal time can be determined by adding the east longitude λ of the observation site to the Greenwich sidereal time θ_G. Owing to the non-spherical shape of the Earth, it is important to differentiate between

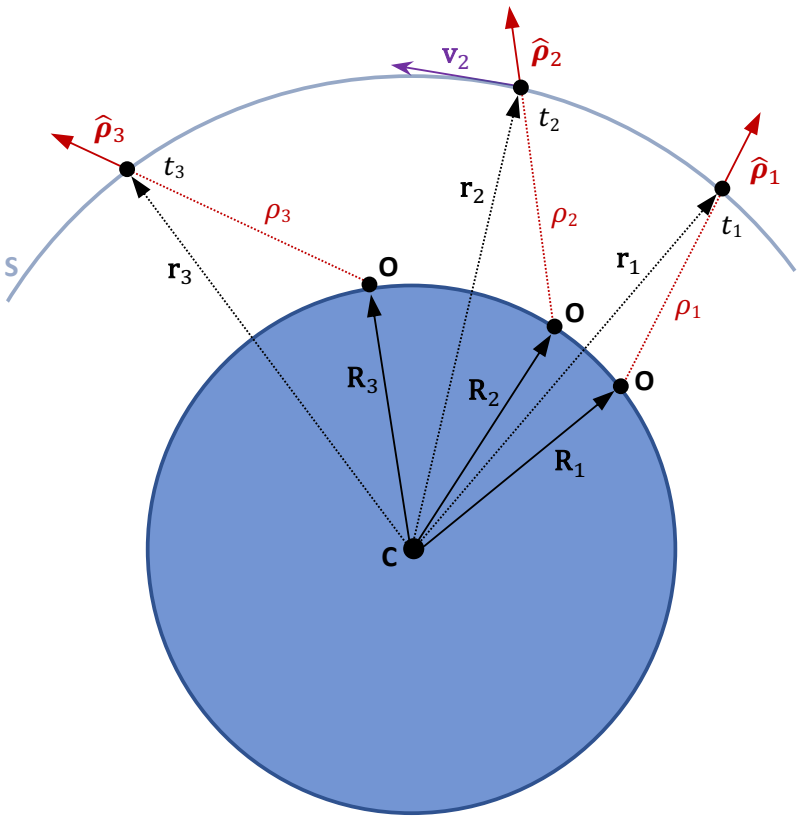

Figure A.1: The geometry underpinning the Gauss method of preliminary orbit determination. Three observations of an orbiting body S are undertaken at times t_i by an observer at O, situated upon the surface of the Earth, with center of attraction C. The geocentric position vectors $\mathbf{r}_i$ are given by the vector sums of the observer position vectors $\mathbf{R}_i$ and the slant vectors $\boldsymbol{\rho}_i = \rho_i \hat{\boldsymbol{\rho}}_i$, where $i \in [1, 3]$.

geodetic and geocentric latitude: the former refers to the angle between the normal and the equatorial plane, while the latter is the angle between the radial vector and the equatorial plane. It is this distinction that warrants the inclusion of oblateness terms in Eq. A.2. Visualisations of the local sidereal time and geodetic latitude are provided in Fig. A.2.

The direction cosine vector may be expressed in terms of the topocentric right ascension α_i and declination δ_i measured by the observer at time t_i as

$$\hat{\boldsymbol{\rho}}_i = \cos\alpha_i \cos\delta_i \hat{\mathbf{I}} + \sin\alpha_i \cos\delta_i \hat{\mathbf{J}} + \sin\delta_i \hat{\mathbf{K}}. \tag{A.4}$$

With knowledge of the position and direction cosine vectors for each observation,

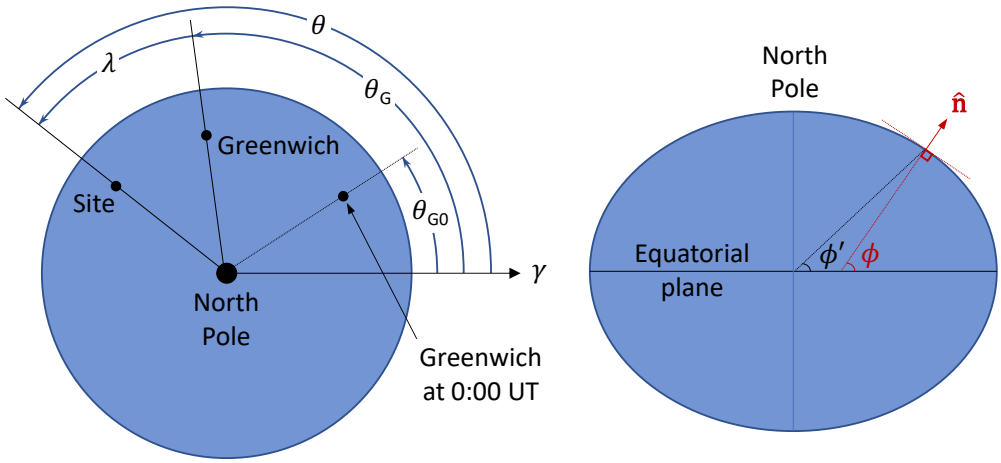

Figure A.2: Left) The local sidereal time θ of an observation site is found by summing its east longitude λ and the Greenwich sidereal time θ_{G}. Right) The geodetic latitude ϕ gives the angle between the normal to the surface and the equatorial plane, while its geocentric counterpart ϕ' refers instead to the angle between the radius and the equatorial plane.

the following algorithm can be performed to obtain a preliminary estimate of the orbiting body's state vector. For brevity, this appendix focuses solely on the key steps of the algorithm, and the interested reader is referred to Curtis [2013] for a complete derivation.

Step 1: Determine the time intervals,

$$\begin{aligned} \tau_1 &= t_1 - t_2 \\ \tau_3 &= t_3 - t_2 \\ \tau &= \tau_3 - \tau_1. \end{aligned} \tag{A.5}$$

Step 2: Compute the cross products,

$$\begin{aligned} \mathbf{p}_1 &= \hat{\boldsymbol{\rho}}_2 \times \hat{\boldsymbol{\rho}}_3 \\ \mathbf{p}_2 &= \hat{\boldsymbol{\rho}}_1 \times \hat{\boldsymbol{\rho}}_3 \\ \mathbf{p}_3 &= \hat{\boldsymbol{\rho}}_1 \times \hat{\boldsymbol{\rho}}_2. \end{aligned} \tag{A.6}$$

Step 3: Compute the scalar triple product,

$$D_0 = \hat{\boldsymbol{\rho}}_1 \cdot \mathbf{p}_1 = \hat{\boldsymbol{\rho}}_1 \cdot (\hat{\boldsymbol{\rho}}_2 \times \hat{\boldsymbol{\rho}}_3)\,. \tag{A.7}$$

Step 4: Determine the scalar quantities,

$$D_{mn} = \mathbf{R}_m \cdot \mathbf{p}_n, \tag{A.8}$$

where $m, n \in [1, 3]$.

Step 5: Calculate the scalar position coefficients,

$$\begin{aligned} A &= \frac{1}{D_0}\left(-D_{12}\frac{\tau_3}{\tau} + D_{22} + D_{32}\frac{\tau_1}{\tau}\right) \\ B &= \frac{1}{6D_0}\left[D_{12}\left(\tau_3^2 - \tau^2\right)\frac{\tau_3}{\tau} + D_{32}\left(\tau^2 - \tau_1^2\right)\frac{\tau_1}{\tau}\right]. \end{aligned} \tag{A.9}$$

Step 6: Determine the scalar quantities,

$$\begin{aligned} E &= \mathbf{R}_2 \cdot \hat{\boldsymbol{\rho}}_2 \\ R_2^2 &= \mathbf{R}_2 \cdot \mathbf{R}_2. \end{aligned} \tag{A.10}$$

Step 7: It is necessary to solve an eighth-order polynomial of the form

$$r_2^8 + ar_2^6 + br_2^3 + c = 0, \tag{A.11}$$

where r_2 is the scalar geocentric radius at time t_2. Compute the coefficients,

$$\begin{aligned} a &= -\left(A^2 + 2AE + R_2^2\right) \\ b &= -2\mu B\left(A + E\right) \\ c &= -\mu^2 B^2. \end{aligned} \tag{A.12}$$

Here, $\mu = 398600\,\mathrm{km^3 s^{-2}}$ is the gravitational parameter of the Earth.

Step 8: Use Newton's method to find the roots of Eq. A.11. An initial starting estimate must be selected in the vicinity of a root by plotting the polynomial for $r_2 > 0$. In cases where there are multiple roots that are physically reasonable, it is necessary to draw upon prior knowledge of the orbit in question and select the most appropriate.

Step 9: Calculate the scalar slant range for time t_2,

$$\rho_2 = A + \frac{\mu B}{r_2^3}, \tag{A.13}$$

alongside those for times t_1 and t_3,

$$\rho_1 = \frac{1}{D_0}\left[\frac{6\left(D_{31}\frac{\tau_1}{\tau_3} + D_{21}\frac{\tau}{\tau_3}\right) r_2^3 + \mu D_{31}\left(\tau^2 - \tau_1^2\right)\frac{\tau_1}{\tau_3}}{6r_2^3 + \mu\left(\tau^2 - \tau_3^2\right)} - D_{11}\right]$$
$$\rho_3 = \frac{1}{D_0}\left[\frac{6\left(D_{13}\frac{\tau_3}{\tau_1} + D_{23}\frac{\tau}{\tau_1}\right) r_2^3 + \mu D_{13}\left(\tau^2 - \tau_3^2\right)\frac{\tau_3}{\tau_1}}{6r_2^3 + \mu\left(\tau^2 - \tau_1^2\right)} - D_{33}\right]. \tag{A.14}$$

Step 10: Using the scalar slant ranges ρ_i, obtain the geocentric position vectors $\mathbf{r}_i$ using Eq. A.1.

Step 11: Compute the approximated Lagrange coefficients,

$$f_1 \approx 1 - \frac{\mu\tau_1^2}{2r_2^3}$$
$$f_3 \approx 1 - \frac{\mu\tau_3^2}{2r_2^3}, \tag{A.15}$$

and,

$$g_1 \approx \tau_1 - \frac{\mu\tau_1^3}{6r_2^3}$$
$$g_3 \approx \tau_3 - \frac{\mu\tau_3^3}{6r_2^3}. \tag{A.16}$$

Step 12: Calculate the velocity vector $\mathbf{v}_2$ at time t_2, as depicted in Fig. A.1, as

$$\mathbf{v}_2 = \frac{1}{f_1 g_3 - f_3 g_1}\left(-f_3\mathbf{r}_1 + f_1\mathbf{r}_3\right). \tag{A.17}$$

Step 13: With knowledge of the state vector $(\mathbf{r}_2, \mathbf{v}_2)$, the algorithm presented in Appendix B can be carried out to obtain the orbital elements for the orbiting body. Prior to this, however, it is possible to iteratively improve the state vector, by determining better-approximated values for the Lagrange coefficients. To achieve this, begin by computing the magnitudes of $\mathbf{r}_2$ and $\mathbf{v}_2$,

$$r_2 = \sqrt{\mathbf{r}_2 \cdot \mathbf{r}_2}$$
$$v_2 = \sqrt{\mathbf{v}_2 \cdot \mathbf{v}_2}. \tag{A.18}$$

Step 14: Calculate α, the reciprocal of the semimajor axis, given by

$$\alpha = \frac{2}{r_2} - \frac{v_2^2}{\mu}. \tag{A.19}$$

Step 15: Find the radial component of $\mathbf{v}_2$,

$$v_{2r} = \frac{\mathbf{v}_2 \cdot \mathbf{r}_2}{r_2}. \tag{A.20}$$

Step 16: Solve the universal Kepler's equation for the universal variables χ_1 and χ_3. Appropriate initial estimates are given by $\chi_{i0} = \sqrt{\mu}|\alpha|\tau_i$. For each updated value χ_{ij}, calculate

$$\begin{aligned} f(\chi_{ij}) &= \frac{r_2 v_{2r}}{\sqrt{\mu}}\chi_{ij}^2 C(\alpha\chi_{ij}^2) + (1-\alpha r_2)\,\chi_{ij}^3 S(\alpha\chi_{ij}^2) + r_2\chi_{ij} - \sqrt{\mu}\Delta t \\ f'(\chi_{ij}) &= \frac{r_2 v_{2r}}{\sqrt{\mu}}\chi_{ij}\left[1-\alpha\chi_{ij}^2 S(\alpha\chi_{ij}^2)\right] + (1-\alpha r_2)\,\chi_{ij}^2 C(\alpha\chi_{ij}^2) + r_2, \end{aligned} \tag{A.21}$$

where $C(z)$ and $S(z)$ are Stumpff functions ($z_i = \alpha\chi_i^2$), which can be expressed in terms of trigonometric functions as

$$C(z) = \begin{cases} \dfrac{1-\cos\sqrt{z}}{z} & (z>0) \\ \dfrac{\cosh\sqrt{-z}-1}{-z} & (z<0) \\ \dfrac{1}{2} & (z=0), \end{cases} \tag{A.22}$$

and

$$S(z) = \begin{cases} \dfrac{\sqrt{z}-\sin\sqrt{z}}{\left(\sqrt{z}\right)^3} & (z>0) \\ \dfrac{\sinh\sqrt{-z}-\sqrt{-z}}{\left(\sqrt{-z}\right)^3} & (z<0) \\ \dfrac{1}{6} & (z=0), \end{cases} \tag{A.23}$$

respectively. Next, evaluate the ratio $\eta_i = f(\chi_{ij})/f'(\chi_{ij})$. If $|\eta_i|$ exceeds a selected tolerance (say, 10^{-8}), compute an updated value for χ_i,

$$\chi_{i(j+1)} = \chi_{ij} - \eta_i, \tag{A.24}$$

and feed this back into Eq. A.21. Repeat this procedure until η_i falls below the desired tolerance.

Step 17: Use χ_1 and χ_3 to recalculate the Lagrange coefficients,

$$\begin{aligned} f_1 &= 1 - \frac{\chi_1^2}{r_2} C(\alpha\chi_1^2) \\ f_3 &= 1 - \frac{\chi_3^2}{r_2} C(\alpha\chi_3^2), \end{aligned} \tag{A.25}$$

and

$$\begin{aligned} g_1 &= \tau_1 - \frac{1}{\sqrt{\mu}} \chi_1^3 S(\alpha\chi_1^2) \\ g_3 &= \tau_3 - \frac{1}{\sqrt{\mu}} \chi_3^3 S(\alpha\chi_3^2). \end{aligned} \tag{A.26}$$

Step 18: Compute the coefficients,

$$\begin{aligned} c_1 &= \frac{g_3}{f_1 g_3 - f_3 g_1} \\ c_3 &= -\frac{g_1}{f_1 g_3 - f_3 g_1}, \end{aligned} \tag{A.27}$$

and use them to update the slant ranges,

$$\begin{aligned} \rho_1 &= \frac{1}{D_0} \left(-D_{11} + \frac{1}{c_1} D_{21} - \frac{c_3}{c_1} D_{31} \right) \\ \rho_2 &= \frac{1}{D_0} \left(-c_1 D_{12} + D_{22} - c_3 D_{32} \right) \\ \rho_3 &= \frac{1}{D_0} \left(-\frac{c_1}{c_3} D_{13} + \frac{1}{c_3} D_{23} - D_{33} \right). \end{aligned} \tag{A.28}$$

Step 19: With the slant ranges updated, recalculate the geocentric position vectors $\mathbf{r}_i$ using Eq. A.1. Then update the velocity vector $\mathbf{v}_2$ by evaluating Eq. A.17 with the updated Lagrange coefficients and position vectors.

Step 20: Repeat the improvement algorithm (Step 13 onwards) until there is no further change in the slant ranges ρ_i, to the desired degree of precision. When this is achieved, the resulting state vector $(\mathbf{r}_2, \mathbf{v}_2)$ can be used to obtain the orbital elements for the orbiting body via the algorithm presented in Appendix B.

Appendix B

Determining orbital elements from the state vector

If all six components of the state vector $(\mathbf{r}, \mathbf{v})$ for an orbiting body are known, it is possible to obtain the corresponding Keplerian orbital elements (e, a, i, Ω, ω, θ), as defined and illustrated for the geocentric frame in Section 1.1. Below, an overview of the necessary steps that must be carried out to determine orbital elements from the state vector of an orbiting body is provided, adapted from Curtis [2013].

Step 1: Calculate the distance and speed,

$$\begin{aligned} r &= \sqrt{\mathbf{r} \cdot \mathbf{r}} \\ v &= \sqrt{\mathbf{v} \cdot \mathbf{v}}, \end{aligned} \tag{B.1}$$

followed by the radial velocity,

$$v_r = \frac{\mathbf{r} \cdot \mathbf{v}}{r}. \tag{B.2}$$

Step 2: Compute the specific angular momentum,

$$\mathbf{h} = \mathbf{r} \times \mathbf{v}, \tag{B.3}$$

and its magnitude,

$$h = \sqrt{\mathbf{h} \cdot \mathbf{h}}. \tag{B.4}$$

Step 3: Compute the inclination,

$$i = \arccos\left(\frac{h_z}{h}\right), \tag{B.5}$$

where h_z is the z-component of the specific angular momentum.

Step 4: Calculate the vector,

$$\mathbf{N} = \hat{\mathbf{K}} \times \mathbf{h}, \tag{B.6}$$

and its magnitude,

$$N = \sqrt{\mathbf{N} \cdot \mathbf{N}}, \tag{B.7}$$

defining the node line.

Step 5: Compute the right ascension of the ascending node,

$$\Omega = \begin{cases} \arccos\left(\dfrac{N_x}{N}\right) & (N_y \geq 0) \\ 2\pi - \arccos\left(\dfrac{N_x}{N}\right) & (N_y < 0), \end{cases} \tag{B.8}$$

where the imposed conditions ensure that the correct quadrant is assigned. Note that the ascending node lies on the positive side of the XZ plane when $N_y \geq 0$, such that $0 \leq \Omega < \pi$, while $N_y < 0$ implies that $\pi \leq \Omega < 2\pi$.

Step 6: Compute the eccentricity vector,

$$\mathbf{e} = \frac{1}{\mu}\left[\left(v^2 - \frac{\mu}{r}\right)\mathbf{r} - r v_r \mathbf{v}\right], \tag{B.9}$$

and its magnitude,

$$e = \sqrt{\mathbf{e} \cdot \mathbf{e}} = \sqrt{1 + \frac{h^2}{\mu^2}\left(v^2 - \frac{2\mu}{r}\right)}. \tag{B.10}$$

This gives the eccentricity.

Step 7: Calculate the argument of perigee,

$$\omega = \begin{cases} \arccos\left(\dfrac{\mathbf{N} \cdot \mathbf{e}}{Ne}\right) & (e_z \geq 0) \\ 2\pi - \arccos\left(\dfrac{\mathbf{N} \cdot \mathbf{e}}{Ne}\right) & (e_z < 0), \end{cases} \tag{B.11}$$

where the imposed conditions once again ensure that the correct quadrant is assigned. Note that the perigee sits above the equatorial plane when $\mathbf{e}$ has a component in the positive Z direction, so $0 \leq \omega < \pi$ is imposed when $e_z \geq 0$. If the perigee lies below the equatorial plane, the opposite is true, such that $\pi \leq \omega < 2\pi$ for $e_z < 0$.

Step 8: Compute the true anomaly,

$$\theta = \begin{cases} \arccos\left(\dfrac{\mathbf{e}\cdot\mathbf{r}}{er}\right) & (v_r \geq 0) \\ 2\pi - \arccos\left(\dfrac{\mathbf{e}\cdot\mathbf{r}}{er}\right) & (v_r < 0), \end{cases} \tag{B.12}$$

where the imposed conditions ensure that the correct quadrant is assigned. In this case, the radial velocity v_r is used as the distinguishing factor. If $v_r \geq 0$, the orbiting body is moving away from perigee and $0 \leq \theta < \pi$. A negative radial velocity instead implies that the body is moving toward perigee, such that $\pi \leq \theta < 2\pi$.

Step 9: Having determined the orbital elements for the orbiting body, other useful parameters can be calculated The perigee radius r_p is given by

$$r_p = \frac{h^2}{\mu\left[1 + e\cos(0)\right]}, \tag{B.13}$$

while the apogee radius r_a is instead calculated as

$$r_a = \frac{h^2}{\mu\left[1 + e\cos(\pi)\right]}. \tag{B.14}$$

The semi-major axis a can then be determined,

$$a = \frac{1}{2}\left(r_p + r_a\right). \tag{B.15}$$

Finally, the period T of the orbit can be found using Kepler's Third Law,

$$T = \frac{2\pi a^{\frac{3}{2}}}{\sqrt{\mu}}. \tag{B.16}$$

Appendix C

MCMC diagnostics for `tlemcee`

This appendix provides supplementary information regarding the inner workings of the `tlemcee` package introduced in Chapter 5. Specifically, the diagnostic plots presented herein correspond to the exemplar model fit for Astra 1N, shown previously in Fig. 5.9.

The prior information used for all GSO test cases in Chapter 5 is given in Table C.1. To set the MCMC underway, walkers are initialised in a small gaussian ball around the initial guesses for the model parameters, and subsequently fed as input to the sampler. The walkers begin to sample from the parameter space, constrained by the limits imposed by the uniform priors, and go on to traverse an explorative path according to the sampling algorithm employed by the `emcee` package (see Section 2.5.2).

In Fig. C.1, time series are shown for the three angular model parameters that are poorly determined by the Gauss method for circular and equatorial GEO cases,

Table C.1: Uniform priors employed by the `tlemcee` orbit refiner for all GSO test cases in Chapter 5.

Parameter	Lower limit	Upper limit	Justification
Inclination [deg]	0.0	60.0	GSO catalogue
Eccentricity	0.0	0.1	Generous range
RAAN [deg]	0.0	360.0	Full parameter space
Argument of Perigee [deg]	0.0	360.0	Full parameter space
Mean Anomaly [deg]	0.0	360.0	Full parameter space
Mean Motion [revs/day]	0.99	1.01	GSO catalogue
Ballistic Coefficient	-4e-6	+2e-6	GSO catalogue

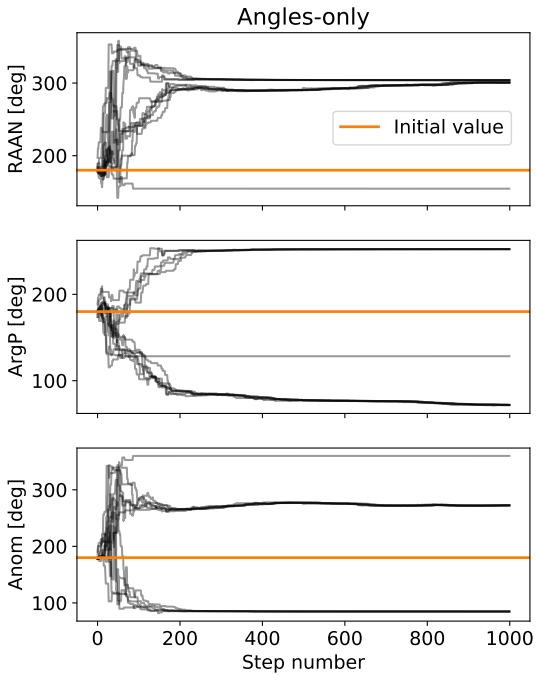

Figure C.1: Time series of parameters in the `tlemcee` sampler chain for the preliminary angles-only MCMC run undertaken as part of the Astra 1N case study, testing the 'IOD input' approach described in Chapter 5. The input dataset comprises a pair of 4 hour orbital arcs extracted from two consecutive nights of RASA observations (20180618, 20180619). Initial values (orange) are set to 180° for the three variable parameters. The other model parameters remain fixed at their IOD value for the duration of the angles-only MCMC run. The chain is mapped out by 12 walkers over the course of 1000 steps.

namely the RAAN, argument of perigee and mean anomaly. With the other elements fixed to their preliminary IOD values, these three 'problem' parameters are allowed to explore the full parameter space [0°, 360°]. The walkers very rapidly (within 50 steps) fan out and sample from a wide range of angles, eventually converging on high likelihood solutions.

This is a particularly effective example for conveying the potential degeneracies that can arise in the search for an orbital solution. For the argument of perigee and mean anomaly (which are co-dependent, as both are defined relative to the perigee), two dominant streams of walkers are observed to converge upon different solutions. In order to find the 'best' solution for these cases, the parameter values resulting in the maximum likelihood solutions over the course of the MCMC must be extracted from the sampler chain. For cases that converge upon a single solution, a very good approximation of this maximal likelihood parameter set can be obtained

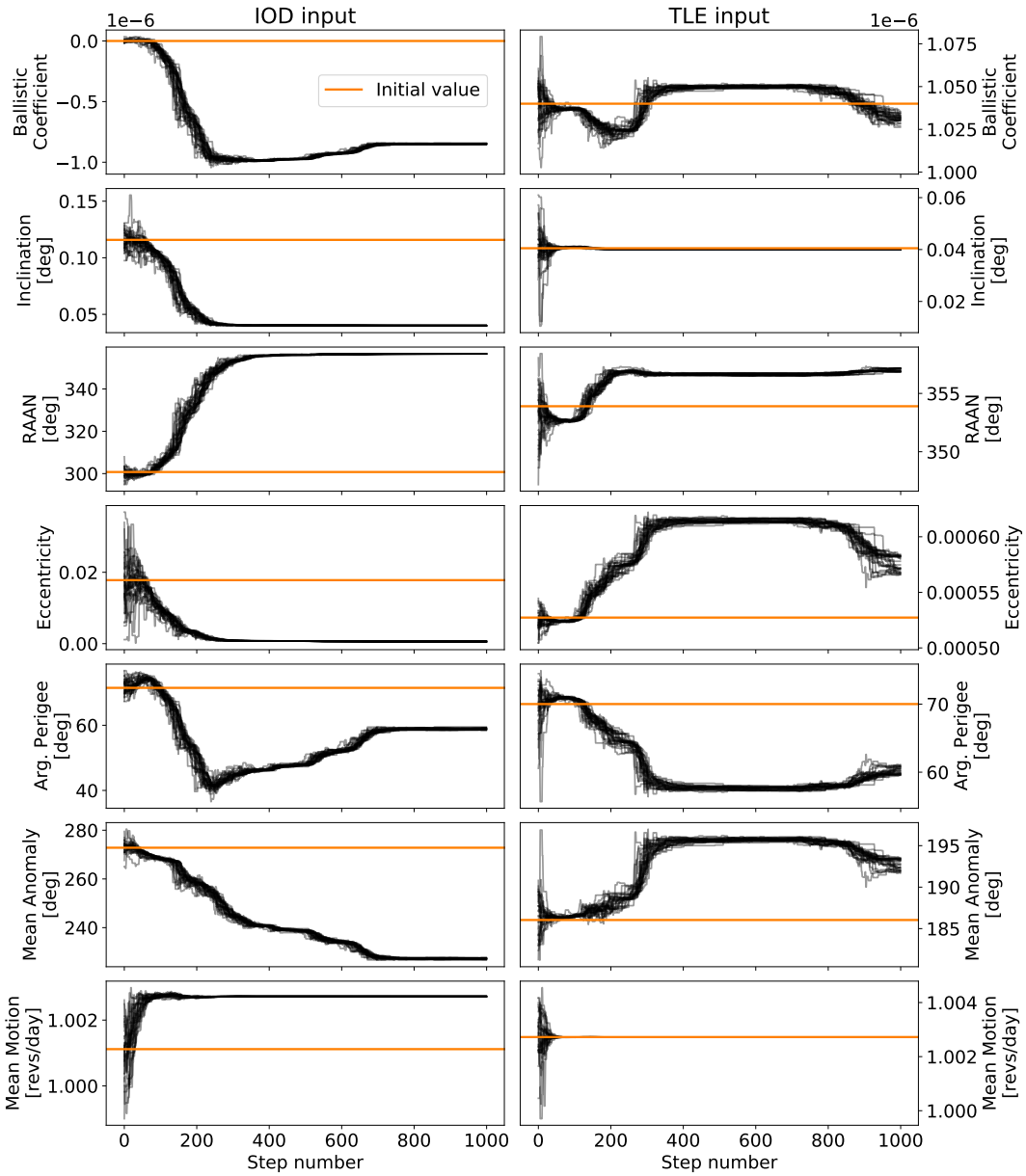

Figure C.2: Time series of parameters in the `tlemcee` sampler chains for the full MCMC runs undertaken as part of the Astra 1N case study, testing the 'IOD input' (left) and 'TLE input' (right) approaches described in Chapter 5. The input dataset for both cases comprises a pair of 4 hour orbital arcs extracted from two consecutive nights of RASA observations (20180618, 20180619). Initial values are marked in orange. For the 'IOD input' case, initial estimates of the model parameters are based on the IOD solution or the angles-only MCMC run, as appropriate. In the 'TLE input' case, the initial values are instead informed by the TLE. The chains are mapped out by 28 walkers over the course of 1000 steps.

by taking the median of the flattened region of the sampler chain. This method provides a simple way of estimating the uncertainties in the parameter values, as the standard deviations can be computed for the same region.

With reasonable estimates for the RAAN, argument of perigee and mean anomaly, a second run of the sampler is conducted with initial values updated appropriately, this time allowing all relevant parameters to vary. The time series for this run are shown in the left-hand column of Fig. C.2. In the right-hand column, time series for an analogous run are provided, using initial values derived from the relevant TLE, with a reference epoch closest to the start time of the first night of RASA observations. As expected, a greater degree of wandering from the initial values is observed for the 'IOD input' case, as the walkers are initialised further from the 'truth'. After roughly 600 steps, the walkers converge on a high likelihood solution and the chain flattens. For all the MCMC runs presented in this work, the number of walkers is set to four times the number of parameters and the sampler chain is limited to 1000 steps. This configuration has been found to strike a reasonable balance between computational runtime and convergence.

In the 'TLE input' run, however, the walkers begin to wander again even after the chain has seemingly flattened. Future development of the code will aim to implement a check for convergence, to ensure that the chain has settled for a reasonable number of steps prior to the extraction of a 'best' set of parameters. Within the scope of this work, the solution with the maximal likelihood uncovered by the chain is taken for the TLE-informed case. For the 'IOD input' case, the flattened region of the sampler chain is easily extracted by applying a 'burn-in' cut of 700 steps. The resulting sub-sample is used to construct the corner plot provided in Fig. C.3. The corner plot is a useful diagnostic tool which demonstrates the covariances between the parameters; it gives the 1D and 2D projections of the posterior probability distributions.

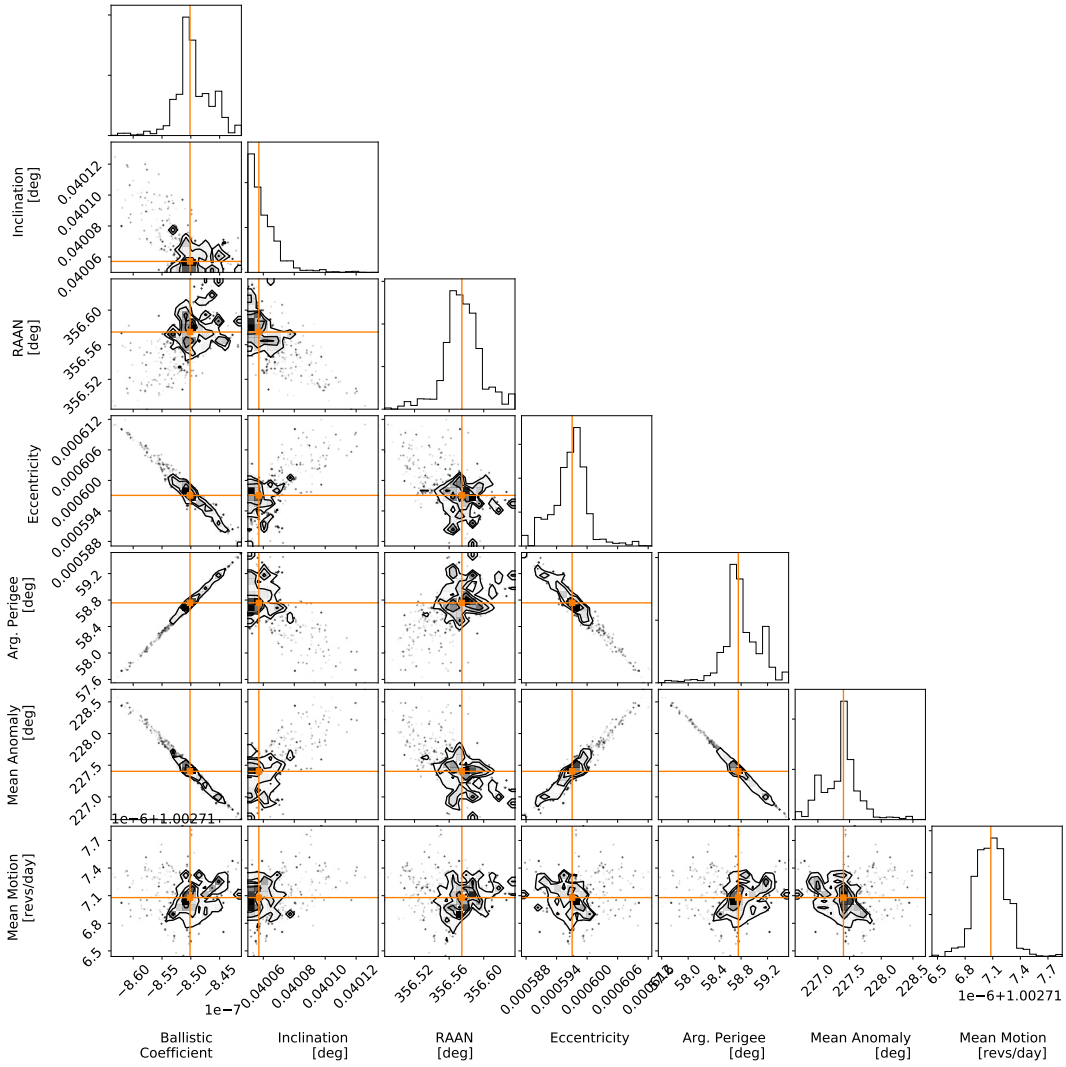

Figure C.3: Corner plot showing the 1D and 2D projections of the posterior probability distribution for the full `tlemcee` MCMC run undertaken as part of the Astra 1N case study, testing the 'IOD input' approach described in Chapter 5. The input dataset comprises a pair of 4 hour orbital arcs extracted from two consecutive nights of RASA observations (20180618, 20180619). A 'burn-in' cut of 700 steps is applied to sample from the flattened regions in the parameter time series shown in Fig. C.2. The 'best' model is obtained by taking the median values of these regions within the sampler chain, marked in orange for each panel.

Bibliography

Y. A. Abdel-Aziz. An analytical theory for avoidance collision between space debris and operating satellites in LEO. *Applied Mathematical Modelling*, 37(18-19):8283–8291, 2013.

K. J. Abercromby, P. Seitzer, H. M. Rodriguez, E. S. Barker, et al. Survey and chase: A new method of observations for the Michigan Orbital DEbris Survey Telescope (MODEST). *Acta Astronautica*, 65(1-2):103–111, 2009.

K. J. Abercromby, P. Seitzer, H. M. Cowardin, E. S. Barker, et al. Michigan Orbital DEbris Survey Telescope Observations of the Geosynchronous Orbital Debris Environment. Observing Years: 2007-2009. 2011.

J. Africano, P. Kervin, D. Hall, P. Sydney, et al. Understanding photometric phase angle corrections. In *Proceedings of the 4^{th} European Conference on Space Debris*, volume 587, pages 141–146, 2005.

G. S. Aglietti, B. Taylor, S. Fellowes, T. Salmon, et al. The active space debris removal mission RemoveDebris. Part 2: in orbit operations. *Acta Astronautica*, 168:310–322, 2020.

V. Akhmetov, S. Khlamov, V. Savanevych, and E. Dikov. Cloud Computing Analysis of Indian ASAT Test on March 27, 2019. In *2019 IEEE International Scientific-Practical Conference Problems of Infocommunications, Science and Technology (PIC S&T)*, pages 315–318. IEEE, 2019a.

V. Akhmetov, V. Savanevych, and E. Dikov. Analysis of the Indian ASAT test on 27 March 2019. *arXiv preprint arXiv:1905.09659*, 2019b.

A. A. Albuja, D. J. Scheeres, and J. W. McMahon. Evolution of angular velocity for defunct satellites as a result of YORP: An initial study. *Advances in Space Research*, 56(2):237–251, 2015.

A. A. Albuja, D. J. Scheeres, R. L. Cognion, W. Ryan, et al. The YORP effect on the GOES 8 and GOES 10 satellites: A case study. *Advances in Space Research*, 61(1):122–144, 2018.

F. Alby, E. Lansard, and T. Michal. Collision of Cerise with space debris. In *Second European Conference on Space Debris*, volume 393, page 589, 1997.

F. Alby, M. Boer, B. Deguine, I. Escane, et al. Status of CNES optical observations of space debris in geostationary orbit. *Advances in Space Research*, 34(5):1143–1149, 2004.

P. V. Anderson and H. Schaub. Local debris congestion in the geosynchronous environment with population augmentation. *Acta Astronautica*, 94(2):619–628, 2014.

P. V. Anderson, D. S. McKnight, F. D. Pentino, and H. Schaub. Operational considerations of GEO debris synchronization dynamics. In *66th International Astronautical Congress, IAC-15 A*, volume 6, page 7, 2015.

P. D. Anz-Meador, J. N. Opiela, D. Shoots, and J.-C. Liou. History of on-orbit satellite fragmentations. 2018.

G. D. Badhwar and P. D. Anz-Meador. Determination of the area and mass distribution of orbital debris fragments. *Earth, Moon, and Planets*, 45(1):29–51, 1989.

K. Barbary. SEP: Source Extractor as a library. *The Journal of Open Source Software*, 1(6):59, 2016.

E. Barker, K. Jarvis, J. Africano, K. Jorgensen, et al. The GEO environment as determined by the CDT between 1998 and 2002. In *4^{th} European Conference on Space Debris*, volume 587, page 135, 2005.

B. Bastida Virgili, J. C. Dolado, H. G. Lewis, J. Radtke, et al. Risk to space sustainability from large constellations of satellites. *Acta Astronautica*, 126:154–162, 2016.

D. Bédard, G. A. Wade, and A. Jolley. Interpretation of spectrometric measurements of active geostationary satellites. In *Proceedings of the Advanced Maui Optical and Space Surveillance (AMOS) Technology Conference*, 2014.

D. Beisecker, F. Seiz, N. Bartels, W. Riede, et al. Surface Modification of Space Materials Induced by Low Energetic Particle Irradiation. In *Proceedings of the*

Advanced Maui Optical and Space Surveillance (AMOS) Technologies Conference, 2020.

C. J. Benson, D. J. Scheeres, W. H. Ryan, E. V. Ryan, et al. GOES spin state diversity and the implications for GEO debris mitigation. *Acta Astronautica*, 167:212–221, 2020.

N. Bérend and X. Olive. Bi-objective optimization of a multiple-target active debris removal mission. *Acta Astronautica*, 122:324–335, 2016.

E. Bertin and S. Arnouts. SExtractor: Software for source extraction. *Astronomy and Astrophysics Supplement Series*, 117(2):393–404, 1996.

C. R. Binz, M. A. Davis, B. E. Kelm, and C. I. Moore. Optical survey of the tumble rates of retired GEO satellites. Technical report, NAVAL RESEARCH LAB WASHINGTON DC, 2014.

C. Blackerby, A. Okamoto, Y. Kobayashi, K. Fujimoto, et al. The ELSA-d End-of-life Debris Removal Mission: Preparing for Launch. In *70th International Astronautical Congress*, 2019.

J. A. Blake, P. Chote, D. Pollacco, D. Veras, et al. Optical imaging of faint geosynchronous debris with the Isaac Newton Telescope. In *Proceedings of the Advanced Maui Optical and Space Surveillance (AMOS) Technologies Conference*, 2019.

J. A. Blake, P. Chote, D. Pollacco, D. Veras, et al. Supplementing a survey of geosynchronous debris with commercial-off-the-shelf equipment. In *Proceedings of the Advanced Maui Optical and Space Surveillance (AMOS) Technologies Conference*, 2020a.

J. A. Blake, P. Chote, D. Pollacco, and R. West. GEOMON (DASA Phase 1) Deliverable 6: Data Rate Analysis. Technical report, Harwell Associates Ltd and University of Warwick, 2020b.

J. A. Blake, P. Chote, D. Pollacco, W. Feline, et al. DebrisWatch I: A survey of faint geosynchronous debris. *Advances in Space Research*, 67(1):360–370, 2021.

M. Bolden, P. Sydney, and P. Kervin. Pan-STARRS status and GEO Observations Results. Technical report, Air Force Research Lab Kihei Maui HI Detachment 15, 2011.

M. Bolden, T. Craychee, and E. Griggs. An Evaluation of Observing Constellation Orbit Stability, Low Signal-to-Noise, and the Too-Short-Arc Challenges in

the Cislunar Domain. In *Proceedings of the Advanced Maui Optical and Space Surveillance (AMOS) Technologies Conference*, page (in press), 2020.

C. Bonnal, J.-M. Ruault, and M.-C. Desjean. Active debris removal: Recent progress and current trends. *Acta Astronautica*, 85:51–60, 2013.

E. M. Botta, I. Sharf, and A. K. Misra. Contact dynamics modeling and simulation of tether nets for space-debris capture. *Journal of Guidance, Control, and Dynamics*, 40(1):110–123, 2017.

W. H. Boyce. Examination of NORAD TLE accuracy using the iridium constellation. *Spaceflight mechanics*, 119:2133–2142, 2004.

L. Bradley, B. Sipocz, T. Robitaille, E. Tollerud, et al. Photutils: Photometry tools. *Astrophysics Source Code Library*, pages ascl–1609, 2016.

V. Braun, A. Lüpken, S. Flegel, J. Gelhaus, et al. Active debris removal of multiple priority targets. *Advances in Space Research*, 51(9):1638–1648, 2013.

V. Braun, T. Flohrer, H. Krag, K. Merz, et al. Operational support to collision avoidance activities by ESA's space debris office. *CEAS Space Journal*, 8(3): 177–189, 2016.

V. Braun, A. Horstmann, B. Reihs, S. Lemmens, et al. Exploiting orbital data and observation campaigns to improve space debris models. *The Journal of the Astronautical Sciences*, 66(2):192–209, 2019.

E. J. Breen, R. Jones, and H. Talbot. Mathematical morphology: A useful set of tools for image analysis. *Statistics and Computing*, 10(2):105–120, 2000.

M. J. Bruno and H. J. Pernicka. Tundra constellation design and stationkeeping. *Journal of spacecraft and rockets*, 42(5):902–912, 2005.

M. Capderou. *Satellites: orbits and missions*. Springer Science & Business Media, 2002.

M. Capderou. *Handbook of Satellite Orbits: From Kepler to GPS*. Springer Science & Business, Berlin, Germany, 2014.

T. Cardona, P. Seitzer, A. Rossi, F. Piergentili, et al. BVRI photometric observations and light-curve analysis of GEO objects. *Advances in Space Research*, 58 (4):514–527, 2016.

S. Chib and E. Greenberg. Understanding the metropolis-hastings algorithm. *The american statistician*, 49(4):327–335, 1995.

P. Chote. EUSST Deliverable 2: Variety and basic characteristics of debris/satellite rotation as evidenced from light curves. Technical report, University of Warwick, 2020.

P. Chote, J. A. Blake, and D. Pollacco. Precision Optical Light Curves of LEO and GEO Objects. *Proceedings of the Advanced Maui Optical and Space Surveillance (AMOS) Technology Conference*, page 52, 2019.

P. Chote, J. A. Blake, D. Pollacco, and R. West. GEOMON (DASA Phase 1) Deliverables 2–5: Pipeline Performance; Survey Depth; Astrometric Analysis; Rotation Analysis. Technical report, Harwell Associates Ltd and University of Warwick, 2020.

C. C. Chow, C. J. Wetterer, K. Hill, C. Gilbert, et al. Cislunar Periodic Orbit Families and Expected Observational Features. In *Proceedings of the Advanced Maui Optical and Space Surveillance (AMOS) Technologies Conference*, page (in press), 2020.

E. L. Christiansen, J. L. Hyde, and R. P. Bernhard. Space shuttle debris and meteoroid impacts. *Advances in Space Research*, 34(5):1097–1103, 2004.

A. C. Clarke. Extra-terrestrial relays: can rocket stations give world-wide radio coverage? In *Progress in Astronautics and Rocketry*, volume 19, pages 3–6. Elsevier, 1966.

R. L. Cognion. Rotation Rates of Inactive Satellites Near Geosynchronous Earth Orbit. In *Proceedings of the Advanced Maui Optical and Space Surveillance (AMOS) Technologies Conference*, 2014.

E. Cordelli, P. Schlatter, and T. Schildknecht. Simultaneous multi-filter photometric characterization of space debris at the Swiss Optical Ground Station and Geodynamics Observatory Zimmerwald. In *Proceedings of the Advanced Maui Optical and Space Surveillance (AMOS) Technology Conference*, 2018.

R. Corey, N. Gascon, J. Delgado, G. Gaeta, et al. Performance and evolution of stationary plasma thruster electric propulsion for large communications satellites. In *28th AIAA International Communications Satellite Systems Conference (ICSSC-2010)*, page 8688, 2010.

H. Cowardin, P. Anz-Meador, and J. A. Reyes. Characterizing GEO Titan IIIC transtage fragmentations using ground-based and telescopic measurements. 2017.

H. M. Cowardin, J. M. Hostetler, J. I. Murray, J. A. Reyes, et al. Optical Characterization of DebriSat Fragments in Support of Orbital Debris Environmental Models. In *Proceedings of the Advanced Maui Optical and Space Surveillance (AMOS) Technologies Conference*, 2020.

M. W. Craig, S. M. Crawford, C. Deil, C. Gomez, et al. ccdproc: Ccd data reduction software. *Astrophysics Source Code Library*, pages ascl–1510, 2015.

P. M. Cunio, M. Bantel, B. R. Flewelling, W. Therien, et al. Photometric and Other Analyses of Energetic Events Related to 2017 GEO RSO Anomalies. In *Proceedings of the Advanced Maui Optical and Space Surveillance (AMOS) Technologies Conference*, 2017.

P. M. Cunio, B. R. Flewelling, M. Bantel, D. Hendrix, et al. Remote Sensing-Enabled Methods for Attributing Energetic On-Orbit Anomalies to Natural or Artificial Causes. *LPICo*, 2109:6160, 2019.

H. D. Curtis. *Orbital mechanics for engineering students*, pages 187–293. Butterworth-Heinemann, Oxford, UK, 2013.

G. Curzi, D. Modenini, and P. Tortora. Large constellations of small satellites: A survey of near future challenges and missions. *Aerospace*, 7(9):133, 2020.

Y. Dai, D. Han, and H. Minn. Impacts of Large-Scale NGSO Satellites: RFI and A New Paradigm for Satellite Communications and Radio Astronomy Systems. *IEEE Transactions on Communications*, 67(11):7840–7855, 2019.

P. Dao, K. Weasenforth, J. Hollon, T. Payne, et al. Machine learning-based stability assessment and change detection for geosynchronous satellites. *Proceedings of the Advanced Maui Optical and Space Surveillance (AMOS) Technology Conference*, page 39, 2018.

P. Dao, K. Haynes, V. Frey, C. Hufford, et al. Simulated Photometry of Objects in Cislunar Orbits. In *Proceedings of the Advanced Maui Optical and Space Surveillance (AMOS) Technologies Conference*, page (in press), 2020.

T. Dautermann. Civil air navigation using GNSS enhanced by wide area satellite based augmentation systems. *Progress in Aerospace Sciences*, 67:51–62, 2014.

G. K. Davis. History of the NOAA satellite program. *Journal of Applied Remote Sensing*, 1(1):012504, 2007.

L. T. DeLuca, F. Bernelli, F. Maggi, P. Tadini, et al. Active space debris removal by a hybrid propulsion module. *Acta Astronautica*, 91:20–33, 2013.

V. Dicky, Z. Khutorovsky, A. Kuricshah, A. Menshicov, et al. The Russian space surveillance system and some aspects of spaceflight safety. *Advances in Space Research*, 13(8):21–31, 1993.

H. N. Do, T.-J. Chin, N. Moretti, M. K. Jah, et al. Robust foreground segmentation and image registration for optical detection of GEO objects. *Advances in Space Research*, 64(3):733–746, 2019.

J. C. Dolado-Perez, R. Di Costanzo, and B. Revelin. Introducing medee-a new orbital debris evolutionary model. *ESASP*, 723:33, 2013.

E. Doornbos and H. Klinkrad. Modelling of space weather effects on satellite drag. *Advances in Space Research*, 37(6):1229–1239, 2006.

J. M. Dow, R. E. Neilan, and C. Rizos. The international GNSS service in a changing landscape of global navigation satellite systems. *Journal of geodesy*, 83(3-4):191–198, 2009.

G. Drolshagen. Impact effects from small size meteoroids and space debris. *Advances in Space Research*, 41(7):1123–1131, 2008.

G. Drolshagen, J. A. M. McDonnell, T. J. Stevenson, S. Deshpande, et al. Optical survey of micrometeoroid and space debris impact features on EURECA. *Planetary and Space Science*, 44(4):317–340, 1996.

R. Dudziak, S. Tuttle, and S. Barraclough. Harpoon technology development for the active removal of space debris. *Advances in Space Research*, 56(3):509–527, 2015.

M. A. Earl, P. W. Somers, K. Kabin, D. Bédard, et al. Estimating the spin axis orientation of the Echostar-2 box-wing geosynchronous satellite. *Advances in Space Research*, 61(8):2135–2146, 2018.

T. Ebisuzaki, M. N. Quinn, S. Wada, L. W. Piotrowski, et al. Demonstration designs for the remediation of space debris from the International Space Station. *Acta Astronautica*, 112:102–113, 2015.

P. Enge, T. Walter, S. Pullen, C. Kee, et al. Wide area augmentation of the global positioning system. *Proceedings of the IEEE*, 84(8):1063–1088, 1996.

D. P. Engelhart, R. Cooper, H. Cowardin, J. Maxwell, et al. Space weathering experiments on spacecraft materials. *The Journal of the Astronautical Sciences*, 66(2):210–223, 2019.

ESA. Space Debris Office: ESA's Annual Space Environment Report. GEN-DB-LOG-00288-OPS-SD(4), 2020.

S. Fan and C. Frueh. A direct light curve inversion scheme in the presence of measurement noise. *The Journal of the Astronautical Sciences*, 67(2):740–761, 2020.

S. Flegel, J. Gelhaus, C. Wiedemann, P. Vorsmann, et al. The MASTER-2009 space debris environment model. In *Fifth European Conference on Space Debris*, volume 672, 2009.

T. Flohrer, H. Krag, and H. Klinkrad. Assessment and categorization of TLE orbit errors for the US SSN catalogue. *risk*, 8(9):10–11, 2008.

A. Flores-Abad, O. Ma, K. Pham, and S. Ulrich. A review of space robotics technologies for on-orbit servicing. *Progress in Aerospace Sciences*, 68:1–26, 2014.

D. Foreman-Mackey, D. W. Hogg, D. Lang, and J. Goodman. emcee: the MCMC hammer. *Publications of the Astronomical Society of the Pacific*, 125(925):306, 2013.

J. L. Forshaw, G. S. Aglietti, N. Navarathinam, H. Kadhem, et al. RemoveDEBRIS: An in-orbit active debris removal demonstration mission. *Acta Astronautica*, 127: 448–463, 2016.

W. Fraser, M. Alexandersen, M. E. Schwamb, M. Marsset, et al. TRIPPy: trailed image photometry in python. *The Astronomical Journal*, 151(6):158, 2016.

C. Früh and T. Schildknecht. Variation of the area-to-mass ratio of high area-to-mass ratio space debris objects. *Monthly Notices of the Royal Astronomical Society*, 419(4):3521–3528, 2012.

C. Früh, T. M. Kelecy, and M. K. Jah. Coupled orbit-attitude dynamics of high area-to-mass ratio (HAMR) objects: influence of solar radiation pressure, Earth's shadow and the visibility in light curves. *Celestial Mechanics and Dynamical Astronomy*, 117(4):385–404, 2013.

R. Furfaro, R. Linares, and V. Reddy. Space objects classification via light-curve measurements: deep convolutional neural networks and model-based transfer learning. In *Proceedings of the Advanced Maui Optical and Space Surveillance (AMOS) Technology Conference*, 2018.

Gaia-Collaboration, T. Prusti, J. H. J. De Bruijne, A. G. A. Brown, et al. The gaia mission. *Astronomy & Astrophysics*, 595:A1, 2016.

Gaia-Collaboration, A. G. A. Brown, A. Vallenari, T. Prusti, et al. Gaia Data Release 2. Summary of the contents and survey properties. *Astronomy and Astrophysics*, 616, 2018.

S. George, A. Ash, T. Bessell, J. Frith, et al. PHANTOM ECHOES: A Five-Eyes SDA Experiment to Examine GEO Rendezvous and Proximity Operations. In *Proceedings of the Advanced Maui Optical and Space Surveillance (AMOS) Technologies Conference*, page 97, 2020.

J. Geul, E. Mooij, and R. Noomen. TLE uncertainty estimation using robust weighted differencing. *Advances in Space Research*, 59(10):2522–2535, 2017.

A. Ginsburg, B. M. Sipőcz, C. E. Brasseur, P. S. Cowperthwaite, et al. Astroquery: an astronomical web-querying package in python. *The Astronomical Journal*, 157 (3):98, 2019.

R. M. Goldstein, S. J. Goldstein, and D. J. Kessler. Radar observations of space debris. *Planetary and Space Science*, 46(8):1007–1013, 1998.

N. O. Gómez and S. J. Walker. Earth's gravity gradient and eddy currents effects on the rotational dynamics of space debris objects: Envisat case study. *Advances in Space Research*, 56(3):494–508, 2015.

G. A. Graham, N. McBride, A. T. Kearsley, G. Drolshagen, et al. The chemistry of micrometeoroid and space debris remnants captured on hubble space telescope solar cells. *International journal of impact engineering*, 26(1-10):263–274, 2001.

J. Greaves and D. Scheeres. Maneuver Detection for Cislunar Vehicles Using Optical Measurements. In *Proceedings of the Advanced Maui Optical and Space Surveillance (AMOS) Technologies Conference*, page (in press), 2020.

C. M. Green and M. Lomask. *Project Vanguard: The NASA History*. Courier Corporation, 2012.

T. Hadas, K. Kazmierski, and K. Sośnica. Performance of Galileo-only dual-frequency absolute positioning using the fully serviceable Galileo constellation. *GPS Solutions*, 23(4):108, 2019.

J. A. Haimerl and G. P. Fonder. Space fence system overview. In *Proceedings of the Advanced Maui Optical and Space Surveillance (AMOS) Technology Conference*, 2015.

O. R. Hainaut and A. P. Williams. Impact of satellite constellations on astronomical observations with ESO telescopes in the visible and infrared domains. *Astronomy & Astrophysics*, 636:A121, 2020.

D. Hall, B. Calef, K. Knox, M. Bolden, et al. Separating attitude and shape effects for non-resolved objects. In *Proceedings of the Advanced Maui Optical and Space Surveillance (AMOS) Technology Conference*, pages 464–475, 2007.

T. D. Haws, J. S. Zimmerman, and M. E. Fuller. SLS, the gateway, and a lunar outpost in the early 2030s. In *2019 IEEE Aerospace Conference*, pages 1–15. IEEE, 2019.

M. D. Hejduk, H. M. Cowardin, and E. G. Stansbery. Satellite Material Type and Phase Function Determination in Support of Orbital Debris Size Estimation. 2012.

A. A. Henden, D. L. Welch, D. Terrell, and S. E. Levine. The AAVSO photometric all-sky survey (APASS). *American Astronomical Society*, 214:407–02, 2009.

A. A. Henden, M. Templeton, D. Terrell, T. C. Smith, et al. VizieR Online Data Catalog: AAVSO Photometric All Sky Survey (APASS) DR9. *VizieR Online Data Catalog*, 2016.

K. G. Henize, J. F. Stanley, C. A. O'Neill, and B. S. Nowakowski. Detection of orbital debris with GEODSS telescopes. In *Space Debris Detection and Mitigation*, volume 1951, pages 76–84. International Society for Optics and Photonics, 1993.

P. Hickson. A fast algorithm for the detection of faint orbital debris tracks in optical images. *Advances in Space Research*, 62(11):3078–3085, 2018.

P. Hickson. OCS: A Flexible Observatory Control System for Robotic Telescopes with Application to Detection and Characterization of Orbital Debris. In *Proceedings of the First International Orbital Debris Conference, Sugarland, Texas*, 2019.

J. C. Hinks and J. L. Crassidis. Angular velocity bounds via light curve glint duration. In *AIAA Guidance, Navigation, and Control Conference*, page 0627, 2016.

J. C. Hinks, R. Linares, and J. L. Crassidis. Attitude observability from light curve measurements. In *AIAA Guidance, Navigation, and Control (GNC) Conference*, page 5005, 2013.

B. Hofmann-Wellenhof, H. Lichtenegger, and E. Wasle. *GNSS–global navigation satellite systems: GPS, GLONASS, Galileo, and more*. Springer Science & Business Media, 2007.

F. R. Hoots and R. L. Roehrich. Models for propagation of NORAD element sets. Technical report, AEROSPACE DEFENSE COMMAND PETERSON AFB CO OFFICE OF ASTRODYNAMICS, 1980.

F. R. Hoots, P. W. Schumacher Jr, and R. A. Glover. History of analytical orbit modeling in the US space surveillance system. *Journal of Guidance, Control, and Dynamics*, 27(2):174–185, 2004.

S. B. Howell. *Handbook of CCD astronomy*, volume 5. Cambridge University Press, 2006.

M. Hussein, G. Jakllari, and B. Paillassa. On routing for extending satellite service life in leo satellite networks. In *2014 IEEE Global Communications Conference*, pages 2832–2837. IEEE, 2014.

IADC. Space Debris Mitigation Guidelines. IADC-02-01, Revision 1, 6, 2007.

H. Ikeda, T. Hanada, and T. Yasaka. Searching for lost fragments in GEO. *Acta Astronautica*, 63(11-12):1312–1317, 2008.

M. K. Jah. Space surveillance, tracking, and information fusion for space domain awareness. *NATO STO-EN-SCI-292*, 2016.

K. S. Jarvis, J. L. Africano, P. F. Sydney, E. G. Stansbery, et al. Observations of the geosynchronous Earth orbital debris environment using NASA's CCD Debris Telescope. In *Space Debris*, volume 473, pages 95–99, 2001.

A. D. Jaunzemis, M. J. Holzinger, and M. K. Jah. Evidence-based sensor tasking for space domain awareness. In *Proceedings of the Advanced Maui Optical and Space Surveillance (AMOS) Technology Conference*, 2016.

R. Jehn, V. Agapov, and C. Hernández. The situation in the geostationary ring. *Advances in space research*, 35(7):1318–1327, 2005.

A. B. Jenkin, J. P. McVey, J. R. Wilson, and M. E. Sorge. Tundra disposal orbit study. In *Proceedings of the 7^{th} European Conference on Space Debris, Darmstadt*, 2017.

N. L. Johnson. Preliminary analysis of the fragmentation of the Spot 1 Ariane third stage. *Orbital Debris from Upper-Stage Breakup, Washington, DC: American Institute of Aeronautics and Astronautics*, pages 41–100, 1989.

N. L. Johnson. The cause and consequences of a satellite fragmentation: A case study. *Advances in Space Research*, 23(1):165–173, 1999a.

N. L. Johnson. Protecting the GEO environment: policies and practices. *Space Policy*, 15(3):127–135, 1999b.

N. L. Johnson. Evidence for historical satellite fragmentations in and near the geosynchronous regime. *EUROPEAN SPACE AGENCY-PUBLICATIONS-ESA SP*, 473:355–360, 2001.

N. L. Johnson. Orbital debris: the growing threat to space operations. 2010.

E. Jones, T. Oliphant, P. Peterson, et al. SciPy: Open source scientific tools for Python. 2001.

R. Kanzler, T. Schildknecht, T. Lips, B. Fritsche, et al. Space debris attitude simulation-iota (in-orbit tumbling analysis). page 33, 2015.

T. Kelecy and M. Jah. Analysis of high area-to-mass ratio (HAMR) GEO space object orbit determination and prediction performance: Initial strategies to recover and predict HAMR GEO trajectories with no a priori information. *Acta Astronautica*, 69(7-8):551–558, 2011.

T. Kelecy, I. I. Hussein, K. Miller, and J. Coughlin. Probabilistic Analysis of Light Curves. *The Journal of the Astronautical Sciences*, 66(2):142–161, 2019.

T. Kelecy, E. Lambert, S. Akram, and J. Paffett. Characterization of Resident Space Object States Using Functional Data Analysis. In *Proceedings of the Advanced Maui Optical and Space Surveillance (AMOS) Technology Conference*, 2020.

T. S. Kelso. Basics of the geostationary orbit. *Satellite Times*, 4(7):76–7, 1998.

T. S. Kelso. Analysis of the 2007 Chinese ASAT Test and the Impact of its Debris on the Space Environment. In *Proceedings of the Advanced Maui Optical and Space Surveillance (AMOS) Technology Conference*, volume 7, 2007.

T. S. Kelso. Analysis of the Iridium 33 Cosmos 2251 collision. 2009.

J. A. Kennewell and B.-N. Vo. An overview of space situational awareness. In *Proceedings of the 16th International Conference on Information Fusion*, pages 1029–1036. IEEE, 2013.

D. J. Kessler. Report on Orbital Debris by Interagency Group (Space) for National Security Council. *Washington, DC*, 1989.

D. J. Kessler and B. G. Cour-Palais. Collision frequency of artificial satellites: The creation of a debris belt. *Journal of Geophysical Research: Space Physics*, 83(A6): 2637–2646, 1978.

D. J. Kessler, M. J. Maatney, R. C. Reynolds, R. P. Beernhard, et al. A search for a previously unknown source of orbital debris- The possibility of a coolant leak in radar ocean reconnaissance satellites. In *IAF, International Astronautical Congress, 48 th, Turin, Italy*, 1997.

D. J. Kessler, N. L. Johnson, J. C. Liou, and M. Matney. The Kessler Syndrome: implications to future space operations. *Advances in the Astronautical Sciences*, 137(8):2010, 2010.

H. Klinkrad. *Space debris: models and risk analysis*. Springer Science & Business Media, 2006.

C. A. Kluever. Optimal geostationary orbit transfers using onboard chemical-electric propulsion. *Journal of spacecraft and rockets*, 49(6):1174–1182, 2012.

N. I. Koshkin, V. Savanevich, A. Pohorelov, L. Shakun, et al. Ukrainian database and Atlas of light curves of artificial space objects. *Odessa Astronomical Publications*, 30:226–229, 2017.

H. Krag, H. Klinkrad, R. Jehn, S. Flegel, et al. Conclusions from ESA Space Debris Telescope Observations on Space Debris Environment Modelling. In *Proceedings of the European Conference on Space Debris, Darmstadt, Germany*, 2009.

H. Krag, M. Serrano, V. Braun, P. Kuchynka, et al. A 1 cm space debris impact onto the Sentinel-1A solar array. *Acta Astronautica*, 137:434–443, 2017.

W. E. Krag. Visible magnitude of typical satellites in synchronous orbits. Technical report, Massachusetts inst of tech lexington Lincoln Lab, 1974.

P. H. Krisko. The new NASA orbital debris engineering model ORDEM 3.0. In *AIAA/AAS Astrodynamics Specialist Conference*, page 4227, 2014.

P. H. Krisko, S. Flegel, M. J. Matney, D. R. Jarkey, et al. ORDEM 3.0 and MASTER-2009 modeled debris population comparison. *Acta Astronautica*, 113: 204–211, 2015.

V. I. Kudak, V. P. Epishev, V. M. Perig, and I. F. Neybauer. Determining the orientation and spin period of TOPEX/Poseidon satellite by a photometric method. *Astrophysical Bulletin*, 72(3):340–348, 2017.

M. Laas-Bourez, G. Blanchet, M. Boër, E. Ducrotté, et al. A new algorithm for optical observations of space debris with the TAROT telescopes. *Advances in Space Research*, 44(11):1270–1278, 2009.

E. Lacruz, C. Abad, J. J. Downes, F. Hernández-Pérez, et al. High astrometric precision in the calculation of the coordinates of orbiters in the GEO ring. *Revista mexicana de astronomía y astrofísica*, 54(1):0–0, 2018.

J. Lambert. Fengyun-1C Debris Cloud Evolution Over One Decade. In *Proceedings of the Advanced Maui Optical and Space Surveillance (AMOS) Technology Conference*, 2018.

M. H. Lane. The development of an artificial satellite theory using a power-law atmospheric density representation. In *2nd Aerospace Sciences Meeting*, page 35, 1965.

D. Lang, D. W. Hogg, K. Mierle, M. Blanton, et al. Astrometry. net: Blind astrometric calibration of arbitrary astronomical images. *The Astronomical Journal*, 139(5):1782, 2010.

D. Lawrence, D. Bunce, N. G. Mathur, and C. E. Sigler. Wide area augmentation system (WAAS)-program status. In *Proceedings of the 20th International Technical Meeting of the Satellite Division of The Institute of Navigation (ION GNSS 2007)*, pages 892–899, 2007.

S. M. Lederer, E. G. Stansbery, H. M. Cowardin, P. Hickson, et al. The NASA meter class autonomous telescope: Ascension Island. Technical report, National Aeronautics and Space administration Houston TX Lyndon B Johnson, 2013.

S. M. Lederer, C. L. Cruz, B. A. Buckalew, P. Hickson, et al. NASA's Orbital Debris Optical Program: ES-MCAT Nearing Full Operational Capability (FOC). In *Proceedings of the Advanced Maui Optical and Space Surveillance (AMOS) Technology Conference*, 2019.

F. Letizia, S. Lemmens, D. Wood, M. Rathnasabapathy, et al. Contribution from SSA data to the definition of a Space Sustainability Rating. 2020.

M. Levesque. Automatic reacquisition of satellite positions by detecting their expected streaks in astronomical images. In *Proceedings of the Advanced Maui Optical and Space Surveillance (AMOS) Technologies Conference*, 2009.

H. G. Lewis, G. Swinerd, N. Williams, and G. Gittins. DAMAGE: a dedicated GEO debris model framework. *EUROPEAN SPACE AGENCY-PUBLICATIONS-ESA SP*, 473:373–378, 2001.

H. G. Lewis, A. Saunders, G. Swinerd, and R. J. Newland. Effect of thermospheric contraction on remediation of the near-Earth space debris environment. *Journal of Geophysical Research: Space Physics*, 116(A2), 2011.

Z. Li, M. Ziebart, S. Bhattarai, D. Harrison, et al. Fast solar radiation pressure modelling with ray tracing and multiple reflections. *Advances in Space Research*, 61(9):2352–2365, 2018.

R. Liemer and C. F. Chyba. A verifiable limited test ban for anti-satellite weapons. *The Washington Quarterly*, 33(3):149–163, 2010.

R. Linares, M. K. Jah, J. L. Crassidis, and C. K. Nebelecky. Space object shape characterization and tracking using light curve and angles data. *Journal of Guidance, Control, and Dynamics*, 37(1):13–25, 2014.

J.-C. Liou. An active debris removal parametric study for LEO environment remediation. *Advances in Space Research*, 47(11):1865–1876, 2011.

J.-C. Liou. The 2019 US government orbital debris mitigation standard practices. 2020a.

J.-C. Liou. Risks from orbital debris and space situational awareness. In *Proceedings of the 2nd IAA Conference on Space Situational Awareness, Washington DC*, 2020b.

J.-C. Liou and N. L. Johnson. Instability of the present LEO satellite populations. *Advances in Space Research*, 41(7):1046–1053, 2008.

J.-C. Liou and N. L. Johnson. Characterization of the cataloged Fengyun-1C fragments and their long-term effect on the LEO environment. *Advances in Space Research*, 43(9):1407–1415, 2009.

J.-C. Liou, D. T. Hall, P. H. Krisko, and J. N. Opiela. LEGEND–A three-dimensional LEO-to-GEO debris evolutionary model. *Advances in Space Research*, 34(5):981–986, 2004.

J.-C. Liou, N. L. Johnson, and N. M. Hill. Controlling the growth of future LEO debris populations with active debris removal. *Acta Astronautica*, 66(5-6):648–653, 2010.

J.-C. Liou, A. K. Anilkumar, B. Bastida, T. Hanada, et al. Stability of the future LEO environment–an IADC comparison study. In *Proceedings of the 6th European Conference on Space Debris*, volume 723, 2013.

F. Liu, R. Cutri, G. Greanias, V. Duval, et al. Development of the wide-field infrared survey explorer (WISE) mission. In *Modeling, Systems Engineering, and Project Management for Astronomy III*, volume 7017. International Society for Optics and Photonics, 2008.

S. G. Love, D. E. Brownlee, N. L. King, and F. Hörz. Morphology of meteoroid and debris impact craters formed in soft metal targets on the LDEF satellite. *International journal of impact engineering*, 16(3):405–418, 1995.

Y. Lu, C. Zhang, R.-Y. Sun, C.-Y Zhao, et al. Investigations of associated multi-band observations for GEO space debris. *Advances in Space Research*, 59(10): 2501–2511, 2017.

H. Luo, Y.-D. Mao, Y. Yu, and Z.-H. Tang. FocusGEO observations of space debris at Geosynchronous Earth Orbit. *Advances in Space Research*, 64(2):465–474, 2019.

D. J. C. MacKay. *Information theory, inference and learning algorithms*. Cambridge university press, 2003.

J. Mackey. Recent US and Chinese antisatellite activities. Technical report, AIR UNIV MAXWELL AFB AL AIR FORCE RESEARCH INST, 2009.

A. Manis, M. Matney, P. Anz-Meador, and H. Cowardin. The Updated GEO Population for ORDEM 3.1. 2019.

G. Matheron and J. Serra. The birth of mathematical morphology. In *Proceedings of the 6th International Symposium of Mathematical Morphology*, pages 1–16. Sydney, Australia, 2002.

M. Matney, T. Settecerri, N. Johnson, and E. Stansbery. Characterization of the breakup of the pegasus rocket body 1994-029b. In *Second European Conference on Space Debris*, volume 393, page 289, 1997.

M. Matney, R. Goldstein, D. Kessler, and E. Stansbery. Recent results from Goldstone orbital debris radar. *Advances in Space Research*, 23(1):5–12, 1999.

J. McCormac, D. Pollacco, I. Skillen, F. Faedi, et al. DONUTS: A science frame autoguiding algorithm with sub-pixel precision, capable of guiding on defocused stars. *Publications of the Astronomical Society of the Pacific*, 125(927):548, 2013.

G. A. McCue, J. G. Williams, and J. M. Morford. Optical characteristics of artificial satellites. *Planetary and Space Science*, 19(8):851–868, 1971.

J. C. McDowell. The Low Earth Orbit Satellite Population and Impacts of the SpaceX Starlink Constellation. *The Astrophysical Journal Letters*, 892(2):L36, 2020.

J. T. McGraw, P. C. Zimmer, and M. R. Ackermann. Ever Wonder What's in Molniya? We Do. In *Proceedings of the Advanced Maui Optical and Space Surveillance (AMOS) Technology Conference*, page 107, 2017.

D. McKnight. Pay me now or pay me more later: start the development of active orbital debris removal now. In *Proceedings of the Advanced Maui Optical and Space Surveillance (AMOS) Technologies Conference*, 2010.

D. McKnight, R. Arora, and R. Witner. Intact Derelict Deposition Study. In *International Orbital Debris Conference (IOC)*, 2019.

D. S. McKnight and F. R. Di Pentino. New insights on the orbital debris collision hazard at GEO. *Acta Astronautica*, 85:73–82, 2013.

A. Medina, A. Tomassini, M. Suatoni, M. Avilés, et al. Towards a standardized grasping and refuelling on-orbit servicing for geo spacecraft. *Acta Astronautica*, 134:1–10, 2017.

D. Mehrholz, L. Leushacke, W. Flury, R. Jehn, et al. Detecting, tracking and imaging space debris. *ESA Bulletin(0376-4265)*, (109):128–134, 2002.

W. P. Menzel and J. F. W. Purdom. Introducing GOES-I: The first of a new generation of geostationary operational environmental satellites. *Bulletin of the American Meteorological Society*, 75(5):757–782, 1994.

S. R. Messenger, F. Wong, B. Hoang, C. D. Cress, et al. Low-thrust geostationary transfer orbit (LT2GEO) radiation environment and associated solar array degradation modeling and ground testing. *IEEE Transactions on Nuclear Science*, 61 (6):3348–3355, 2014.

M. Micheli, A. Buzzoni, D. Koschny, G. Drolshagen, et al. The observing campaign on the deep-space debris WT1190F as a test case for short-warning NEO impacts. *Icarus*, 304:4–8, 2018.

I. Molotov, V. Agapov, V. Titenko, Z. Khutorovsky, et al. International Scientific Optical Network for space debris research. *Advances in Space Research*, 41(7): 1022–1028, 2008.

I. Molotov, V. Agapov, Z. Khutorovsky, V. Titenko, et al. Faint high orbit debris observations with ISON optical network. In *Proceedings of the Advanced Maui Optical and Space Surveillance (AMOS) Technologies Conference*, volume 21, 2009.

I. Molotov, M. Zakhvatkin, L. Elenin, L. C. Ros, et al. ISON network tracking of space debris: current status and achievements. *Revista Mexicana de Astronomía y Astrofísica*, 51:144–149, 2019.

F. J. Montojo, T. L. Moratalla, and C. Abad. Astrometric positioning and orbit determination of geostationary satellites. *Advances in Space Research*, 47(6):1043–1053, 2011.

T. J. Muelhaupt, M. E. Sorge, J. Morin, and R. S. Wilson. Space traffic management in the new space era. *Journal of Space Safety Engineering*, 6(2):80–87, 2019.

J. Murray-Krezan, S. Howard, P. D. Dao, and D. Surka. GEO collisional risk assessment based on analysis of NASA-WISE data and modeling. Technical report, Air Force Research Laboratory Kirtland AFB United States, 2015.

J. Murray-Krezan, K. Meng, and P. Seitzer. Estimation of the GEO belt debris population by two independent remote sensing techniques. *Optical Engineering*, 58(4):41608, 2019.

A. M. Nafi and D. Geller. Survey Design for Small Autonomous Ground-Based Telescopes To Detect Uncontrolled/Debris GEO Objects. *Proceedings of the Advanced*

Maui Optical and Space Surveillance (AMOS) Technologies Conference, page 68, 2019.

NASA. Orbital Debris Program Office. *Quaterly News*, 12(2), 2008.

NASA. Orbital Debris Program Office. *Quaterly News*, 15(3), 2011.

NASA. Orbital Debris Program Office. *Quaterly News*, 18(3), 2014.

NASA. Orbital Debris Program Office. *Quaterly News*, 19(1), 2015a.

NASA. Orbital Debris Program Office. *Quaterly News*, 19(4), 2015b.

NASA. Orbital Debris Program Office. *Quaterly News*, 24(1), 2020.

G. Nir, B. Zackay, and E. O. Ofek. Optimal and efficient streak detection in astronomical images. *The Astronomical Journal*, 156(5):229, 2018.

S.-I. Nishida and S. Kawamoto. Strategy for capturing of a tumbling space debris. *Acta Astronautica*, 68(1-2):113–120, 2011.

S.-I. Nishida, S. Kawamoto, Y. Okawa, F. Terui, et al. Space debris removal system using a small satellite. *Acta Astronautica*, 65(1-2):95–102, 2009.

G. W. Ojakangas, H. Cowardin, and N. Hill. Toward Realistic Dynamics of Rotating Orbital Debris, and Implications for Lightcurve Interpretation. *Proceedings of the Advanced Maui Optical and Space Surveillance (AMOS) Technology Conference*, 2011.

D. L. Oltrogge, S. Alfano, C. Law, A. Cacioni, et al. A comprehensive assessment of collision likelihood in Geosynchronous Earth Orbit. *Acta Astronautica*, 147: 316–345, 2018.

D. L. Oltrogge, T. S. Kelso, and T. Carrico. Characterizing the India ASAT Debris Evolution using Diverse Complimentary Tools. *Astrodynamics Specialist Conference, Portland, ME*, 2019. URL http://celestrak.com/publications/AAS/19-889/.

J. T. Olympio and N. Frouvelle. Space debris selection and optimal guidance for removal in the SSO with low-thrust propulsion. *Acta Astronautica*, 99:263–275, 2014.

J. E. Palmer, B. Hennessy, M. Rutten, D. Merrett, et al. Surveillance of Space using passive radar and the Murchison Widefield Array. In *2017 IEEE radar conference (Radarconf)*, pages 1715–1720. IEEE, 2017.

P. Papushev, Y. Karavaev, and M. Mishina. Investigations of the evolution of optical characteristics and dynamics of proper rotation of uncontrolled geostationary artificial satellites. *Advances in Space Research*, 43(9):1416–1422, 2009.

C. Pardini. Survey of past on-orbit fragmentation events. *Acta Astronautica*, 56(3): 379–389, 2005.

C. Pardini and L. Anselmo. Review of past on-orbit collisions among cataloged objects and examination of the catastrophic fragmentation concept. *Acta Astronautica*, 100:30–39, 2014.

C. Pardini and L. Anselmo. Characterization of abandoned rocket body families for active removal. *Acta Astronautica*, 126:243–257, 2016.

C. Pardini and L. Anselmo. Environmental sustainability of large satellite constellations in low earth orbit. *Acta Astronautica*, 170:27–36, 2020.

C. Pardini, T. Hanada, and P. H. Krisko. Benefits and risks of using electrodynamic tethers to de-orbit spacecraft. *Acta Astronautica*, 64(5-6):571–588, 2009.

S.-Y. Park, J. Choi, D.-G. Roh, M. Park, et al. Development of a data reduction algorithm for optical wide field patrol (OWL) II: improving measurement of lengths of detected streaks. *Journal of Astronomy and Space Sciences*, 33(3): 221–227, 2016.

R. Peldszus and P. Faucher. European Space Surveillance and Tracking Support Framework. *Handbook of Space Security: Policies, Applications and Programs*, pages 883–904, 2020.

A. Petit, D. Casanova, M. Dumont, and A. Lemaître. Creation of a synthetic population of space debris to reduce discrepancies between simulation and observations. *Celestial Mechanics and Dynamical Astronomy*, 130(12):79, 2018.

C. R. Phipps, K. L. Baker, S. B. Libby, D. A. Liedahl, et al. Removing orbital debris with lasers. *Advances in Space Research*, 49(9):1283–1300, 2012.

F. Piergentili, F. Santoni, and P. Seitzer. Attitude determination of orbiting objects from lightcurve measurements. *IEEE Transactions on Aerospace and Electronic Systems*, 53(1):81–90, 2017.

L. Pirovano, G. Principe, and R. Armellin. Data association and uncertainty pruning for tracks determined on short arcs. *Celestial Mechanics and Dynamical Astronomy*, 132(1):1–23, 2020a.

L. Pirovano, D. A. Santeramo, R. Armellin, P. Di Lizia, et al. Probabilistic data association: the orbit set. *Celestial Mechanics and Dynamical Astronomy*, 132 (2):1–27, 2020b.

J.-N. Pittet, J. Šilha, and T. Schildknecht. Spin motion determination of the Envisat satellite through laser ranging measurements from a single pass measured by a single station. *Advances in space research*, 61(4):1121–1131, 2018.

D. L. Pollacco, I. Skillen, A. C. Cameron, D. J. Christian, et al. The WASP project and the SuperWASP cameras. *Publications of the Astronomical Society of the Pacific*, 118(848):1407, 2006.

D. S. F. Portree. *Orbital debris: A chronology*. NASA, 1999.

A. M. Price-Whelan, B. M. Sipőcz, H. M. Günther, P. L. Lim, et al. The Astropy project: Building an open-science project and status of the v2. 0 core package. *The Astronomical Journal*, 156(3):123, 2018.

G. Privett, S. George, W. Feline, A. Ash, et al. An Autonomous Data Reduction Pipeline for Wide Angle EO Systems. In *Proceedings of the Advanced Maui Optical and Space Surveillance (AMOS) Technologies Conference*, 2017.

J. Radtke and E. Stoll. Comparing long-term projections of the space debris environment to real world data–Looking back to 1990. *Acta Astronautica*, 127:482–490, 2016.

J. Radtke, C. Kebschull, and E. Stoll. Interactions of the space debris environment with mega constellations—Using the example of the OneWeb constellation. *Acta Astronautica*, 131:55–68, 2017.

R. P. Rajagopalan. India's changing policy on space militarization: The impact of China's ASAT test. *India Review*, 10(4):354–378, 2011.

J. Read, J. C. Liou, H. Cowardin, M. Mulrooney, et al. Optical Measurements of Tumbling Rocket Bodies. *Proceedings of the Advanced Maui Optical and Space Surveillance (AMOS) Technologies Conference*, page 86, 2012.

D. Reintsema, J. Thaeter, A. Rathke, W. Naumann, et al. DEOS–the German robotics approach to secure and de-orbit malfunctioned satellites from low earth orbits. In *Proceedings of the i-SAIRAS*, pages 244–251. Japan Aerospace Exploration Agency (JAXA) Japan, 2010.

B. A. Renfro, M. Stein, N. Boeker, and A. Terry. An analysis of global positioning system (GPS) standard positioning service (SPS) performance for 2017. *Applied Research Laboratories, The University of Texas at Austin*, 2018.

B. Rhodes. Skyfield: High precision research-grade positions for planets and Earth satellites generator. *Astrophysics Source Code Library*, pages ascl–1907, 2019.

T. P. Robitaille, E. J. Tollerud, P. Greenfield, M. Droettboom, et al. Astropy: A community Python package for astronomy. *Astronomy & Astrophysics*, 558:A33, 2013.

A. Rossi, C. Pardini, L. Anselmo, A. Cordelli, et al. Effects of the RORSAT NaK drops on the long term evolution of the space debris population. In *48th International Astronautical Congress*, 1997.

A. Rossi, L. Anselmo, C. Pardini, R. Jehn, et al. The new space debris mitigation (SDM 4.0) long term evolution code. In *Proceedings of the Fifth European Conference on Space Debris, ESA SP-672, CD-ROM, ESA Communication Production Office, Noordwijk, The Netherlands*, 2009.

W. Ryan and E. Ryan. Photometric studies of rapidly spinning decommissioned GEO satellites. In *Proceedings of the Advanced Maui Optical and Space Surveillance (AMOS) Technology Conference*, 2015.

L. V. Rykhlova, T. V. Kasimenko, A. M. Mikisha, and M. A. Smirnov. Explosions in the geostationary orbit. *Advances in Space Research*, 19(2):313–319, 1997.

L. V. Rykhlova, A. V. Bagrov, S. I. Barabanov, T. V. Kasimenko, et al. Search and observations of space debris and near earth objects at Inasan. *Advances in Space Research*, 28(9):1301–1307, 2001.

F. Santoni, E. Cordelli, and F. Piergentili. Determination of disposed-upper-stage attitude motion by ground-based optical observations. *Journal of Spacecraft and Rockets*, 50(3):701–708, 2013.

A. V. Schaeperkoetter. *A comprehensive comparison between angles-only initial orbit determination techniques*. PhD thesis, Texas A & M University, 2012.

T. Schildknecht. Optical surveys for space debris. *The Astronomy and Astrophysics Review*, 14(1):41–111, 2007.

T. Schildknecht, U. Hugentobler, and A. Verdun. Algorithms for ground based optical detection of space debris. *Advances in Space Research*, 16(11):47–50, 1995.

T. Schildknecht, R. Musci, M. Ploner, W. Flury, et al. An optical search for small-size debris in GEO and GTO. In *Proceedings of the Advanced Maui Optical and Space Surveillance (AMOS) Technologies Conference*, pages 1–11, 2003.

T. Schildknecht, R. Musci, M. Ploner, G. Beutler, et al. Optical observations of space debris in GEO and in highly-eccentric orbits. *Advances in Space Research*, 34(5):901–911, 2004.

T. Schildknecht, R. Musci, and T. Flohrer. Properties of the high area-to-mass ratio space debris population at high altitudes. *Advances in Space Research*, 41 (7):1039–1045, 2008a.

T. Schildknecht, R. Musci, C. Früh, and M. Ploner. Color photometry and light curve observations of space debris in GEO. In *Proceedings of the Advanced Maui Optical and Space Surveillance (AMOS) Technology Conference*, pages 17–19, 2008b.

T. Schildknecht, E. Linder, J. Silha, M. Hager, et al. Photometric monitoring of non-resolved space debris and databases of optical light curves. In *Proceedings of the Advanced Maui Optical and Space Surveillance (AMOS) Technology Conference*, page 25, 2015.

T. Schildknecht, A. Vananti, E. Cordelli, and T. Flohrer. ESA optical surveys to characterize recent fragmentation events in GEO and HEO. *Proceedings of the Advanced Maui Optical and Space Surveillance (AMOS) Technologies Conference*, page 34, 2019.

J. Schmetz, P. Pili, S. Tjemkes, D. Just, et al. An introduction to Meteosat second generation (MSG). *Bulletin of the American Meteorological Society*, 83(7):977–992, 2002.

R. Scott and B. Wallace. Satellite characterization using small aperture instruments at DRDC Ottawa. In *Proceedings of the Advanced Maui Optical and Space Surveillance (AMOS) Technologies Conference*, pages 337–347, 2008.

P. Seitzer. Large Constellations of LEO Satellites and Astronomy. In *Proceedings of the Advanced Maui Optical and Space Surveillance (AMOS) Technologies Conference*, 2020.

P. Seitzer, R. Smith, J. Africano, K. Jorgensen, et al. MODEST observations of space debris at geosynchronous orbit. *Advances in Space Research*, 34(5):1139–1142, 2004.

P. Seitzer, H. M. Cowardin, E. Barker, K. J. Abercromby, et al. Optical photometric observations of GEO debris. In *Proceedings of the Advanced Maui Optical and Space Surveillance (AMOS) Technology Conference*, pages 14–17, 2010.

P. Seitzer, S. M. Lederer, E. S. Barker, H. Cowardin, et al. A search for optically faint GEO debris. Technical report, National Aeronautics and Space Administration Houston TX Lyndon B. Johnson, 2011.

P. Seitzer, S. M. Lederer, H. Cowardin, T. Cardona, et al. Visible Light Spectroscopy of GEO Debris. 2012.

P. Seitzer, E. Barker, B. Buckalew, A. Burkhardt, et al. The Population of Optically Faint GEO Debris. In *Proceedings of the Advanced Maui Optical and Space Surveillance (AMOS) Technologies Conference*, 2016.

P. Seitzer, E. Barker, B. Buckalew, A. Burkhardt, et al. A Search for Debris from Two Titan 3C Transtage Breakups at GEO with a 6.5-m Magellan Telescope. *Proceedings of the Advanced Maui Optical and Space Surveillance (AMOS) Technologies Conference*, page 33, 2017.

J. Serra and P. Soille. *Mathematical morphology and its applications to image processing*, volume 2. Springer Science & Business Media, 2012.

T. J. Settecerri, E. G. Stansbery, and M. J. Matney. Haystack measurements of the orbital debris environment. *Advances in Space Research*, 23(1):13–22, 1999.

T. J. Settecerri, A. D. Skillicorn, and P. C. Spikes. Analysis of the eglin radar debris fence. *Acta Astronautica*, 54(3):203–213, 2004.

L. S. Shakun and N. I. Koshkin. Determination of visible coordinates of the low-orbit space objects and their photometry by the CCD camera with the analogue output. Initial image processing. *Advances in Space Research*, 53(12):1834–1847, 2014.

M. Shan, J. Guo, and E. Gill. Review and comparison of active space debris capturing and removal methods. *Progress in Aerospace Sciences*, 80:18–32, 2016.

M. Shan, J. Guo, and E. Gill. Contact dynamic models of space debris capturing using a net. *Acta Astronautica*, 158:198–205, 2019.

A. K. Sharma and N. Sridhara. Degradation of thermal control materials under a simulated radiative space environment. *Advances in space research*, 50(10): 1411–1424, 2012.

H.-X. Shen, T.-J. Zhang, L. Casalino, and D. Pastrone. Optimization of active debris removal missions with multiple targets. *Journal of Spacecraft and Rockets*, 55(1):181–189, 2018.

M. Siergiejczyk, A. Rosiński, and K. Krzykowska. Reliability assessment of supporting satellite system EGNOS. In *New Results in Dependability and Computer Systems*, pages 353–363. Springer, 2013.

J. Šilha, T. Schildknecht, A. Hinze, T. Flohrer, et al. An optical survey for space debris on highly eccentric and inclined MEO orbits. *Advances in space research*, 59(1):181–192, 2017a.

J. Šilha, T. Schildknecht, J. N. Pittet, A. Rachman, et al. Extensive light curve database of Astronomical Institute of the University of Bern. In *Proc. of 7th European Conference on Space Debris, Darmstadt, Germany*, 2017b.

J. Šilha, J.-N. Pittet, M. Hamara, and T. Schildknecht. Apparent rotation properties of space debris extracted from photometric measurements. *Advances in space research*, 61(3):844–861, 2018.

J. Šilha, S. Krajčovič, M. Zigo, J. Tóth, et al. Space debris observations with the Slovak AGO70 telescope: Astrometry and light curves. *Advances in Space Research*, 2020.

E. Stansbery and T. Settecerri. A comparison of Haystack and HAX measurements of the orbital debris environment. In *Second European Conference on Space Debris*, volume 393, page 59, 1997.

E. G. Stansbery, D. J. Kessler, T. E. Tracy, M. J. Matney, et al. Characterization of the orbital debris environment from Haystack radar measurements. *Advances in Space Research*, 16(11):5–16, 1995.

G. Stansbery, M. Matney, J.-C. Liou, and D. Whitlock. A comparison of catastrophic on-orbit Collisions. In *Proceedings of the Advanced Maui Optical and Space Surveillance (AMOS) Technology Conference*, page E50, 2008.

C. L. Stokely, E. G. Stansbery, and R. M. Goldstein. Debris flux comparisons from the Goldstone Radar, Haystack Radar, and Hax Radar prior, during, and after the last solar maximum. *Advances in Space research*, 44(3):364–370, 2009.

M. Sznajder, U. Geppert, and M. Dudek. Degradation of metallic surfaces under space conditions, with particular emphasis on Hydrogen recombination processes. *Advances in space research*, 56(1):71–84, 2015.

A. Tan and R. Ramachandran. Velocity perturbations analysis of the Spot 1 Ariane rocket fragmentation. *The Journal of the Astronautical Sciences*, 53(1):39–50, 2005.

A. Tan and R. C. Reynolds. *Theory Of Satellite Fragmentation In Orbit*. World Scientific, 2019.

A. Tan, G. D. Badhwar, F. A. Allahdadi, and D. F. Medina. Analysis of the Solwind fragmentation event using theory and computations. *Journal of spacecraft and rockets*, 33(1):79–85, 1996.

A. Tan, R. C. Reynolds, and M. Schamschula. NOAA-16 Satellite Fragmentation in Orbit: Genesis of the Gabbard Diagram and Estimation of the Intensity of Breakup. *Adv. Aerospace Sci. Appl*, 7:37–47, 2017.

S.-Y. Tan. *Meteorological satellite systems*. Springer Science & Business Media, 2013.

B. Thompson, J. R. Gossner, B. J. Sais, and E. A. Cunningham. Fast Covariance Propagation for Two-Line Element Sets. In *Proceedings of the Advanced Maui Optical and Space Surveillance (AMOS) Technologies Conference*, 2019.

Y. Tian, L. Sui, G. Xiao, D. Zhao, et al. Analysis of Galileo/BDS/GPS signals and RTK performance. *GPS Solutions*, 23(2):37, 2019.

C. Underwood, A. Viquerat, M. Schenk, B. Taylor, et al. InflateSail de-orbit flight demonstration results and follow-on drag-sail applications. *Acta Astronautica*, 162:344–358, 2019.

D. Vallado and P. Crawford. SGP4 orbit determination. In *AIAA/AAS Astrodynamics Specialist Conference and Exhibit*, page 6770, 2008.

D. Vallado, P. Crawford, R. Hujsak, and T. S. Kelso. Revisiting spacetrack report# 3. In *AIAA/AAS Astrodynamics Specialist Conference and Exhibit*, page 6753, 2006.

D. A. Vallado and P. J. Cefola. Two-line element sets–practice and use. In *63rd International Astronautical Congress, Naples, Italy*, 2012.

D. A. Vallado and J. D. Griesbach. Simulating space surveillance networks. In *Paper AAS 11-580 presented at the AAS/AIAA Astrodynamics Specialist Conference. July*, 2011.

P. G. Van Dokkum. Cosmic-ray rejection by Laplacian edge detection. *Publications of the Astronomical Society of the Pacific*, 113(789):1420, 2001.

A. Vananti, T. Schildknecht, and H. Krag. Reflectance spectroscopy characterization of space debris. *Advances in space research*, 59(10):2488–2500, 2017.

Q. Verspieren. Opening Keynote: Day 2 at the Advanced Maui Optical and Space Surveillance (AMOS) Technologies Conference, September 17, 2020. URL http://dx.doi.org/10.13140/RG.2.2.18428.16006.

R. Walker, C. E. Martin, P. H. Stokes, J. E. Wilkinson, et al. Analysis of the effectiveness of space debris mitigation measures using the DELTA model. *Advances in Space Research*, 28(9):1437–1445, 2001.

T. Wang. Analysis of Debris from the Collision of the Cosmos 2251 and the Iridium 33 Satellites. *Science & Global Security*, 18(2):87–118, 2010.

Brian Weeden. US Policy and Capabilities on SSA. In *Perspectives on the Future Directions for Korea, Seoul, South Korea*, 2019. URL https://swfound.org/media/206348/weeden-us-policy-and-capabilities-for-ssa.pdf.

C. J. Wetterer and M. Jah. Attitude determination from light curves. *Journal of Guidance, Control, and Dynamics*, 32(5):1648–1651, 2009.

A. E. White and H. G. Lewis. The many futures of active debris removal. *Acta Astronautica*, 95:189–197, 2014.

C. Wiedemann, M. Oswald, S. Stabroth, H. Klinkrad, et al. Size distribution of NaK droplets released during RORSAT reactor core ejection. *Advances in Space Research*, 35(7):1290–1295, 2005.

S. Wootton. Enabling GEODSS for Space Situational Awareness (SSA). In *Proceedings of the Advanced Maui Optical and Space Surveillance (AMOS) Technology Conference*, 2016.

K. Wormnes, R. Le Letty, L. Summerer, R. Schonenborg, et al. ESA technologies for space debris remediation. In *6th European Conference on Space Debris*, volume 1, pages 1–8. ESA Communications ESTEC Noordwijk, The Netherlands, 2013.

W. Xu, B. Liang, B. Li, and Y. Xu. A universal on-orbit servicing system used in the geostationary orbit. *Advances in Space Research*, 48(1):95–119, 2011.

T. Yanagisawa and H. Kurosaki. Shape and motion estimate of LEO debris using light curves. *Advances in Space Research*, 50(1):136–145, 2012.

T. Yanagisawa, A. Nakajima, K.-I Kadota, H. Kurosaki, et al. Automatic detection algorithm for small moving objects. *Publications of the Astronomical Society of Japan*, 57(2):399–408, 2005.

T. Yanagisawa, H. Kurosaki, H. Banno, Y. Kitazawa, et al. Comparison between four detection algorithms for geo objects. In *Proceedings of the Advanced Maui Optical and Space Surveillance (AMOS) Technologies Conference*, 2012.

T. Yasaka, T. Hanada, and H. Hirayama. GEO debris environment: a model to forecast the next 100 years. *Advances in Space Research*, 23(1):191–199, 1999.

S. Yun and R. Zanetti. Nonlinear filtering of light-curve data. *Advances in Space Research*, 66(7):1672–1688, 2020.

M. Ziebart, S. Adhya, A. Sibthorpe, S. Edwards, et al. Combined radiation pressure and thermal modelling of complex satellites: Algorithms and on-orbit tests. *Advances in Space Research*, 36(3):424–430, 2005.

M. Zigo, J. Šilha, and S. Krajcovic. BVRI photometry of space debris objects at the astronomical and geophysical observatory in Modra. In *Proceedings of the Advanced Maui Optical and Space Surveillance (AMOS) Technology Conference*, 2019.

P. C. Zimmer, M. R. Ackermann, and J. T. McGraw. GPU-accelerated faint streak detection for uncued surveillance of LEO. In *Proceedings of the Advanced Maui Optical and Space Surveillance (AMOS) Technologies Conference*, 2013.